

The Mixed Glass Former Effect- Modeling of the Structure and Ionic Hopping Transport

Dissertationsschrift zur Erlangung des akademischen Grades
Doktor der Naturwissenschaften (Dr. rer. nat.)
des Fachbereiches Physik der Universität Osnabrück

vorgelegt von

Dipl.-Ing. Michael Schuch

geboren am 09.09.1980 in Erfurt

Betreuer: Prof. Dr. Philipp Maass

Datum der Verteidigung: 28. 02. 2013

"Numquam ponenda est pluralitas sine necessitate"
"Plurality must never be posited without necessity"
William of Ockham (1285-1349)

Kurzzusammenfassung

Die vorliegende Arbeit behandelt den *Mischglasbildnerereffekt* (engl. *mixed glass former effect*, MGFE). Dieser zeichnet sich durch eine nichtmonotone Abhängigkeit der Aktivierungsenergie für den Ionentransport vom Mischungsgrad aus, wenn eine Glasbildnerspezies teilweise durch eine andere substituiert wird.

Das Hauptaugenmerk dieser Arbeit liegt auf der Entwicklung und Diskussion zweier Modellkonzepte, das *Mischbarrierenmodell* und das *Netzwerkeinheitenfallenmodell*. Diese Modelle beschreiben verschiedene Mechanismen die den MGFE verursachen können.

Das *Mischbarrierenmodell* geht von der Vermutung aus, dass Energiebarrieren, welche die Kationen überwinden müssen, um von einem Kationenplatz zu einem anderen zu gelangen, durch die Mischung zweier Glasbildner beeinflusst werden. Das bedeutet, dass sie in Gebieten mit gemischter Zusammensetzung im Vergleich zu reinen Gebieten verringert sind. Ausgehend von dieser Vermutung wird mit Hilfe von Perkolationsargumenten ein mathematischer Ausdruck entwickelt, der das Verhalten der Aktivierungsenergie in Abhängigkeit der Glasbildnerzusammensetzung für eine Reihe von Gläsern beschreibt.

Alternativ zu diesem Modell wurde das *Netzwerkeinheitenfallenmodell* entwickelt, das unter anderem dazu geeignet ist, den MGFE in Alkali-Borophosphaten zu beschreiben. Dieses Modell geht von der Tatsache aus, dass die effektiven Ladungen einer Glasbidereinheit auf die ladungstragenden Sauerstoffe verteilt werden. Die damit verbundene Verschmierung der Ladungsverteilung beeinträchtigt die Platzenergien angrenzender Kationenplätze. Durch dieses Modell ist es möglich den eindeutigen Zusammenhang zwischen der Aktivierungsenergie und den Konzentrationen der verschiedenen Borat- und Phosphateinheiten zu verstehen. Diese Borat- und Phosphateinheiten unterscheiden sich durch die Anzahl verbrückender Sauerstoffe, die mit dem Zentralatom verbunden sind. Um die Konzentration dieser sog. $Q^{(n)}$ -Spezies vorherzusagen, wird ein Netzwerkmodell für Borophosphate diskutiert. Dieses Modell stellt in Kombination mit dem NUT-Modell einen vielversprechenden Ansatz für den MGFE in Alkali-Borophosphatgläsern dar.

Zusätzlich zu den oben erwähnten Fragestellungen wird in dieser Arbeit eine *Reverse Monte Carlo*- (RMC) Studie an Natrium-Borophosphaten basierend auf Röntgen- und Neutronenstreudaten vorgestellt. Hierbei lag das Hauptaugenmerk auf der Untersuchung des Einflusses struktureller Eigenschaften auf den MGFE. Dabei wurde zum Beispiel untersucht, ob die von Swenson und Adams postulierte Beziehung zwischen Aktivierungsenergie und Volumenanteil der Transportpfade auch in Natrium-Borophosphatgläsern zu finden ist. Dieser Zusammenhang konnte jedoch in der vorliegenden Arbeit nicht bestätigt werden.

Abstract

The present work examines the *Mixed Glass Former Effect* (MGFE) which is characterized by a non-monotonous relation between the activation energy for long range transport of mobile cations and the mixing ration between two glass formers, if one of them is replaced by the other one.

Most notably two models are proposed, the *mixed barrier model* and the *network unit trap* model. These concepts describe distinct mechanisms accounting for the MGFE. The *mixed barrier* model is based on the assumption that energy barriers between the sites of the cations are affected by the mixing of the glass formers. This means that these energy barriers are reduced in regions of mixed composition. Combining this concept with percolation arguments a mathematical expression is developed which accounts for the behavior of the activation energy in dependency of the glass former mixing in several ion conducting glasses. The *network unit trap* model is mainly developed for the explanation of the MGFE in alkali borophosphate glasses. It is based on the fact that effective charges have to be distributed over all charge carrying oxygens of the glass forming units. This spreading of the charge affects then the binding energies of nearby alkali ion sites. This approach successfully connects the change in the activation energy with the concentration of the different borate and phosphate species. These species are distinct in respect to the number of bridging oxygens bonded to the central atom. To predict the concentrations of these so called $Q^{(n)}$ species a network model was applied. In combination with the *network unit trap* approach a promising approach for the understanding of the MGFE in borophosphate glasses is established.

Additionally, a *Reverse Monte Carlo* (RMC) study on sodium borophosphate glasses is presented in this work, which utilizes neutron and X-ray diffraction data. The purpose of these studies is the examination of influence of structural features on the MGFE. In particular, the relationship between activation energy and and the volume fraction of the conduction pathways, as postulated by Swenson and Adams, was revisited in the RMC study. Nevertheless, this theory could not be verified in the present work.

Contents

1. Introduction	2
1.1. Possible applications of fast ion conducting glasses and mixed glass former systems	6
1.2. The mixed glass former effect in various systems	9
1.3. Some remarks on theoretical concepts of ionic transport in glasses	11
1.4. Outline and aim of the present thesis	16
2. Mixed Barrier Model for the Mixed Glass Former Effect in Ion Conducting Glasses¹	19
3. The Effect of Spatially Correlated Barrier Energies on the Frequency-Dependent Conductivity	27
3.1. Introduction	28
3.2. Effects of correlated barrier energies	29
3.2.1. Generation of uniformly distributed barrier energies with spatial correlations	29
3.2.2. Discussion of the influence of correlations	30
3.3. Summary	33
4. Network Forming Units in Alkali Borate and Borophosphate Glasses and the Mixed Glass Former Effect²	34
4.1. Introduction	35
4.2. NFU concentrations in alkali borate glasses	36
4.2.1. Beekenkamp model	37
4.2.2. Constant fraction of B ⁽⁴⁾ -B ⁽⁴⁾ linkages	39
4.2.3. Balancing mutually linked B ⁽⁴⁾ with B ⁽²⁾ units	40
4.3. NFU concentrations in alkali borophosphate glasses	41
4.3.1. $\{\mathbf{M}\} \geq \{\mathbf{M}\}_*$: Constant fraction of B ⁽⁴⁾ -B ⁽⁴⁾ linkages	45
4.3.2. $\{\mathbf{M}\} \geq \{\mathbf{M}\}_*$: Mutual balancing of phosphate unit fractions	48
4.3.3. $\{\mathbf{M}\} \geq \{\mathbf{M}\}_*$: B ⁽⁴⁾ -B ⁽⁴⁾ linkages constrained by P ⁽²⁾ units	50
4.4. Modeling of the effect of different NFU types on the activation energy	52

¹This chapter is published as: M. Schuch, C. R. Müller, P. Maass and, S. W. Martin, *Phys. Rev. Lett.*, **102**, 145902, (2009)

²This chapter is published as: M. Schuch, C. Trott, and P. Maass, *RSC Adv.*, **1**, 1370, (2011)

4.5. Summary	57
5. Discussion and Extended Application of the Modeling in Chapter 4	61
5.1. Introduction	62
5.2. Further modeling of the NFU concentrations	63
5.2.1. Discussion of the f -Parameter	63
5.2.2. NFU concentrations for other stoichiometries of sodium borophosphate glasses	64
5.2.3. An alternative scenario for the low $\{M\}$ regime in sec. 4.3	70
5.3. Further remarks on the NUT approach	73
5.3.1. Calculation of the site energy distribution	73
5.3.2. The activation energy for long range transport	76
5.3.3. The MICE effect in binary alkali borate glasses	81
5.4. Summary	84
6. Investigation of the Structures of Sodium Borophosphate Glasses by Reverse Monte Carlo Modeling to Examine the Origins of the Mixed Glass Former Effect³	86
6.1. Introduction	87
6.2. RMC modeling: Global constraints and simulation procedure	89
6.2.1. RMC Model A: No incorporation of further information on $Q^{(n)}$ -species concentrations	93
6.2.2. RMC Model B: Phosphate groups limited to $P^{(2)}$ and $P^{(3)}$ groups	93
6.2.3. RMC Model C: Consideration of oxygen coordination around sodium ions	94
6.3. The bridging oxygen connectivity and partial pair distribution functions	96
6.4. Volume fraction of conduction pathways compared to the activation energy	101
6.5. Summary and outlook	103
7. Improvement of the RMC Models from Chapter 6 by Inclusion of Neutron Diffraction Data	105
7.1. Introduction	106
7.2. Methodology	109
7.3. Results and discussion	109
7.4. Summary	118
7.5. Appendix: Constraining the number of bOs connecting two $B^{(4)}$	118
8. Summary and Conclusions	121
A. Testing the Mean Field Approach for Hopping Transport in Disordered Energy Landscapes on the Basis of a novel Linearized Pair Approximation	I

³This chapter is published as: M. Schuch, R. Christensen, C. Trott, P. Maass, and S. W. Martin, *J. Phys. Chem. C.*, **116**, 1503, (2012)

B. References	VII
C. List of Figures	XVII
D. Acknowledgments	XXV

1. Introduction

Glasses belong to the oldest materials utilized by mankind. Natural glasses (e.g. obsidian) have been used since the stone age and the first evidence of artificial glass production dates back approximately 3500 years. Despite this long history of glasses, many questions related to the physical and chemical behavior, like the exact nature of glass transition, are still not fully answered.

An important class of glasses are so-called network glasses of general chemical composition X_nY_m , where X are elements like Si, B or P and Y are O or S. As their crystalline analogues, these systems are built of well-defined structures on short length scales, but like all other glasses they do not show long range translational symmetry. The short-range structures¹ consist of a central atom X , which are coordinated in a well-prescribed manner by atoms of the element Y , which connect two atoms of type X with each other. The addition of metal-cations, like Li^+ , Na^+ , Ag^+ or Ca^{2+} increases, in many cases, the ability of the material to form a glass and decreases also the glass formation temperature T_g . A possible explanation for this effect was given 1932 by Zachariassen [1](see fig 1.1). He proposed a model where two kinds of Y atoms exist. The first one connects two X -atoms with each other, it will be denoted in the present work as bridging Y atom (b Y). In contrast, only one glass forming unit is bonded to the second class of Y -atoms. This Y -atom will be indicated in the present work as non-bridging Y (nb Y). In the original version of the Zachariassen model the glass forming units form a continuous random network, where the X atoms are considered as nodes, which are linked by the b Y atoms. In comparison to the mostly covalent bonds between X and Y the cations Z bond weakly to the Y atoms. As a consequence, the typical timescales of the cation dynamics are several order of magnitudes smaller than the typical relaxation times of the network. In the case of monovalent cations one could consider the cations as freely diffusing between sites formed by the glassy network, which can be considered in first approximation as frozen on the timescales, which are relevant for the cation dynamics. This movement of cations in network glasses and its temperature dependency is known since the early 19th century [2] and the mobility of alkali ions was investigated first by the German Emil Warburg [3].

If the mobility and the number density of the cations in the glass are high enough, an applied electrical field gives rise to a significant current. In this case these modified glasses

¹In the present work these structures are denoted as *units*

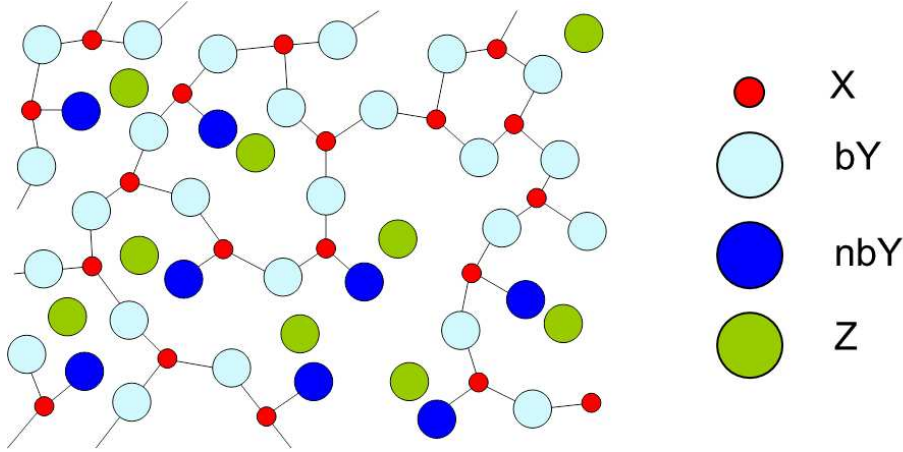


Figure 1.1.: Sketch of the original version of the Zachariasen model [1] for network-forming glasses (for details see text)

are called ion conducting glasses². These materials are in the focus of the present work, since they are considered as promising material systems with a notable industrial impact due to their physical and chemical properties. These properties allow applications as solid state electrolytes in rechargeable batteries, super-capacitors, electro-chrome windows and chemical sensors. This issue will be reviewed in more detail in sec. 1.1 because in literature this topic is touched usually on a very cursory level. From the point of an interested scientific reader this fact is unsatisfying because further information about topics like underlying physical principles or alternative realizations are missing. In addition, a large number of alternatives of solid state electrolyte materials to glasses exists, e.g. polymeric, ceramic, crystalline and glassy systems. Typically literature about this issue is focused on the preferred material-system of the corresponding authors. As an example for this issue one could refer to an excellent and much cited review article on lithium batteries, which elaborately describes the progress in polymeric electrolyte systems but avoids mentioning alternatives, in particular inorganic crystalline and glassy electrolytes [4]. Hence, it seems to be fruitful to give some more detailed information about these issues, which will be done in sec. 1.1.

For many of the technical applications (see, e.g. sec. 1.1), a high cationic conductivity σ_{dc} is desired in a certain temperature range. This conductivity is related to the diffusion-constant $D_{lt} = \lim_{t \rightarrow \infty} \langle r^2(t) \rangle / (6t)$ via the Nernst-Einstein-relation ($\langle r^2 \rangle$ is the mean squared displacement as a function of time):

$$k_B T \sigma_{dc} = Z e n_c D_{lt} / H_R \quad (1.1)$$

where n_c are the number density and Ze the number of charges, which are generated by the cations. The Haven ratio H_R depends on the concentration of modifying cations and shows

²sometimes they are also called amorphous fast ion conductors

typically values in the order of 0.1-1 [5, 6, 7]. Assuming n_c and H_R are varying weakly with the temperature³, the strong temperature dependency of σ_{dc} is mainly affected by the Arrhenius-like temperature dependency of D_{lt} .

$$D_{lt} \propto \exp\left(-\frac{E_a}{k_B T}\right) \quad (1.2)$$

where E_a is the activation energy for long range transport which is typically in the order of $0.1 - 1 \text{ eV} \approx 4 - 40 k_B T$ (for room temperature).

This activation energy is strongly affected by the stoichiometry of the system. Therefore, this fact gives rise to several physico-chemical effects known in ion conducting network glasses, which are related to E_a [9]. A very prominent effect, which was ubiquitously found in ion conducting glasses, is the *mixed alkali effect* (MAE). The MAE is sometimes also referred as mixed mobile ion effect because it has been found for other monovalent cation types, which are different from alkali ions (e.g. Ag^+). This effect is characterized by the property that E_a is increased in a glass, which contains two different species of mobile cations A and B in comparison to systems, which contain exclusively one species A or B but the same mobile cation concentration. Typically, this effect is explained by the idea that sites are exclusively adapted to one cation species, i.e. there is an energetic mismatch if a cation of type A occupies a site which is more favorable for a cation B and vice versa [10, 11, 12, 13]. Therefore, the fraction of B favoring sites interfere with the long range transport of cation species A . This concept is supported by a large number of experimental data [14, 15, 16, 17].

For many technical applications it is desired to increase the conductivity by a minimization of E_a . A straightforward approach is the enhancement of the mobile cation concentration in the glass that results in a significant reduction of E_a . This *mobile ion concentration effect* (MICE) is reported for a large number of glassy ion conductors. In particular, it was found for several systems that the activation energy decreases in good approximation logarithmically with increasing cation concentration [11, 12]. Several origins for this effect are discussed in the literature: (i) filling of energy landscape with a fixed site-energy-distribution with exponential [11, 18] or gaussian shape [19], (ii) lowering of the hopping length [20], (iii) decreasing the cation-cation separation distance [21] and (iv) the dynamic formation of cation sites in the melt or the glass [11, 12, 13]. Nevertheless, the increasing of the cation concentration has the crucial disadvantage that further addition of cations strongly affects other properties, e.g. glass forming ability or mechanical durability. This fact limits therefore the applicability of the MICE to decrease E_a .

Alternatively, one can reduce E_a by preparing thio-analogues of the oxygen based network glasses [22]. The reduction of E_a is usually explained by the fact that the interaction between the mobile cations and the sulfur atoms is much weaker than the interaction between

³A weak temperature dependency for H_R is found in many systems [5, 6, 7]. One has to note Rb-doped borate glasses as an exceptional case, where H_R seems to be thermally activated [8]

the cations and the oxygen atoms. However, the chemical stability of thio-analogues is quite poor, for instance they show often a high degree of hygroscopy [23]. Hence, the application of this effect is also limited.

Another possibility to increase the conductivity is the addition of halide anions to the glass (*halide ion doping effect*, HIDE), which is well known particularly for Ag and Li ion conducting borate [24, 25], phosphate [22, 26, 27] and molybdate [28, 29] glasses. Different concepts were suggested to explain the HIDE. Tuller and Button [24] propose a decrease of compactness of the glass network by adding the halide salt (e.g. AgI in the case of Ag modified network glass). This mechanism results in a more open structure and lower typical barriers. The ideas of Tuller and Button were later supported by findings of Swenson and Börjesson [30]. These authors show that the room temperature conductivity is proportional to the cube of the relative volume expansion $((V_d - V_u)/V_u)$ between the glass former volume of the undoped glass V_u and the doped glass V_d . In a later review Swenson *et al.* [31] consider also the possibility of a kind of indirect correlation with other physical properties. An alternative explanation of the HIDE is the clustering of the halide anions in amorphous salt like regions [32, 33, 34]. This idea is supported by some quasi-elastic and inelastic neutron scattering data. For the sake of completeness it should be noted that Novita *et al.* [26] recently proposed a further alternative based on a combined Raman-/Infrared spectroscopy and conductivity study for silver phosphate glasses. By interpreting the results in the framework of the Anderson-Stuart model [35] (details of the model see sec. 1.3) the transition from a rigid glass network to a floppy one is proposed as the relevant mechanism for the HIDE.

Among the stoichiometric effects that alter E_a , the *mixed glass former effect* (MGFE) can be considered as an exceptional case. This effect is characterized by a non monotonous change of the activation energy, if one replaces one glass former species partially by another one. In comparison to the previously described effects, the MGFE can be distinguished by a manifold behavior of E_a depending upon the composition. In many systems one finds that the activation energy shows a single minimum at a certain glass former mixing ratio. But in a few glass systems the occurrence of a maximum, more than one minimum or a monotonous change in E_a were also reported. This distinct property is interesting because it enables the tailoring of the conductivity to the desired demands. In addition, this effect can be considered as an important experimental window to systematically study the microscopic mechanisms that affect the mobile cation transport. Up to now, no consistent theoretical picture is presented to explain the MGFE. Beside a few molecular dynamic simulation studies on alkali-borosilicates and alkali-borophosphates, only a little effort was done to address this issue on a theoretical level. *Driven by this fact, the present thesis is considered as a step to identify and characterize possible model-candidates as the origin of the MGFE.* In the view of manifold behavior of the MGFE the present overview of the MGFE is rather introductory and a more detailed description will be given in sec. 1.2

The rich variety of effects, which alter the value of E_a and the complexity of these materials

resulted in a considerable number of theoretical concepts and modeling methods to address the issue of connecting structural features with long range ionic transport. For a better understanding and classification of the concepts used in the present thesis a short overview will be given in sec. 1.3.

After the discussion of possible applications, the characteristics of the MGFE and the theoretical modeling the present introductory chapter will be completed by a section which addresses the outline and aims of the current thesis in detail.

1.1. Possible applications of fast ion conducting glasses and mixed glass former systems

The field of solid state ionics grew quickly over the last decades and fast ion conducting glasses are one of the most promising material class in this area because they show high ionic conductivities combined with the possibility to easily adjust their physical and chemical properties by the variation of their stoichiometric composition. To illustrate the perspectives of these interesting materials, possible fields of applications will be discussed briefly in the following paragraphs.

The most prominent example for application is the utilization as electrolyte materials in rechargeable batteries, which are used, for instance, in mobile telecommunication and hybrid or all electric driven cars. In the following discussion this issue will be discussed on the example of lithium batteries because they are nowadays the most important electrochemical devices. Most of the arguments presented here will hold true in similar form for any other rechargeable energy storage devices. As an example, one could consider batteries which use other metals like sodium [36, 37]⁴ or silver instead of lithium.

In 1991 Sony Cooperation introduced the first lithium ion battery on the market. This kind of energy storage device has gained to the dominating position in the field of mobile energy supply [38]. The electrolyte material is the key factor for the electric power, stability, performance and long term reusability of such batteries [4]. Since the electric power increases with the rate of reduction of the Li^+ at the electrode, the rate of migration of the cations through the electrolyte has to be optimized. But this is not the only criterion for a good electrolyte. A device which has to be used by a broad audience must also be safe. Further prerequisites for an ideal electrolyte material are sufficient high flash points, security against explosions and environmental sustainability. Additionally, it is important for long term usage that the material of the electrolyte will not change the chemical and physical properties during the utilization time. These requirements include also the fact that the material must be mechanically, thermally and chemically stable under ambient

⁴It should be noted that up to now no sodium based battery have reached the marketability, but a recent study shows the possibility of realization of a rechargeable sodium based battery which is working at room temperature [37]

conditions.

The most common liquid electrolytes containing lithium salt complexes, e.g. LiBC_4O_8 , LiPF_6 , $\text{Li}[\text{PF}_3(\text{C}_2\text{F}_5)_3]$, solved in an organic solvent [39]⁵. Typically they show the desired very high cationic mobility (up to $\sigma_{\text{dc}} = 10^{-2}$ S/cm at room temperatures) [41, 42] and an easy reproducibility. But the very low boiling and flash points of the organic solvents (≈ 30 °C) are critical drawbacks because electrochemical reactions involving lithium are strongly exothermic. This fact leads often to a phenomenon called "thermal runaway" and results often in the explosion of the device [39]. Therefore, the search of alternative, more stable materials is an important issue. The most promising candidates are polymeric, crystalline/polycrystalline and glassy solid-state electrolytes.

At first glance, polymer based batteries would be the optimal candidates since they show an increased stability, mechanic flexibility, reasonable high cationic mobility (up to $\sigma_{\text{dc}} = 10^{-3}$ S/cm at room temperatures [43, 44]) and can be easily and cheaply produced. Hence, they are nowadays the most common electrolyte materials for Li batteries and there is a huge number of possible realizations like plasticized polymer-salt complexes, polymer gel electrolytes or composite polymer systems⁶ [44]. Each of these electrolyte systems has distinct disadvantages. For instance, the conductivity and the mechanical stability are comparatively low for plasticized polymer-salt complexes. Polymer gel electrolytes, conversely, show typically excellent ionic conductivities (e.g. $\sigma_{\text{dc}} \approx 10^{-3}$ S/cm) but the stability of the electrode-electrolyte interface is poor and the polymer hosts tends to be vulnerable to Li salts [44]. The composite polymer systems are fabricated by adding ceramic nanoparticles (like TiO_2) to a polymeric system, which leads to an enhancement of chemical and mechanical durability on the cost of the ionic conductivity [44]. The most relevant problems of many polymeric systems are still the flammability and the negative environmental impact.

An alternative to polymer based electrolytes is the application of crystalline or amorphous inorganic ion conductors. Crystalline solid electrolyte materials, like the perovskite $(\text{LaLi})\text{-}2\text{TiO}_3$ [46], $\text{Li}_{3.25}\text{Ge}_{0.25}\text{P}_{0.75}\text{S}_4$ [47] or the recently reported $\text{Li}_{10}\text{GeP}_2\text{S}_{12}$ system [42] show room temperature mobilities in the order of $\sigma_{\text{dc}} = 10^{-3} - 10^{-2}$ S/cm and significantly increased thermal and chemical stabilities. In addition the environmental impact can be decreased. However, the major drawbacks for these materials are the extremely complex and expensive preparation [39] and the inherent anisotropy of physical properties like ionic conductivity [42, 48]. A further disadvantage is the very narrow stoichiometric window of these materials that prohibits further tailoring of material properties. In the case of polycrystalline materials, interface effects at the boundaries of the crystallites also decrease the ionic conductivity [46] of the electrolyte.

Hence, fast ion conducting glasses are considered as promising alternatives to the material classes discussed above because they have in principle similar advantages as the crystalline systems. Actually, they are considered to have higher ionic mobilities than their crystalline analogues due to their more open structure [49, 50, 51]. Further advantages are the isotropy

⁵In the case of sodium or silver it is also possible to use aqueous solutions [40]

⁶Polymer based electrolytes were also tested in the 1980s for Sodium cells [45]

and the absence of any grain boundaries [50]. An additional plus is the broad spectrum of stoichiometric realizations, which allows additional tailoring of material properties and the comparatively easy preparation. The biggest disadvantages are the low mechanic flexibility and expensive production process compared to the polymeric electrolyte system [39]. But it is important to note that in comparison to the corresponding crystalline systems their manufacturing process is much cheaper and easier [50].

Another possible area of application is in super-capacitors, which could be used, for instance, as short time energy storage devices [52]. The physical background of these devices could be explained by the fact that a double-layer is formed by the positive charges of the cations at the interface between an electrolyte and an electrode with a high effective surface (e.g. activated char coal), when an electrical field is applied between the plate and the electrolyte. The energy density of electric field E_{dl} , which is generated by this double-layer is proportional to E_{dl}^2 . For electronic applications and for the usage as a kind of energy storage device it is important to decrease/increase the time to charge/discharge the super-capacitor by increasing the mobility of the ions. To increase the energy density of such devices it is also necessary for the material to show a low conductivity for electrons and a high disruptive discharge voltage. These criteria could be archived by many solid state electrolytes, like glasses, glass ceramics, polymers and crystalline systems and the discussion of their advantages and disadvantages is very similar to the criteria for rechargeable batteries.

Another application for amorphous ion conducting materials, are electrochrome devices. These devices are sometimes referred as "smart windows" or "smart lenses", but they are also very interesting for optoelectronic applications. The effect of electrochromism is characterized by the property that an applied electrical current results in the change of the transparency of the device. The principle for operation can be described by an electrochemical reduction of metal-atoms (e.g. W) in a transparent oxide layer (e.g. WO_3), which is coated by a transparent electrode and coupled to an also transparent solid electrolyte, which acts as a cation source [53, 54]. The electrochemical reaction is induced by the electrons from the electric current and the charge balance, which would be violated due to the change of the oxidation state, is counter-balanced by the cations from the electrolyte [55]. An ideal electrolyte material for this application must have a high cationic conductivity to allow fast switching of the transparency. But high transparency and the producibility by thin film techniques are also desired properties of such materials. Of course, some glassy electrolytes are promising candidates that match these demands.

Ion conducting glasses are typically ion selective; they show different mobilities for different kinds of ions. Therefore, one could consider many other possible applications where this property is desired. A possible perspective, for instance, could be the replacement of crystalline electrolytes by glassy ion conductors in recently reported electrochemical gas sensors for NO_2 and SO_2 [56, 57] to gain better performance.

1.2. The mixed glass former effect in various systems

Considering a mixed glass former (MGF) system $yC - (1 - y)[xA - (1 - x)B]$ with the two glass formers A, B and a network modifying additive C, one would expect that any physical property like density ρ , T_g , σ_{dc} or E_a is altered by the mixing ratio $x = [A]/([A] + [B])$. However, in the present work the MGFE is used exclusively to address the effect of x on σ_{dc} via a non monotonous decrease/increase of the activation energy for cationic conductivity. The occurrence of lower (or higher) values E_a in the MGF system as in the pure systems will be denoted in the following as positive (or negative) MGFE. In the view of these definitions, the MGFE is reported in many systems like silver and alkali borophosphate glasses, alkali borosilicate glasses, $\text{GeS}_2\text{-SiS}_2$ [58], $\text{P}_2\text{O}_5\text{-TeO}_2$ [59], $\text{B}_2\text{O}_3\text{-TeO}_2$ [60], $\text{MoO}_3\text{-TeO}_2$ [61], $\text{MoO}_3\text{-B}_2\text{O}_3$ [62] or $\text{GeO}_2\text{-GeS}_2$ [63, 64]. Borophosphates glasses are systems, where always a positive MGFE occurs [65, 66, 67, 68, 69, 70, 71, 72]. In contrast, in borosilicate systems a positive [73], a negative [74] or the absence of a MGFE [75, 76] according to the definition are reported. Other examples for the occurrence of negative MGFE are lithium modified thio-phospho- and thio-alumino-silicates [77].

It should be also noted that the activation energy is not the only property, which shows a manifold behavior in MGF glasses. As an example, some MGF systems, like $\text{GeS}_2\text{-SiS}_2$ [58], $\text{GeO}_2\text{-GeS}_2$ or $\text{B}_2\text{O}_3\text{-SiO}_2$ [76], show the tendency of phase separation. Whereas various experimental data support the assumption that in borophosphate glasses borate NFUs are strongly intermixed with phosphate NFUs. The tendency of phase separation could also alter E_a . For instance, it was reported by Pradel *et al.* [58] for $\text{Li}_2\text{S-GeS}_2\text{-SiS}_2$ glasses that demixing in almost unmodified GeS_2 and highly modified Li_2SiS_3 micro-phases occurs within a certain composition range. Therefore, this behavior shows some similarities to the MICE in a Li modified SiS_3 glass micro-phases.

As described above, a very large number of systems shows the MGFE with different characteristics. Therefore we restrict our selves to give a more detailed review on the experimental data for only two exemplary MGF systems, i.e. borophosphate and borosilicate glasses.

The borosilicate system shows a quite large variety of behaviors. For example an early study for a large number of different Li- and Na-borosilicates (in an alkali concentration range of 25-40 mol %) shows an almost monotonous (linear) decrease of E_a with increasing SiO_2 content [75] - a finding, which was compatible with the recent findings for a tracer diffusion study of Wu *et al.* [78] for $0.2(\text{Na}_2\text{O})\text{-}0.8[x\text{B}_2\text{O}_3\text{-(}1 - x\text{)SiO}_2]$. Different results were reported by Klúvanek *et al.* [76]. These authors found in an ac-conductivity study that E_a decreases linearly with x for $0.4(\text{Li}_2\text{O})\text{-}0.6[x\text{B}_2\text{O}_3\text{-(}1 - x\text{)Si}_2\text{O}_4]$ glasses, i.e. a behavior opposite to the findings mentioned in [78]⁷. In contrast, a clear maximum of E_a was

⁷Note that in this work two borate network forming units (NFU) are replaced by only one silicate NFU, i.e. the ratio of the number of alkali ions to the number of NFU is not kept constant.

found by Maia and Rodriguez at $x \approx 0.3$ for the same glass compositions [74]. This finding corresponds to the occurrence of a negative MGFE. The most significant deviation from the findings previously discussed was observed by Tatsumisago and coworkers for $\text{Li}_4\text{SiO}_4\text{-Li}_3\text{BO}_3$ glasses [73]. They report a minimum in E_a in intermediate mixing regions, i.e. a positive MGFE.

There are two main factors which could be responsible for this seemingly contradictory behavior. The first one is related to the differences of the mobile cation distribution in the binary systems. It is sometimes assumed that in alkali-silicates the cations form clusters and this clustering facilitates the ion transport. This picture is experimentally supported by Raman spectroscopy studies on alkali silicates [79], X-ray absorption fine structure (XAFS) studies on sodium silicates [80] and spin-echo NMR-investigations on lithium-silicate glasses [81]. In contrast, it was argued that the alkali distribution is homogeneous in alkali borate glasses [82]. Hence, it is natural to assume that the introduction of borate leads to the distortion of cation transport clusters and therefore to an increase of E_a . The second possible reason for the complicated behavior of the MGFE in borosilicates is the finding of micro-phases that correspond to pure silicate and pure borate regions [76]. The process of micro-phase formation depends crucially on the production protocol, e.g. cooling rates and starting materials. The interfaces of such micro-phases also alter the behavior of $E_a(x)$. Up to now, no comparative experimental study about this problem is known. Thus, a detailed investigation of this issue is a very interesting perspective for future studies.

For borophosphate glasses the MGFE is known since the early eighties. A positive MGFE is commonly reported for these glasses. The first study was reported in 1980 by Tsuchiya and Moriya on lithium- and sodium- modified glasses with an alkali concentration of 30 and 40 mol % [65]. In the aforementioned study a sharp minimum in E_a was found for the lithium borophosphate system independent of the cation content. In contrast, for the sodium ion conducting glasses, a sharp minimum was reported only for 30 mol % modifier content. For the glasses with 40 mol % sodium content an decrease of E_a was reported for $x \lesssim 0.4$ followed by an almost constant value for $0.4 < x \lesssim 0.9$. For higher x E_a was found to increase again. A similar behavior was also reported in a more recent study for $0.333(\text{Li}_2\text{O})\text{-}0.666(x\text{B}_2\text{O}_3\text{-}(1-x)\text{P}_2\text{O}_5)$ glasses. In this study it was found that E_a also approaches an almost constant value for $x \gtrsim 0.4$ [71]. A finding which could be also confirmed by other studies containing 50 mol% [70] and 45 mol% [72] Li_2O . An almost constant value in E_a was also reported for 35 mol % (e.g. [83]⁸) and 40 mol % [69] sodium borophosphate glasses.

Such a behavior was also found in silver borophosphate glasses. The first comparative study addressing E_a for a couple of glasses with a cation to glass former ratio $[\text{Ag}]/([\text{P}_2\text{O}_5]+[\text{B}_2\text{O}_3])$ between 1/3 and 1.5 was published by Magistris *et al.* [66] in the early eighties. These authors have reported that the conductivity increases until it reaches for $x \gtrsim 0.4$ an almost

⁸see chapters 6 and 7

constant value. For small Ag content this plateau was followed by a peak in the conductivity for $x \approx 0.8$. This peak disappears with increasing Ag concentrations.

Borosilicate glasses tend to form silicate or borate rich micro-phases. In contrast, the intermixing of borate and phosphate NFU in alkali-modified borophosphates seems to be more effective than a pure random crosslinking. This means that bOs, which connect borate to phosphate units, are preferred [69, 84, 85, 86, 87]. This behavior corresponds to an exothermic mixing reaction and thus to a high negative mixing enthalpy, which is reported for sodium [88] and potassium borophosphate [89] glasses.

In addition, other important physical properties are affected by the mixing of the glass-formers. In particular, it was found for alkali borophosphates that the Young's modulus [90] and T_g (e.g. [69, 91]) increase with increasing borate content until a maximum value is reached in intermediate mixing regimes. In contrast, the molar volume V_m decreases in an almost linear manner [69, 71, 91]. These observations can be related to the formation of fourfold coordinated borate NFU (denoted as $B^{(4)}$) with a formal negative charge. This NFU replaces nbOs by bOs. This structural feature leads to a higher connectivity and a more compact glassy network. This higher connectivity also results in a higher chemical stability, e.g. a lower hygroscopicity, and an increase of the thermal stability and a stabilization with respect to devitrification [92]. The concentration of $B^{(4)}$ is in some way limited [69, 71, 93] and is correlated to the behavior of E_a and therefore also σ_{dc} [69, 70, 94]. The origin of this effect will be discussed in chapter 4.

Summarizing the present section, one can state that the MGFE shows a larger variety of characteristics than other stoichiometric effects in ion conducting glasses. Therefore, one has to consider that several different mechanisms are related to the MGFE. To give an overview about previous theoretical work that addresses these mechanisms, the following section will provide a review of theoretical concepts and modeling approaches.

1.3. Some remarks on theoretical concepts of ionic transport in glasses

Due to the lack of a well-established working theory for ion transport in glasses, a number of theoretical concepts have been proposed to improve the theoretical understanding. The aim of the present section is the discussion of the most important ones with a focus on the MGFE.

The first approach to understand the behavior of E_a was given by Anderson and Stuart (A-S model) for silicate glasses in the 1950s [35]. This semi-empirical model is based on the assumption that the activation energy is the sum of two contributions $E_a^{(s)}$ and $E_a^{(c)}$.

$$E_a = E_a^{(s)} + E_a^{(c)} \quad (1.3)$$

The first term on the RHS is the strain energy, which is needed to open a doorway for the mobile ion and the second one is the typical energy to overcome a Coulomb barrier. In the

original approach of the A-S model $E_a^{(s)}$ was set to

$$E_a^{(s)} = 4\pi G r_d (r - r_d)^2 \quad (1.4)$$

where G is the Young modulus and r and r_d are the cation and doorway radii. It is important to note that eq. 1.4 was taken from the Frenkel theory for diffusion in closed packed liquids [95] and modified by dividing it by an empirical factor of 2.⁹ Anderson and Stuart explain this factor by the assumption that in network-glasses the typical density is much lower as in close-packed liquids. Later approaches modify eq. 1.4 by introducing the average jump length λ :

$$E_a^{(s)} = 0.5\pi G \lambda (r - r_d)^2 \quad (1.5)$$

because it was noticed that for large atoms or cations with $r_d < r/3$, the function $E_a^{(s)}$ in eq. 1.4 would be a decreasing function of r [96]. The Coulomb part $E_a^{(c)}$ of eq. 1.3 is typically given as [35]

$$E_a^{(c)} \approx \frac{A z z_O e^2}{\hat{\gamma}} \left(\frac{1}{(r + r_O)} - \frac{1}{\lambda/2} \right) = \frac{\hat{\beta} z z_O e^2}{\hat{\gamma} (r + r_O)} \quad (1.6)$$

where A is a constant value, which is an analogue to the Madelung constant¹⁰, and r_O is the Pauling radius of the oxygen atom. In the original approach by Anderson and Stuart γ was introduced as the "covalency parameter", which describes the deformation of the electron cloud of the oxygen atom. It was found empirically by Anderson and Stuart that γ should be roughly the real part of the dielectric permittivity function in the high frequency limit $\epsilon_\infty = \lim_{\omega \rightarrow \infty} \epsilon'(\omega)$. The A-S model recently gained some support by molecular dynamic (MD) simulations for alkali silicate glasses, where it was found that the immobilization of the glass network leads to an enhancement for E_a by a factor of 1.7 [97]. It should be noted that this factor would rise to infinity for $G \rightarrow \infty$ and the authors show in a later article that this effect could be explained by a kind of "sliding door mechanism" [98]. The most critical aspect of the A-S model is the fact that it largely ignores the amorphous state of the glass. In particular, the variation of the number of oxygens, which are in the coordination sphere of a cation, the variation of the oxygen-cation neighbor distances and the spatial variation of the Young modulus G are not taken into account. Furthermore, no variations in the binding energies for the mobile ions are included. Therefore, this approach is not able to describe correctly the MAE, where at least two types of ion sites must exist- with different binding energies for each kind of cation [10, 11, 12, 13]. A further chink of the A-S model is the intrinsic lack of unoccupied sites. Since every mobile ion is bonded to one nbO, no unoccupied sites are available for cation jumps. Despite these severe problems, the A-S model was used to discuss the MGFE in a lithium thiogermanate-germanate mixed glass former system [63].

⁹which were estimated by Anderson and Stuart considering literature data for the diffusion of noble gases, H₂, O₂ and N₂ in glassy SiO₂

¹⁰ A is in the order of 1.

Another model to describe the ion dynamics is the *interstitial pair* (IP) ansatz [99], which is conceptually different than the A-S model. This approach is used to discuss the *mobile ion concentration effect* in binary silicate glasses [100] or alkali phosphate glasses [101] and the MGFE in $x\text{Ag}_2\text{P}_2\text{O}_6-(1-x)\text{Ag}_2\text{Te}_2\text{O}_5$ [59] and $\text{SiO}_2\text{-B}_2\text{O}_3\text{-Na}_2\text{O}$ [102] glasses. The starting point for this model is the Nernst-Einstein relation, which connects the ionic conductivity with the mobility μ_σ of the cations:

$$\sigma_{\text{dc}} = Z e n_c \mu_\sigma \quad (1.7)$$

where n_c is the number density of the charge carriers, Z is charge number of the cations and e the elementary charge. The temperature dependence of μ_σ is then given in the framework of the IP approach as:

$$\mu_\sigma = \frac{e \lambda^2 \nu_0 \exp\left(\frac{-E_m}{k_B T}\right)}{k_B T} \quad (1.8)$$

where ν_0 is the attempt frequency of a jump ($\nu_0 \approx 10^{-13} \text{s}^{-1}$) and E_m is the activation energy for the hopping of the particles. The key assumption of this approach is the additional Arrhenius-like temperature dependency for n_c :

$$n_c = n_{c0} \exp\left(\frac{E_p}{2k_B T}\right) \quad (1.9)$$

where n_{c0} is the extrapolated particle number density for infinite high temperatures, and E_p is the formation energy for the formation of a Frenkel-like defect structure. This defect structure consists of a pair of cations which are occupying the same site and an unoccupied site respectively. Hence, the IP model solves apparently the problem with the lack of unoccupied sites. However, the most important critical drawback of this model is the fact that the activation energy for conductivity must be $E_p/2$ higher than the activation energy for the diffusion constant D_{lt} because $\mu_\sigma \propto D_{\text{lt}}$. This prediction is not compatible with experimental findings for many ion conducting glasses, because it is typically reported that $\sigma k_B T \propto D_{\text{lt}}/H_R$ and the Haven ratio H_R are not Arrhenius activated. A possible way out of this difficulty would be the introduction of disorder in the binding energies of the sites, where the typical energy scale of disorder must be sufficient larger than $E_p/2$. This mechanism would lead to intrinsic interstitial pairs, which are not disappearing for $T \rightarrow 0$ because it would be energetically more favorable to occupy a low energy site twice than to occupy an high and a low energy site with single cations. In this case, the mechanism introduced by the IP approach could be described well by a vacancy transport mechanism in the low temperature regime.

At this point, it should be noted that both the A-S and the IP approach are not able to explain the behavior of the frequency dependent conductivity $\sigma(\omega)$ for low temperatures (e.g. see fig. 1.2). This behavior is characterized by the asymptotic behavior $\sigma(\omega \rightarrow 0) = \sigma_{\text{dc}}$ and an apparent power-law increase of the conductivity for frequencies larger than a characteristic frequency ω_c . For sufficiently low temperatures this enhancement of the conductivity

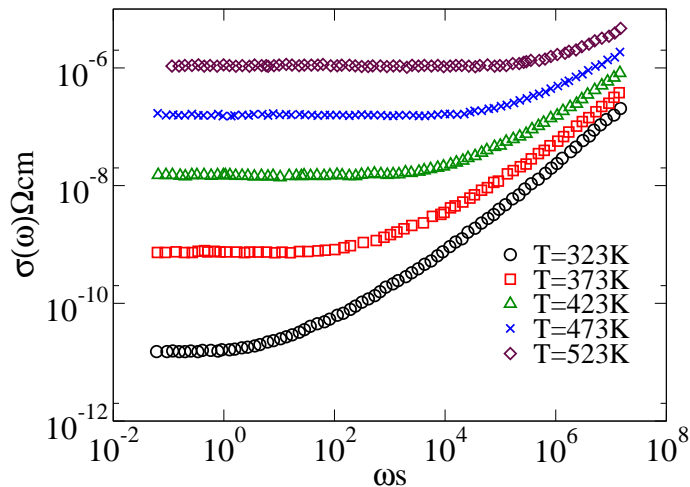


Figure 1.2.: Typical behavior of the frequency dependent conductivity in disordered systems shown for $0.2\text{Na}_2\text{O}-0.8\text{GeO}_2$ glasses (redrawn from [104])

covers several orders of magnitude. This finding is explained by a strong disorder in the transition rates. Such behavior is reproduced well by hopping models considering hopping transport in random energy landscapes with quenched disorder. The choice of a static energy landscape implies the approximation of time-averaged contributions from the interactions between the charge carrying mobile particles. This approximation is not as critical as it seems on first view, since it was shown by Lammert and Heuer with molecular dynamic simulations [103] that the consideration of vacancy hopping instead of cation dynamics leads to a remarkable decrease of multi-particle effects. Within the approximation of static energy landscapes, one can distinguish between two different types of disorder (i) thermally activated hops over an energetic barrier \mathcal{E}_{ij} and (ii) a transition between sites of different energies ϵ_i . In general, both types of disorder are present in a real system. However, one can consider two different situations, where one mechanism is dominating process.

In the first one, the typical differences between the sites are less important than the typical barrier energies. This situation is captured by the *random barrier model* (RBM). This model can be considered as the "ideal gas model" of hopping conduction [18, 105, 106, 107, 108] because it is the conceptually simplest approach that reveals most of the aspects of hopping transport in disordered systems. In particular, the mathematical behavior of $\sigma(\omega)$ ¹¹ is well described. In the RBM the particles perform random hops between different sites i and j , with symmetric hopping rates $\Gamma_{ij} = \exp(-\mathcal{E}_{ij}/(k_B T))$. For small time scales the hopping occurs on finite clusters, which consist of sites connected by barriers $\mathcal{E}_{ij} \leq \mathcal{E}^*$, where \mathcal{E}^* is a typical maximum barrier. Increasing \mathcal{E}^* leads to an increase of the typical size of these clusters. Approaching a critical $\mathcal{E}^* = \mathcal{E}_c$ an infinite cluster is formed. This \mathcal{E}_c can be

¹¹It should be noted that it is possible to map mechanism (ii) on mechanism (i) in the framework of a mean field approach [18, 109]

calculated from the percolation theory, by using the distribution of barriers $\Psi(\mathcal{E}_{ij})$

$$p_c = \int_0^{\mathcal{E}_c} \Psi(\mathcal{E}) d\mathcal{E} \quad (1.10)$$

The percolation threshold p_c depends in general on the underlying lattice and the stochastic properties, i.e. spatial correlations of the barriers. Since the transition rates Γ_{ij} decrease exponentially with increasing $\mathcal{E}_{ij}/(k_B T)$, transition processes corresponding to $\mathcal{E}_{ij} > \mathcal{E}_c$ have no influence on the long range transport. This fact leads to $E_a = \mathcal{E}_c$. It is hard to determine the distribution $\Psi(\mathcal{E}_{ij})$ of barriers in an *a priori* manner. Svare *et al.* proposed the estimation of the barrier distribution by fitting of the NMR spin lattice relaxation functions [110]. This approach was successfully applied to LiS₂-SiS₂ [110], LiCl-Li₂O-B₂O₃ [111] and a couple of mixed alkali silicate glasses [112].

Situation (ii), where differences in the site energies are the dominating factor for the broad distribution of transition rates, is captured by the *random site energy model* (RSEM). It was shown by Porto *et al.* for the MICE that the nearest neighbor hopping in an energy landscape with Gaussian distributed site energies leads in good approximation to a logarithmic decrease of activation energy with the particle concentration [19]. A similar behavior was found for exponentially distributed site energies [18, 113]. Moreover, the MAE is explained by introducing different site energies, which result from a mismatch-energy if a site, which was formerly adapted to a cation of type A, is occupied by a cation of type B. Application of the RSEM leads to a successful explanation not only the behavior of E_a as a function of the substitution ratio $x_s = [B]/([A] + [B])$ [18, 10] but also for the behavior of the internal friction [10]. Nevertheless, one could ask if the approximation of a static energy landscape is sufficient to describe the dynamics of the cations properly. This question was addressed by a recent series of articles by Lammert *et al.* [103, 114] on the basis of molecular dynamic simulations of a model for alkali-silicate glasses. They found significant deviations in the equilibrium occupation probabilities and the expected cation dynamics, if one uses the time average of the site energies and neglects dynamic changes [114]. By comparing the local mean waiting time with the standard deviations of the waiting time for each ion site and analyzing the back-hop probability of a particle (i.e. cation or vacancy) they found that collective transport processes could be well described in a picture of non-interacting particles if one focuses on a vacancy picture [103]¹².

For the sake of completeness, it should be noted that MGFE could be also studied applying Molecular Dynamics (MD) simulations, which has been already mentioned. This method gains an increasing influence in the study of network glasses [115, 116, 117, 118, 119, 120]. The basic idea in this approach is to solve Newtons equations of motion numerically, e.g. by application of the Verlet algorithm. Mapping the quantum chemical forces on

¹²Lammert and Heuer also note that a site could be occupied by 2 or in rare case 3 mobile cations- a fact which gives some support to the IP model

a quasi-classical potential with a set of parameter typically depending on the chemical elements in the simulated system but not on the stoichiometry. Some studies were performed on MGFE systems like $\text{LiO}-2\text{-P}_2\text{O}_5\text{-B}_2\text{O}_3$ [72, 121] or alkali borosilicate glasses [122, 123]. A more precise alternative to quasiclassical MD simulations are *ab initio* MD (AIMD) methods, which were used, for example, in unmodified borate [124] and bioactive phosphate glasses [125]. First attempts to study MGF systems with AIMD were done on aluminate-silicate-glasses [126] and bioactive phosphosilicate glasses [127]. However, due to the very high computing time this method is limited not only to small systems but also to very short time in the order of 10-100 ps. Therefore, it is not clear if this method describes the physical properties of real glasses properly.

1.4. Outline and aim of the present thesis

As it was discussed in sec. 1.2, the MGFE shows a rich variety of characteristics. The fact that the MGFE has no unique behavior, gives rise to the assumption that more than a single mechanism is underlying the MGFE. Therefore, one has to ask the key question:

”What are the microscopic origins of the MGFE?”

The main issue addressed in this work is the development of model candidates that capture the key-mechanisms of the MGFE. Two models will be proposed and the main findings are reported in chapter 2 and 4. These models are conceptually different from each other and suitable to describe the MGFE sufficiently in different situations.

The first model, which will be introduced in chapter 2 applies for the situation, where the site energies are weakly varying and the energy barriers are dominating the value of E_a . The presented model implies the fact that the doorway radii or the local elastic constants depend on the local glass-former mixing ratio. More specifically, that the barrier energies, which correspond to the process of a cation transition through a doorway, are lowered along the boundaries of regions formed by the two different network formers. As a consequence, the activation energy will be decreased (*mixed barrier model* (MBM)).

The second model in the present thesis could be applied for the case that energies of the cationic sites are the major factor that alters E_a . This model will be introduced in chapter 4 and discussed in particular for sodium borophosphate glasses. The fundamental assumption of this model is that different NFUs contribute differently to energies of adjacent cation sites. This mechanism changes the distributions of site energies in the glasses as a function of composition (*network unit trap* model (NUT)). To apply this model, it is necessary to know the NFU concentration in borophosphate glasses. To this end, an approach including one parameter f will be described in chapter 4 that permits to calculate the NFU concentration in dependence of the stoichiometry of the glass.

For both models, extensions and supplementary results are presented in chapter 3 respectively chapter 5.

It will be shown in chapter 2 that the ac-conductivity $\sigma(\omega)$ for different compositions and different typical sizes of the micro-phases collapse to a single master curve, if a rescaling operation $\sigma(\omega)/\sigma_{\text{dc}} = F(\omega/\omega_c)$ is applied¹³. This feature is revisited in chapter 3, because this scaling behavior seems to be universal and independent of the correlations introduced by the MBM. To this end, the random barrier model will be discussed by the inclusion of well defined spatial correlations and a distribution of the barrier energies that is not affected by these correlations.

Chapter 4 gives rise to further questions, which are addressed in chapter 5. The first issue discussed in chapter 5 is the justification of a single parameter model to calculate the NFU concentrations. Within these discussions, it will be shown that a single parameter f can be sufficient to reproduce the complicated behavior of the NFU concentrations and how this parameter must be interpreted. The second issue addressed in chapter 5 is the extension of the approach, which can be used to calculate the NFU concentrations by the introduction of a positive charged phosphate unit with four bOs. This extended model will be also checked on additional experimental data on two additional systems. Applying the aforementioned approach, it is possible to calculate E_a directly within the framework of the NUT model. To this end, one has to find the distributions of site energies that could be used in a subsequent step to determine E_a . The derivation of the site energy distributions is shown in sec. 5.3.1 and a discussion of the calculation of E_a will be done in sec. 5.3.2. The values of E_a , which were calculated by two different concepts to calculate the activation energies in random energy landscapes, are compared with results from the Monte Carlo simulations. In addition, it will be shown in the last section of chapter 5 that the NUT model could be also successfully used to describe the MICE in binary borate glasses.

A further important issue of the present thesis is the question whether the MGFE in sodium borophosphate glasses could be related to some structural peculiarities of the glasses. This question is addressed by Reverse Monte Carlo (RMC) simulation studies. The RMC procedure, was performed with X-ray diffraction (XRD) data taken from [128] and neutron diffraction (ND) data provided by coworkers from USA and Sweden¹⁴ for borophosphate glasses with 35 mol% sodium. Chapter 6 revisits the previous RMC study reported in [128] because chemical constraints, e.g. charge balance, were not captured well and the NFU concentrations, which were estimated in this study were not compatible to our models. The outcome of this study, which only includes XRD data, will be presented in chapter 6. However, it is a well-known fact that the relationship between the diffraction data and the microscopic structures is not unique, even though many RMC-studies on glasses are based on data of a single probe (XRD or ND). This fact gives rise to the question, to which extent

¹³with the onset frequency for dispersive transport ω_c

¹⁴This data were provided by the groups of S. W. Martin (Iowa State University, USA) and M. Karlsson (Chalmers University, Sweden) [129]

the RMC models presented in chapter 6, could reproduce the ND data. The answer to this question and further refinements of the RMC structures with respect to the ND data are presented in chapter 7.

2. Mixed Barrier Model for the Mixed Glass Former Effect in Ion Conducting Glasses¹

Abstract

Mixing of two types of glass formers in ion conducting glasses can be exploited to lower the conductivity activation energy and thereby increasing the ionic conductivity, a phenomenon known as the Mixed Glass Former Effect (MGFE). We develop a model for this MGFE, where activation barriers for individual ion jumps get lowered in inhomogeneous environments containing both types of network forming units. Fits of the model to experimental data allow one to estimate the strength of the barrier reduction, and they indicate a spatial clustering of the two types of network formers. The model predicts a time-temperature superposition of conductivity spectra onto a common master curve independent of the mixing ratio.

¹This chapter is published as: M. Schuch, C. R. Müller, P. Maass and, S. W. Martin, *Phys. Rev. Lett.*, **102**, 145902, (2009)

Ion conducting glasses are attractive electrolyte materials since their composition can be varied to a large extent and hence adapted to specific needs. They can be used in many devices, such as, batteries, electrochromic windows, chemical sensors and supercapacitors. High ionic conductivities are needed for optimizing glassy electrolytes in these applications and it is important to find methods for enhancing them in a systematic way.

One method for increasing the ionic conductivity is the mixing of different types of glass formers. Considering an ion-conducting network glass of general composition $yM_2X+(1-y)[(1-x)A+xB]$ with two network formers A, B and an alkali modifier M_2X (where X is O, or S) with fixed mole fraction y , the activation energy $E_a(x)$ of the dc-conductivity $\sigma_{dc}(x)$ often passes through a minimum as a function of the mixing ratio x , causing a pronounced maximum in the conductivity. This phenomenon is commonly referred to as the “mixed glass former effect” (MGFE) [9]. The MGFE has been found in various glass systems, e.g., $\text{SiO}_2\text{-B}_2\text{O}_3$ [73], $\text{P}_2\text{O}_5\text{-B}_2\text{O}_3$ [69, 130], $\text{GeS}_2\text{-SiS}_2$ [58], $\text{P}_2\text{O}_5\text{-TeO}_2$ [59], $\text{TeO}_2\text{-B}_2\text{O}_3$ [60], $\text{MoO}_3\text{-TeO}_2$ [61], and $\text{GeO}_2\text{-GeS}_2$ [63] mixed glass former systems.

Different from the prominent mixed alkali effect [131], the MGFE appears to be less universal. For example, in borosilicates it has been argued that it occurs only in rapidly quenched glasses with high concentration of mobile ions [74] and in the $\text{P}_2\text{O}_5\text{-TeO}_2$ system more than one minimum in the activation energy has been observed [59]. With respect to a classification of different systems, we distinguish between a situation I, where, upon varying x , the local geometry of the units of each of the network formers remains the same (as, e.g., in the $\text{GeO}_2\text{-GeS}_2$ system with tetrahedral units) from a situation II, where the coordination number of elementary units of a network former changes (e.g., in borophosphates, the ratio of tetrahedral BO_4 to trigonal BO_3 units).

Due to the mixing of glass formers, the free-energy landscape for the ion migration changes and in general both the energy levels for the residence sites of the mobile ions and the saddle point energies for ion jumps between neighboring sites are affected. In situation II, one can expect that the dominant effect is associated with a change of the site energies, since different local geometries of the network forming units are associated with strong variations in the spatial counter-charge distribution. In situation I in contrast, it can be expected that the dominant effect is associated with reduced barrier energies along jump paths with heterogeneous local environments (i.e. containing different glass forming units) compared to those with homogeneous local environments.

In this Letter, we concentrate on situation I, where a basic modeling should have at least two components: A measure for the strength of the barrier reduction and a prescription of how the fraction of homogeneous to heterogeneous environments and their spatial distribution changes with the mixing ratio x . Based on these minimal ingredients we develop a “mixed barrier model” (MBM) and show that a simple realization of this model allows one to fit experimental data and to give an estimate of the strength of the barrier reduction effect. This strength turns out to be only weakly affected by spatial clustering of the two types of network formers. As an universal feature independent of specific model implementations, the MBM predicts a scaling of the ac-conductivity with respect to both

temperature and mixing ratio x . The MBM can be considered as a variant of the random barrier model (RBM) [105] with a distribution of activation barriers changing with x . The mobile ions in the glassy network (or mobile charge carriers²) perform thermally activated jumps between neighboring sites with rate $\nu \exp(-\mathcal{E}_i/k_B T)$, where ν is an attempt frequency ($\sim 10^{12}$ Hz) and \mathcal{E}_i a microscopic energy barrier, whose mean value is different for different environments of the surrounding network former units. For simplicity we distinguish between a homogeneous environment (A or B), where the surrounding units are all of the same type and a mixed environment (AB), where both types of units are present. For each of these environments we introduce a smooth distribution $\psi_\alpha(\mathcal{E})$ of barriers ($\alpha = A, AB, B$), with ψ_{AB} having a lower mean than ψ_A and ψ_B to account for reduced barrier energies in heterogeneous environments³. If the environments occur randomly along the migration path (subset of all possible transitions) with probabilities $p_\alpha(x)$, the activation energy $E_a(x)$ can be calculated from the critical path analysis of percolation theory [132]: $\int_0^{E_a} d\mathcal{E} \psi(\mathcal{E}, x) = p_c$, where $\psi(\mathcal{E}, x) = \sum_\alpha p_\alpha(x) \psi_\alpha(\mathcal{E})$, and p_c is the percolation threshold for the occurrence of a connected path of transitions through the system.

If we choose box distributions with support $0 \leq \mathcal{E} \leq E_\alpha$ with $E_{AB} < E_A \leq E_B$, only the E_α are needed for parameterization, and we obtain

$$E_a(x) = \begin{cases} \frac{p_c}{p_A(x)E_A^{-1} + p_B(x)E_B^{-1} + p_{AB}(x)E_{AB}^{-1}} & (2.1a) \\ \frac{p_c - p_{AB}(x)}{p_A(x)E_A^{-1} + p_B(x)E_B^{-1}} & (2.1b) \\ \frac{p_c - p_{AB}(x) - p_A(x)}{p_B(x)E_B^{-1}} & (2.1c) \end{cases} \quad (2.1)$$

where the three different cases refer to: (a) $E_a(x) \leq E_{AB} \leq E_A$, (b) $E_{AB} \leq E_a(x) \leq E_A$, and (c) $E_{AB} \leq E_A \leq E_a(x)$.

Despite the simplicity of this model, Eq. 2.1 can be used to estimate the strength E_{AB}/E_B of barrier reduction by fitting experimental data. For this fitting we first note that cases (2.1b) and (2.1c) require $E_{AB}/E_B < p_c$, since $E_a(1) = p_c E_B$ gives the maximum of the activation energy. Hence, with percolation thresholds smaller than 0.5 and variations of activation energies not larger than by a factor of two, the generic situation corresponds to Eq. (2.1a). For the probabilities $p_\alpha(x)$ we make the ansatz $p_A(x) \sim (1-x)^z$ and $p_B(x) \sim x^z$ [$p_{AB}(x) = 1 - p_A(x) - p_B(x)$], where z is a mean number of network forming units influencing the local transition barriers. The activation energies of the pure systems are used to determine the ratio $E_A/E_B = E_a(0)/E_a(1)$.

²Molecular dynamics simulations and general theoretical considerations suggest that only a relatively small fraction of about 10% of the ionic residence sites are empty at any given time. This gives reason to consider the vacancies as the mobile charge carriers.

³In first approximation, the Coulomb interaction between the mobile ions can be considered to be included in these distributions as a constant contribution, since the total mobile ion concentration is almost independent of x .

Knowing this value, $E_a(x)/E_a(1)$ from Eq. (2.1a) is only a function of E_{AB}/E_B and z (independent of p_c), $E_a(x)/E_a(1) = f(E_{AB}/E_B, z)$, which allows us to determine these remaining two parameters by a least-square fit.

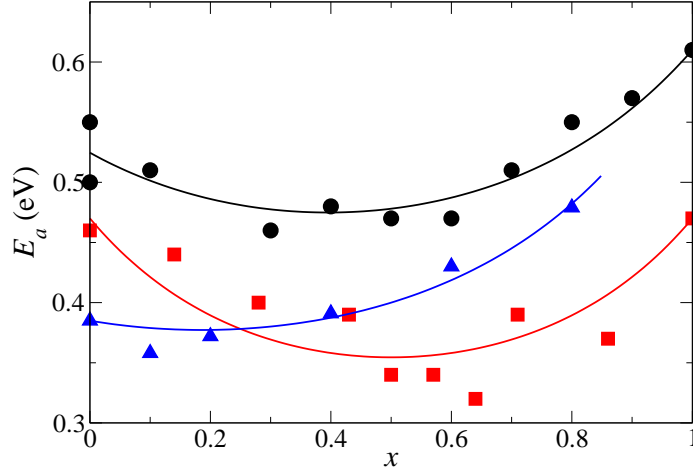


Figure 2.1.: Conductivity activation energy for $0.3\text{Li}_2\text{S}+0.7[(1-x)\text{SiS}_2+x\text{GeS}_2]$ (\blacksquare) [58], $\text{Li}_2\text{S}+[(1-x)\text{GeS}_2+x\text{GeO}_2]$ (\blacktriangle) [63], and rapidly quenched $x\text{Li}_4\text{SiO}_4+(1-x)\text{Li}_3\text{BO}_3$ (\bullet) [73] glasses. The fits (solid lines) according to Eq. (2.1a) yield $E_{AB}/E_B = 0.69$, $z = 2.8$ for the SiS_2 - GeS_2 -system and $E_{AB}/E_B = 0.67$, $z = 2.0$ for the SiO_2 - B_2O_3 -system. Due to the missing value for $x = 1$ in the GeS_2 - GeO_2 -system, we fixed $z = 2$ and fitted $E_a(x)/E_a(x = 0.8)$, yielding $E_A/E_B = 0.63$ and $E_{AB}/E_B = 0.57$.

Figure 2.1 shows such an analysis for the two systems $y\text{Li}_2\text{S}+(1-y)[x\text{GeS}_2+(1-x)\text{SiS}_2]$ [58] and $y\text{Li}_2\text{S}+(1-y)[x\text{GeO}_2+(1-x)\text{GeS}_2]$ [63]. In view of the scatter in the experimental data (squares, triangles), the fitted curves (solid lines) are in fair agreement for parameter values $z \simeq 2$ and a barrier reduction $E_{AB}/E_B \simeq 60\%$ (the accurate values are given in the figure caption). As a further example, we also fit the MGFЕ found in the rapidly quenched system $(1-x)\text{Li}_4\text{SiO}_4+x\text{Li}_3\text{BO}_3$ (circles), which exhibits no network structure but can be viewed as an ionic glass composed of SiO_4^{4-} and BO_3^{3-} anions, and Li^+ cations. Since the Coulomb traps created by the anions are of comparable strength per Li ion, we can also for this system conjecture that the dominant changes of the energy landscape are associated with energy barriers, corresponding to situation I. Again we find a reasonable agreement with the experiment with similar values for z and E_{AB}/E_B . The value of $z \simeq 2$, which describes the mean number of network forming units influencing the local transition barriers, appears to be rather small. For example, when distributing A and B units randomly among the centers of a cubic lattice, where the mobile charge carriers jump along the lattice bonds, one would have $z = 4$. The small value points to the presence of an effective (renormalized) z when fitting with Eq. (2.1a), which could be caused by spatial correlations between the jump barriers. Indeed, partial phase-separation effects of different network formers are often

discussed in the literature. For the $\text{GeO}_2\text{-GeS}_2$ system, evidence for spatial correlations was provided recently by RMC modeling [133], where it was found that the glass structure is built up from independent chains of each of the network formers with the charge carriers occupying the space in between the chains. In the $\text{GeS}_2\text{-SiS}_2$ system, SAXS measurements [58] showed clear phase separation tendencies of the two network formers.

In order to study the effect of partial demixing in the MBM, we proceed by investigating the consequences of a kinetically suppressed phase separation. We presume that during cooling, phase separation sets in above the glass transition temperature T_g , which below T_g freezes in. Inside the resulting domains the pure environments prevail and the barrier reduction occurs in the interfacial regions. Specifically we consider the spinodal decomposition of A and B units with nearest neighbor interactions corresponding to an Ising model at temperature $T = 0.22T_c$. The network former units are placed on the centers of a cubic lattice with random start configuration, and the demixing is carried out by exchanging units A and B according to the Kawasaki exchange dynamics until the characteristic domain size reaches a given value l^4 . Energy barriers are assigned to the lattice bonds with pure (either 4 A or 4 B units) or mixed environments by drawing them from the box distributions considered above with a symmetric choice of parameters $E_A = E_B = 2E_{AB}$.

Again we can determine the activation energy from a critical path analysis, but the equation $\int_0^{E_a} d\mathcal{E}\psi(\mathcal{E}, x) = p_c$ can no longer be used since it applies only to a random distribution of the barriers. We calculated E_a directly from the disorder configurations by determining the critical barrier that a charge carrier needs to surmount in order to move through the system.

In addition we calculated the frequency-dependent conductivity $\sigma(\omega, T)$ by the velocity auto-correlation method [135]. Using these spectra (cf. Fig. 2.3), we can determine E_a from Arrhenius plots of the low-frequency limit $\sigma_{\text{dc}}(T)$. As shown for representative examples in the inset of Fig. 2.2, the slopes of the lines in the Arrhenius plot are in excellent agreement with the E_a values calculated from the critical path analysis.

The dependence of the function E_a on the domain size l (in units of the lattice spacing a) is displayed in Fig. 2.2. For small $l \lesssim 2.3$, the behavior is almost indistinguishable from a random barrier distribution, corresponding to E_a from Eq. (2.1a) with $z = 4$ (solid line). For larger l the curves $E_a(x)$ flatten and the MGF becomes weaker. We find that these curves for larger l can still be well described by Eq. (2.1a), if we use an effective z value (dashed lines). The effective z decreases with l , and for $l = 6.2$ reaches $z = 2.6$. This value is comparable to those found from the analysis of the experimental data in Fig. 2.1. The agreement with Eq. (2.1a) moreover demonstrates that we would obtain barrier reductions close to the exact one ($E_{AB} = 0.5E_B$), if we fitted the curves for larger l as in Fig. 2.1. This gives some confidence in the above estimate of the barrier reduction effect.

⁴For details of the Kawasaki dynamics, see [134]. The domain size l characterizes the spatial extent of regions with A and B excess. It is the same here for both components and determined in the standard way by taking the first zero in the AA (or BB) correlation function.

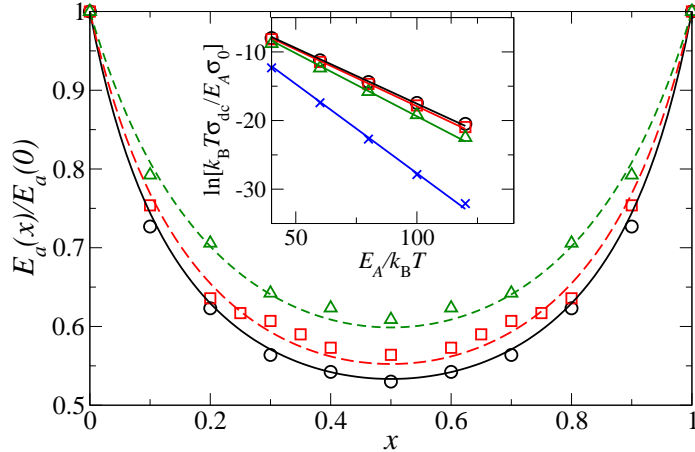


Figure 2.2.: Normalized activation energy $E_a(x)/E_a(0)$ for different domain sizes $l = 2.4$ (\circ), 4.3 (\square) and 6.2 (\triangle). The solid line marks the solution Eq. (2.1a) with $z = 4$, and the dashed lines are fits to Eq. (1a) with z as fitting parameter ($E_{AB}/E_B = 0.5$ fixed). Inset: Arrhenius plots of the conductivity (in units of σ_0 , cf. caption of Fig. 2.3) calculated by using the velocity auto-correlation method [135] for $x = 0.0$ (\times), and for $x = 0.2$ with $l = 2.4$ (\circ), 4.3 (\square), and 6.2 (\triangle). The slopes of the lines agree with the E_a obtained from the critical path analysis.

It is clear that the MBM is a simple approach, but it does allow us to see how barrier reduction in inhomogeneous environments leads to the MGFE and how large the strength of this reduction might be expected. For a more microscopic description one would need to incorporate detailed structural information specific for the glass system under consideration.

On the other hand, we can ask if there exist universal features of the ion transport behavior independent of microscopic details. For a given ion conducting glass composition, an universal feature is the time-temperature (or frequency-temperature) scaling of conductivity spectra [105]. This scaling means that conductivity spectra at different temperatures fall onto a common master curve, if one divides $\sigma(\omega, T)$ by σ_{dc} and ω by $\omega_c(T)$, where $\omega_c(T)$ is the crossover frequency to the dispersive regime, as determined, e.g., by the condition $\sigma(\omega_c(T), T) = 2\sigma_{dc}$. The question arises whether this scaling can be extended so that spectra of different glass compositions collapse onto a common curve. For variations of the modifier content (mobile ion concentration) such “super-scaling” has been observed approximately [136], while deviations from super-scaling have been found when mixing different types of mobile ions [137]. In the following we investigate what behavior can be expected for the MGFE based on the MBM. In the limit of $l \rightarrow 0$, where the barriers are randomly distributed in space, super-scaling is expected, since it was shown in the RBM that time-temperature scaling is independent of the form of the barrier distribution. Indeed, we have

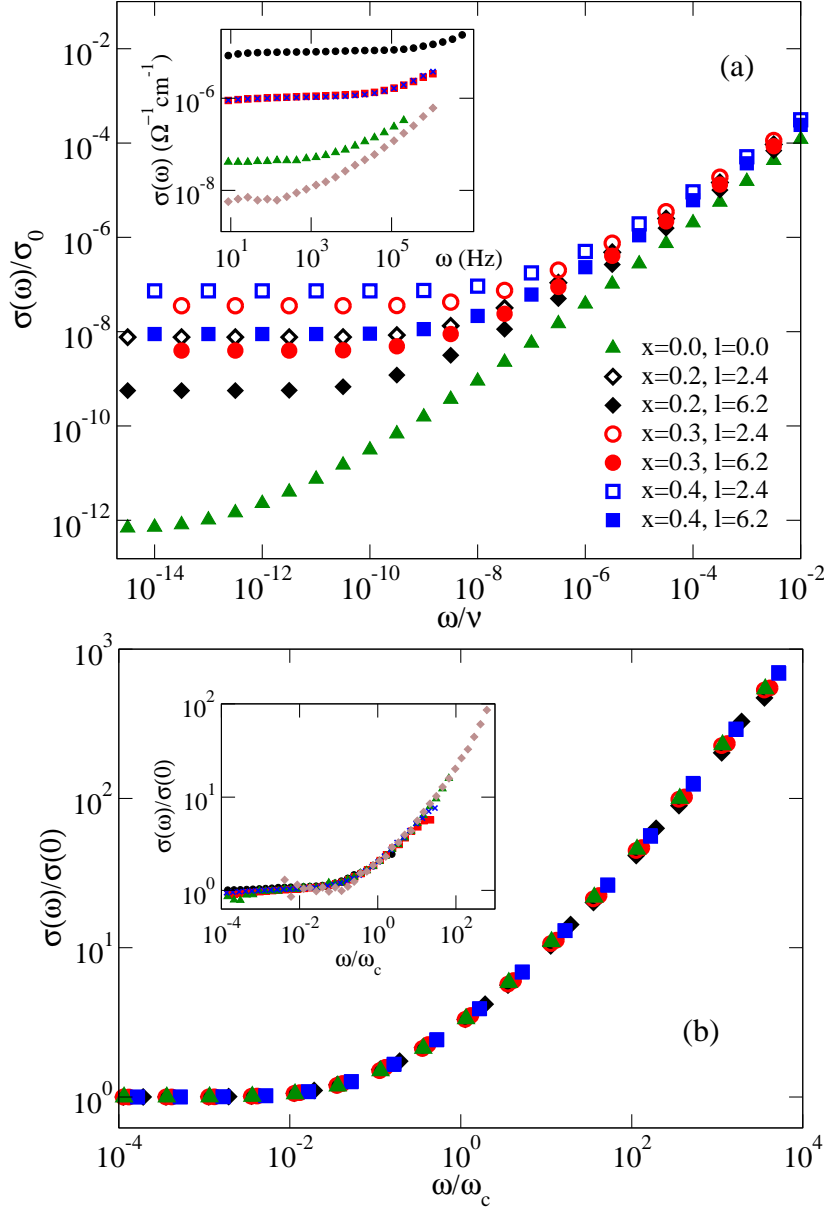


Figure 2.3.: (a) Conductivity spectra $\sigma(\omega)$ (in units of $\sigma_0 = ne^2\nu a^2/E_A$ with n the number concentration of mobile ions) for fixed temperature, $k_B T/E_A = 0.01$, and $x = 0.0$ (triangles), 0.1 (diamonds), 0.2 (circles), and 0.4 (squares). Open symbols refer to the domain size $l = 2.4$ and full symbols to $l = 6.3$; Inset: Conductivity spectra of $\text{LiS}_2 + (1-x)\text{GeS}_2 + x\text{GeO}_2$ glasses [138] for $x = 0.1$ (circles), $x = 0.2$, (crosses), and $x = 0.4$ (squares) at $T = 253\text{ K}$, as well as for $x = 0.6$, $T = 224\text{ K}$ (triangles), and $x = 0.8$, $T = 231\text{ K}$ (diamonds) (b) Scaled conductivity spectra for the data shown in (a).

confirmed this expectation by our simulations for the differing distributions with varying x . So far, however, it has not been investigated, whether the scaling remains valid in the presence of spatial correlations of the barriers, as they occur in the course of the partial phase separation discussed above. Indeed we find a super-scaling with respect to variations of both x and l . This is shown in Fig. 2.3, where various conductivity spectra for different x and l in panel (a) are superimposed onto a common master curve in panel (b).

In the inset of Figs. 2.3a,b we show corresponding unscaled and scaled conductivity data for the $\text{Li}_2\text{S}+[(1-x)\text{GeS}_2+x\text{GeO}_2]$ system. The collapse of these data in Fig. 2.3b nicely supports the prediction of super-scaling by the MBM. It is noted that the spectra in Fig. 2.3a also show that the MGFE becomes weaker for higher frequencies, as expected for an ion dynamics governed by lower barriers with decreasing length scale (or increasing frequency) [108].

In summary a model for the MGFE has been developed, which is based on a reduction of jump barriers for the mobile charge carriers in local environments containing different types of network forming units. This model has been applied to mixed network former glasses with the same local geometry of the two types of network forming units upon mixing. It was shown that the model is able to fit experimental data for the conductivity activation energy for representative systems and thus allows one to estimate the strength of the barrier reduction effect. Further it was shown how a kinetically frozen phase separation of the two types of network formers influences the MGFE and can be effectively described by a renormalized coordination in the environments of the jump paths, in agreement with values obtained from the fits. The MBM predicts a time-temperature superposition of conductivity spectra onto a common master curve independent of the mixing ratio x . This prediction could be confirmed by data available for one mixed network former glass system. It should be tested for other glass compositions in the future. From the theoretical perspective, it would be important to critically test the underlying model assumptions by calculations on the molecular level, as e.g. electronic structure calculations of representative clusters and molecular dynamics simulations.

3. The Effect of Spatially Correlated Barrier Energies on the Frequency-Dependent Conductivity

Abstract

In the present chapter the influence of spatially correlated barrier energies on the scaling of the frequency dependent conductivity is re-investigated. In order to address this issue, a 2-dimensional random barrier model is examined, where the barrier energies are spatially correlated with short range correlations. It was found that these correlations have almost no influence on the activation energy for the dc-conductivity and do not alter the scaling in the medium frequency regime.

3.1. Introduction

It was shown in the previous chapter that the correlations, which are introduced by the MBM with microphase separation, have no influence on an apparent universality with respect to the scaling of the frequency dependent conductivity $\sigma(\omega)/\sigma_{\text{dc}} = F(\omega/\omega_c)$. Such a relation is found in a large number of alternative systems, for instance disordered semiconductors [139], ion conductive polymers [140] and room temperature ionic liquids [141]. But in a few systems, in particular mixed alkali systems [108, 142], significant deviations from the commonly observed behavior are found. And it was argued that the additional typical length scale introduced by these correlations disturb this property [108]. Since the MBM implies the fact that only the barriers along the boundaries of the micro-phases are reduced, one could assume that these correlations are rather short ranged and only a fraction of barriers are affected by these correlations. Therefore, it is possible that the effects of such correlations are too weak, to affect the scaling properties significantly. Moreover, the activation energy could be also affected by the introduced correlations. This fact was shown for instance by a mapping procedure from a *random site energy model* to a *random barrier model* (RBM) [143] applying the Ambegaokar, Langer and Halperin approach [109].

Therefore, following questions have to be addressed:

- Could correlations, which include all barriers, affect the usual scaling of the ac-conductivity?
- Do these correlations alter the activation energy in a significant manner?
- How is the typical length scale related to σ_{dc} and ω_c ?

To address these questions, a two-dimensional version of the RBM is studied. The model, which is described in 3.2.1 implies 3 properties: (i) there is no influence of the correlations on the probability function for the barrier energies (ii) the correlation function of the barriers are not affected by the spatial position of the barriers and (iii) the correlations are considered to decrease more slowly than in the MBM. The principal trends should occur in both 2-dimensional systems and 3-dimensional systems. But there are two reasons for using 2-dimensional systems in the present study. First: since the number of possible energetically equivalent pathways is expected to increase with the dimensionality, one has to expect that effects introduced by the correlations are more significant in systems with 2 instead of 3 dimensions. The second reason is the fact that the investigations of 2 dimensional systems are computationally less expensive than a corresponding study in 3-dimensional systems. This fact allows the examination of systems which are much larger than the chosen correlation-length.

3.2. Effects of correlated barrier energies

3.2.1. Generation of uniformly distributed barrier energies with spatial correlations

The algorithm is an adapted version of a previously proposed method (e.g. [144]) and allows to produce a field of spatially correlated random numbers on a discrete lattice with a correlation function of the form:

$$K_f(\mathbf{r}, \mathbf{r}') \approx \exp\left(-\frac{|\mathbf{r} - \mathbf{r}'|^2}{2\xi^2}\right) \quad (3.1)$$

where ξ is the correlation length and \mathbf{r}, \mathbf{r}' are the coordinates of different lattice points. The general idea is to start with "seed" lattices of the same size as the desired model system. Random numbers $x_r^{(0)}$ of a given distribution are assigned to the lattice points. The set of the correlated random numbers $x_r^{(1)}$ is generated by the weighted superposition of $x_r^{(0)}$, i.e.

$$x_r^{(1)}(\mathbf{r}) = 1/\mathcal{A} \sum_{\mathbf{r}'} f_w(\mathbf{r} - \mathbf{r}') x_r^{(0)}(\mathbf{r}') \quad (3.2)$$

[144] where $\mathcal{A} = \sum_{\mathbf{r}} f(\mathbf{r})$ is the normalization factor and $f_w(\mathbf{r})$ is a distance dependent weight. Choosing $f_w(\mathbf{r}) = \Theta(R - |\mathbf{r} - \mathbf{r}'|) \exp(-|\mathbf{r} - \mathbf{r}'|^2/\xi^2)$ (with R as sufficient high cutoff length) one gets a correlation function of the form of eq. 3.1. In the original version the set of $x_r^{(0)}$ was chosen to be uniformly distributed. This has the disadvantage that Gaussian distributed random numbers are only obtained by sufficient large ξ . In the present work random numbers are chosen from a Gaussian distribution to avoid this problem. A straightforward way to obtain uniformly distributed random numbers $x_r^{(2)}$ with a similar correlation function from the $x_r^{(1)}$ is given by the transformation operation:

$$x_r^{(2)} = (1 + \operatorname{erf}(x_r^{(1)}/\sqrt{2}))/2 \quad (3.3)$$

In order to generate the random barrier landscape, a initial lattice \mathfrak{L} is used, which is decorated with random numbers $x_r^{(2)}$. The sidelength of \mathfrak{L} was twice the sidelength L of the final RBM-system. If both indexes (in x and y direction) of a site in \mathfrak{L} were odd (even) the $x_r^{(2)}$ value of this site is taken as the value of the barrier in the final system for the x (y) direction. In the present work a two dimensional system with $L = 256$ and $0 \leq \xi \leq 4$ was chosen¹. The calculation of the ac-conductivity was performed by using the *velocity autocorrelation*-method [135]. In addition, the Hoshen-Kopelman algorithm was applied to calculate E_a .

¹The typical length scale ξ of a correlation must be sufficient smaller than L

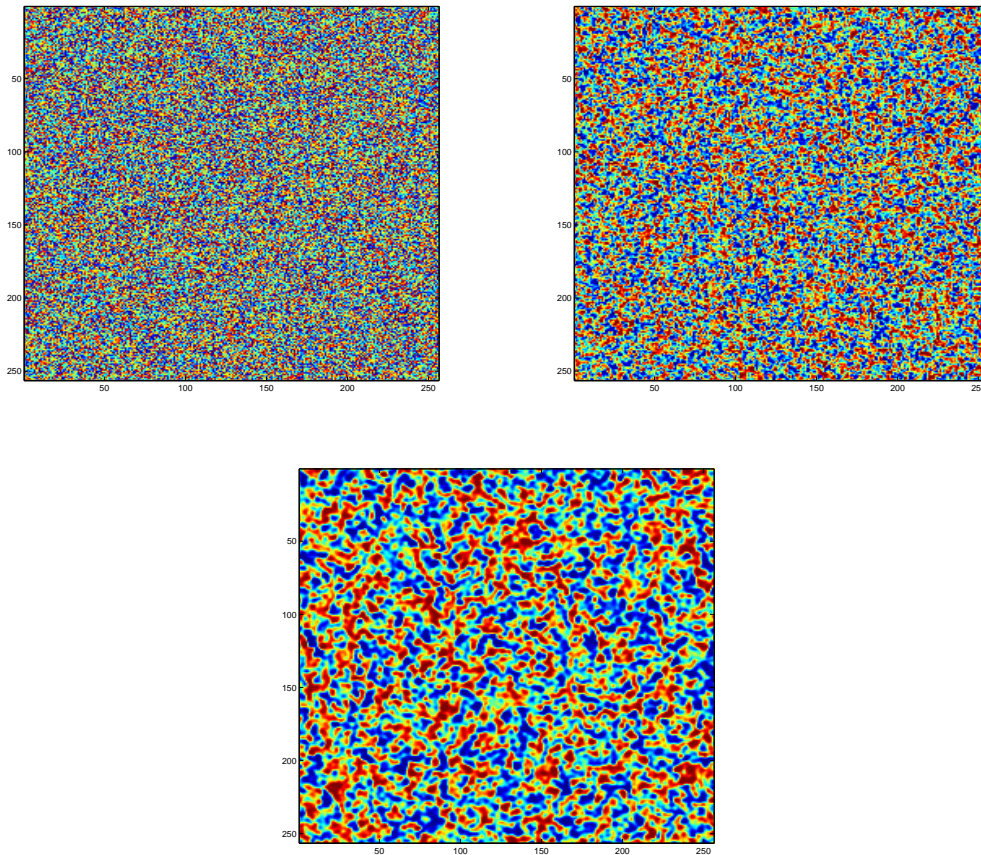


Figure 3.1.: Visualization of a spatial barrier distribution in a squared lattice with $L = 256$ for uniform distributed barrier energies with a Gaussian shaped spatial correlation function and the correlation-length $\xi = 0, 2, 4$ (clockwise starting from upper-left). Blue areas correspond to low energy and red areas to high energy barriers.

3.2.2. Discussion of the influence of correlations

The most surprising result was the fact that the correlations have no measurable influence on the activation energy E_a (see fig. 3.2). In the Hoshen-Kopelman analysis a value $E_a = 0.5$ with no significant dependency on ξ was obtained. This value is in correspondence to the value obtained by the critical path analysis for a 2-dimensional squared lattice with uniformly distributed but uncorrelated barriers². It should be noted that Cordes *et al.* [143] found by mapping of a 3-dimensional RSEM on an effective RBM that the induced correlations lead to a significant decrease of both E_a and p_c . This apparent discrepancy

²The standard deviation increases from 0.006 to 0.026 for $\xi = 0$ to $\xi = 4$.

3. The Effect of Spatially Correlated Barrier Energies on the Frequency-Dependent Conductivity

points to the fact that the influence of the correlations on E_a depends crucially on the definition of the models.

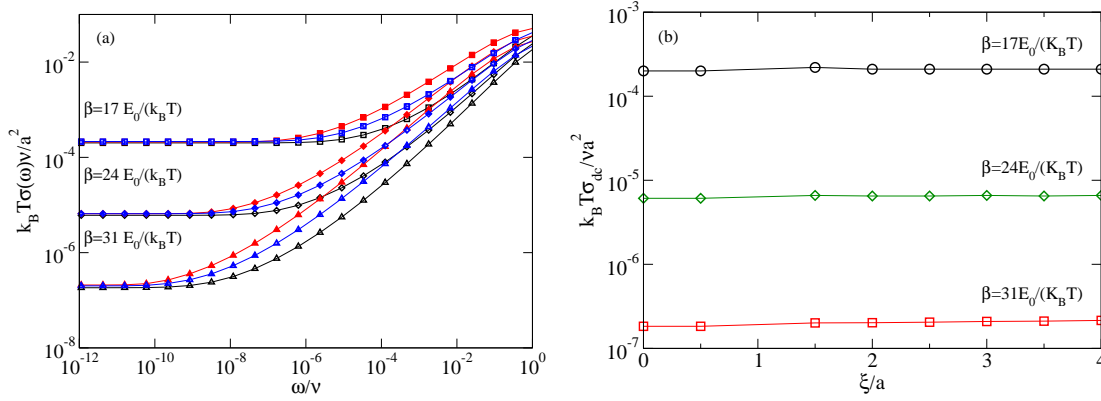


Figure 3.2.: (a) the conductivity isotherms $k_B T \sigma(\omega)$ for a hopping process in a two dimensional system with uniform distributed and spatially correlated random barriers for $\xi = 0.0$ (black open symbols), 1.5 (blue shaded symbols), 3.0 (red closed symbols). (b) The dc conductivity $k_B T \sigma_{dc}$ as function of the characteristic length scale ξ for different β

Moreover, the simulation of the frequency dependent conductivity shows that σ_{dc} is also not affected by the correlation-length. In contrast, the typical frequency ω_c for the onset of dispersive transport shifts to lower frequencies with increasing ξ . This typical frequency corresponds to a typical time scale $t^* \propto \omega_c^{-1}$, which is a measure for the time of the transition from subdiffusive behavior to long-time diffusive behavior. Since the mean squared displacement $\langle r^2(t) \rangle$ is unique function of time, this typical time scale corresponds also to a typical mean squared displacement $\langle r^2(t^*) \rangle$ that is related to σ_{dc} and ω_c by [108]:

$$k_B T \sigma_{dc} / \omega_c \propto \langle r^2(t^*) \rangle \quad (3.4)$$

Since σ_{dc} is not affected and ω_c is decreasing with increasing ξ , eq. 3.4 implies that $\langle r^2(t^*) \rangle$ has to be increased with ξ . In a straightforward approximation one would assume that $\langle r^2(t^*) \rangle$ is roughly proportional to ξ^2 . Figure 3.3a shows the plots $k_B T \sigma_{dc} / \omega_c$ versus ξ^2 . It is found that the linear fits agree well with the simulated $k_B T \sigma_{dc} / \omega_c^3$. In addition, one finds that the incline $k_B T \sigma_{dc} / \omega_c(\xi)$ increases with decreasing temperatures. This finding is explained by the well-known fact that the typical mean squared displacement in the RBM is increased [18, 145, 106] and the influence of the correlations is enhanced with decreasing temperature. Therefore, the incline of $k_B T \sigma_{dc} / \omega_c(\xi) = F(\xi)$ must be increased too, when

³For comparison also a fit $k_B T \sigma_{dc} / \omega_c = A \xi^{2B}$ is shown, where B was found to be $B \approx 0.8$, almost independent of the temperature

3. The Effect of Spatially Correlated Barrier Energies on the Frequency-Dependent Conductivity

the temperature is lowered.

Figure 3.3b shows the fact that for intermediate frequencies ($\omega > \omega_c$) the data collapse for all β to a single mastercurve. Deviations in respect to this "super-scaling" are found only in the high frequency regimes. Probably this behavior is related to finite temperatures, because decreasing the temperature increases the regime, where this scaling can be observed. In order to understand the behavior in the high frequency region, one has to consider the mean squared displacement $\langle r^2(t) \rangle$ as a function of time. In the framework of the RBM $\langle r^2(t) \rangle$ is related to $k_B T \sigma(\omega)$ by the wellknown Green-Kubo-relation [6, 105, 146, 108]:

$$k_B T \sigma(\omega) \propto \omega^2 \lim_{\eta \rightarrow 0} \int_0^{\infty} dt \left(\langle r(t)^2 \rangle e^{i(\omega - \eta)t} \right) \quad (3.5)$$

For short times $\langle r^2(t) \rangle$ increases almost linearly with the time. The corresponding incline is proportional to $k_B T \sigma(\omega \rightarrow \infty)$. With increasing the time, the linear behavior of $\langle r^2(t) \rangle$ crosses over continuously to an apparent power-law behavior, where the exponent is smaller than one (subdiffusive behavior). This subdiffusive behavior of $\langle r^2(t) \rangle$ in the time domain is reflected in the dispersive behavior of the conductivity in the frequency domain. Therefore, the changes, which are observed for $k_B T \sigma(\omega)$ in the high frequency region, are related to the transition of the mean squared displacement from short time to subdiffusive regime in the time domain. Considering these facts, it follows from fig. 3.3 that the characteristic value $\langle \hat{r}^2 \rangle$ of the mean squared displacement, which marks the crossover from short time diffusion to subdiffusive transport, is also increased by the introduction of these correlations. These findings point to the fact that in the present model the scaling is independent of the correlations in the case of $\langle \hat{r}^2 \rangle \ll \langle r^2(t^*) \rangle$.

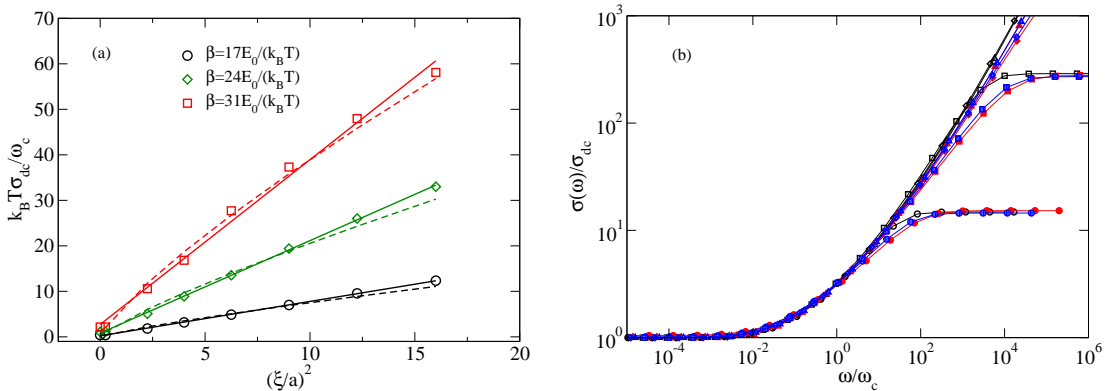


Figure 3.3.: (a) $k_B T \sigma_{dc} / \omega_c = F(\xi^2)$, solid lines are linear fit, dashed lines are fits to a function $k_B T \sigma_{dc} / \omega_c = A \xi^{2B}$ with $B \approx 0.8$. for same data as shown in 3.2(a) (b) Mastercurve of $\sigma(\omega)$ scaled by the relation $\sigma(\omega) / \sigma_{dc} = F(\omega / \omega_c)$

3.3. Summary

In this chapter the RBM was discussed in the framework of a 2-dimensional lattice model with uniformly distributed but spatially correlated barriers. The correlation function of these correlations has approximately a Gaussian shape. In particular, it was shown for this model that the frequency scaled conductivity $\sigma(\omega)/\sigma_{dc} = F(\omega/\omega_c)$ curves tends to a common master curve for sufficient low frequencies. This master curve seems to be independent of the typical length scale. However, the transition to the high frequency plateau is altered by the correlation length. A further important result of the present chapter was the finding that for a given temperature the σ_{dc} is independent from the typical length scale. This corresponds in addition to a decrease of the typical frequency. Interestingly, the activation energy is not affected by the correlations. In addition, it was found that the typical length scale of dispersive transport scales almost linearly with the correlation length. It is important to note that further tests with different shaped correlation functions are required to generalize the presented statements for the scaling of the ac-conductivity in the RBM with spatial correlations of the barrier energies.

4. Network Forming Units in Alkali Borate and Borophosphate Glasses and the Mixed Glass Former Effect¹

Abstract

A theoretical approach is presented for relating structural information to transport properties in ion conducting borophosphate glasses. It relies on the consideration of the different types of glass forming units and the charges associated with them. First it is shown how changes of the unit concentration with the overall glass composition can be understood. Then it is demonstrated how the changes in the unit concentrations upon borate-phosphate mixing lead to a re-distribution of Coulomb traps for the mobile ions and a subsequent change in long-range ionic mobilities. The theories are tested against experiments and yield good agreement with the measured data both for the unit concentrations and the variation of the activation energy.

¹This chapter is published as: M. Schuch, C. Trott, and P. Maass, *RSC Adv.*, **1**, 1370, (2011)

4.1. Introduction

The chemical composition of ion conducting glasses can be varied to a large extent and this offers many possibilities to optimize these materials with respect to different demands, in particular to high ionic conductivities.[9] One important method for enhancing ionic conductivities in glasses is by mixing different glass formers such as silicates, borates, phosphates, etc. The occurrence of a maximum in the ionic conductivity or minimum in the conductivity activation energy upon mixing is commonly referred to as the mixed glass former effect (MGFE). The MGFE has been found in a number of different systems as, for example, the alkali borosilicates [73], alkali borophosphates [69, 130], as well as $\text{GeS}_2 + \text{SiS}_2$ [58], $\text{P}_2\text{O}_5 + \text{TeO}_2$ [59], $\text{TeO}_2 + \text{B}_2\text{O}_3$ [60], $\text{MoO}_3 + \text{TeO}_2$ [61] and $\text{GeO}_2 + \text{GeS}_2$ [63, 64] mixed network former glasses with different types of mobile ions (Li, Na, Ag). It is, however, not always observed. For example, Maia and Rodrigues [74] did not find a maximum in the conductivity in a lithium borosilicate system similar to the one investigated by Tatsumisago *et al.* [73].

The origin of the MGFE is not well understood. For the glass system $0.3\text{Li}_2\text{S} + 0.7[(1-x)\text{SiS}_2 + x\text{GeS}_2]$ Pradel *et al.* [58] showed that the MGFE in the composition range $0.5 \lesssim x \lesssim 0.65$ is caused by a phase separation into an almost Li free GeS_2 glass and a $\text{Li}_2\text{S} + \text{SiS}_2$ glass. The enhancement of Li mobility can thus be traced back to the enrichment of Li ions in the SiS_2 component [11, 12]. When the MGFE is not induced by phase separation, we recently suggested to distinguish between two situations I and II [147]², where in situation I the network forming units (NFUs) remain the same during glass former mixing (as, for example, when germanates are mixed with their thio-analogues), while in situation II different types of NFUs exist for each glass former, which change their concentrations upon mixing. For situation I, it was shown [147] that the MGFE can be caused by reduced activation barriers for ionic jumps in heterogeneous environments containing both glass formers.

In this article we present a theoretical approach applicable to situation II, which relies on the NFUs building the host structure for the ionic motion. We argue that the charges associated with the NFUs and the way how they are localized are of crucial relevance for characterizing the statistical properties of the energy landscape that govern the long-range ionic transport properties. This view is in line with earlier findings that changes of dc-conductivities correlate with the concentration of BO_4 tetrahedra [69, 94].

To demonstrate the new approach we apply it to the mixed glass former effect in sodium borophosphate glasses, where detailed information on the NFU concentrations has been gained recently by magic angle spinning nuclear magnetic resonance (MAS-NMR) [69, 85]. We first show how the observed changes of NFU concentrations with the borate-to-phosphate mixing ratio can be understood from a general modeling. Then we will use this structural information on the NFUs to calculate changes of the conductivity activation energy upon the mixing ratio.

²see chapter 2

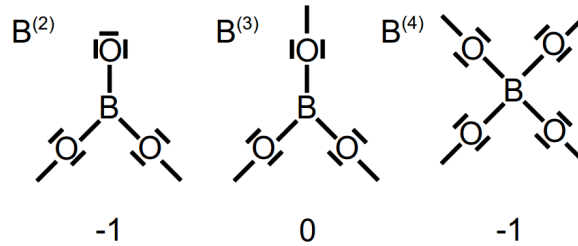


Figure 4.1.: Sketch of the NFUs in alkali borate glasses: Below the chemical representations the charge numbers of the NFUs are given. The charge of the $B^{(4)}$ unit is delocalized over the four bOs, while the charge of the $B^{(2)}$ unit is more localized at the site of the nbO.

4.2. NFU concentrations in alkali borate glasses

Before developing a model for the NFU concentrations in the more complex ternary alkali oxide-borate-phosphate glass compositions, we first revisit here the situation in the simpler binary alkali oxide-borate glasses. Since the pioneering work of Bray and coworkers [148, 149] and further subsequent experimental investigation and theoretical modeling (for a recent overview, see [150]) the behavior of the NFUs in the alkali borate glasses has been clarified to some extent. Overall, three types of NFUs can be distinguished,³ see Fig. 4.1: the trigonal, neutral $B^{(3)}$ unit with three bridging oxygens (bOs), the tetrahedral, negatively charged $B^{(4)}$ unit with four bOs, and the trigonal, negatively charged $B^{(2)}$ unit with two bOs and one non-bridging oxygen (nbO). Since the bOs are shared by two boron atoms, the total number of oxygens attributed to these NFUs is $4 \cdot (1/2) = 2$ for the $B^{(4)}$ unit, $3 \cdot (1/2) = 3/2$ for the $B^{(3)}$ unit, and $2 \cdot (1/2) + 1 = 2$ for the $B^{(2)}$ unit.

For convenient notation let us denote by $\{B^{(n)}\}$, $n = 2, 3, 4$, the fraction of units $\{B^{(n)}\}$, i.e. $\{B^{(n)}\} = [B^{(n)}]/[B]$, where $[B^{(n)}]$ is the concentration of NFUs of type $B^{(n)}$ and $[B] = [B^{(2)}] + [B^{(3)}] + [B^{(4)}]$ the total number concentration of NFUs. The NFU fractions $\{B^{(4)}\}$ as a function of the alkali ion fraction $\{M\} = [M]/[B] = y/(1 - y)$ ($M = \text{Li, Na, K, Rb, or Cs}$) in glasses of composition $yM_2O - (1 - y)B_2O_3$, as measured by MAS-NMR [17, 148, 151, 152, 153, 154] and neutron scattering [155] are redrawn in Fig. 4.2. For small $\{M\} \lesssim 0.4$, each alkali ion M (or, more precisely, each $MO_{1/2}$) converts one $B^{(3)}$ to a $B^{(4)}$ unit, and accordingly $\{B^{(4)}\} = \{M\}$ in Fig. 4.2. This well-known behavior leads to the so-called “borate anomaly”, which refers to the fact that a better connected glassy network (and a correspondingly higher glass transition temperature) is found for larger modifier contents, in contrast to what is commonly seen in other types of modified network glasses, where the cations of the modifier generate nbOs and hence a reduced connectivity.

³In borate glasses with very high alkali content (larger than 50 mole percent), $B^{(1)}$ and $B^{(0)}$ units were also reported [150], but we will not consider such high alkali contents here, where the glassy matrix can be viewed to change from a network to a “salt glass” structure.

For large $\{M\} \gtrsim 0.4$, the one-to-one replacement of $B^{(3)}$ by $B^{(4)}$ units with each addition of M ceases to be valid due to the emergence of $B^{(2)}$ units that compensate for the charges of the alkali ions. As a consequence, $\{B^{(4)}\}$ becomes smaller than $\{M\}$ in Fig. 4.2. The number of charge compensating $B^{(2)}$ units (and the associated reduction of $\{B^{(4)}\}$ with respect to the line $\{B^{(4)}\} = \{M\}$) depends on the type of alkali ion, with a trend of becoming larger with larger alkali ion size, although the $\{B^{(4)}\}$ data for Rb in Fig. 4.2 lie below those for Cs.

4.2.1. Beekenkamp model

A good theoretical description of the overall behavior seen in Fig. 4.2 has been given by Beekenkamp [156] already in 1965. He assumed that the $B^{(4)}$ units are preferentially compensating the charges of the alkali ions, but cannot be directly linked by a bO. This avoidance of $B^{(4)}-B^{(4)}$ linkages likely has its origin in a high effective dipolar interaction between the O-B, B-O bonds forming the links. The NFU fractions then have to obey the following

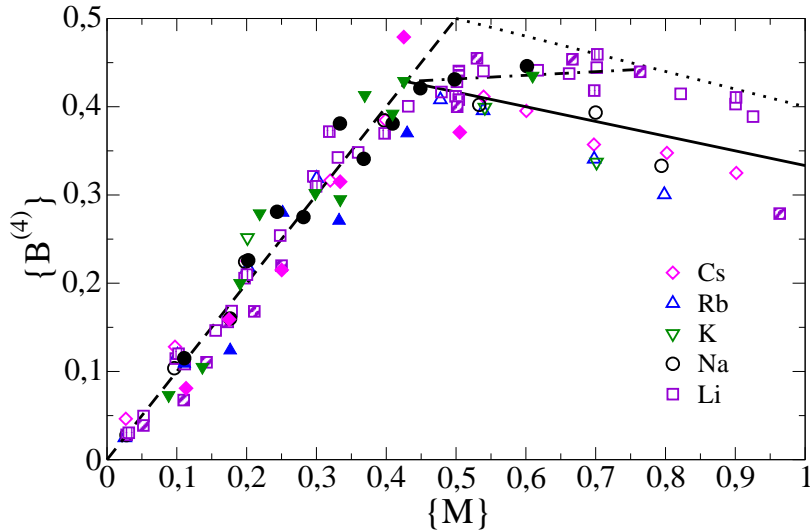


Figure 4.2.: $B^{(4)}$ fraction as a function of alkali fraction $\{M\}$ in alkali borate glasses. The symbols refer to results from MAS-NMR measurements [17, 148, 151, 152, 153, 154] and neutron scattering.[155] Different fillings for the same symbols correspond to different studies. Results from the theoretical modeling are indicated by lines. The dashed line corresponds to the regime of low alkali content ($\{M\} \leq \{M\}_*$). The solid line marks the Beekenkamp result in the regime of high alkali content ($\{M\} > \{M\}_*$) and the dashed line marks the modified Beekenkamp model with $f = 1/4$. The dashed-dotted line indicates the result from the refined modeling in Sec. 4.2.3 for $K = 1.3$.

set of relations:

$$\{B^{(2)}\} + \{B^{(3)}\} + \{B^{(4)}\} = 1 \quad (4.1a)$$

$$\{B^{(2)}\} + \{B^{(4)}\} = \{M\} = \frac{y}{1-y} \quad (4.1b)$$

$$4\{B^{(4)}\} \leq 3\{B^{(3)}\} + 2\{B^{(2)}\} \quad (4.1c)$$

The first equation (4.1a) follows from the given total boron content and the second equation (4.1b) from the requirement of charge neutrality. The relation (4.1c) expresses that the number of bOs linked to $B^{(4)}$ units must be smaller than or equal to the number of bOs linked to $B^{(3)}$ and $B^{(2)}$ units, since a bO bonded to a $B^{(4)}$ has to be linked to either a $B^{(3)}$ or $B^{(2)}$ unit due to the $B^{(4)}$ - $B^{(4)}$ avoidance. Let us note that the two eqs. (4.1a) and (4.1b) automatically imply that the fraction $\{O\}$ of oxygens given by the stoichiometry ($\{O\} = 3/2 + \{M\}/2$) equals the one calculated from the units ($\{O\} = 2\{B^{(2)}\} + 3\{B^{(3)}\} + 2\{B^{(4)}\}$). This condition could thus be used as an equivalent alternative to the requirement of charge neutrality.

For small $\{M\}$, only the favored $B^{(4)}$ units are needed for charge compensation ($\{B^{(2)}\} = 0$) and eqs. (4.1b) and (4.1a) yield $\{B^{(4)}\} = \{M\}$ and $\{B^{(3)}\} = 1 - \{M\}$. This is valid as long as relation (4.1c) is satisfied, i.e. for $4\{M\} \leq 3(1 - \{M\})$ or $\{M\} \leq 3/7 \cong 0.429$. For $\{M\} > 3/7$, in addition $B^{(2)}$ units are needed for charge compensation. Since the $B^{(4)}$ are favoured over the $B^{(2)}$ units, the number of $B^{(4)}$ units has to be taken as large as possible under the constraint (4.1c), i.e. this relation becomes an equation. Inserting it into eq. (4.1a) yields $\{B^{(4)}\} = [3 - \{B^{(2)}\}]/7$, and inserting this into eq. (4.1b) gives $\{B^{(2)}\} = 7\{M\}/6 - 1/2$ and $\{B^{(3)}\} = 1 - \{M\}$. In summary, the Beekenkamp model predicts

$$\{B^{(4)}\} = \begin{cases} \{M\}, & \{M\} \leq 3/7 \\ \frac{1}{2} - \frac{1}{6}\{M\}, & \{M\} > 3/7 \end{cases} \quad (4.2a)$$

$$\{B^{(3)}\} = 1 - \{M\} \quad (4.2b)$$

$$\{B^{(2)}\} = \begin{cases} 0, & \{M\} \leq 3/7 \\ \frac{7}{6}\{M\} - \frac{1}{2}, & \{M\} > 3/7 \end{cases} \quad (4.2c)$$

The predicted behavior for $\{B^{(4)}\}$ is indicated by the dashed and solid lines in Fig. 4.2. The terminal point (intersection of dashed with solid line) $\{M\}_* = 3/7$ of $\{B^{(4)}\} = \{M\}$ is in good agreement with the measurements. Except for the lithium borates, the line $\{B^{(4)}\} = 1/2 - \{M\}/6$ captures quite well the behavior for $\{M\} > \{M\}_*$, although there is a tendency of the measured $\{B^{(4)}\}$ to be a smaller, in particular at larger $\{M\} \gtrsim 0.7$.

The measured $\{B^{(4)}\}$ data for Li are significantly higher than that predicted by the Beekenkamp model. This points to the fact that the constraint of forbidden $B^{(4)}$ - $B^{(4)}$

linkages is too strict in this case. It has been conjectured that the small Li ions can come closer to the bOs in these linkages and thereby are able to stabilise them. With respect to the two other unit types $B^{(2)}$ and $B^{(3)}$, let us note that the result $\{B^{(3)}\} = 1 - \{M\}$ follows already from eqs. (4.1a), (4.1b) and simply expresses the fact that for each additional M , a neutral $B^{(3)}$ unit needs to be replaced by one of the two charged units. With $\{B^{(4)}\}$ and $\{B^{(3)}\}$ known, $\{B^{(2)}\}$ is fixed by the overall boron content.

4.2.2. Constant fraction of $B^{(4)}$ - $B^{(4)}$ linkages

In order to account for the discrepancies between the Beekenkamp model and the measurements, one may release the constraint of strict absence of linkages between $B^{(4)}$ units. In fact, it is known that in crystalline alkali borates such linkages exist [150] and there is evidence that this is the case also in vitreous systems [157]. Gupta [158] proposed a model, where all $B^{(4)}$ are sharing a bO with exactly one other $B^{(4)}$, leading to a replacement of relation (4.1c) by $3\{B^{(4)}\} \leq 3\{B^{(3)}\} + 2\{B^{(2)}\}$, since each of the remaining three bOs bonded to a $B^{(4)}$ unit has to be linked to either a $B^{(3)}$ or a $B^{(2)}$ unit.

More generally, we can introduce the fraction f of B-O bonds belonging to $B^{(4)}$ units that are part of $B^{(4)}$ - $B^{(4)}$ linkages. We then have to replace relation (4.1c) by

$$4(1 - f)\{B^{(4)}\} \leq 3\{B^{(3)}\} + 2\{B^{(2)}\} \quad (4.3)$$

since now a fraction $(1 - f)$ of the B-O bonds belonging to $B^{(4)}$ units must be connected to either $B^{(3)}$ or $B^{(2)}$ units. In this way the Gupta model can be re-interpreted as referring to the case $f = 1/4$, as far as the NFU fractions are concerned. The same type of calculations as outlined above for the Beekenkamp model (that corresponds to $f = 0$) for this model yield

$$\{B^{(4)}\} = \begin{cases} \{M\}, & \{M\} \leq \{M\}_f \\ \frac{3 - \{M\}}{6 - 4f}, & \{M\} > \{M\}_f = \frac{3}{7 - 4f} \end{cases} \quad (4.4)$$

As before, $\{B^{(3)}\} = 1 - \{M\}$ and $\{B^{(2)}\} = 0$ for $\{M\} \leq \{M\}_f$, while $\{B^{(2)}\} = 1 - \{B^{(3)}\} - \{B^{(4)}\}$ for $\{M\} > \{M\}_f$.

According to eq. (4.4), when increasing f from $f = 0$, one obtains a shift of $\{M\}_*$ from $3/7$ to a higher value $\{M\}_f = 3/(7 - 4f)$ and a steeper fall of $\{B^{(4)}\}$ for $\{M\} > \{M\}_f$, corresponding to a change in slope from $(-1/6)$ to $[-1/(6 - 4f)]$. As an example, we have indicated the result for $f = 1/4$ as dotted line in Fig. 4.2. This line overestimates $\{B^{(4)}\}$ in the interval $0.43 < \{M\} < 0.7$ but it appears as a limiting line of the $B^{(4)}$ fraction for $\{M\} \gtrsim 0.7$ in lithium borate glasses. This suggests that the Gupta model corresponds to a limiting case in the sense that a $B^{(4)}$ unit can have at most one linkage to another $B^{(4)}$ unit.

4.2.3. Balancing mutually linked $B^{(4)}$ with $B^{(2)}$ units

While the approach of fixing the fraction f is a straightforward extension of the Beekenkamp model, it is not clear why f should be independent of $\{M\}$. For a refinement of the theoretical treatment, we now assume that a $B^{(4)}$ unit can have at most one linkage to another $B^{(4)}$ unit and invoke the often applied concept that concentrations of different structural subgroups in a glass are balanced via chemical reactions.⁴ Let us consider network configurations with mutually linked $B^{(4)}$ units to be in balance with network configurations without such linkages but additional $B^{(2)}$ units according to



Here $\tilde{B}^{(4)}$ denotes a $B^{(4)}$ unit that is linked to another $B^{(4)}$. The reaction (4.5) represents the most simple one by which a balancing of the respective units is described under conservation of both the charge and the number of oxygens ($2 \times (1/2) + 1 = 4 \times (1/2)$).

Applying the law of mass action to the reaction (4.5) gives

$$\frac{\{\tilde{B}^{(4)}\}}{\{B^{(2)}\}} = K \quad (4.6)$$

where K is the reaction constant. While K may depend on $\{M\}$, one can conjecture that this dependence is weak, since (4.5) is primarily a reaction related to the network structure. It should thus be a good approximation to take K constant.

Since the $\tilde{B}^{(4)}$ units are linked through one bO to another $B^{(4)}$ ($\tilde{B}^{(4)}$) unit, the number of bOs to be connected to either $B^{(2)}$ or $B^{(3)}$ units is proportional to $4(\{B^{(4)}\} - \{\tilde{B}^{(4)}\}) + 3\{\tilde{B}^{(4)}\}$. Relation (4.1c) then has to be replaced by

$$4\{B^{(4)}\} - \{\tilde{B}^{(4)}\} \leq 3\{B^{(3)}\} + 2\{B^{(2)}\} \quad (4.7)$$

Equations (4.1a), (4.1b), (4.6) together with relation (4.7) form a complete set to determine the NFU fractions under the principle of $B^{(4)}$ preference for charge compensation. It is clear that the reaction is only relevant when the $\tilde{B}^{(4)}$ units form and accordingly the low alkali regime described in eqs. (4.2) is not modified, including its end point $\{M\}_\star = 3/7$. For $\{M\} > \{M\}_\star$ (and $\{M\} \leq \{M\}_K$, see eq. (4.9) below) we obtain

$$\{\tilde{B}^{(4)}\} = \frac{7K}{6+K}(\{M\} - \{M\}_\star) \quad (4.8a)$$

$$\{B^{(4)}\} = \frac{3 + (K-1)\{M\}}{6+K} \quad (4.8b)$$

⁴The balancing should occur before the glass structure becomes frozen into a non-equilibrium state, meaning that the corresponding reaction constant is expected to depend on an effective temperature that varies weakly with the cooling rate.

and the fractions for $\{B^{(2)}\}$ and $\{B^{(3)}\}$ follow from eqs. (4.1a) and (4.1b). With increasing $\{M\}$, $\{\tilde{B}^{(4)}\}$ increases until $\{\tilde{B}^{(4)}\} = \{B^{(4)}\}$, where $\{M\}$ equals⁵

$$\{M\}_K = \frac{3(K+1)}{6K+1} \quad (4.9)$$

For $\{M\} > \{M\}_K$, $\{\tilde{B}^{(4)}\} = \{B^{(4)}\}$, that means the limit described by the Gupta model is reached with $\{B^{(4)}\} = (3 - \{M\})/5$.

A success of the refined model is that it can well describe the measured $\{B^{(4)}\}$ in lithium borate glasses when taking $K = 1.3$ (see Fig. 4.2). It is interesting to note that a fitting of the $\{B^{(4)}\}$ dependence on $\{M\}$ in lithium borate glasses by three linear regimes was shown to give a good description by Feller *et al.* already in 1982 [159]. The refined model allows one to reason this finding. Moreover, the model still includes the results of the Beekenkamp model in the limit $K \rightarrow 0$ (no linkages between $B^{(4)}$ units), which describes the behavior fairly well for the other types of alkali ions (K could be also fitted for each type).

Finally, let us note that it is possible to obtain $B^{(4)}$ fractions below the line of the Beekenkamp model for $\{M\} > 3/7$ (eq. (4.2a)) and thus a possibly better agreement with the measured data. $B^{(4)}$ fractions below this line result, for example, when assuming that $B^{(2)}$ - $B^{(4)}$ linkages are less likely and $B^{(2)}$ - $B^{(3)}$ linkages are formed. A more detailed discussion of such further refinements and predictions for linkages will be presented elsewhere.

4.3. NFU concentrations in alkali borophosphate glasses

We now develop a model to describe the NFU concentrations in alkali borophosphate glasses with general composition $yM_2O-(1-y)[xB_2O_3-(1-x)P_2O_5]$. Detailed comparisons with experiments are made for sodium borate glasses of composition $0.4Na_2O-0.6[xB_2O_3-(1-x)P_2O_5]$ as a function of the borate to phosphate mixing parameter x . In these glasses, NFU concentrations were determined recently by MAS-NMR[69, 85] and the results of these measurements has served as a reference in our modeling approach.

Seven NFUs could be distinguished in the work by Zielniok *et al.*[69]: in addition to the three borate units shown in Fig. 4.1, there are four tetrahedral phosphate units $P^{(n)}$, $n = 0, \dots, 3$ with n bOs, $(4-n)$ nbOs, and charges $(n-3)$, see Fig. 4.3. The total number of oxygens attributed to the $P^{(n)}$ unit is $(n/2) + (4-n) = 4 - n/2$. Extending the definition of the previous section, we denote by $\{X\}$ ($X=B^{(n)}$ or $P^{(n)}$) the fraction of network units with respect to the network forming cations, i.e. $\{X\} = [X]/([B] + [P])$.

The equations for fixing the total boron content, the total phosphorous content, and the

⁵Since we are not considering $\{B^{(0)}\}$ and $\{B^{(1)}\}$ units here, the validity of the treatment is restricted $\{M\} \leq 1$, see the comment above.

charge neutrality are

$$\{B^{(4)}\} + \{B^{(3)}\} + \{B^{(2)}\} = x \quad (4.10a)$$

$$\{P^{(3)}\} + \{P^{(2)}\} + \{P^{(1)}\} + \{P^{(0)}\} = (1 - x) \quad (4.10b)$$

$$\{B^{(4)}\} + \{B^{(2)}\} + \{P^{(2)}\} + 2\{P^{(1)}\} + 3\{P^{(0)}\} = \{M\} \quad (4.10c)$$

with $\{M\} = y/(1 - y)$. Analogous to the alkali borate system, it can be checked that eqs. (4.10a)-(4.10c) automatically imply that the fraction $\{O\}$ of oxygens given by the stoichiometry ($\{O\} = \{M\}/2 + 3x/2 + 5(1 - x)/2$) equals the one calculated from the units ($\{O\} = 2\{B^{(2)}\} + 3\{B^{(3)}\}/2 + 2\{B^{(4)}\} + \sum_{n=0}^3(4 - n/2)\{P^{(n)}\}$). Accordingly, this condition could be used as an equivalent alternative to the requirement of charge neutrality. Equations (4.10a)-(4.10c) are three determining equations for the seven unknown NFU fractions. To proceed, we thus need to include additional information in the theoretical modeling.

Corresponding additional information can be included by considering the rank order by which the NFU types are favored with respect to charge compensation of the alkali ions. We assume that the relevant parameter controlling this rank order is the charge delocalization, where higher delocalization makes an NFU type more favorable. As a measure of the delocalization, we take $|q_\alpha|/k_\alpha$, where q_α and k_α denote the charge and the number of "charge carrying oxygens" of NFU α , respectively. For the NFUs $B^{(2)}$, $P^{(2)}$, $P^{(1)}$, and $P^{(0)}$,

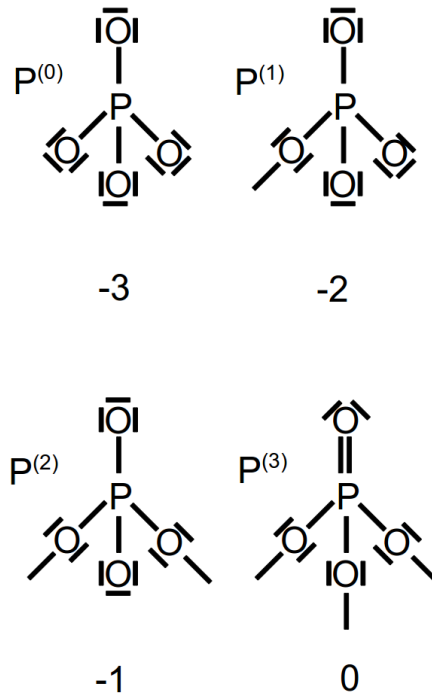


Figure 4.3.: Sketch of the phosphate NFUs with their charge numbers. The charges are considered to be equally spread over the nbOs.

k_α equals the number of nbOs. Note that this implies that the delocalization of electrons belonging to the double bond in the charged $P^{(n)}$ units is taken into account. This means that the nbOs of the $P^{(n)}$ units are considered to be equivalent, which is in agreement with results from ab initio molecular orbital calculations [160, 161] and diffraction studies [162, 163]. For the $B^{(4)}$ unit, the charge (-1) is shared equally between all four bOs. Hence we find $|q_\alpha|/k_\alpha = 1/4, 1/2, 2/3, 3/4,$ and 1 for the $B^{(4)}, P^{(2)}, P^{(1)}, P^{(0)},$ and $B^{(2)}$ unit, respectively, giving the corresponding rank order for charge compensation.

How far this rank order is pivotal for the preferred selection of the charged NFUs depends on the question to what extent the charge delocalization is reflected in certain differences between formation energies of these NFUs (see the Appendix for a further discussion of this point). In the following we first assume that the relevant differences between the formation energies are large compared to the thermal energy (with exceptions to be discussed further below). This leads to the occurrence of different x -regimes, where one particular NFU is replaced by another one and only a limited number of the NFU types need to be considered. As long as this number is small, the three eqs. (4.10a)-(4.10c) are sufficient to predict the NFU concentrations.

In the alkali phosphate glass ($x = 0$), $P^{(2)}$ units are the most favorable NFUs for charge compensation and the network is formed by these units with fraction $\{P^{(2)}\} = \{M\}$ and the neutral $P^{(3)}$ units with fraction $\{P^{(3)}\} = 1 - \{M\}$. When some phosphate is partially substituted by borate, $B^{(4)}$ units become more favorable for the charge compensation. Accordingly, $P^{(2)}$ are replaced by $B^{(4)}$ units rather than $P^{(3)}$ by $B^{(3)}$ units (more precisely, the free energy change for $P^{(3)}$ by $B^{(3)}$ substitution has to be larger than the the free energy change for $P^{(2)}$ by $B^{(4)}$ substitution, see the Appendix). For small x we thus need to consider only the NFUs $P^{(2)}, P^{(3)},$ and $B^{(4)}$. Equations (4.10a)-(4.10c) then yield

$$\{B^{(4)}\} = x \quad (4.11a)$$

$$\{P^{(2)}\} = \{M\} - x \quad (4.11b)$$

$$\{P^{(3)}\} = 1 - \{M\} \quad (4.11c)$$

The question is, at which value $x = x_1$ this simple behavior terminates. Since $\{P^{(2)}\}$ must be positive, we find

$$x_1 = \{M\} \quad (4.12)$$

from eq. (4.11b). However, for large $\{M\}$ this would imply that $\{B^{(4)}\}$ can become large in contrast to what we know from the alkali borate glasses, where the $B^{(4)}$ units are reluctant to become mutually linked. If we assume, as in the Beekenkamp model, that $B^{(4)}$ - $B^{(4)}$ linkages are forbidden, we should add the constraint $4\{B^{(4)}\} \leq 3\{P^{(3)}\} + 2\{P^{(2)}\}$, i.e. $4x \leq 3 - \{M\} - 2x$. This becomes violated at $x = x_1$ if $\{M\} > \{M\}_\star$ with

$$\{M\}_\star = \frac{3}{7} \quad (4.13)$$

That the same critical value $\{M\}_\star$ is obtained here as in the Beekenkamp model is due to

the fact that the number of bOs in the $P^{(2)}$ and $P^{(3)}$ units equals those in the $B^{(2)}$ and $B^{(3)}$ units.

When $\{M\} \leq \{M\}_*$ and phosphate is replaced by borate beyond $x = x_1$, a second x -regime is entered. Since all alkali charges are now compensated by the most favorable $B^{(4)}$ units, $\{B^{(4)}\}$ stays constant at the value $\{B^{(4)}\}_* = x_1 = \{M\}$, while the neutral $B^{(3)}$ replace the neutral $P^{(3)}$ units. According to eqs. (4.10a)-(4.10b) we hence obtain for $x \geq x_1$

$$\{B^{(4)}\} = \{B^{(4)}\}_* = \{M\} \quad (4.14a)$$

$$\{P^{(3)}\} = 1 - x \quad (4.14b)$$

$$\{B^{(3)}\} = x - \{B^{(4)}\}_* = x - \{M\} \quad (4.14c)$$

There is no further x -regime, since the replacement of $P^{(3)}$ by $B^{(3)}$ terminates at $x = 1$, when $\{P^{(3)}\} = 0$.

Equations (4.11), (4.12), and (4.14) describe the NFU concentrations for low alkali contents $\{M\} \leq \{M\}_*$ with $\{M\}_*$ given in eq. (4.13). A plot of these NFU fractions as a function of x is shown in Fig. 4.4a. This predicted behaviour has to be considered with some care though, since in alkali borophosphate glasses with small alkali content, it is possible also that a positively charged $P^{(4)}$ unit is built into the network structure [85]. These units are known to occur in pure borophosphate crystals [164]. In the presence of $P^{(4)}$ units the analysis needs to be modified, but we will not pursue this further here.

When $\{M\}$ exceeds $\{M\}_*$, as in the sodium borophosphate glasses studied by Zielniok *et al.*[69], where $\{M\} = 2/3$, the theoretical treatment becomes more complicated, since we have to address the question how to deal with the $B^{(4)}$ - $B^{(4)}$ linkages. Similar as in the previous section 4.2, we start in Sec. 4.3.1 by introducing a constant (x independent) fraction f of B-O bonds belonging to $B^{(4)}$ units that are part of $B^{(4)}$ - $B^{(4)}$ linkages. In addition, we assume that the appearance of the charged NFUs units is solely controlled by the rank order. As shown below, this leads to different x -regimes, where one particular NFU is replaced by another one. When comparing to the experimental results reported in [69], there is already an overall agreement for $f \simeq 1/10$ (see Fig. 4.5), but finer details are not reproduced. In a next step of the modeling presented in Sec. 4.3.2 we let the fractions of different phosphate units partially balance each other and this leads to a good agreement with the experimental data.

From a theoretical point of view, it is, however, not fully satisfactory to use a constant fraction f . It can be conjectured that f is in fact weakly dependent on x , since in the only known sodium borophosphate crystal with composition $Na_5B_2P_3O_{15}$, the structure exhibits $B^{(4)}$ - $B^{(4)}$ linkages [85, 165]. This suggests that local network configurations resembling this crystalline structure are more likely to occur in the glass at higher phosphate contents. In fact, guided by the crystalline structure one can refine the analysis further and constrain the $B^{(4)}$ fraction to the $P^{(2)}$ fraction. This refined modeling presented in Sec. 4.3.3 provides a theory for the NFU concentrations, where there is no need to specify a f parameter, at least in those cases where the Beekenkamp model is considered to be a valid description of

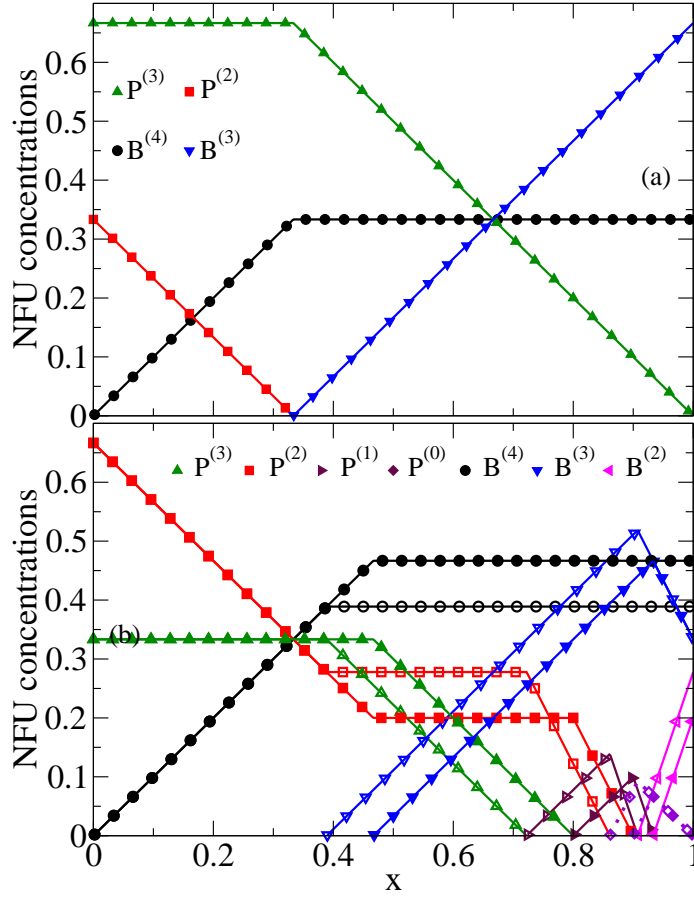


Figure 4.4.: Theoretical NFU fractions as a function of x in alkali borophosphate glasses $yM_2O-(1-y)[xB_2O_3-(1-x)P_2O_5]$ for (a) low alkali content $\{M\} = 1/3$ ($y = 0.25$) as predicted by eqs. (4.11)-(4.14), and (b) large alkali content $\{M\} = 2/3$ ($y = 0.4$) as predicted by eqs. (4.11), (4.20)-(4.26). The open symbols in (b) refer to $f = 0$ and the full symbols to $f = 1/4$.

the pure borate system (forbidden $B^{(4)}$ - $B^{(4)}$ linkages at $x = 1$).

4.3.1. $\{M\} \geq \{M\}_*$: Constant fraction of $B^{(4)}$ - $B^{(4)}$ linkages

With the fraction f , the general relation constraining the $B^{(4)}$ - $B^{(4)}$ linkages is

$$4(1-f)\{B^{(4)}\} \leq 3(\{B^{(3)}\} + \{P^{(3)}\}) + 2(\{B^{(2)}\} + \{P^{(2)}\}) + \{P^{(1)}\} \quad (4.15)$$

This implies that the analysis on the termination of regime 1 given by the set of eqs. (4.11) has to be repeated with the result that $\{M\}_*$ from eq. (4.13) is modified to

$$\{M\}_* = \frac{3}{7-4f} \quad (4.16)$$

and that x_1 from eq. (4.12) is modified to

$$x_1 = \frac{3 - \{M\}}{6 - 4f} \quad (4.17)$$

The NFU fractions in regime 1 are given by eq. (4.11) and the $P^{(2)}$ fraction reached at $x = x_1$ is $\{P^{(2)}\} = \{M\} - x_1 = (7 - 4f)(6 - 4f)^{-1}(\{M\} - \{M\}_\star) > 0$.

Since $B^{(4)}$ is the most favorable NFU for charge compensation, as much as possible $B^{(4)}$ should be kept upon further replacement of phosphate by borate. Relation (4.15) hence becomes an equation for $x \geq x_1$. When expressing the fractions $\{P^{(3)}\}$ and $\{B^{(3)}\}$ of the neutral NFUs by the fractions of the charged NFUs via eqs. (4.10a), (4.10b), and inserting these into eq. (4.15), the charged NFUs in the resulting equation appear only in a linear combination that is identical to the left hand side of eq. (4.10c). This means that with eqs. (4.10a)-(4.10c), eq. (4.15) becomes a closed equation for $\{B^{(4)}\}$ with solution

$$\{B^{(4)}\} = \{B^{(4)}\}_\star = \frac{3 - \{M\}}{6 - 4f} = x_1, \quad x \geq x_1 \quad (4.18)$$

As a consequence, we can, in the following further discussion of the regimes for $x \geq x_1$, disregard relation (4.15) and set $\{B^{(4)}\} = \{B^{(4)}\}_\star$ in eqs. (4.10a)-(4.10c).

Moreover, when defining the subsequent second regime $x_1 \leq x \leq x_2$ as the one, where the least favorable $B^{(2)}$ unit is still not needed for charge compensation ($\{B^{(2)}\} = 0$), we obtain from eq. (4.10a)

$$\{B^{(3)}\} = x - \{B^{(4)}\}_\star \quad (4.19)$$

in this second regime. The reason for defining regime 2 in this way becomes clear below.

Regime 2 ($x_1 \leq x \leq x_2$): Replacements of the $P^{(3)}$, $P^{(2)}$, and $P^{(1)}$ units

When the appearance of the charged NFUs is solely determined by their rank order with respect to charge compensation, the regime 2 is divided into three sub-regimes I-III with a simple one-to-one replacement of NFUs.

Subregime I ($x_1 \leq x \leq x_2^I$): Replacement of $P^{(3)}$ by $B^{(3)}$

Since $\{B^{(4)}\}$ has saturated and $B^{(2)}$ is the least favorable NFU for charge compensation, $B^{(3)}$ are replacing $P^{(3)}$ units and the network is formed by the $B^{(3)}$, $B^{(4)}$, $P^{(2)}$, and $P^{(4)}$ units. Equations (4.10b), (4.10c) provide a closed pair for the left unknown $\{P^{(2)}\}$ and $\{P^{(3)}\}$ with solution

$$\{P^{(2)}\} = \{M\} - \{B^{(4)}\}_\star \quad (4.20a)$$

$$\{P^{(3)}\} = (1 - \{M\} + \{B^{(4)}\}_\star) - x \quad (4.20b)$$

The replacement of $P^{(3)}$ by $B^{(3)}$ terminates when $P^{(3)}$ is no longer available, i.e. at

$$x_2^I = 1 - \{M\} + \{B^{(4)}\}_\star \quad (4.21)$$

Subregime II ($x_2^I \leq x \leq x_2^{II}$): Replacement of $P^{(2)}$ by $P^{(1)}$

According to the rank order, $P^{(2)}$ are replaced by $P^{(1)}$ units with further increasing x and

4. Network Forming Units in Alkali Borate and Borophosphate Glasses and the Mixed Glass Former Effect

the network is formed by the $B^{(3)}$, $B^{(4)}$, $P^{(1)}$, and $P^{(2)}$ units. Equations (4.10b), (4.10c) yield

$$\{P^{(1)}\} = x - (1 - \{M\} + \{B^{(4)}\}_\star) \quad (4.22a)$$

$$\{P^{(2)}\} = (2 - \{M\} + \{B^{(4)}\}_\star) - 2x \quad (4.22b)$$

The replacement of $P^{(2)}$ by $P^{(1)}$ terminates when $P^{(2)}$ is no longer available, i.e. at

$$x_2^{\text{II}} = 1 - \frac{\{M\} - \{B^{(4)}\}_\star}{2} \quad (4.23)$$

Subregime III ($x_2^{\text{II}} \leq x \leq x_2$): Replacement of $P^{(1)}$ by $P^{(0)}$
 $P^{(1)}$ are replaced by $P^{(0)}$ units and the network is formed by the $B^{(3)}$ and $B^{(4)}$ units, and the $P^{(0)}$ and $P^{(1)}$ units with fractions

$$\{P^{(0)}\} = 2x - (2 - \{M\} + \{B^{(4)}\}_\star) \quad (4.24a)$$

$$\{P^{(1)}\} = (3 - \{M\} + \{B^{(4)}\}_\star) - 3x \quad (4.24b)$$

The replacement terminates when $\{P^{(1)}\} = 0$, i.e. at

$$x_2 = 1 - \frac{\{M\} - \{B^{(4)}\}_\star}{3} \quad (4.25)$$

Regime 3 ($x_2 \leq x \leq 1$): Replacement of $P^{(0)}$ by $B^{(2)}$

Eventually, when the charges of the alkali ions can no longer be compensated by the $B^{(4)}$ and charged phosphate units, the least favorable $B^{(2)}$ substitute the $P^{(0)}$ units. The network is formed by the $B^{(2)}$, $B^{(3)}$, $B^{(4)}$, and $P^{(0)}$ units and eqs. (4.10a)-(4.10c) yield

$$\{B^{(2)}\} = 3x - (3 - \{M\} + \{B^{(4)}\}_\star) \quad (4.26a)$$

$$\{B^{(3)}\} = (3 - \{M\}) - 2x \quad (4.26b)$$

$$\{P^{(0)}\} = 1 - x \quad (4.26c)$$

The NFU fractions as a function of x , as predicted by eqs. (4.11), (4.17)-(4.26) for high alkali contents $\{M\} > \{M\}_\star$ with $\{M\}_\star$ given by eq. (4.16), are shown in Fig. 4.4b for two different fractions $f = 0$ and $1/4$. By its definition f controls the saturation value $\{B^{(4)}\}_\star$ [eq. (4.18)], and with a change of f goes along a small shift of the regimes [cf. eqs. (4.17), (4.21), (4.23), (4.25)]. The slopes of the one-to-one replacement lines in the various regimes are not affected by f [cf. eqs. (4.11) (4.20), (4.22), (4.24), (4.26)], since these are fixed by the condition of charge neutrality (or, equivalently, by the oxygen content).

We thus have found that the behavior of the NFU concentrations becomes quite simple also for large alkali contents, once f is fixed and the rank order of the charged NFUs for charge compensation is known. In principle, there is no freedom to choose f , when fixing it by its value in the pure alkali borate glass ($x = 1$), see Sec. 4.2. However, as discussed above, we should expect f to be only approximately constant in the borophosphate glass

and for comparison with experiments it can be more practical to determine f from the (mean) value of $\{B^{(4)}\}$ measured on the boron rich side (e.g. for $x > 0.5$).

Figure 4.5 shows such comparison with the MAS-NMR measurements [69] on sodium borophosphate glasses with composition $0.4Na_2O-0.6[xB_2O_3-(1-x)P_2O_5]$, where we find $f = 1/10$, corresponding to $\{B^{(4)}\}_* = 5/12 \cong 0.417$, to give a good account of the indeed almost constant $B^{(4)}$ fraction on the boron rich side for x in the range $0.5 - 0.9$. For $x = 1$, the value for $\{B^{(4)}\}$ reported in [69] is much smaller than $\{B^{(4)}\}_*$ but in view of the analysis of the alkali borate glasses in the previous Sec. 4.2 we believe that this discrepancy is due to a measurement error or a consequence of some peculiarity in the glass preparation. In fact, MAS-NMR measurements for sodium borate glasses reported in [154] give $\{B^{(4)}\} = 0.40$ for $\{M\} = 0.53$ and $\{B^{(4)}\} = 0.39$ for $\{M\} = 0.7$ (see Fig. 4.3), from which we can estimate $\{B^{(4)}\} = 0.39$ for $\{M\} = 2/3 = 0.66$ in the system investigated in [69]. The corresponding NFU fractions are marked by the open symbols in Fig. 4.5, which are in agreement with the general behavior discussed in Sec. 4.2. For $x = 1$ we will use these data for further comparison in the following. Note that the unexpected low value of $\{B^{(4)}\}$ at $x = 1$ reported in [69, 85] necessarily affects also the $B^{(2)}$ and $B^{(3)}$ fractions.

While the overall behavior of the measured NFU fractions in Fig. 4.5 is captured by the modeling (with the values at $x = 1$ taken as those reported by [154]), the following deviations can be identified:

- (i) In the experimental data, $P^{(1)}$ units start to emerge between $x = 0.6$ and 0.7 , that means at a significantly lower value than $x_{\frac{1}{2}}^I = 3/4$ predicted by eq. (4.21) for $\{M\} = 2/3$ and $f = 1/10$ ($\{B^{(4)}\}_* = 5/12 \cong 0.417$). Correlated with this behaviour is a corresponding decrease of $\{P^{(2)}\}$ when approaching the end of subregime I. This is in contrast to eq. (4.20a) that predicts $\{P^{(2)}\} = 1/4$ to stay constant in this regime.
- (ii) In the experimental data, $P^{(2)}$, $P^{(1)}$ and $P^{(0)}$ units occur simultaneously in subregimes II and III (no strict rank order of their appearance).

4.3.2. $\{M\} \geq \{M\}_*$: Mutual balancing of phosphate unit fractions

The simultaneous appearance of charged phosphate units suggests that the relevant differences in the formation energies of these units are not much larger than the thermal energy.⁶

⁶Note that the charge delocalizations $|q_\alpha|/k_\alpha$ discussed above differ by $1/6 = 0.167$ between the $P^{(1)}$ and $P^{(2)}$ units and by $1/12 = 0.083$ between the $P^{(0)}$ and $P^{(1)}$ units, while there is a larger difference $1/4 = 0.25$ both between the $P^{(2)}$ and $B^{(4)}$ units and between the $B^{(2)}$ and $P^{(0)}$ units. Hence one could argue that the phosphate NFUs should more likely occur simultaneously in the network formation than the charged borate and phosphate NFUs in regimes 1 and 3. This view is supported by the behavior observed in the sodium borophosphate glasses. However, whether the charge delocalization discussed above can be really used also for a quantitative estimate of differences between relevant formation energies, see the Appendix, is not clear. It would be interesting to conduct electronic structure calculations for small clusters to get more insight into the correlation between charge delocalization and formation energies.

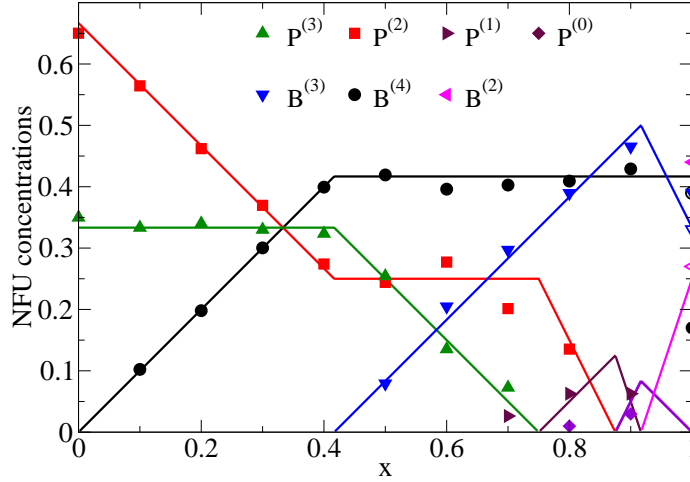


Figure 4.5.: NFU concentrations in the glass $0.4\text{Na}_2\text{O}-0.6[x\text{B}_2\text{O}_3-(1-x)\text{P}_2\text{O}_5]$. The symbols mark MAS-NMR results from [69] and the open symbols at $x = 1$ correspond to the MAS-NMR measurements by [154]. The lines mark the results from the modeling in Sec. 4.3.1 with $f = 1/10$ [eqs. (4.11), (4.20)-(4.26)].

To account for this effect we can consider, as earlier suggested in polyphosphate glasses, [166, 167] the disproportionation reactions



which imply a balancing of the NFU fractions by the corresponding reaction constants

$$K_1 = \frac{\{\text{P}^{(1)}\}\{\text{P}^{(3)}\}}{\{\text{P}^{(2)}\}^2} \quad (4.28a)$$

$$K_2 = \frac{\{\text{P}^{(0)}\}\{\text{P}^{(2)}\}}{\{\text{P}^{(1)}\}^2} \quad (4.28b)$$

Note that the charge and the oxygen number are conserved in the reactions (4.27a) and (4.27b). In general, both K_1 and K_2 will depend on the composition (x and $\{M\}$) but we may assume that this dependence is weak and can be neglected.

Reaction (4.27a) implies that, if $\text{P}^{(2)}$ and $\text{P}^{(3)}$ are present in the network, $\text{P}^{(1)}$ units are also present. For consistency we hence should include this reaction in regime 1 as well. However, if K_1 is very small $\{\text{P}^{(1)}\} = K_1\{\text{P}^{(2)}\}^2/\{\text{P}^{(3)}\}$ will become negligible as long as $\{\text{P}^{(3)}\}$ does not become small too. Hence, for $K_1 \ll 1$, we can ignore the influence of (4.27a) in regime 1. In an approximation where K_1 is set to zero, sub-regime I would be left unchanged and only sub-regimes II and III were modified according to reaction (4.27b), without change of the terminal points x_1^I and x_2 given in eqs. (4.21), (4.25).

Equations (4.28a), (4.28b) together with eqs. (4.10b), (4.10c) form a complete set of determining equations for the fractions $\{\text{P}^{(0)}\}$, $\{\text{P}^{(1)}\}$, $\{\text{P}^{(2)}\}$, and $\{\text{P}^{(3)}\}$ in regime 2. Due to

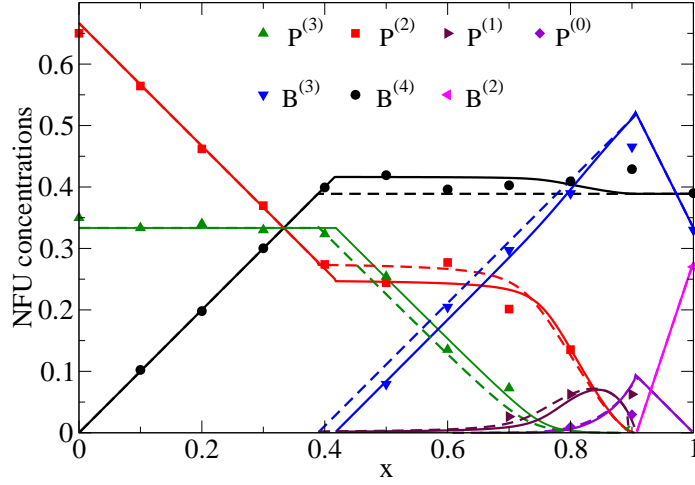


Figure 4.6.: NFU concentrations in the glass $0.4\text{Na}_2\text{O}-0.6[x\text{B}_2\text{O}_3-(1-x)\text{P}_2\text{O}_5]$. The symbols mark MAS-NMR results [69, 154] and the lines indicate results from the theoretical modeling. The dashed lines refer to the first refinement in Sec. 4.3.2 and the solid lines to the second refinement in Sec. 4.3.3.

the two coupled quadratic equations (4.28a), (4.28b), the analytical solution becomes unhandy and it is more convenient to use a numerical root finding procedure. Figure 4.6 shows results for $K_1 = 0.01$ and $K_2 = 0.29$ (dashed lines) in comparison with the experimental data for the sodium borophosphate glass. As can be seen from the figure, the measured fractions for the phosphate units in the regime $0.6 < x < 0.9$ are now better accounted for than by the model with a strict rank order. It would be interesting to check if a temperature dependence of these fractions can be observed because of a temperature dependence of the reaction constants K_1 and K_2 . Whether the reactions (4.27a), (4.27b) are taking place in the glassy phase is, however, not clear. We note that the non-equilibrium glassy state does not preclude this, since local structural configurations may rearrange, while long-range structural disorder is frozen on all accessible time scales. It is on the other

hand possible that the reactions (4.27a), (4.27b) are only relevant during the glass formation. Then we expect them to be reflected in a cooling rate dependence of the respective NFU fractions.

4.3.3. $\{M\} \geq \{M\}_*$: $\text{B}^{(4)}\text{-B}^{(4)}$ linkages constrained by $\text{P}^{(2)}$ units

So far f has to be taken as an a priori unknown parameter, although it can be estimated from its value in the pure borate glass ($x = 1$) or, for closer description of the experimental data, it can be determined from the mean $\text{B}^{(4)}$ fraction for $x > 0.5$. A further refinement of the modeling allows us to avoid the use of f . The idea is to assume that the $\text{B}^{(4)}\text{-B}^{(4)}$ linkages are, as in the crystal with composition $\text{Na}_5\text{B}_2\text{P}_3\text{O}_{15}$, associated with the diborate

configuration shown in Fig. 4.7.⁷ To include this rule in the modeling, we denote, as in Sec. 4.2, by $\tilde{B}^{(4)}$ a $B^{(4)}$ unit that is linked to another $B^{(4)}$, i.e. in the present case one that is part of a diborate configuration. As discussed above in connection with eqs. (4.11)-(4.13), $B^{(4)}$ - $B^{(4)}$ linkages can be avoided for all x , when $M \leq M_* = 3/7$. For $M > M_*$, the formation of such linkages is now constrained to the condition

$$3\{\tilde{B}^{(4)}\} \leq 2\{P^{(2)}\} \quad (4.29)$$

since 3 bOs of each $\tilde{B}^{(4)}$ unit must be linked to $P^{(2)}$ units, cf. Fig. 4.7. $B^{(4)}$ units can replace $P^{(2)}$ units in regime 1 [eqs. (4.11a)-(4.11c)] until all $P^{(2)}$ units are used for the formation of $\tilde{B}^{(4)}$ in diborate configurations and the maximal fraction $\{\tilde{B}^{(4)}\} = 2\{P^{(2)}\}/3$ is reached. At this point $x = x_1$, the other $B^{(4)}$ units are all linked to $P^{(3)}$ units, yielding $4(\{B^{(4)}\} - \{\tilde{B}^{(4)}\}) = 4(\{B^{(4)}\} - 8\{P^{(2)}\})/3 = 3\{P^{(3)}\}$. With the NFU fractions from eqs. (4.11a)-(4.11c), this gives

$$x_1 = \frac{9}{20} - \frac{1}{20}\{M\} \quad (4.30)$$

for the termination point of regime 1. For $x > x_1$, relation (4.29) becomes an equation to generate the maximal $B^{(4)}$ fraction for charge compensation, and inserting this into $4(\{B^{(4)}\} - \{\tilde{B}^{(4)}\}) = 3(\{B^{(3)}\} + \{P^{(3)}\}) + 2\{B^{(2)}\} + \{P^{(1)}\}$ (condition for linkages of $B^{(4)}$ not connected to other $B^{(4)}$ if all $P^{(2)}$ are linked to $\tilde{B}^{(4)}$), we obtain

$$4\{B^{(4)}\} = 3(\{B^{(3)}\} + \{P^{(3)}\}) + 2\{B^{(2)}\} + \frac{8}{3}\{P^{(2)}\} + \{P^{(1)}\}, \quad x > x_1 \quad (4.31)$$

Note that this implies that the $B^{(4)}$ fraction for $x \rightarrow 1$ is approaching the result of the Beekenkamp model discussed in the previous Sec. 4.2. If necessary, one can include in the modeling also the refinements discussed there with respect to the $\{B^{(2)}\}$ - $\{B^{(4)}\}$ balancing.

Equation (4.31) replaces eq. (4.15) for $x > x_1$ and one can proceed as in Sec. 4.3.1 or Sec. 4.3.2 to determine the NFU concentrations. We refrain from giving here the explicit formulas corresponding to eqs. (4.20)-(4.26). For comparison with experiment, we have included in Fig. 4.6 the results (solid line), when using the approach in Sec. 4.3.2 with the same reaction constants K_1 and K_2 used before to fit the experimental data. The measured $B^{(4)}$ fraction is well reproduced now without parameter adjustment. Otherwise, there are only small changes of the NFU fractions compared to the model considered before in Sec. 4.3.2.

Conceptually the theoretical modeling presented in this section relies on a rank order of the NFUs for compensating the charges of the alkali ions and simple constraints given by

⁷The $Na_5B_2P_3O_{13}$ system is the most prominent crystalline alkali ion borophosphate structure. Crystals with compositions $Na_3BP_2O_8$ and $Na_3B_6PO_{13}$ where one-dimensional borophosphate chains are held together by sodium ions were reported more recently by [168]. With respect to alkali types other than sodium, crystalline structures were obtained for a few borophosphate-hydroxide compounds,[169] as, for example, $Li[B_3PO_6(OH)_2]$ or $K[B_6PO_{10}(OH)_4]$.

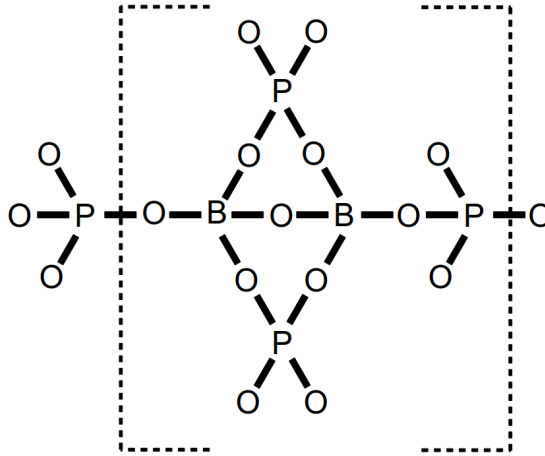


Figure 4.7.: Schematic view of a diborate superstructural unit in $\text{Na}_5\text{B}_2\text{P}_3\text{O}_{13}$ -crystals.

the stoichiometry and with respect to $\text{B}^{(4)}$ - $\text{B}^{(4)}$ linkages. The simultaneous appearance of certain NFUs can be taken into account by a balancing of their concentrations via reactions. It would be interesting to clarify whether the assumed balancing can occur in the glassy phase or whether it is taking place in the melt during the cooling process.

The same underlying concepts can be introduced into a statistical mechanics approach, which we present in the Appendix. An advantage of this approach is that it starts out with the formation energies as parameters and that it allows one to include interactions in a systematic manner. Future experiments on the temperature dependence or cooling rate dependence of the NFU concentrations could give access to corresponding energy parameters. Particular values of the formation energies, however, become irrelevant if certain differences between them become much larger than the thermal energy.

4.4. Modeling of the effect of different NFU types on the activation energy

Next we show how one can, based on the information on the NFU concentrations, successfully model long-range ionic transport properties. To this end we developed a model, which we call the Network Unit Trapping (NUT) model. It relies on the following idea: the nbOs create localized Coulomb traps for the mobile ions, while delocalized charges, as those of the $\text{B}^{(4)}$ units, give a partial Coulomb contribution to several neighboring ion sites. In this way the structural energy landscape for the ionic pathways is modified with the mixing concentration x and this effect can be conjectured to govern the change of the activation energy $E_a(x)$ for the long-range ionic transport.

To test this model we randomly distribute the NFUs with their concentrations from the model in Sec. 4.3.3 on the sites of a simple cubic lattice, see Fig. 4.8. These sites are

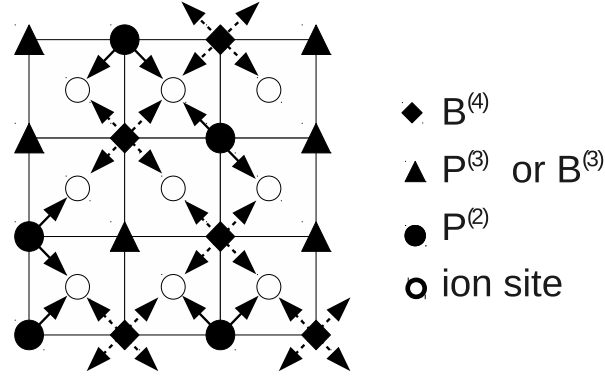


Figure 4.8.: Two-dimensional sketch of the NUT model. The arrows indicate charge transfer to ion sites as described in the text.

called NFU sites. The mobile ions are considered to perform a hopping motion between the centers of the lattice cells, which represent the ion sites.

An NFU α with $k_\alpha > 0$ nbOs and charge q_α adds a Coulomb contribution $\propto q_\alpha/k_\alpha$ to k_α distinct and randomly selected neighboring ion sites, as illustrated in Fig. 4.8. The delocalized charge of a $B^{(4)}$ unit is spread equally among the neighboring ion sites, which implies $k = 8$ for this unit. The neutral $B^{(3)}$ and $P^{(3)}$ units give no Coulomb contribution. Finally, Gaussian fluctuations are added to the site energies in order to take into account the disorder in the glassy network⁸. In summary we can write for the energy of ion site i

$$E_i = -E_0 \left[\sum_{\alpha,j} \frac{q_\alpha}{k_\alpha} \xi_{i,j}^\alpha + \eta_i \right] \quad (4.32)$$

where the sum over j runs over all neighboring NFU sites of ion site i . The occupation number $\xi_{i,j}^\alpha$ is equal to one, if an NFU α on site j contributes a Coulomb contribution $\propto q_\alpha/k_\alpha$ to ion site i ; otherwise it is equal to zero. The η_i are independent Gaussian random numbers with zero mean and standard deviation Δ . The parameter $E_0 > 0$ sets an energy scale and is irrelevant if we are interested in the relative change of the activation energy with the mixing, i.e. the normalized activation energy $E_a(x)/E_a(0)$. The standard deviation Δ is then the only tunable parameter in the modeling.

To determine $E_a(x)$ we have chosen a lattice with 64^3 sites⁹, occupied all NFU sites according to the occupation probabilities derived in Sec. 4.3.3, and the ion sites randomly with concentration $\{M\} = y/(1-y)$. The mobile ions can jump to vacant nearest neighbor sites and the energetic barriers for these jumps are following from eq. (4.32) by calculating the total energy difference ΔE between the (attempted) target configuration after a jump

⁸The Gaussian fluctuations are needed, since, by using a regular arrangement of sites, we disregard the complex network topology. For long-range ionic motion at large length scales, we do not expect our results to be strongly influenced by the lattice structure.

⁹By varying the box size it was confirmed that the results are not affected by finite size effects.

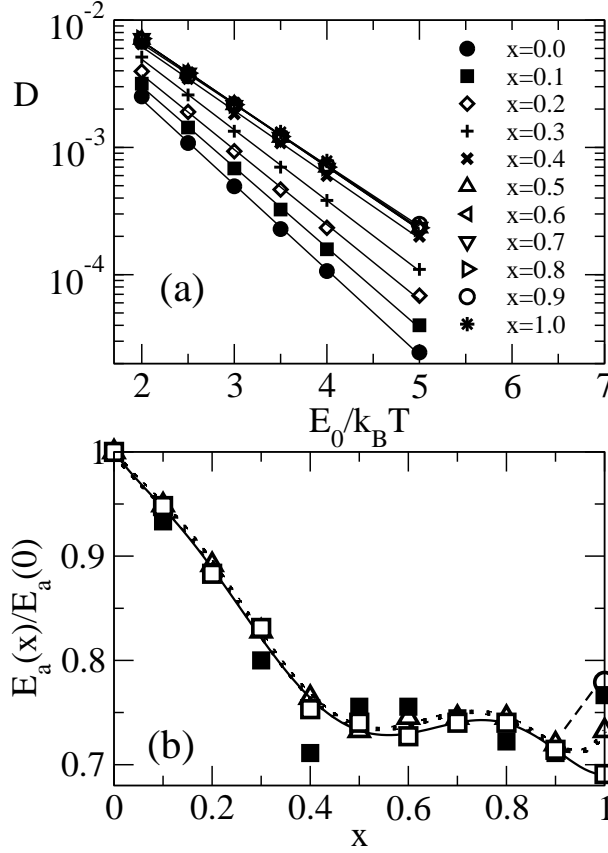


Figure 4.9.: (a) Arrhenius plot of the simulated Na⁺ diffusion coefficients D in $0.4\text{Na}_2\text{O}-0.6[x\text{B}_2\text{O}_3-(1-x)\text{P}_2\text{O}_5]$ for various x and $\Delta = 0.25$ in the case, where no ionic sites were blocked. D is given in units of νa^2 , where ν is the attempt frequency of the ion jumps and a is the lattice constant (mean jump distance). The slope of the regression lines yields the activation energies. (b) Comparison of simulated activation energies (open symbols) with the measured conductivity activation energy from [69] (full squares). The open squares and open triangles refer to the results for the modeling without and with blocked sites, respectively, and the solid and dotted lines are least square fits of sixth order polynomials to these data. For the system without blocked sites $\Delta = 0.25$, and for the system with blocked sites $\Delta = 0.3$. The open circle at $x = 1$ (connected with the dashed line) corresponds to the simulated E_a without blocked sites, if the NFU concentrations from [69] are taken.

and the initial configuration before this jump. To model the jump motion, kinetic Monte-Carlo simulations with periodic boundary conditions and Metropolis transition rates are performed, as described, for example, in [19]. Since the ion concentration is high, it is, for the technical implementation, advantageous here to use a vacancy algorithm. In this algorithm, one of the vacancies is picked randomly in each elementary step and attempted

to move to a randomly selected neighboring ion site. If this site is empty, the attempt is rejected. If the site is occupied by an ion, the attempt is accepted with a probability $\min[1, \exp(-\Delta E/k_B T)]$. After each attempt, the time is incremented by $(\nu N_V)^{-1}$, where $\nu \simeq 10^{12} \text{ s}^{-1}$ is an attempt frequency and N_V is the number of vacancies. After thermalization the time-dependent mean-square displacement $R^2(t)$ of the mobile ions and the diffusion coefficient $D = \lim_{t \rightarrow \infty} R^2(t)/6t$ are determined. Averages are performed over typically 10 realizations of the disorder.

The diffusion coefficient is shown for $\Delta = 0.25$ and various x in an Arrhenius plot in Fig. 4.9a. From the slopes of the straight lines we calculated the activation energy $E_a(x)$, and the behavior of the normalized activation energy $E_a(x)/E_a(0)$ is compared with the experimental results from [69] in Fig. 4.9b. The overall agreement between the theoretical (open squares, solid line) and the experimental data (full squares) is surprisingly good. Note that we needed to fit only the parameter Δ to achieve this agreement. A significant difference between the theoretical and experimental curve can be seen for $x \rightarrow 1$: while the theoretical $E_a(x)$ decreases, the experimental $E_a(x)$ finally rises to a higher value in the sodium borate glass at $x = 1$. Interestingly, this rise is reproduced by the NUT model (dashed line), if instead of the NFU concentrations shown in Fig. 4.6, the NFU concentrations reported by [69] are used. On the other hand, a much smaller experimental value $E_a = 0.54 \text{ eV}$ for the sodium borate glass has been reported by [21], corresponding to a ratio $E_a(1)/E_a(0) = 0.6$. The differing measured E_a values likely result from varying NFU concentrations as a consequence of different glass preparation processes.

It is obvious that the model presented here does not take into account important aspects of ion motion in glasses. In this respect, we should in particular address the following questions:

- (i) Why should a hopping between regular sites of a simple cubic lattice be appropriate for a modeling of the ionic jump motion between irregularly distributed sites in a disordered glassy network?
- (ii) How can one reason that the energy barriers, or "doorways", between the ionic sites should not be considered in more detail?
- (iii) Why should it be allowed to neglect the long-range Coulomb interaction between the mobile ions?

The answer to the question (i) is twofold. Firstly, we are interested in the long-range ionic motion, where the chosen regular lattice structure for ionic sites becomes of minor importance. Secondly, by the random distribution of the NFUs and the additional Gaussian energy fluctuations in eq. (4.32) the sites are in fact not equivalent so that, dependent on the realization of the disorder, favorable pathways without regular structure are formed.

Question (ii) is answered by noting that the Gaussian energy fluctuations are in effect generating disorder in the jump barriers. One could, in addition to the Gaussian fluctuations

in eq. (4.32), also add a random barrier distribution for the jumps. As long as the width of these distributions is sufficiently small compared to the site energy fluctuations induced by the NFU charges, the behavior of E_a is dominated by the latter. We note that the assumption of a dominant role of the trapping effect by the NFU charges is the actual starting point of our approach as we discussed in the introduction when considering the two different situations I and II as possible origins for the MGFE.

The answer to question (iii) is more subtle. One could argue that the Coulomb interaction can, due to its long range nature, be treated in a mean-field approximation as a weakly varying, almost constant contribution to the energy of the alkali ions [108]. However, results from molecular dynamics (MD) simulations suggest that the Coulomb part has a decisive influence on the differences between the energies of the mobile ions on their sites. The interesting point on the other hand is, that in the same MD simulations it was also found that in a vacancy (hole) description the structural energy part (i.e., the part without Coulomb interactions between the mobile ions) is indeed largely determining the energy of the vacancies [103].

The fraction of vacancies found in molecular dynamics simulations, with respect to all available ion sites, is smaller than 10% [103, 120, 170]. This result is in line with the picture that a glass constitutes a dense system with a low free energy and hence should not exhibit too many empty sites [171, 172, 173]. It is also supported by a theoretical explanation of the occurrence of surprisingly large internal friction peaks in some mixed alkali glasses upon small exchanges of one type of alkali ion by another [10]. In our lattice modeling described above, we have occupied two-thirds of the ionic sites (cell centers between the NFUs) with the ions in order to ensure the overall charge neutrality for the stoichiometry of our experimental reference system. The other one-third of ionic sites, however, were left empty, implying that the vacancy concentration is indeed too large compared to the ones found in MD simulations.

In order to see how the results of our modeling change when decreasing the vacancy fraction to a typical value of 7% found in MD simulations, we have performed additional kinetic Monte-Carlo simulations, in which 26% of the ionic sites are randomly blocked. This blocking of the cell centers is done before the NFUs are distributed among the lattice sites. Thereafter the NFUs are randomly placed on their sites as before, but their charges are distributed randomly among the neighboring non-blocked sites only. Hence, if an NFU α with k_α nBOs on site i is surrounded by m_i non-blocked ion sites, k_α of these sites are now randomly selected and the Coulomb contribution $\propto q_\alpha/k_\alpha$ added to them.¹⁰ The delocalized charge of a B⁽⁴⁾ unit on site i is spread equally among the m_i neighboring nonblocked ion sites, implying that a Coulomb contribution $\propto (-1/m_i)$ is added to them.

¹⁰In the rare case, where the number m_i of surrounding non-blocked sites is smaller than k_α , an attempt is made to exchange the NFU α on site i with another randomly selected NFU α' on site i' . If, after the attempted exchange, the numbers k_α and $k_{\alpha'}$ of nBOs should be still smaller than the number of surrounding non-blocked sites, another attempt is started until all partial charges carried by the nBOs can be assigned to neighboring non-blocked ion sites.

Finally, the Gaussian fluctuations from eq. (4.32) are added to the site energies resulting from this procedure.

In the same way as described above, the activation energy E_a for this refined model with 7% vacancy fraction was determined from the temperature dependence of the long-time diffusion coefficients of the mobile ions at different x . Interestingly, this activation energy shows almost the same behavior as the model with 33% vacancies, when the parameter Δ is increased from $\Delta = 0.25$ to $\Delta = 0.3$, see Fig. 4.9. This finding thus gives us some confidence in our modeling with neglect of the Coulomb interaction between the mobile ions. It also demonstrates, as discussed above, that with respect to long-range transport properties the parameter Δ effectively takes into account modifications of the randomness (more irregular topology of ionic sites here).

4.5. Summary

In summary we have presented a theoretical approach for the mixed glass former effect in borophosphate glasses. This approach is based on a consideration of the properties of the different NFUs building the network structure with respect to total charge and charge delocalization. In addition, we showed how NFU concentrations can be successfully modeled.

We believe that our approach is applicable also to other mixed glass former systems, where concentrations of different types of NFUs associated with the glass formers vary with the mixing ratio. Due to its generality, the basic concept may have even wider applicability for describing other compositional effects, as, for example, changes of ionic mobilities with the content of the network modifier.

We would like to thank H. Eckert and S. W. Martin for very valuable discussions and gratefully acknowledge financial support of this work by the Deutsche Forschungsgemeinschaft in the Materials World Network (DFG Grant number MA 1636/3-1).

Appendix: Statistical mechanics approach to NFU concentrations

Without detailed consideration of the network topology, the NFUs can be considered to occupy N sites i in the glass, where $N = N_B + N_P$ is the total number of boron and phosphorous atoms. To specify the distribution of the NFUs among the sites, we introduce the occupation numbers n_i^α , where $n_i^\alpha = 1$ if an NFU of type α ($\alpha = B^{(2)}, B^{(3)}, \text{etc.}$) is occupying site i and zero else. Using a coarse-grained Landau-type description, we introduce a free energy $\mathcal{F}(\mathbf{n})$ as a function of the set $\mathbf{n} = \{n_i^\alpha\}$ of occupation numbers,

$$\mathcal{F}(\mathbf{n}) = \sum_{i,\alpha} f(\alpha)n_i^\alpha + \mathcal{F}'(\mathbf{n}) \quad (4.33)$$

where the first term on the right hand side describes an ideal non-interacting part with $f(\alpha)$ specifying a formation energy of NFU type α and the second term $\mathcal{F}'(\mathbf{n})$ accounts for interactions between the NFUs. For example, for sites i and j being neighbors one

could include a term $\propto n_i^{\text{B}^{(4)}} n_j^{\text{B}^{(4)}}$ to describe the unlikelihood of $\text{B}^{(4)}\text{-B}^{(4)}$ linkages. The formation energies $f(\alpha)$ depend in general on the composition (x and $\{M\}$) and they are expected to depend also on the cooling rate. One can question whether an equilibrium type description underlying this coarse-grained approach can at all be appropriate for glasses whose structures are frozen into a non-equilibrium state. The hope is that on small length scales the glass structure has found sufficient time to equilibrate during the cooling process and that this equilibration can be accounted for by an effective temperature T' . The structural disorder on large length scales should have no significant influence on the NFU concentrations.

If only the ideal part in eq. (4.33) is kept, the NFU fractions can be calculated under the constraints eqs. (4.10a-4.10c). These constraints can be rewritten in the form

$$\sum_{\alpha} \zeta_{\text{B}}(\alpha) \sum_i n_i^{\alpha} = x N \quad (4.34\text{a})$$

$$\sum_{\alpha} \zeta_{\text{P}}(\alpha) \sum_i n_i^{\alpha} = (1 - x) N \quad (4.34\text{b})$$

$$\sum_{\alpha} \zeta_{\text{M}}(\alpha) \sum_i n_i^{\alpha} = \{M\} N \quad (4.34\text{c})$$

where $\zeta_X(\alpha)$ ($X = \text{B}, \text{P}, \text{M}$) are the integers appearing in eqs. (4.10a)-(4.10c), e.g. $\zeta_{\text{B}}(\text{B}^{(3)}) = 1$, $\zeta_{\text{B}}(\text{P}^{(n)}) = 0$ for $n = 0, 1, 2$ and 3 , $\zeta_{\text{M}}(\text{P}^{(0)}) = 3$, etc. Assigning Lagrangian multipliers (generalised chemical potentials) $\mu_{\text{B}}, \mu_{\text{P}}, \mu_{\text{M}}$ to the constraints eqs. (4.34a)-(4.34c), the grand canonical potential becomes

$$\begin{aligned} \Phi &= -\frac{1}{\beta'} \log \sum_{\mathbf{n}} \exp \left(-\beta' \sum_{\alpha} u(\alpha) \sum_i n_i^{\alpha} \right) \\ &= -\frac{N}{\beta'} \sum_{\alpha} \log (1 + \exp[-\beta' u(\alpha)]) , \end{aligned} \quad (4.35)$$

$$u(\alpha) = g(\alpha) - \zeta_{\text{B}}(\alpha) \mu_{\text{B}} - \zeta_{\text{P}}(\alpha) \mu_{\text{P}} - \zeta_{\text{M}}(\alpha) \mu_{\text{M}} \quad (4.36)$$

where $\beta' = 1/(k_{\text{B}}T')$. If interactions were included in the description, an excess part had to be added to the ideal part in eq. (4.35). For the NFU fractions we obtain the Fermi distributions

$$\{\alpha\} = \frac{1}{N} \frac{\partial \Phi}{\partial u(\alpha)} = \frac{1}{\exp[\beta' u(\alpha)] + 1} \quad (4.37)$$

The generalised chemical potentials entering the $u(\alpha)$ [see eq. (4.36)] are to be determined from the constraints eqs. (4.34a)-(4.34c).

With respect to the appearance of the NFUs at a given composition only certain differences between the formation energies are relevant. If these are much larger than $k_{\text{B}}T'$, the change of the NFU concentrations with x can be inferred from a $T' \rightarrow 0$ limit.

To demonstrate the procedure, we consider a situation similar to the one addressed in Sec. 4.3.2. The rank order of the NFUs with respect to charge compensation introduced

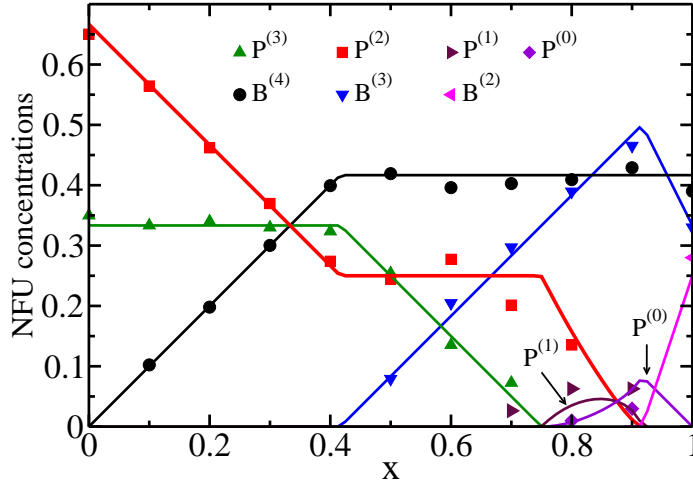


Figure 4.10.: NFU concentrations from the statistical mechanics approach with $f = 1/10$ (lines) for the glass $0.4\text{Na}_2\text{O}-0.6[x\text{B}_2\text{O}_3-(1-x)\text{P}_2\text{O}_5]$ in comparison with MAS-NMR results [69, 154] (symbols).

in Sec. 4.3 implies $f(\text{B}^{(4)}) < f(\text{P}^{(2)})$, $2f(\text{P}^{(2)}) < f(\text{P}^{(1)})$, $3f(\text{P}^{(2)}) < f(\text{P}^{(0)})$, $3f(\text{P}^{(1)}) < 2f(\text{P}^{(0)})$, and $f(\text{P}^{(0)}) < 3f(\text{B}^{(2)})$. In order that the $\text{P}^{(2)}$ are replaced by the $\text{B}^{(4)}$ units rather than the $\text{P}^{(3)}$ by the $\text{B}^{(3)}$ units for small x , it should hold $[f(\text{B}^{(4)}) - f(\text{P}^{(2)})] < [f(\text{B}^{(3)}) - f(\text{P}^{(3)})]$. All these conditions can be fulfilled by introducing just one energy parameter δ and by setting

$$f(\text{B}^{(3)}) = f(\text{P}^{(3)}) = f(\text{B}^{(4)}) = 0 \quad (4.38a)$$

$$f(\text{P}^{(2)}) = \delta, \quad f(\text{B}^{(2)}) = 3\delta \quad (4.38b)$$

$$f(\text{P}^{(1)}) = 3\delta, \quad f(\text{P}^{(0)}) = 5\delta \quad (4.38c)$$

The parameter δ is just a convenient tool to evaluate the low-temperature limit $T' \rightarrow 0$ under the chosen conditions and does not have any physical meaning.

For determining the NFU fractions $\{\alpha\}$ we insert the $f(\alpha)$ from eqs. (4.38a)-(4.38c) into eq. (4.37) and calculate the chemical potentials numerically from eqs. (4.34a)-(4.34c). To extract the values in the limit $(\beta'\delta) \rightarrow \infty$, the calculations are performed for successively increasing $(\beta'\delta)$ until changes in the NFU fractions become negligible. In order to include the additional constraint (4.15) into the description, it is checked if the resulting $\text{B}^{(4)}$ fraction fulfills relation (4.15). If it does, the solution is taken. Otherwise, $\{\text{B}^{(4)}\}$ is set equal to $[4(1-f)]^{-1}$ times the right hand side of (4.15)¹¹.

The NFU fractions calculated in this way for $f = 1/10$ are compared to the experimental data for the sodium borophosphate glass in Fig. 4.10. Note that, different from the situation shown in Fig. 4.5, the $\text{P}^{(0)}$ units occur before the $\text{P}^{(2)}$ units have disappeared. The

¹¹the calculations have to be done self-consistently by using the corresponding expressions for the determination of μ_{B} in eq. (4.34a)

simultaneous appearance of $P^{(0)}$, $P^{(1)}$, and $P^{(2)}$ units in an interval around $x = 0.8$ is caused by the fact that, for the parameters in eqs. (4.38b), (4.38b), the compensation of 4 charges by either two $P^{(1)}$ units or by one $P^{(0)}$ and one $P^{(2)}$ unit are energetically equivalent. Since the same basic ingredients have been included in the theoretical description as in Sec. 4.3, the agreement between model and experiment is of comparable quality as in Fig. 4.6.

The formulation by the statistical mechanics approach is valuable to our view, since it gives additional insight into the underlying assumptions and indicates a way how to access energy parameters. Knowledge of these parameters would allow one to make contact to another theoretical modeling, which has been successfully applied to predict thermodynamic (and some other) properties of borate, silicate, and borosilicate glasses [174, 175].

5. Discussion and Extended Application of the Modeling in Chapter 4

Abstract

This chapter is intended for the extension and revision of the theoretical concepts given in chapter 4.

In particular, some additional remarks to the f -parametermodel from sec. 4.3 are given. It is shown that f has to be interpreted as an effective measure for the $B^{(4)}$ - $B^{(4)}$ -connectivity, which masks the real $B^{(4)}$ - $B^{(4)}$ -connectivity and some contribution of non- $B^{(4)}$ that are not connected to $B^{(4)}$ -NFU.

In addition, the concepts introduced in chapter 4 to calculate the NFU species concentrations were extended by the introduction of positive charged $P^{(4)}$ unit. This extension is compared with two further data sets for $x_A \text{Na}_2\text{O}-(1-x_A) (\text{PBO}_4)$ and $x_B \text{B}_2\text{O}_3-(1-x_B) \text{NaPO}_3$ [85, 87, 176]. It is shown that the predictions for the NFU-species concentrations are in good agreement with the experimental values. For the NUT approach presented in sec. 4.4 a mathematical expression for the probability of site energies is developed and compared to the simulation results. In order to calculate the activation energy directly from these distributions, the simulation results were compared with predictions from different theoretical concepts, which are given in the literature. This comparison reveals that the predictions of the *effective circuit approach* [109] are in good agreement to the simulation data for $T \rightarrow 0$. Furthermore, it will be shown that NUT approach is also able to describe the *mobile ion concentration effect*. To this end, Monte Carlo Simulations are performed and also compared with the predictions of the aforementioned theoretical concepts.

5.1. Introduction

In the previous chapter it was shown that the behavior of the NFU concentrations in pure alkali borate and mixed alkali-phosphate glasses can be well understood by the consideration of charge balancing condition and the extension and generalization of the concepts proposed by Beekenkamp [156] and Gupta [158]. In addition, it was shown by using computer simulations, how the behavior of E_a as a function x could be related to the variations of the NFU concentrations. Below, further insights will be given to the results presented in chapter 4. In particular, following issues are addressed in the present chapter:

- The modeling of the NFU concentrations in chapter 4 is based on the crucial assumption that the number bOs bridging two $B^{(4)}$ units is limited. The maximization of the number of $B^{(4)}$ NFU in this picture implies the fact that the fraction of bOs connecting two P vanishes above $\{B^{(4)}\}^*$. In contrast, it was shown in MAS-NMR experiments [69] that a small but significant fraction P-bO-P linkages is present for $\{B^{(4)}\} \geq \{B^{(4)}\}^*$. In sec. 5.2.1 this issue will be addressed and it will be shown, how the f -parameter must be interpreted to be consistent with the experimental findings.
- This model should be applicable for borophosphate systems with other stoichiometries. A corresponding discussion is performed on other available experimental data [85, 87]. To this end, the modeling must be extended by inclusion of $P^{(4)}$ NFUs. The solution of these problems is given in sec. 5.2.2.
- With the knowledge of the NFU species concentrations, one can calculate the site energy distribution that follows from the NUT approach under minor approximations¹. These calculations will be outlined in sec. 5.3.1.
- It should be possible to calculate the activation energy from this site energy distribution by the application of arguments given by the percolation theory. In the literature different proposals are found to perform this calculation. A comparison which of these approaches is adequate will be given in sec. 5.3.2, where the NUT model for $0.4Na_2O-0.6[xB_2O_3-(1-x)P_2O_5]$ glasses is used as a test case.
- In binary alkali borate glasses one often finds an unique dependency of the activation energy on the modifier content, which could be written as $E_a(\{M\}) \approx a + bln(\{M\})$ [11, 177]. In sec. 5.3.3 it will be tested whether the NUT approach can account also for this behavior. The results are also used for further testing of the concepts to calculate E_a .

¹For the NUT approach without site blocking and without avoiding $B^{(4)}$ - $B^{(4)}$ neighbors

5.2. Further modeling of the NFU concentrations

5.2.1. Discussion of the f -Parameter

One may ask whether a single parameter f is sufficient to describe the species distribution properly. In general, one could introduce a set of parameters f_{B2} , f_{B3} , f_{P3} , f_{P2} , f_{P1} and f_{B4} . These parameters correspond to the deviation of the ideal connectivity given by the condition 4.15. The condition 4.15 can therefore be generalized to:

$$\begin{aligned} 4(1 - f_{B4}) \{B^{(4)}\} &\leq 3(1 - f_{B3}) \{B^{(3)}\} + 2(1 - f_{B2}) \{B^{(2)}\} \\ &\quad + 3(1 - f_{P3}) \{P^{(3)}\} + 2(1 - f_{P2}) \{P^{(2)}\} \\ &\quad + 1(1 - f_{P1}) \{P^{(1)}\} P^{(4)} \end{aligned} \quad (5.1)$$

Condition 5.1 implies, that f_{B3} , f_{B2} , f_{P3} , f_{P2} and f_{P1} are the fractions of bO bonded to a $B^{(3)}$, $B^{(2)}$, $P^{(3)}$, $P^{(2)}$ and $P^{(1)}$ but not to a $B^{(4)}$ NFU. Whereas the f_{B4} correspond to the real fraction of bOs bonded to 2 $B^{(4)}$ NFU. It is easy to show that such an ansatz reduces to a single parameter model if:

$$\begin{aligned} \frac{(1 - f_{B4})}{(1 - f)} &= (1 - f_{B3}) = (1 - f_{B2}) \\ &= (1 - f_{P3}) = (1 - f_{P2}) = (1 - f_{P1}) \end{aligned} \quad (5.2)$$

Equation 5.2 implies:

$$f_{B3} = f_{B2} = f_{P3} = f_{P2} = f_{P1} \quad (5.3)$$

This result has to be interpreted as the fact that a real system can be described as the combination of an ideal system in the sense of the connectivity arguments presented in chapter 4 and a random network characterized by f_{B2} , f_{B3} , f_{P3} , f_{P2} and f_{P1} . Where the *real* fraction of bOs connecting two $B^{(4)}$ (i.e. f_{B4}) is significantly higher than the effective f -parameter from eqs. 4.1c and 4.15.

An explanation of this assumption will be given in the following discussion. In a melt at high temperatures a significant fraction of bOs exist, which are not connected to any $B^{(4)}$ -NFU, because the additional energetic cost of a lower concentration of $B^{(4)}$ is balanced by the thermal energy. Cooling down the melt rapidly will result in an increase of the $B^{(4)}$ content², but a small but significant fraction of bOs is not connected to any $B^{(4)}$, since the breakup and reconnection of the bOs are thermally activated. Hence, one has to assume that a part of the bO network is frozen in a rather random configuration between non- $B^{(4)}$ -NFU species for large cooling rates. However, as discussed in chapter 4, in the case of pure alkali borate glasses a significant amount of $B^{(4)}$ -NFU can exist, which share a bO with another $B^{(4)}$ -NFU. Therefore, it is natural to assume that the f -parameter includes

²Indeed the increase of the $B^{(4)}$ content with decreasing temperature of the melt is wellknown at least for binary borate systems [178, 179]

information on both mechanisms in a mean field manner. This picture can be tested by the careful analysis of the $B^{(4)}$ -content in stoichiometrically identical systems prepared by different preparation protocols (e.g. different cooling rates).

5.2.2. NFU concentrations for other stoichiometries of sodium borophosphate glasses

As it was shown in chapter 4 and the previous discussion, charge balancing constraints and the effective suppression of bOs bonded to two $B^{(4)}$ -NFU are sufficient to model the species distribution for $0.4(\text{Na}_2\text{O}) - 0.6[x\text{B}_2\text{O}_3 - (1-x)\text{P}_2\text{O}_5]$ glasses. Some further insights to this model were given in the previous section. Up to this point, the concepts were only tested at one experimental data set and the comparison with additional systems is required. To address this issue, the modeling is tested on further sodium borophosphate glasses along different composition-lines x_i ($i = 1, 2$). These data were obtained by the combination MAS-NMR, Raman- and X-ray-Photoelectron spectroscopy for the composition $x_A\text{Na}_2\text{O} - (1-x_A)(\text{PBO}_4)$ [87, 176] and $(1-x_B)\text{NaPO}_3 - x_B\text{B}_2\text{O}_3$ [85, 176]³. Since it was found that $P^{(4)}$ units occur along these composition lines with a significant concentration, the modeling will be extended by the introduction of the corresponding species. First, the model will be compared with the system of the general composition $x_A\text{Na}_2\text{O} - (1-x_A)(\text{PBO}_4)$ [87, 176]. For low x_A this system is characterized by the finding that $P^{(4)}$ is the dominating phosphate species. This finding agrees well with the fact that a crystalline phase of PBO_4 exists, where $B^{(4)}$ units are mutually linked to $P^{(4)}$ units. The charge balance constraint requires that the number of positive charged $P^{(4)}$ is reduced, if alkali cations are added to the glass, implying the formation of neutral $P^{(3)}$ NFU. Since this fact leads to a reduction of the bOs, $B^{(4)}$ has to be replaced by $B^{(3)}$. Applying the concepts of chapter 4 one could describe these mechanisms mathematically by:

$$4\{B^{(4)}\} - 3\left(\{B^{(3)}\} + \{P^{(3)}\}\right) - 4\{P^{(4)}\} = 0 \quad (5.4a)$$

$$\{B^{(4)}\} - \{P^{(4)}\} = \frac{x_A}{1-x_A} \quad (5.4b)$$

$$\{B^{(4)}\} + \{B^{(3)}\} + \{P^{(4)}\} + \{P^{(3)}\} = 1 \quad (5.4c)$$

$$\{B^{(4)}\} + \{B^{(3)}\} - \{P^{(4)}\} - \{P^{(3)}\} = 0 \quad (5.4d)$$

Equation 5.4a corresponds to the effective avoidance of bOs bridging two $B^{(4)}$. Since the $P^{(4)}$ -NFU are positively charged, one has to consider them in the charge balance equation 5.4b. Equation 5.4c accounts for the fact that the network former fraction is constant and 5.4d ensures that the P/B ratio is one for all x_A .

³ x_A and x_B are here the molar fractions of these systems

The NFU fractions following from eqs. 5.4 are:

$$\{B^{(4)}\} = -\frac{4x_A - 3}{6(1 - x_A)} \quad (5.5a)$$

$$\{B^{(3)}\} = \frac{x_A}{6(1 - x_A)} \quad (5.5b)$$

$$\{P^{(4)}\} = -\frac{10x_A - 3}{6(1 - x_A)} \quad (5.5c)$$

$$\{P^{(3)}\} = \frac{7x_A}{6(1 - x_A)} \quad (5.5d)$$

A comparison of eq. 5.5a with eq. 5.5c reveals that the $P^{(4)}$ content decreases much faster than the $B^{(4)}$ content with increasing x_A . The boundary for the regime defined by eqs. 5.4 is given by the point, where the $P^{(4)}$ fraction reaches zero, i.e. $x_A = \hat{x}_A = 3/10$. For $x_A > \hat{x}_A$ one has to consider two different scenarios. In the first scenario $B^{(4)}$ - $B^{(4)}$ connections via a bO are always forbidden (model 1). An alternative scenario allows $B^{(4)}$ - $B^{(4)}$ connections within $Na_5B_2P_3O_{13}$ like superstructures (see sec. 4.3.3). This model is denoted in the following discussion as model 2.

Let us start with model 1. For $x_A > \hat{x}_A$ one has to assume, that $P^{(2)}$ must appear for charge compensation. Hence, the following conditions have to be fulfilled:

$$4\{B^{(4)}\} - 3\left(\{B^{(3)}\} + \{P^{(3)}\}\right) - 2\{P^{(2)}\} = 0 \quad (5.6a)$$

$$\{B^{(4)}\} + \{P^{(2)}\} = \frac{x_A}{1 - \hat{x}_A} \quad (5.6b)$$

$$\{B^{(4)}\} + \{B^{(3)}\} + \{P^{(3)}\} + \{P^{(2)}\} = 1 \quad (5.6c)$$

$$\{B^{(4)}\} + \{B^{(3)}\} - \{P^{(3)}\} - \{P^{(2)}\} = 0 \quad (5.6d)$$

Solving the system of eqs. 5.6 leads to:

$$\{B^{(4)}\} = -\frac{4x_A - 3}{6(1 - x_A)} \quad (5.7a)$$

$$\{B^{(3)}\} = \frac{x_A}{6(1 - x_A)} \quad (5.7b)$$

$$\{P^{(3)}\} = -\frac{13x_A - 6}{6(1 - x_A)} \quad (5.7c)$$

$$\{P^{(2)}\} = \frac{10x_A - 3}{6(1 - x_A)} \quad (5.7d)$$

Since all concentrations must be positive, it follows from eq. 5.7c that the subsequent change of the behavior of the system will occur at $x_A = \bar{x}_A = 6/13$, where the $P^{(3)}$ units vanish. Since there are no further uncharged phosphate-NFU, a further increase of the cation content could be only counter-balanced by more unfold charged borate or two-fold charged phosphate NFU. The first possibility implies the formation of bOs connecting two $B^{(4)}$ or the formation of energetically unfavorable $B^{(2)}$. Therefore, the formation of $P^{(1)}$

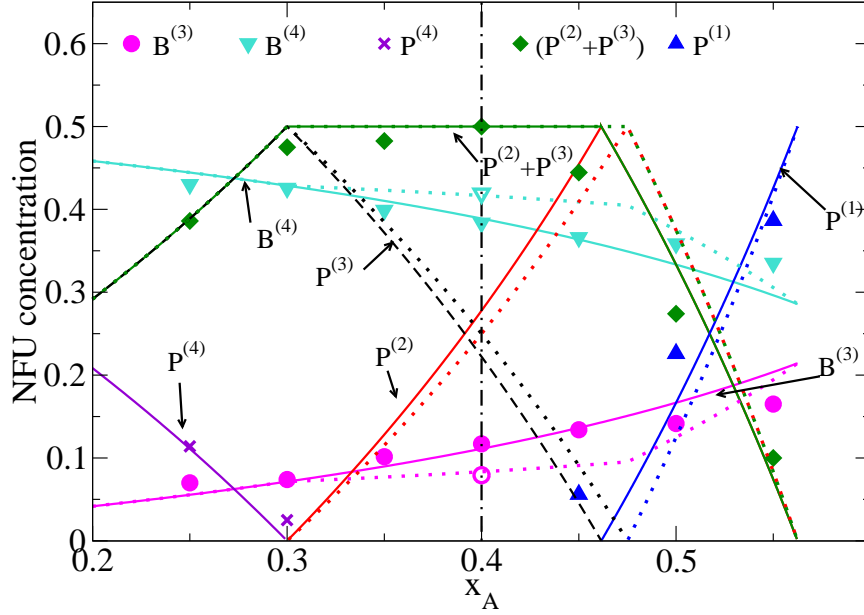


Figure 5.1.: The experimental species distribution for $x_A \text{Na}_2\text{O}-(1-x_A)(\text{BPO}_4)$ determined by a combined MAS-NMR and XPS analysis [87, 176] in comparison to the modeling. Solids lines correspond to a model where $\text{B}^{(4)}\text{-B}^{(4)}$ linkages are effectively forbidden ($f = 0$), whereas the dotted lines correspond to a model where $\text{B}^{(4)}\text{-B}^{(4)}$ are stabilized by $\text{P}^{(2)}$ units. The vertical dashed-dotted line at $x_A = 0.4$ shows the composition, where the stoichiometry should be the same as $0.4\text{Na}_2\text{O}-0.6[x\text{B}_2\text{O}_3-(1-x)\text{P}_2\text{O}_5]$ (with $x = 0.5$) described by Zielniok *et al.* [69] corresponding to the open symbols

units is more likely. The corresponding conditions are:

$$4\{\text{B}^{(4)}\} - 3\{\text{B}^{(3)}\} - 2\{\text{P}^{(2)}\} - \{\text{P}^{(1)}\} = 0 \quad (5.8a)$$

$$\{\text{B}^{(4)}\} + \{\text{P}^{(2)}\} + 2\{\text{P}^{(1)}\} = \frac{x_A}{1-x_A} \quad (5.8b)$$

$$\{\text{B}^{(4)}\} + \{\text{B}^{(3)}\} + \{\text{P}^{(2)}\} + \{\text{P}^{(1)}\} = 1 \quad (5.8c)$$

$$\{\text{B}^{(4)}\} + \{\text{B}^{(3)}\} - \{\text{P}^{(2)}\} - \{\text{P}^{(1)}\} = 0 \quad (5.8d)$$

these equations lead to:

$$\{\text{B}^{(4)}\} = -\frac{4x_A - 3}{6(1-x_A)} \quad (5.9a)$$

$$\{\text{B}^{(3)}\} = \frac{x_A}{6(1-x_A)} \quad (5.9b)$$

$$\{\text{P}^{(2)}\} = -\frac{16x_A - 9}{6(1-x_A)} \quad (5.9c)$$

$$\{\text{P}^{(1)}\} = \frac{13x_A - 6}{6(1-x_A)} \quad (5.9d)$$

Figure 5.1 reveals an excellent agreement of model 1 to the experimental points for $x_A \lesssim 0.5$. For larger x_A the $B^{(4)}$ concentration decreases slower than one would expect from model 1.

Model 2 is characterized by the feature that bOs bonded to two $B^{(4)}$ are stabilized due to the formation of $Na_5B_2P_3O_{13}$ -like super-structures. To include this mechanism different classes of $B^{(4)}$ -NFU must be distinguished. $B^{(4)}$, which are sharing no bO with other $B^{(4)}$ will be denoted in the following as $B_I^{(4)}$. In contrast to the $B_I^{(4)}$ units, the $B_{II}^{(4)}$ NFU are build in structures that are similar to diborate super-structures. For the first regime with $x_A > \hat{x}_A$ one obtains following conditions:

$$3\{B_{II}^{(4)}\} - 2\{P^{(2)}\} = 0 \quad (5.10a)$$

$$4\{B_I^{(4)}\} - 3\{B^{(3)}\} - 3\{P^{(3)}\} = 0 \quad (5.10b)$$

$$\{B_I^{(4)}\} + \{B_{II}^{(4)}\} + \{P^{(2)}\} = \frac{x_A}{1 - x_A} \quad (5.10c)$$

$$\{B_I^{(4)}\} + \{B_{II}^{(4)}\} + \{B^{(3)}\} + \{P^{(3)}\} + \{P^{(2)}\} = 1 \quad (5.10d)$$

$$\{B_1^{(4)}\} + \{B_2^{(4)}\} + \{B^{(3)}\} - \{P^{(3)}\} - \{P^{(2)}\} = 0 \quad (5.10e)$$

resulting in:

$$\{B_I^{(4)}\} = -\frac{30x_A - 15}{20(1 - x_A)} \quad (5.11a)$$

$$\{B_{II}^{(4)}\} = \frac{20x_A - 6}{20(1 - x_A)} \quad (5.11b)$$

$$\{B^{(3)}\} = \frac{1}{20(1 - x_A)} \quad (5.11c)$$

$$\{P^{(3)}\} = -\frac{40x_A - 19}{20(1 - x_A)} \quad (5.11d)$$

$$\{P^{(2)}\} = \frac{30x_A - 9}{20(1 - x_A)} \quad (5.11e)$$

Eqs. 5.11 reveal that the end of the second regime is also characterized in model 2 by the vanishing of the $P^{(3)}$ concentration. The modifier oxide concentration for model 2 is slightly increased in comparison to model 1 to a value $x_A = \bar{x}_A = 19/40$. For higher x_A values phosphate NFU with two negative charges has to be formed, yielding:

$$3\{B_{II}^{(4)}\} - 2\{P^{(2)}\} = 0 \quad (5.12a)$$

$$4\{B_I^{(4)}\} - 3\{B^{(3)}\} - \{P^{(1)}\} = 0 \quad (5.12b)$$

$$\{B_I^{(4)}\} + \{B_{II}^{(4)}\} + \{P^{(2)}\} + 2\{P^{(1)}\} = \frac{x_A}{1 - x_A} \quad (5.12c)$$

$$\{B_I^{(4)}\} + \{B_{II}^{(4)}\} + \{B^{(3)}\} + \{P^{(2)}\} + \{P^{(1)}\} = 1 \quad (5.12d)$$

$$\{B_I^{(4)}\} + \{B_{II}^{(4)}\} + \{B^{(3)}\} - \{P^{(2)}\} - \{P^{(1)}\} = 0 \quad (5.12e)$$

The solution of eqs. 5.12 is given by:

$$\{B_I^{(4)}\} = \frac{16x_A - 4}{16(1 - x_A)} \quad (5.13a)$$

$$\{B_{II}^{(4)}\} = -\frac{32x_A - 18}{16(1 - x_A)} \quad (5.13b)$$

$$\{B^{(3)}\} = \frac{8x_A - 3}{16(1 - x_A)} \quad (5.13c)$$

$$\{P^{(1)}\} = -\frac{48x_A - 27}{16(1 - x_A)} \quad (5.13d)$$

$$\{P^{(2)}\} = \frac{40x_A - 19}{16(1 - x_A)} \quad (5.13e)$$

Model 2 was also compared to the experimental data and shown in fig. 5.1. For the high- x_A regime the agreement of model 2 to the experimental data is better than model 1. However, it should be noted that the $x_A = 0.4$ system studied by Rinke and Eckert [176, 87] has the same stoichiometry as the $0.4\text{Na}_2\text{O}-0.6[x\text{B}_2\text{O}_3-(1-x)\text{B}_2\text{O}_5]$ studied by Zielniok *et al.* [69](open symbols in fig. 5.1). It is obvious that the deviations of the results from different experimental studies are comparable to the differences in the predictions of model 1 and model 2. Therefore, only model 1 will be considered for the following discussion of the system $(1 - x_B)\text{NaPO}_3-x_B\text{B}_2\text{O}_3$. For $x_B = 0$ the phosphate network consists almost only of $P^{(2)}$ NFUs. Since $B^{(4)}$ units are energetically favored, $P^{(2)}$ is replaced by $B^{(4)}$ and $P^{(3)}$ accordingly:

$$\{B^{(4)}\} = \frac{2x_B}{1 + x_B} \quad (5.14a)$$

$$\{P^{(3)}\} = \frac{2x_B}{1 + x_B} \quad (5.14b)$$

$$\{P^{(2)}\} = \frac{1 - 3x_B}{1 + x_B} \quad (5.14c)$$

until no further $B^{(4)}$ could be produced without formation of bOs, which are not connecting two $B^{(4)}$ NFU. The corresponding $x_B = \hat{x}_B$ is given by the solution of:

$$4\{B^{(4)}\} - 3\{P^{(3)}\} - 2\{P^{(2)}\} = 0 \quad (5.15a)$$

$$\{B^{(4)}\} = \frac{2\hat{x}_B}{1 + \hat{x}_B} \quad (5.15b)$$

$$\{B^{(4)}\} + \{P^{(2)}\} = \frac{1 - \hat{x}_B}{1 + \hat{x}_B} \quad (5.15c)$$

$$\{P^{(3)}\} + \{P^{(2)}\} = \frac{1 - \hat{x}_B}{1 + \hat{x}_B} \quad (5.15d)$$

Eqs. 5.15 lead to $\hat{x}_B = 1/4$. Since the concentration of $B^{(4)}$ is controlled by the formation of further bOs, the increase of the amount of $B^{(4)}$ is reduced and $B^{(3)}$ -NFU must be produced.

This fact is described by:

$$4\{B^{(4)}\} - 3\left(\{B^{(3)}\} + \{P^{(3)}\}\right) - 2\{P^{(2)}\} = 0 \quad (5.16a)$$

$$\{B^{(4)}\} + \{B^{(3)}\} = \frac{2x_B}{1 + x_B} \quad (5.16b)$$

$$\{B^{(4)}\} + \{P^{(2)}\} = \frac{1 - x_B}{1 + x_B} \quad (5.16c)$$

$$\{P^{(3)}\} + \{P^{(2)}\} = \frac{1 - x_B}{1 + x_B} \quad (5.16d)$$

This set of equations leads to:

$$\{B^{(4)}\} = \frac{2x_B + 1}{3 + 3x_B} \quad (5.17a)$$

$$\{B^{(3)}\} = \frac{4x_B - 1}{3 + 3x_B} \quad (5.17b)$$

$$\{P^{(3)}\} = \frac{2x_B + 1}{3 + 3x_B} \quad (5.17c)$$

$$\{P^{(2)}\} = -\frac{5x_B - 2}{3 + 3x_B} \quad (5.17d)$$

Eq. 5.17d implies the characteristic point $x_B = \bar{x}_B = 2/5$, which corresponds to the borate concentration where the $P^{(2)}$ -NFU vanishes. In the subsequent regime the increasing of x_B decreases the content of sodium ions further and the number of $B^{(4)}$ units formed due to the alkali cations falls below the theoretical maximum. Therefore, the additional $B^{(4)}$ units could be generated which are counterbalanced by newly formed $P^{(4)}$ units. This feature is described by:

$$4\{B^{(4)}\} - 3\left(\{B^{(3)}\} + \{P^{(3)}\}\right) - 4\{P^{(4)}\} = 0 \quad (5.18a)$$

$$\{B^{(4)}\} + \{B^{(3)}\} = \frac{2x_B}{1 + x_B} \quad (5.18b)$$

$$\{B^{(4)}\} - \{P^{(4)}\} = \frac{1 - x_B}{1 + x_B} \quad (5.18c)$$

$$\{P^{(4)}\} + \{P^{(3)}\} = \frac{1 - x_B}{1 + x_B} \quad (5.18d)$$

yielding:

$$\{B^{(4)}\} = \frac{2x_B + 1}{3 + 3x_B} \quad (5.19a)$$

$$\{B^{(3)}\} = \frac{4x_B - 1}{3 + 3x_B} \quad (5.19b)$$

$$\{P^{(4)}\} = \frac{5x_B - 2}{3 + 3x_B} \quad (5.19c)$$

$$\{P^{(3)}\} = -\frac{8x_B - 5}{3 + 3x_B} \quad (5.19d)$$

The content of $P^{(3)}$ is decreased up to a value $x_B = \tilde{x}_B = 5/8$ by the decrease of the phosphate concentration and the formation of additional $P^{(4)}$ NFU. For $x_B > \tilde{x}_B$ the

concentration of $B^{(4)}$ NFU decreases, since the the overall positive charge decreases linearly. This mechanism leads to:

$$\{B^{(4)}\} = \frac{2(1 - x_B)}{1 + x_B} \quad (5.20a)$$

$$\{B^{(3)}\} = \frac{4x_B - 2}{1 + 1x_B} \quad (5.20b)$$

$$\{P^{(4)}\} = -\frac{1 - x_B}{3 + 3x_B} \quad (5.20c)$$

A comparison (see fig. 5.2) of the theoretical predictions (see eqs. 5.14, 5.17, 5.19 and 5.20) with the experimental results for the $(1 - x_B)\text{NaPO}_3 - x_B\text{B}_2\text{O}_3$ glasses shows that the theoretical results are in good compliance with the experimental data. However, the quality of the agreement is lower than in the other two systems. The overall behavior of the $B^{(4)}$ and $B^{(3)}$ NFU is captured very well, but the concentrations of phosphate NFUs are not always in good agreement with the model predictions. In particular, it was found that the concentration of $P^{(4)}$ for small x_B is much higher than expected by the modeling. Nevertheless, one should note that the composition $x_B = 0.2$ (the first vertical line in fig. 5.2) corresponds to a glass $0.4\text{Na}_2\text{O} - 0.6[x\text{B}_2\text{O}_3 - (1 - x)\text{P}_2\text{O}_3]$ with $x = 1/3$. In contrast to the findings of Rinke *et al.*, no $P^{(4)}$ NFUs were reported by Zielniok and coworkers in the corresponding mixing range. The second line corresponds to a theoretical point of the mixing line $x_A\text{Na}_2\text{O} - (1 - x_A)(\text{PBO}_4)$ with $x_A = 1/3$ [176, 87] and $0.333\text{Na}_2\text{O} - 0.667[x\text{B}_2\text{O}_3 - (1 - x)\text{P}_2\text{O}_5]$ [180]⁴, where no $P^{(4)}$ content is also reported. It is not possible to discuss here the origin of this discrepancy, since more experimental information is required. Perhaps this fact is related in some way to the fabrication process. Systematic studies varying the reaction route have to be performed, in order to address this issue. However, the most remarkable discrepancy of the model is found for $0.6 \lesssim x_B \lesssim 0.9$, where the $P^{(4)}$ concentration is found to be significantly below the predicted line and the combined $P^{(2)}/P^{(3)}$ concentration above it. One could assume (i) that this discrepancy is due the uncertainty of estimation of the concentrations determining the different phosphate species or (ii) that the concepts discussed here are limited to sufficient high alkali content.

However, the excellent agreement of the additional consideration of $P^{(4)}$ in the $x_A\text{Na}_2\text{O} - (1 - x_A)(\text{BPO}_4)$ glasses supports the presented modeling. In the view of the present discussion an alternative scenario is plausible for the low alkali concentration (i.e. $\{M\} = y/(1 - y) \leq \{M\}_* = 3/7$), because the $P^{(4)}$ NFU were not considered in sec. 4.3. This issue will be addressed in the following paragraph.

5.2.3. An alternative scenario for the low $\{M\}$ regime in sec. 4.3

When the formation of $P^{(4)}$ units is included in the theoretical modeling of the NFU concentrations in sec. 4.3, the analysis has to refine the low- $\{M\}$ predictions.

⁴For systems with other alkali ions also no $P^{(4)}$ was found at the corresponding alkali content [181]

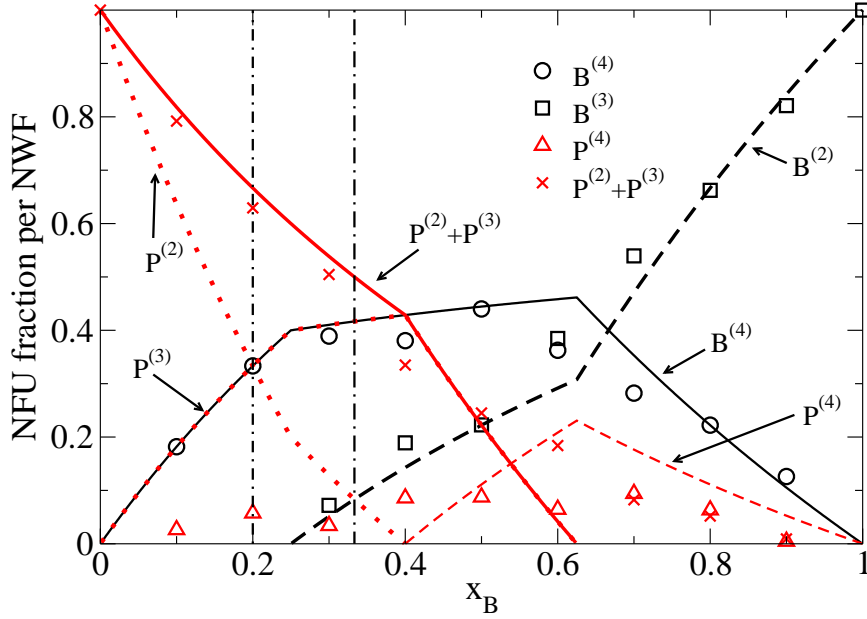


Figure 5.2.: The experimental species distribution for $(1 - x_B)\text{NaPO}_3 - x_B\text{B}_2\text{O}_3$ determined by a combined MAS-NMR and XPS analysis [85, 176] in comparison with the modeling

The first regime $x < \{M\}$ will be unchanged, i.e. $\{P^{(2)}\} = \{M\} - x$, $\{P^{(3)}\} = 1 - \{M\}$ and $\{B^{(4)}\} = x$. Approaching the point $x = \{M\}$, the $P^{(2)}$ concentration vanishes, but the $B^{(4)}$ concentration is below its allowed maximum. Thus, it is possible to generate further $B^{(4)}$ for $x > M$, which are counter-balanced by positively charged $P^{(4)}$ units that are formed on the cost of the uncharged $P^{(3)}$ units:

$$\{B^{(4)}\} = x \quad (5.21a)$$

$$\{P^{(4)}\} = x - \{M\} \quad (5.21b)$$

$$\{P^{(3)}\} = 1 - 2x + \{M\} \quad (5.21c)$$

At a certain point $x = x_c$ the concentration of the $B^{(4)}$ units reaches its allowed maximum given by the set of equations:

$$\{B^{(4)}\} - 4\{P^{(4)}\} - 3\{P^{(3)}\} = 0 \quad (5.22a)$$

$$\{B^{(4)}\} - \{P^{(4)}\} = \{M\} \quad (5.22b)$$

$$\{P^{(3)}\} + \{P^{(4)}\} = 1 - x_c \quad (5.22c)$$

$$\{B^{(4)}\} = x_c \quad (5.22d)$$

from which follows $x_c = (3 - \{M\})/6$. At this point no further $B^{(4)}$ and $P^{(4)}$ will be produced and the $P^{(3)}$ will be replaced by $B^{(3)}$. This process is described by the following

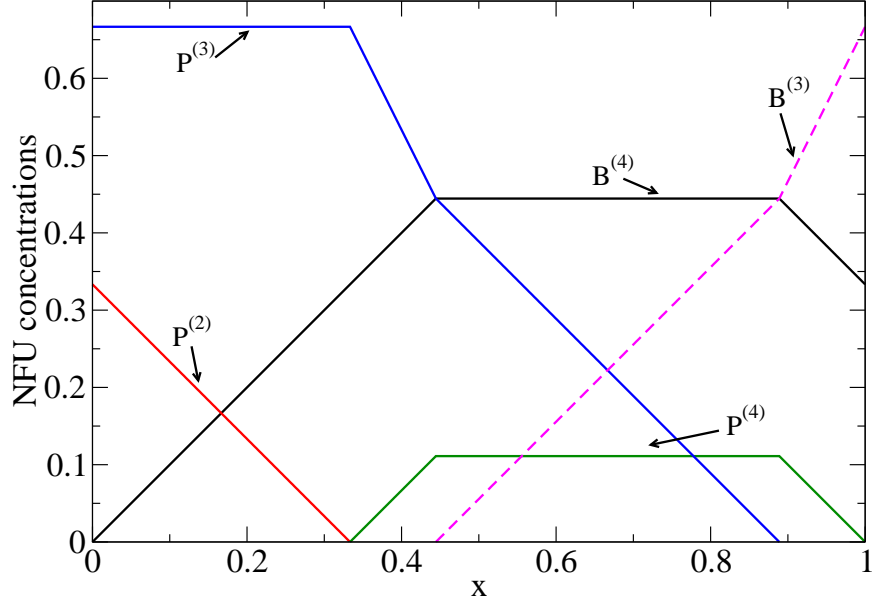


Figure 5.3.: The prediction of the NFU concentrations in an alternative scenario (Eqs. 5.21-5.24 for $\{M\} \leq \{M\}_* = 3/7$ (here $\{M\}=1/3$), which includes the formation of $P^{(4)}$ units

conditions:

$$\{B^{(4)}\} - 4\{P^{(4)}\} - 3(\{P^{(3)}\} + \{P^{(3)}\}) = 0 \quad (5.23a)$$

$$\{B^{(4)}\} - \{P^{(4)}\} = \{M\} \quad (5.23b)$$

$$\{P^{(3)}\} + \{P^{(4)}\} = 1 - x \quad (5.23c)$$

$$\{B^{(4)}\} + \{B^{(3)}\} = x \quad (5.23d)$$

From these conditions follows:

$$\{B^{(3)}\} = \frac{\{M\} - 3}{6} + x \quad (5.24a)$$

$$\{B^{(4)}\} = \frac{3 - \{M\}}{6} \quad (5.24b)$$

$$\{P^{(3)}\} = \frac{7\{M\} + 3}{6} - x \quad (5.24c)$$

$$\{P^{(4)}\} = \frac{3 - 7\{M\}}{6} \quad (5.24d)$$

Since all concentrations must be positive it follows that for $x = (7\{M\} + 3)/6$ where $\{P^{(3)}\}$ becomes zero, a new regime must begin. Since $P^{(4)}$ is the only phosphate species, it is

straightforward to calculate the NFU concentrations:

$$\{B^{(3)}\} = 2x - 1 - \{M\} \quad (5.25a)$$

$$\{B^{(4)}\} = 1 + \{M\} - x \quad (5.25b)$$

$$\{P^{(4)}\} = 1 - x \quad (5.25c)$$

Figure 5.3 shows the predictions of the modeling for $\{M\} = 1/3$. The maximum of the $B^{(4)}$ concentration is higher than $\{M\}_* = 3/7$. Experimental work need to be done to check our predictions.

In summary, it was shown in the present section that the generalization and extension of the concepts of Beekenkamp and Gupta have to be interpreted as the superposition of a random network exclusively formed by non- $B^{(4)}$ -units and a subset of NFUs connected via bOs to $B^{(4)}$ -units, where the number of bOs bonded to two $B^{(4)}$ -NFU is somewhat limited. This interpretation leads to an excellent agreement of the experimentally derived bO-conectivities.

In addition, it was shown that this modeling is supported by further experimental data of alkali borophosphate glasses. In particular, one finds that the overall behavior of the NFU-concentrations is reproduced well with only minor discrepancies between theoretical predictions and experimental data. These discrepancies, however, were found to be in the order of experimental deviations.

Finally, we introduce an alternative scenario for the NFU-concentrations in the low alkali regime that could be used as a test case for further experimental verification of the concepts presented here.

5.3. Further remarks on the NUT approach

5.3.1. Calculation of the site energy distribution

In sec 4.4 the distribution of site energies was introduced by a computer algorithm. However, it is possible to calculate the site energy distribution in an analytic way applying some minor approximations. The derivation of the analytic expression is shown in the present section. For the sake of simplicity all calculations are performed in the approximation of a simple cubic lattice, i.e. each ion or NFU site is coordinated by 8 NFU- or ion- sites. It should be noted that the general concepts underlying this derivation do not depend on the choice of lattice.

It is convenient to start from a pure alkali phosphate system with $\{M\} \leq 1$, where it was found that only $P^{(3)}$ and $P^{(2)}$ [167] are present. As a first step, it is necessary to calculate the probability p_n that in the environment of one ion site exactly n $P^{(2)}$ units are present. Since the occupation of a NFU-site is not correlated with other NFU sites, one obtains:

$$p_n = \frac{8!}{n!(8-n)!} \{P^{(2)}\}^n \left(1 - \{P^{(2)}\}\right)^{(8-n)} \quad (5.26)$$

where the factor $8!/(n!(8-n)!)$ is the number of possible realizations for n of 8 $P^{(2)}$ units.

Assuming that a cation site has n $P^{(2)}$ -NFUs in its nearest neighbor environment, the conditional probability $p(m|n)$ that exactly m nbOs are contributing to the site energy needs to be considered. For an exact calculation one has to take into account correlations between neighboring ion sites. These correlations are introduced by the fact that if an NFU already contributes to the site energies of two other adjacent ion sites, it certainly does not contribute to the actual site. For the sake of simplicity these correlations were neglected. Since the $P^{(2)}$ units affect the site energies for 2 out of 8 adjacent sites, the probability that the NFU contributes to a randomly chosen site is $(1/4)$. Accordingly the probability is equal to $(3/4)$ that it does not contribute to the chosen site. Taking into account again the number of possible realizations one obtains:

$$p(m|n) = \frac{n!}{m!(n-m)!} 3^{-m} \left(\frac{3}{4}\right)^n \quad (5.27)$$

For the probability w_m that m nbOs are contributing to the actual site follows:

$$\begin{aligned} w_m &= \sum_n p(m|n)p_n \\ &= \sum_n \frac{8!}{(8-n)!m!(n-m)!} 3^{-m} \left(\frac{3}{4}\right)^n \{P^{(2)}\}^n \left(1 - \{P^{(2)}\}\right)^{(8-n)} \end{aligned} \quad (5.28)$$

This m nbOs correspond to a "bare" site energy $E^{(m)} = 0.5m$, which is a set of discrete random numbers distributed with w_m . According to our model, long-range interactions are introduced by an additional random contribution η , which is distributed by a Gaussian with a zero mean and a standard deviation Δ . Therefore, the conditional probability $P(E|m)$ for a siteenergy of E can be calculated by:

$$P(E|m) = \frac{1}{\sqrt{2\pi\Delta^2}} \exp\left(-0.5 \left(\frac{E - E^{(m)}}{\Delta}\right)^2\right) \quad (5.29)$$

Hence, we find for the total site energy distribution $P(E_i)$ in the case of pure alkali phosphate glasses:

$$\begin{aligned} P(E) &= \sum_{m=0}^8 w_m P(E|m) \\ &= \sum_{m=0}^8 w_m \frac{1}{\sqrt{2\pi\Delta^2}} \exp\left(-0.5 \left(\frac{E - E^{(m)}}{\Delta}\right)^2\right) \end{aligned} \quad (5.30)$$

The complexity of the calculations increases, if one adds $B^{(4)}$ units to the system. In this case one has to consider that from eight NFU sites l sites are occupied by a $B^{(4)}$, n by a $P^{(2)}$ and $8-l-n$ by a $P^{(3)}$ or a $B^{(3)}$. The probability to find such a site is:

$$p_{ln} = \frac{8!}{n!l!(8-n-l)!} \{P^{(2)}\}^n \{B^{(4)}\}^l \left(1 - \{P^{(2)}\} - \{B^{(4)}\}\right)^{(8-n-l)} \quad (5.31)$$

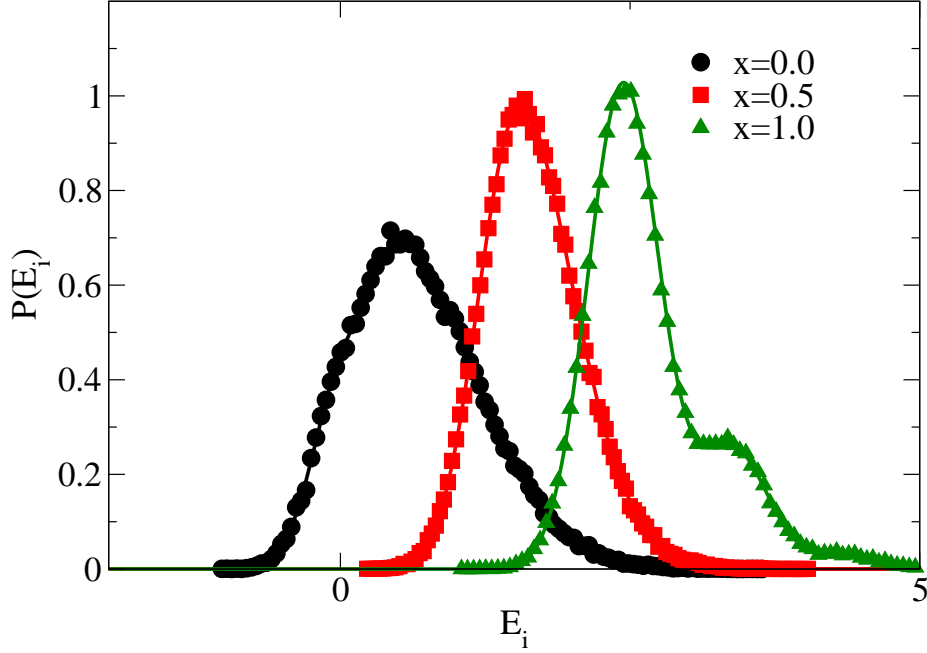


Figure 5.4.: The site energy distribution generated by the model described in sec. 4.4 for a single cubic lattice with 48^3 lattice sites (symbols) and the corresponding values calculated eqs. 5.33 and 5.36 (solid lines). The curves for $x=0.5$ and $x=1.0$ are shifted by 1 and 2 for the sake of clarity

The probability that m nbO are contributing to the site energy now depends also on l , i.e. $w_m \rightarrow w_m^{(l)}$, with:

$$\begin{aligned} w_m^{(l)} &= \sum_n p(m|n)p_{ln} \\ &= \sum_n \frac{8!}{m!l!(8-n-l)!(n-m)!} 3^{-m} \left(\frac{3}{4}\right)^n \{P^{(2)}\}^n \{B^{(4)}\}^l \left(1 - \{P^{(2)}\} - \{B^{(4)}\}\right)^{(8-n-l)} \end{aligned} \quad (5.32)$$

For the total site energy distribution $P(E_i)$ the following expression is obtained:

$$P(E) = \sum_{n=0}^8 \sum_{m=0}^n \sum_{l=0}^{8-n} \frac{8!}{m!l!(8-n-l)!(n-m)!} 3^{-m} A_{nl} P(E|m, l) \quad (5.33)$$

with:

$$A_{nl} = \left(\frac{3}{4}\right)^n \{P^{(2)}\}^n \{B^{(4)}\}^l \left(1 - \{P^{(2)}\} - \{B^{(4)}\}\right)^{(8-n-l)} \quad (5.34)$$

$$P(E_i|m, l) = \frac{1}{\sqrt{2\pi\Delta^2}} \exp\left(-0.5 \left(\frac{E_i - 0.5m - 0.125l}{\Delta}\right)^2\right) \quad (5.35)$$

Similar expressions could be derived for systems with $P^{(1)}$, $P^{(0)}$ and $B^{(2)}$. In the view of the increasing complexity of the mathematical expressions and the low $P^{(1)}$ and $P^{(0)}$ only an expression for the pure alkali borate system will be given here with n^* as the number of $B^{(2)}$ units around a given site

$$P(E) = \sum_{n^*=0}^8 \sum_{m^*=0}^{n^*} \sum_{l=0}^{8-n^*} \frac{8!}{m^*! l! (8-n^*-l)! (n^*-m^*)!} 7^{-m^*} A_{n^*l}^* P(E|m^*, l) \quad (5.36)$$

with

$$A_{n^*l}^* = \left(\frac{7}{8}\right)^{n^*} \{B^{(2)}\}^{n^*} \{B^{(4)}\}^l \left(1 - \{B^{(2)}\} - \{B^{(4)}\}\right)^{(8-n^*-l)} \quad (5.37)$$

$$P(E|m^*, l) = \frac{1}{\sqrt{2\pi\Delta^2}} \exp\left(-0.5 \left(\frac{E - 1m^* - 0.125l}{\Delta}\right)^2\right) \quad (5.38)$$

Fig. 5.4 shows that the calculated site energy distributions are in excellent agreement with the site energy distributions generated with the computer algorithm described in sec. 4.4.

5.3.2. The activation energy for long range transport

With the knowledge of the site energy distribution it is also possible to calculate the activation energy in the NUT model analytically. In the literature two methods are suggested to calculate the activation energy as a function of the site energy distribution and the concentration of particles c . Both methods are based on different interpretations of the underlying percolation concept. In the first one (*critical path analysis*) it is assumed that the long range transport of the particles takes place on an infinite cluster formed by interconnected sites i , which have to fulfill $E_i \leq E_c$, where the characteristic energy E_c must fulfill [19, 182, 183, 184, 185]:

$$\int_{E^{\min}}^{E_c} dEP(E) = p_c^{(\text{site})} \quad (5.39)$$

The percolation threshold for site percolation $p_c^{(\text{site})}$ depends crucially on the geometry of the underlying lattice. In many cases the lower critical energy E^{\min} was taken to be $-\infty$ [19, 183, 184]. This fact implies that every site with an energy smaller than the Fermi level E_f defined by:

$$\int_{-\infty}^{E_f} dEP(E) = c \quad (5.40)$$

contributes also to the long range transport. The activation energy E_a is assumed to be $E_a = E_c - E_f$. This assumption implies that E_a becomes negative⁵ for $c > p_c^{(\text{site})}$, since E_c becomes smaller than E_f . In addition to this behavior, it is questionable that sites with energies far below E_f contribute also to the long range transport. Therefore, it was suggested

⁵i.e. the conductivity would be increased if the temperature is decreased

alternatively to set $E^{\min} = E_f$ [185]. The *critical path analysis* was successfully tested in systems with uncorrelated random site energies chosen from a Gaussian distribution for $c \leq 0.16$ [19, 183, 184].

The second approach, which is denoted here as *effective circuit approach*, starts from the (mean-field) rate equation [18, 109, 186, 187]:

$$\frac{\partial n_i}{\partial t} = \sum_{j \neq i} [\Gamma_{ji} n_j (1 - n_i) - \Gamma_{ij} n_i (1 - n_j)] \quad (5.41)$$

which describes the change of the expectation value $n_i = \langle s_i \rangle$ of the occupation state $s_i \in \{0, 1\}$ by the sum of the ingoing current $J_{ij} = \Gamma_{ji} n_j (1 - n_i)$ and the outgoing current $J_{ji} = -\Gamma_{ij} n_i (1 - n_j)$. If the system reaches a canonical equilibrium, the mean occupation numbers n_i become constant, i.e. $n_i^{(\text{eq})} = f_i$ with:

$$f_i = \frac{1}{\exp(\beta(E_i - E_f)) + 1} \quad (5.42)$$

Such a set of f_i will be sufficiently achieved by the detailed balance condition, i.e.:

$$\Gamma_{ij} f_i (1 - f_j) = \Gamma_{ji} f_j (1 - f_i) \quad (5.43)$$

Equation 5.41 implies for the correlation function $\langle s_i s_j \rangle = n_i n_j$ ⁶. Recent studies indicate [188] that this approximation gives reasonable results for fermionic models with variable range hopping. In contrast, it was shown for some systems⁷ that the quality of this approximation [189, 190, 191] could be low. For higher dimensional fermionic systems with nearest neighbor hopping ($d \leq 3$)⁸ it is, however, often assumed that this approximation should be quite adequate. Nevertheless, now no numerical tests are known, which address this issue in 3-dimensional systems.

The main idea behind the *effective circuit approach* is the mapping of the hopping process given by eq. 5.41 on a network of random resistors. The mathematical procedure and the physical arguments will be given in the following discussion.

Applying an sufficient small electric field \mathbf{E} in x-direction, with $|\mathbf{E}|a \ll \Delta E_{ij}^{(\text{typ})}$ (a lattice spacing, and $\Delta E_{ij}^{(\text{typ})}$ is the typical energy difference between adjacent sites) one gets a change in the rates Γ_{ji} , because the site energy differences between adjacent sites are changed by an additional term linear in $E(x_i - x_j)$ ⁹. The mean occupation numbers n_i must be also affected because the ingoing and outgoing currents are affected due the change in the Γ_{ji} . This change in the n_i corresponds to an additional (local) contribution $\delta E_f^{(i)}$ to the fermi energy, which yields in linear approximation:

$$n_i \approx f_i - \beta f_i (1 - f_i) \delta E_f^{(i)} \quad (5.44)$$

⁶See Appendix A for further information

⁷in particular one dimensional systems

⁸since the number of pathways increases with dimensionality, variable range hopping could be considered as a transport on very high dimensional lattices

⁹ x_i is the x-component of position vector of site i

This gives for the currents in linear order [187]:

$$J_{ij} = \beta \Gamma_{ij} f_i (1 - f_j) \left[E(x_i - x_j) - \delta E_f^{(i)} + \delta E_f^{(j)} \right] \quad (5.45)$$

Since the terms inside the square brackets are energies, one could interpret the expression as a voltage. Therefore, $\beta \Gamma_{ij} f_i (1 - f_j)$ can be viewed as the conductivity σ_{ij} between site i and j . Using Metropolis type hopping rates (i.e. $\Gamma_{ij} = \min(1, \exp(-\beta(E_j - E_i)))$), this ansatz leads for the conductivities to¹⁰:

$$\sigma_{ij} = \beta \frac{\exp(-\beta(E_f - E_i))}{(1 + \exp(\beta(E_i - E_f)))(1 + \exp(\beta(E_j - E_f)))} \quad (5.46)$$

For low temperatures the largest energy difference is dominating the behavior of σ_{ij} in eq. 5.46. Therefore, one has to consider three cases:

$$\sigma_{ij} \approx \beta \exp(-\beta(E_f - E_i)) \quad , \text{ for } E_i < E_j < E_f \quad (5.47a)$$

$$\sigma_{ij} \approx \beta \exp(-\beta(E_j - E_i)) \quad , \text{ for } E_i < E_f < E_j \quad (5.47b)$$

$$\sigma_{ij} \approx \beta \exp(-\beta(E_j - E_f)) \quad , \text{ for } E_f < E_i < E_j \quad (5.47c)$$

It was shown by Ambegaokar, Langer and Halperin [109] that these three cases could be mapped on an effective single particle model with symmetric hopping rates:

$$\sigma_{ij} \approx \beta \exp(-\beta \zeta_{ij}) \quad (5.48)$$

with the effective barrier $\zeta_{ij} = (|E_f - E_i| + |E_f - E_j| + |E_i - E_j|)/2$. This procedure maps a site percolation problem on a bond percolation problem. The activation energy $E_a = \zeta_c$ is given by the condition [18]:

$$p_c^{(\text{bond})} = \int_{E_f}^{E_f + \zeta_c} P(E_i) \int_{E_i - \zeta_c}^{E_f + \zeta_c} P(E_j) dE_i dE_j \\ + \int_{E_f - \zeta_c}^{E_f} P(E_i) \int_{E_f - \zeta_c}^{E_i + \zeta_c} P(E_j) dE_i dE_j \quad (5.49)$$

At first glance, one may expect that $p_c^{(\text{bond})}$ has the same value as determined for standard bond percolation (e.g., for single cubic lattices $p_c^{(\text{bond})} = 0.2488$ [192]). Nevertheless, it was shown by Cordes *et al.* [143] that the correct $p_c^{(\text{bond})}$, which has to be applied in this procedure, significantly differs from the standard values. The explanation of this effect is given by the following arguments. Assuming that all adjacent sites are connected by bonds and a fraction p of these sites is randomly chosen¹¹, the fraction of bonds between adjacent sites is p^2 . Therefore, the corresponding bond percolation threshold introduced by this procedure should be roughly $(p_c^{(\text{site})})^2$. Cordes *et al.* claim that the percolation threshold should be close to that value for $c \rightarrow 0$ [143]. Due to the fact that a site with an energy far away

¹⁰without loss of generality $E_i < E_j$

¹¹i.e. if the probability to choose a site does not depend on the fact that adjacent sites are chosen

from the fermi level has a low probability to be effectively connected to an adjacent site, some further correlations are introduced that give rise to some concentration dependency of $p_c^{(\text{bond})}$. The percolation threshold was found in the range of $0.096 \leq p_c^{(\text{bond})} \leq 0.114$ for site energies with exponential and Gaussian distribution [143].

Both approaches were tested with the site energy distributions calculated in sec. 5.3.1. Since the percolation threshold for a simple cubic lattice ($p_c^{(\text{site})} = 0.3116$ [192]) is smaller than the particle concentrations $c = 1/3$, it is only possible within the *critical path analysis* to test this concept for $E^{\text{min}} = E_f$. Since the shape of the distribution functions have only a weak influence on the effective percolation thresholds in the *effective circuit approach* [143], it is reasonable to assume that the percolation thresholds have similar values. Therefore, it was supposed that the real percolation threshold is roughly in the regime $0.08 \lesssim p_c^{(\text{bond})} \lesssim 0.12$.

The analysis shown in fig. 5.5 reveals that the compositional trends in E_a are qualitatively reproduced for both concepts. However, the simulated values of E_a are significantly higher than the corresponding values determined numerically by the *effective circuit approach* independent of x . The predictions made by the *critical path analysis* are much higher than the simulated results.

In order to explain the differences between the simulated and calculated E_a , the apparent activation energy $E_a^{(\text{app})}(\beta)$ defined as the local apparent incline of the constant of diffusion for two inverse temperatures β and $\beta + \Delta\beta$ in the Arrhenius plots (see fig. 4.9a), must be investigated, i.e.:

$$E_a^{(\text{app})}(\beta) = \frac{\ln(D(\beta + \Delta\beta)) - \ln(D(\beta))}{\Delta\beta} \quad (5.50)$$

Plotting these values against $1/\beta$ reveals a significant reduction of $E_a^{(\text{app})}$ with decreasing temperature. It is important to note that this finding corresponds to an "anomalous" Non-Arrhenius behavior of the activation energy, which was found for instance in alkali-borate glasses [193]. The linear extrapolation of $E_a^{(\text{app})} \rightarrow E_a^\infty$ for $1/\beta \rightarrow 0$ gives some reasonable estimate for the low temperature value of E_a . Note that even for temperatures which are in the order of $k_B T \lesssim E_a^{(\infty)}/(6 * E_0)$ a significant difference between $E_a^{(\text{app})}$ and $E_a^{(\infty)}$ was found. This could be interpreted as the energy costs to the thermal activated formation of vacancies/particles below/above the Fermi level. Since a higher number of vacancies/particles below/above the Fermi level leads to a higher mobility, the activation E_a of long range transport properties will get an additional contribution $\propto k_B T \propto 1/\beta$.

It seems to be important to point out here that there is the possibility of some systematic under estimation of the $E_a^{(\text{app})}(\beta)$ because the lowest $D(t) = D(t_{\text{max}})$ (t_{max} corresponds the maximum simulation time) values were taken as the $D(t \rightarrow \infty)$. Nevertheless, these values not fully converged to the long time diffusion constants (i.e. $D(t_{\text{max}})/D(t \rightarrow \infty) \lesssim 1.05$, see fig. 5.5 d).

However, the comparison of the values for $E_a \rightarrow E_a^{(\infty)}(x)$ shows a remarkable tendency towards the predictions given by the *effective circuit approach*. This fact gives some sup-

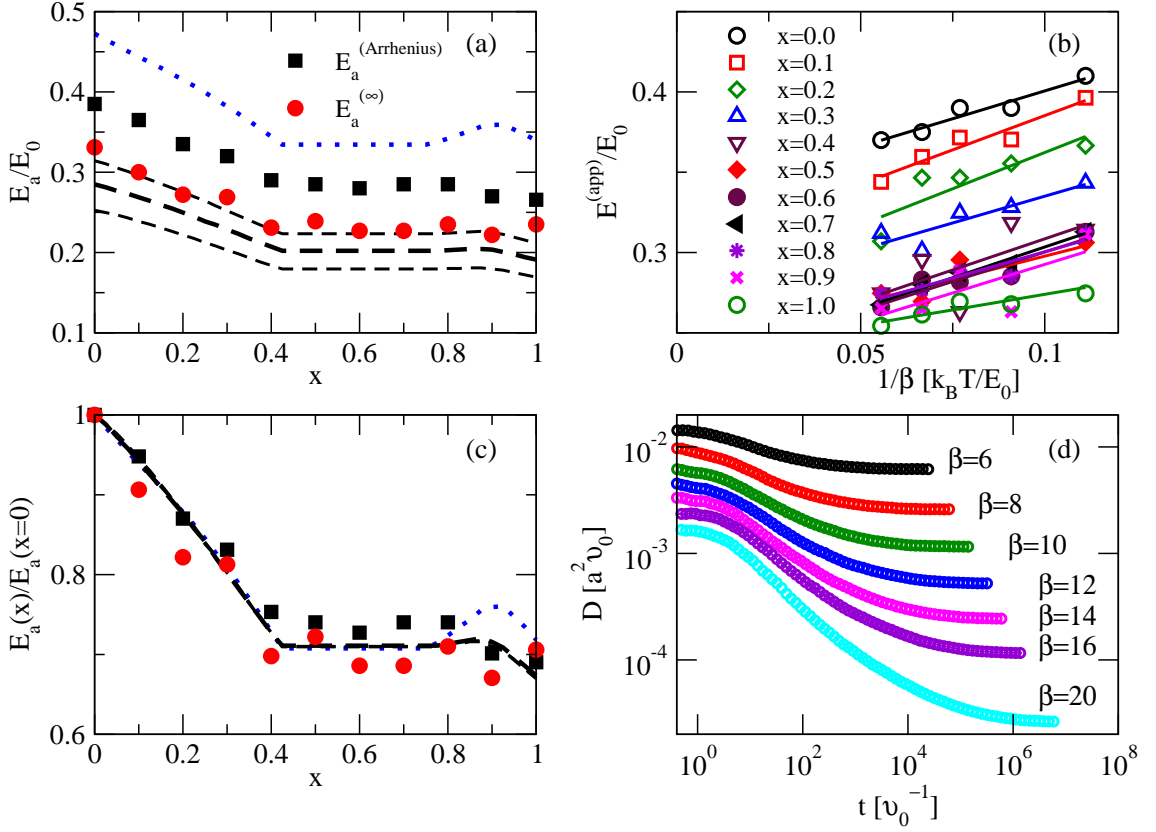


Figure 5.5.: (a) The activation energy calculated with the *critical path analysis* (dotted lines) and the *effective circuit approach* (solid and dashed lines) in comparison with E_a estimated by the Arrhenius plots and the linear extrapolation of the apparent activation energies to $1/\beta \rightarrow 0$ as a function of x . (b) apparent activation energy for all x . Symbols are the simulation results and solid lines are the corresponding least squared fits. (c) Rescaling of $E_a \rightarrow E_a(x)/E_a(x=0)$. The species distributions used in the simulations were generated with the f -model described in sec. 4.3. (d) The time dependent diffusion function $D(t) = \langle r^2(t) \rangle / (6t)$ for $x=0.0$. The MC-simulations were performed according the NUT model with $\Delta = 0.25$.

port to the adequacy of the *effective circuit approach*. In addition, one can state that the *critical path analysis* is less applicable in the model studied here¹². Despite some minor differences between simulated and predicted values, the simulation results points to the fact that the *effective circuit approach* is the best candidate for a reasonable low temperature approximation to calculate E_a in fermionic hopping systems. It should be noted that to the best of our knowledge the different theories were never compared in detail by applying

¹²at least for the case $c > p_c^{(\text{site})}$ and $E^{\text{min}} = E_f$

Monte Carlo simulations.

Nevertheless, the results for the MGFE, i.e. the change of the normalized activation energy $E_a(x)/E_a(0)$ (see fig. 5.5c), are almost not affected by the choice of the calculation method. Therefore, one can finish the present discussion with the important conclusion that the NUT approach for alkali-borophosphate glasses is also analytically threadable.

5.3.3. The MICE effect in binary alkali borate glasses

In many glasses it was found that the activation energy decreases approximately as:

$$E_a = a \ln\{M\} + b \quad (5.51)$$

The most prominent examples for this behavior are binary alkali borate glasses [11, 177]. The present section is dedicated to the question to what extent this behavior could be also reproduced by the NUT approach. In addition, it has to be checked whether the *effective circuit approach* is still more adequate than the *critical path analysis* if one varies $\{M\}$.

To this end, the hopping transport was simulated utilizing the Monte Carlo procedure as described in sec. 4.4. The size of the simple cubic lattices was varied from $N = 64^3$ (for $\{M\} = 0.160$) up to $N = 96^3$ (for $\{M\} = 0.005$). The results were averaged over 8 realizations for each $\{M\}$. In the present study the diffusion of the cations was directly simulated with the number of mobile ions was $N_{\text{ions}} = \{M\}N$. Assuming that the disorder of the site energies Δ should be a weakly varying function of $\{M\}$, one can use in first approximation a constant value within a sufficiently small range of $\{M\}$. Therefore, this value was set to $\Delta(\{M\}) \approx \text{const.} = 0.25$.

The data in the Arrhenius plots suggest again a linear behavior between $\ln(D(t \rightarrow \infty))$ and β . Plotting E_a obtained from the inclines of the Arrhenius plots against $\ln(\{M\})$ a linear behavior is obtained in reasonable approximation.

However, as it was discussed in the previous section, E_a can still show significant changes in the simulated temperature regime. This finding could be also confirmed by the present results. Nevertheless, a closer look at the apparent activation energies reveals a more manifold behavior of $E_a^{(\text{app})}$ depending on $\{M\}$. For sufficiently small $\{M\}$ the apparent activation energy increases with decreasing temperature. This finding corresponds to the "normal" non-Arrhenius behavior found in many fast ion conductors [183, 194]. If one increases $\{M\}$, this effect becomes weaker and it seems that above a certain $\{M\}$ $E_a^{(\text{app})}$ becomes a decreasing function with decreasing $1/\beta$. This finding could be explained by the interplay of two mechanisms (i) the additional costs of thermal activated particle occupations above the fermi-level (see sec. 5.3.2) and (ii) the fact that for high enough temperatures the hopping particles are allowed to move at energy levels $E_f + k_B T$. This mechanism corresponds to the hopping motion on alternative percolation clusters formed by new subsets of sites, where $E_a^{(\text{app})}$ is the energy difference of the minimum site energy E_1 and the maximum site

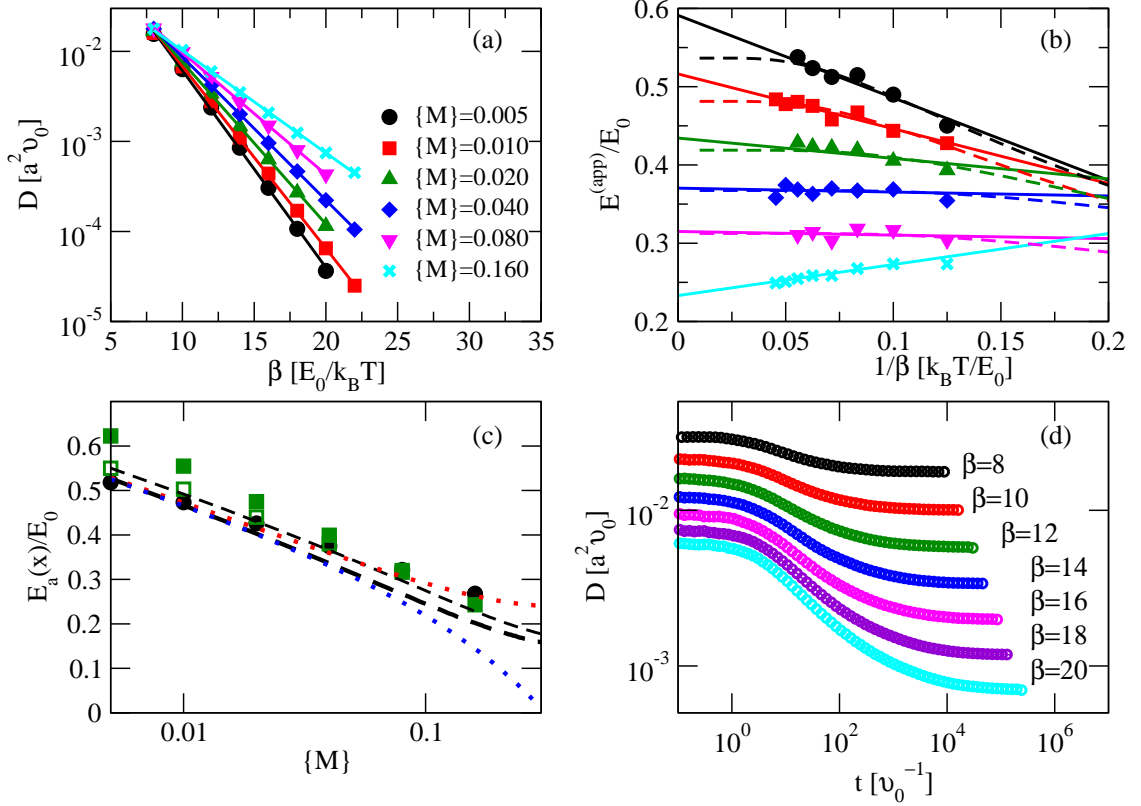


Figure 5.6.: (a) Arrhenius plots for the diffusion constant for $0.005 \leq \{M\} \leq 0.16$. (continuous decrease of the incline with increasing $\{M\}$) (b) apparent activation energy for all $\{M\}$ (symbols are the same as in (a)) as a function of β^{-1} . Solid lines corresponds to linear fits. Dashed lines are fitted by eq. 5.52 (c) The comparison between activation energies predicted by the *critical path analysis* with $E^{min} = -\infty$ (blue dotted line), $E^{min} = E_f$ (red dotted line) and the *effective circuit approach* with $p_c^{\text{bond}} = 0.08, 0.10, 0.12$ (lower dashed, solid, upper dashed line) with the results given by the incline of the Arrhenius plots (circles), linear extrapolation (filled squares) and the extrapolation according eq. 5.52 (open squares) of E_a^{app} to the zero temperature limes. (d) The time dependent diffusion function for $\{M\} = 0.16$. The MC-simulations were performed according to the NUT model with $\Delta = 0.25$.

energy E_2 on such a cluster, with $E_1 < E_f + k_B T < E_2$. Therefore, the apparent activation energies must be strongly affected by the shape of the site energy distributions (see fig. 5.7).

Coming now to the question concerning which of the proposed concepts are more adequate

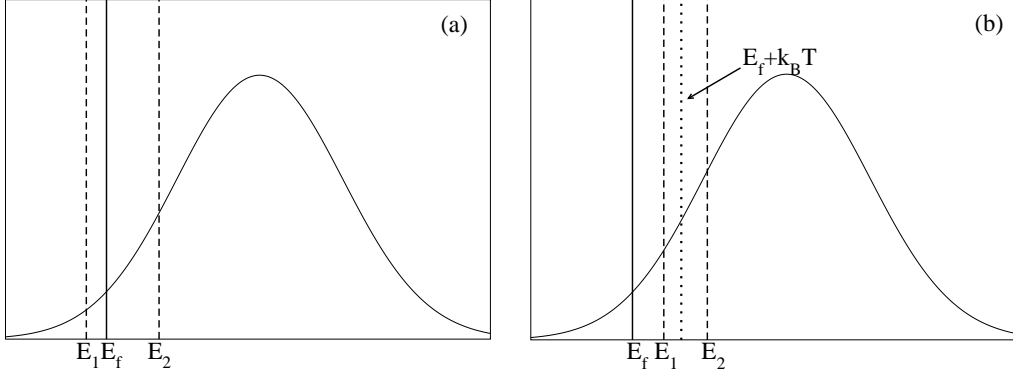


Figure 5.7.: Schematic explanation why $E_a^{(\text{app})}(T)$ increases with decreasing T . The energies E_1 and E_2 are the boundaries of the subset of sites, which form the relevant cluster for long range transport (a) $T \rightarrow 0$ $E_a^{(\text{app})}(0) = E_a^{(\infty)} = E_2(0) - E_1(0)$ is larger than the apparent activation energy for case (b) $T \gg 0$ with $E_a^{(\text{app})}(T) = E_2(T) - E_1(T)$

Note: The area under the curve between E_1 and E_2 has the same value

to calculate E_a . To this end, both the linearly extrapolated apparent activation energies¹³ and the inclines of the Arrhenius plots were compared to the predictions of these concepts. First, both versions of the *critical path analysis* are discussed in the view of these data. For small $\{M\}$ the choice of the lower boundary E^{min} has only weak effects on E_a . But with the increase of $\{M\}$, the theoretical values calculated with $E^{\text{min}} = -\infty$ (blue dotted line in fig. 5.6c) decrease significantly faster than results from the simulations. Whereas the E_a values determined as the incline of the Arrhenius plots are in very good agreement with the expected results in the case $E^{\text{min}} = E_f$ (red dotted line in fig. 5.6c).

For low $\{M\}$ results predicted by the *effective circuit approach* were also found to be in good agreement with the E_a values calculated from the Arrhenius plots. However, for $\{M\} \geq 0.16$, these values are higher than the predictions of the *effective circuit approach*. Furthermore, it was found that the linearly extrapolated values are significantly higher than any prediction for small $\{M\}$. Nevertheless, they show a better agreement with the effective circuit approach predictions with increasing $\{M\}$. Probably this finding is related to the mechanisms (i) and (ii) proposed above. Assuming that mechanism (i) dominates the overall behavior of $E_a^{(\text{app})}$, an approximately linear relation to $k_B T$ should be expected (see discussion in sec. 5.3.2). In contrast, if mechanism (ii) is the dominating effect for the temperature dependence of $E_a^{(\text{app})}(\{M\})$, one may assume that an adequate extrapolation function reaches a plateau for $1/\beta \rightarrow 0$, because the fraction of particles moving on percolating clusters with higher energies should be $\propto \exp(-\hat{E}\beta)$ with a characteristic energy \hat{E} . Unfortunately the exact form of $E_a^{(\text{app})} = E_a^{(\text{app})}(\beta)$ is not known. For the sake of simplicity,

¹³for $T \rightarrow 0$

the effect of saturation in $E_a^{(\text{app})}(\beta)$ is included by the extrapolation function¹⁴.

$$E_a^{(\text{app})}(\beta) = E_a^{(\infty)} \left(1 - \exp(-\hat{E}\beta) \right) \quad (5.52)$$

The activation energies estimated by this procedure are plotted as open squares in fig. 5.6 c. Obviously, they are in much better agreement with the predictions from the *effective circuit approach* than the *critical path analysis*. This finding is again an indication that the *effective circuit approach* is the most adequate algorithm to calculate E_a in fermionic hopping systems.

The main finding of the present section is the fact that the NUT model is also able to describe MICE in binary alkali borate glasses for $\{M\} \lesssim 0.16$. This finding is independent of the concept for predicting E_a from the distribution of the site energies. Deviations from the linear behavior for large $\{M\}$ are probably related to the approximation of a constant value of Δ . In addition, the results from the present section and sec. 5.3.2 strongly support the *effective circuit approach* as the most adequate candidate to calculate the activation energy in fermionic hopping systems. This finding permits the analytical estimation of the activation energy in comparable models. However, the support of the *effective circuit approach* is not perfect and it will be interesting to investigate this mechanism in more detail in some future studies. The interested reader may refer to some preliminary work described in appendix A, where a closer analysis beyond the mean field level gives some additional support for the *effective circuit approach*.

5.4. Summary

In this chapter the theoretical concepts given by chapter 4 are revisited.

First, it was shown that the f -parameter model described in sec. 4.3 is still valid, if the fractions of bOs, which are bonded randomly to two non-B⁽⁴⁾ NFU are equal for all NFU species. This finding justifies a single parameter model, where f is an effective measure for the B⁽⁴⁾-B⁽⁴⁾-connectivity.

In addition, the concepts from chapter 4 used to calculate the NFU species were extended by the introduction of positive charged $P^{(4)}$ units. These concepts were applied to sodium borophosphate glasses of the mixing regimes $x_A \text{Na}_2\text{O} - (1 - x_A) (\text{PBO}_4)$ and $x_B \text{B}_2\text{O}_3 - (1 - x_B) \text{NaPO}_3$. The outcome of these discussions was compared to the experimental results reported for corresponding systems estimated by MAS-NMR and XPS experiments [85, 87, 176]. In the view of experimental uncertainties, the theoretical values agree well with the experimental ones for $f = 0$. Furthermore, it was shown that the consideration of P⁽⁴⁾-NFU could alter the low $\{M\}$ regime discussed in chapter 4 because additional B⁽⁴⁾-NFU could be produced. These B⁽⁴⁾-NFU are counter-balanced by the positive charged P⁽⁴⁾.

¹⁴The fit of this extrapolation function is shown as dotted lines in fig 5.6b

For the NUT model presented in sec. 4.4 an exact mathematical expression for the distribution of site energies was derived. To calculate the activation energy directly from these distributions, it was necessary to check, which of the concepts, proposed in the literature, is adequate. It turned out that the mathematical description introduced by Ambegaekar, Langer and Halperin [109] and later applied by Baranovskii and Cordes [18, 143] (i.e. *effective circuit approach*) is an adequate algorithm to estimate E_a for $T \rightarrow 0$ in comparable models. To the knowledge of the author, such an analysis was not performed before. In addition, it was shown that the MICE in binary borates glasses¹⁵ could be explained within the framework of the NUT approach.

¹⁵which is characterized by a linear relation between E_a and the logarithm of $\{M\}$

6. Investigation of the Structures of Sodium Borophosphate Glasses by Reverse Monte Carlo Modeling to Examine the Origins of the Mixed Glass Former Effect¹

Abstract

We present new results for the Reverse Monte Carlo modeling of $0.35\text{Na}_2\text{O}-0.65[x\text{B}_2\text{O}_3-(1-x)\text{P}_2\text{O}_5]$ glasses based on X-ray diffraction (XRD) data reported by Le Roux *et al.* [128]. Structural models have been generated that accurately reproduce the pair correlation functions and structure factors determined by XRD while maintaining nearly perfect charge neutrality between the positively charged cations and the negatively charged phosphate and borate oxyanion groups, and while maintaining appropriate bond distances between the various atom pairs. These models, however, are not successful in accounting for the concentrations of network forming units (NFUs) as predicted by recent theoretical modeling [195]² and by magic angle spinning nuclear magnetic resonance (MAS-NMR) data [69] for sodium borophosphate glasses with similar stoichiometry. By a further refinement of the modeling, the NFU concentrations can be successfully reproduced as well. For the optimized structures we investigate the question if the conductivity activation energy correlates with the volume fraction of the sodium long-range diffusion paths as identified in the RMC modeling.

¹This chapter is published as: M. Schuch, R. Christensen, C. Trott, P. Maass, and S. W. Martin, *J. Phys. Chem. C.*, **116**, 1503, (2012)

²see chapters 4 and 5

6.1. Introduction

Ion conducting glasses are promising material systems for a large number of applications, such as rechargeable batteries, super-capacitors, and photo-chromic windows and mirrors because the cation mobility in these systems can be optimized over many orders of magnitudes by adjusting of their chemical compositions. One way to increase (and decrease in some cases) the ionic conductivity is to use the so-called Mixed Glass Former Effect (MGFE) [58, 59, 60, 63, 64, 73, 74, 130, 147, 196, 197], which manifests itself by a pronounced non-monotonous change in both the ionic conductivity and activation energy for long-range ion transport due to the mixing of two different glass formers, such as P_2O_5 and B_2O_3 . Such behavior is found, for example, in alkali borophosphate glasses where significant positive deviations from simple linear behavior are observed [195, 69, 196]. In similar alkali borosilicate glasses, the opposite behavior is observed and the deviations in the alkali ion conductivity are strongly negative from linear behavior [74].

Since the understanding of the relationships between the ionic conductivity of these mobile cations and the structure of the host glass is the key step for a further optimization of these glasses, a detailed understanding of the structure is required at both the short range, first coordination sphere, and intermediate range, second and beyond, coordination spheres.

Reverse Monte Carlo (RMC) simulation is a commonly used method to obtain three-dimensional atomic structures from diffraction data of disordered materials [198, 199]. The basic idea [200] is to minimize the mismatch between the experimentally determined X-ray (XRD) and/or neutron (ND) diffraction total structure factor $S(q)$ and/or the total radial distribution function $G(r)$ of an n -species system and a test structure which is iteratively optimized by a Monte Carlo procedure. $S(q)$ is typically expressed as:

$$S(q) = \sum_{\alpha=1}^n \sum_{\beta=\alpha}^n \gamma_{\alpha\beta} (S_{\alpha\beta}(q) - 1) \quad (6.1)$$

and $G(r)$ as:

$$G(r) = \sum_{\alpha=1}^n \sum_{\beta=\alpha}^n \gamma_{\alpha\beta} (g_{\alpha\beta}(r) - 1) \quad (6.2)$$

In eqs. 6.1 and 6.2 above, $\gamma_{\alpha\beta}$ is a weighting factor for a pair of species α and β that describes how strongly the partial structure factor $S_{\alpha\beta}(q)$ or the partial pair distribution function $g_{\alpha\beta}(r)$ affects the total structure factor. The weighting factors $\gamma_{\alpha\beta}$ are given by:

$$\gamma_{\alpha\beta} = \frac{c_{\alpha}c_{\beta}f_{\alpha}f_{\beta}}{(\sum_{\alpha} c_{\alpha}f_{\alpha})^2} \quad (6.3)$$

where the c_{α} are the concentrations of atoms of type α , and f_{α} are the atomic form factors in the case of XRD ³ and the bound coherent scattering lengths in ND.

³It is important to note, that in case of XRD the form factors depend in general on q , i.e $f_{\alpha} = f_{\alpha}(q)$.

But usually this dependency is neglected in the case of high energies and one could consider in good approximation $f_{\alpha} \propto Z_{\alpha}$ [201] (Z_{α} is the atomic number)

The first XRD experiments with subsequent RMC modeling on alkali borophosphate glasses were reported in a recent paper by Le Roux *et al.* [128] for the system $0.35\text{Na}_2\text{O}-0.65 [x\text{B}_2\text{O}_3-(1-x)\text{P}_2\text{O}_5]$. Starting from a configuration of pure sodium borate or sodium phosphate crystalline phases with iterative substitution of P_2O_5 (for B_2O_3 on the borate rich side) and B_2O_3 (for P_2O_5 on the phosphate rich side) with subsequent adjustments to the correct stoichiometry, the authors of this article generated a glassy configuration and achieved a structure whose calculated $S(q)$ and $G(r)$ functions agreed well with the experimental values and further fulfilled the minimum distance constraints given in Table 6.1. In agreement with previous magic angle spinning nuclear magnetic resonance (MAS-NMR) data collected on a related system, $0.40\text{Na}_2\text{O}$ instead of $0.35\text{Na}_2\text{O}$ [69], their model also reproduced the finding that for small B_2O_3 concentrations, B is predominantly in four-fold coordination with oxygen until the fraction of such tetrahedral borons saturates at approximately 43% of all network forming units, a value that can be rationalized by theoretical modeling [195]⁴.

However, the RMC modeling in [128] is not free of criticism. It is a well-known fact that the $S(q)$ and $G(r)$ functions do not have a unique relationship to the structure of the material giving rise to these functions [202]. Structures generated by RMC modeling tend to be among the most disordered ones, yet which are still compatible with the experimental $S(q)$ or $G(r)$ functions and the given constraints [202]. For these reasons, one should inform the RMC modeling with as much as possible further experimental and/or chemical information about the system. In the present case, the MAS-NMR investigations [69] and related theoretical modeling [195] call for a more detailed consideration of coordinations and the charge neutrality between the positively charged mobile cations and the negatively charged borate and phosphate oxyanions.

Both of these considerations were not taken into account in the work of Le Roux *et al.* [128]. In particular, the concentrations of the various $\text{Q}^{(n)}$ -species in their RMC models strongly violate the requirement of charge neutrality. A $\text{Q}^{(n)}$ -species, $\text{Q} = \text{P}$ or B , is a network forming unit with n bridging oxygens (bOs), see figs. 4.1 and 4.3. A bO is shared by two Q-species and accordingly contributes a charge -1 to each of them, while a non-bridging oxygen (nbO) contributes a charge -2. With the oxidation numbers +3 and +5 for the boron and phosphorous atoms, respectively, the charges q can be expressed as $q_c = n - 3$ for the $\text{P}^{(n)}$ units ($n = 0$ to 4) and $q_c = -|n - 3|$ for the $\text{B}^{(n)}$ units ($n = 2$ to 4), cf. Figs. 4.1 and 4.3. The sum of all positive charges, Na^+ ions and $\text{P}^{(4)}$ units and negative charges, negatively charged $\text{Q}^{(n)}$ -species, has to be zero. This constraint is violated in the RMC models in [128]. For example, in the RMC structure generated for the pure sodium phosphate system, $0.35\text{Na}_2\text{O} + 0.65\text{P}_2\text{O}_5$, about 36% more negative than positive charges were present. In addition, the $\text{Q}^{(n)}$ concentrations deviated from those predicted by theoretical modeling in [195], which succeeded to reproduce MAS-NMR data [69] for a sodium borophosphate glass series with the slightly different composition $0.4\text{Na}_2\text{O}-0.6 [x\text{B}_2\text{O}_3-(1-x)\text{P}_2\text{O}_5]$. It

⁴see chapter 4

is noted that our more recent ^{31}P MAS-NMR measurements across all glasses for the glass series $0.35\text{Na}_2\text{O}-0.65[x\text{B}_2\text{O}_3-(1-x)\text{P}_2\text{O}_5]$ shows good agreement with this theory [203]. Moreover, $\text{B}^{(4)}$ units with 1, 2, 3, and even 4 nbOs were identified by Le Roux *et al.*, all of which have not been reported so far in all studies of alkali borate glasses. Furthermore, Le Roux *et al.* also reported the presence of large amounts of $\text{P}^{(4)}$ units in certain P_2O_5 rich glasses, $x \approx 0$, when no such groups are known to exist in any phosphate glass produced at normal pressures.

These problems were the reason for improving the RMC modeling. In this new RMC study of these glasses, we take into account the charge neutrality and the concentrations of $\text{Q}^{(n)}$ -species, and in particular address the following questions:

- i. Is it possible to generate RMC models that are charge neutral, contain $\text{B}^{(4)}$ units exclusively bonded to bOs, and are in good agreement with the XRD data?
- ii. Do these models give good agreement with the experimentally determined concentrations of the various $\text{Q}^{(n)}$ -species in these glasses? If not, is it possible to generate RMC models that are in good agreement with the measured $\text{Q}^{(n)}$ concentrations?
- iii. With access to this new modeling, are there new structural features that become available under these constraints? For example, can we learn more about the connectivity of the cation sites in these glasses?
- iv. With access to the new and refined models of the structures, can we gain additional insight into the nature and type of the cationic environments and the alkali ion conduction pathways?

To answer these questions, we have improved the overall quality of the RMC modeling by adding new constraints in a stepwise manner.

6.2. RMC modeling: Global constraints and simulation procedure

In order to identify the $\text{Q}^{(n)}$ -species in a given structural RMC configuration, we have to specify in which cases an oxygen atom is considered to be connected to a boron or phosphorous atom. To this end, oxygen coordination shells between a minimum and maximum distance around a B and P atom are defined. The minimum distances are the distances of closest approach of oxygen atoms to B and P atoms allowed in the RMC modeling. These correspond to the onset of the first peaks in $G(r)$ for the binary sodium borate ($x = 1$) and phosphate ($x = 0$) glasses and are given in Table 6.1. The maximum distance is chosen as 1.8 Å for both B and P and corresponds to the first minimum in $G(r)$ for the binary glasses. The mean P-O and B-O bond lengths refer to the maximum of the respective $G(r)$ functions within the coordination shells. The typical P-O bond distance in binary phosphate glasses is in the range of 1.5 to 1.6 Å [167]. For borate glasses, the value for a B-O bond distance

depends whether the B is threefold or fourfold coordinated by oxygen. In the former case, the typical bond lengths lie between 1.3 to 1.4 Å [150, 204, 205, 206], and in the latter they lie between 1.4 and 1.5 Å [204, 205, 206].

pair	P-P	P-B	P-O	P-Na	B-B	B-O	B-Na	O-O	O-Na	Na-Na
min. distance in Å	2.4	2.5	1.3	2.5	2.3	1.3	2.5	2.0	2.1	2.4

Table 6.1.: Distances of Closest Approach (Minimum Distances) Used in the RMC Modeling (Distances involving O are for both nbO and bO)

In our RMC modeling, we require that each phosphorous atom is coordinated to 4 oxygens, while a boron atom is coordinated to either 3 or 4 oxygens. An oxygen atom must be either one-fold coordinated, corresponding to an nbO, or two-fold coordinated, corresponding to a bO shared by two B, two P, or one B and one P. These are our "global" coordination constraints. In addition, the minimum distances shown in Table 6.1 were applied. Except in the case of the O-O minimal distance, these are the same cut-off distances used in [128]⁵.

The requirements of charge neutrality as well as the global coordination and minimum distance constraints, in connection with the information from $G(r)$ and $S(q)$, are not sufficient to provide structures where $B^{(4)}$ units are exclusively connected to bOs. To avoid the occurrence of such units, we further require all four-fold B atoms to be coordinated with only 4 bOs. To implement this further $B^{(4)}$ constraint in the RMC procedure, the oxygens are assigned to be either a bO or nbO. The number N_{nbO} of nbOs is given by (cf. figs. 4.1 and 4.3):

$$N_{nbO} = N_{P3} + 2N_{P2} + 3N_{P1} + 4N_{P0} + N_{B2} \quad (6.4)$$

Connecting this with the requirement of charge neutrality,

$$N_{P2} + 2N_{P1} + 3N_{P0} + N_{B4} + N_{B2} - N_{P4} - N_{Na} = 0 \quad (6.5)$$

leads, with $N_P = N_{P4} + N_{P3} + N_{P2} + N_{P1} + N_{P0}$, to

$$N_{nbO} = N_P + N_{Na} - N_{B4} \quad (6.6)$$

This means that N_{nbO} is fixed once the number N_{B4} of $B^{(4)}$ units is known. The complete dependence of the concentrations of all network forming units on the mixing-parameter x was successfully modeled recently in [195]⁶. Based upon these results, the number of $B^{(4)}$ can, to a good approximation, be written as:

$$N_{B4} = \min[N_B, 0.43(N_B + N_P)] \quad (6.7)$$

⁵In former studies of $Ag_xNa_{(1-x)}PO_3$ the O-O minimum distance had to be quite low, 2 Å [207], to improve the quality of the fit results. This fact was explained by the presence of additional water in the phosphate glass. In the present article, we can exclude the presence of water because in the IR spectra the typical signatures for OH groups near 3000 cm^{-1} are absent [196]

⁶see chapter 4

where N_B and N_P are the total number of B and P atoms. From the $Q^{(n)}$ -species distribution, it is moreover known that for $x < 1$ the three-fold coordinated boron atoms are exclusively connected to bOs as well. Accordingly, this constraint is also included in the modeling. For the RMC modeling at $x = 1$, the three-fold coordinated boron atoms are allowed to exhibit at most one nbO.

In RMC modeling, the starting point is often a crystalline structure or a quasi-random structure which satisfies the coordination constraints. Subsequently, the discrepancy between the measured and simulated total pair distribution function $G(r)$ and/or the total structure factor $S(q)$ is minimized by Monte-Carlo moves of the particles. In this work, a slightly different approach was chosen to avoid any dependency of the finally arrived at structure upon the starting atomic configurations. For Model A and Model B (see below), RMC simulations for each composition were performed by starting from a random configuration of atoms (ions) in a box with a 10 to 20 % lower particle density than that found experimentally. The optimized RMC structures were obtained by simultaneously adapting the density, coordinations, and charges to the required ones and by minimizing the cost function of the mismatch between experimental and simulated $G(r)$ and $S(q)$. The weights $\gamma_{\alpha\beta}$ needed for the determination of the simulated $G(r)$ and $S(q)$ were calculated from Eq. 6.3 and are listed in Table 6.2. The densities and total number of particles for the simulated structures of composition $0.35\text{Na}_2\text{O}-0.65[x\text{B}_2\text{O}_3-(1-x)\text{P}_2\text{O}_5]$ are given in Table 6.3.

The box size adaption was included because we are also interested in the nature and type of the second nearest neighbor coordinations, which could be heavily biased away from a fully random network structure or a fully crystalline structure. On the basis of MD simulations, it was shown [208] that such starting configurations can lead to artifacts in the intermediate- to long-range length scales of the atomic structures. After good agreement between desired and obtained coordination constraints among the many atom pair coordinations was gained, the box size was iteratively decreased until the experimental densities were reached. Good agreement is considered to be achieved if more than 95% of the corresponding central atoms have the desired coordination constraint⁷.

In the following, we will develop different RMC models by taking into account additional RMC constraints in a successive manner. In Model A, we do not add any further information than described above, meaning that the model involves the following constraints: (i) the minimum distances given in Table 6.1, (ii) the charge neutrality, (iii) the global requirements on the coordinations, and (iv) the $B^{(4)}$ constraints of all bOs and Eq. 6.7. The resulting RMC structures are then checked whether they can successfully reproduce the $Q^{(n)}$ -species distributions or not. Because this was not found to be the case, we include in Model B the further constraint that a phosphorous atom can have either one or two nbOs. This

⁷Because the optimization of the coordination is considered to be sufficient if at least 95% of the global coordination constraints are fulfilled, there exist in the final RMC structures a few boron not satisfying these constraints. These are taken out from the analysis of the $Q^{(n)}$ species distribution discussed below. To keep the right stoichiometry, a corresponding number of sodium atoms is excluded from the analysis

6. Investigation of the Structures of Sodium Borophosphate Glasses by Reverse Monte Carlo Modeling to Examine the Origins of the Mixed Glass Former Effect

x	0.0	0.2	0.4	0.6	0.8	1.0
P-P	0.121	0.092	0.063	0.035	0.011	-
P-B	-	0.015	0.028	0.035	0.030	-
P-bO	0.159	0.176	0.182	0.153	0.097	-
P-nbO	0.199	0.140	0.083	0.047	0.018	-
P-Na	0.096	0.091	0.083	0.068	0.043	-
B-B	-	0.001	0.003	0.007	0.019	0.040
B-bO	-	0.015	0.041	0.077	0.129	0.211
B-nbO	-	0.012	0.018	0.023	0.024	0.014
B-Na	-	0.008	0.018	0.034	0.058	0.094
bO-bO	0.052	0.084	0.132	0.170	0.215	0.281
bO-nbO	0.131	0.133	0.120	0.100	0.080	0.037
bO-Na	0.063	0.087	0.120	0.150	0.192	0.250
nbO-nbO	0.082	0.053	0.027	0.016	0.007	0.001
nbO-Na	0.079	0.069	0.054	0.046	0.036	0.016
Na-Na	0.019	0.023	0.027	0.034	0.043	0.056

Table 6.2.: Weights $\gamma_{\alpha\beta}$ (see Equation 6.3) Calculated for the Composition $0.35\text{Na}_2\text{O} + 0.65 [x\text{B}_2\text{O}_3 + (1-x)\text{P}_2\text{O}_5]$ (In the calculation, f_α from the NIST form factor table [209] were taken)

x	$\rho_N [\text{\AA}^{-3}]$	N
0.0	0.072	5816
0.2	0.077	5546
0.4	0.082	5276
0.6	0.083	5006
0.8	0.088	4736
1.0	0.092	4466

Table 6.3.: Number Densities, ρ_N , of the Finally Arrived at RMC structures and Total Number N of Atoms Used in the Simulation (Densities agree with the values determined from experiments [196])

model successfully accounts for the $Q^{(n)}$ -species distributions, but in the resulting RMC structures, there is a significant fraction of the sodium ions that have no oxygens in their local environment. This unphysical feature is resolved with Model C, where a minimum and a mean oxygen coordination number for the sodium ions is prescribed. In addition, we consider in Model C the implications of known correlation effects between $\text{B}^{(4)}$ units.

6.2.1. RMC Model A: No incorporation of further information on $Q^{(n)}$ -species concentrations

As shown in Figs. 6.1 and 6.2, Model A provides fits to $S(q)$ and $G(r)$ of similar quality as the original RMC-approach by Le Roux *et al.* [128], while providing for appropriate charge neutrality at the same time, see Table 6.4. In this Table, we have listed the charge balance value as defined by the total amount of negative charge carried by the $Q^{(n)}$ -species (absolute value) divided by the total charge of the sodium ions. This charge balance value is 1.01 ± 0.03 for all compositions. Hence, a positive answer to question (i) posed in the introduction is possible. As can be furthermore seen in Table 6.4, the charge neutrality is also obeyed for the refined Models B and C that are discussed further below.

However, the distribution of $Q^{(n)}$ -species is not successfully accounted for by Model A. As shown in Fig. 6.3, there are significant deviations to the calculated values from the theory in [195], which succeeded reproducing MAS-NMR data [69] for a borophosphate glass series with the slightly different composition $0.4Na_2O-0.6[xB_2O_3-(1-x)P_2O_5]$. In particular, the $P^{(2)}$ fraction is much too low and, as described above, there are significant fractions of $P^{(4)}$ groups in all of the simulated glasses, containing phosphorous that are not observed experimentally [203]. Hence, a negative answer has to be given to the first part of question (ii) posed in the introduction. This fact shows that the information content in $S(q)$ is not sufficient to predict such important feature as the $Q^{(n)}$ -species distribution, which is essential for the formation of the network structure.

6.2.2. RMC Model B: Phosphate groups limited to $P^{(2)}$ and $P^{(3)}$ groups

In order to account for the $Q^{(n)}$ -species distribution, we extend Model A by the additional constraint that the only charged phosphate units are $P^{(2)}$ units. Their number is $N_{P2} = N_{Na} - N_{B4}$ required by charge neutrality. According to the findings reported in [195], $P^{(0)}$, $P^{(1)}$, and $P^{(4)}$ units are absent for all glasses of the mixing-parameter x , where XRD data have been reported in [128]⁸. Hence, we can further set $N_{P3} = N_P - N_{P2}$. Figures 6.1 and 6.2 show that the $S(q)$ and $G(r)$ are again in excellent agreement with the experimental results. Moreover, the distribution of $Q^{(n)}$ -species is now in good agreement with the expected one, see Fig. 6.3. Hence, we can now give a positive answer also to question (ii) posed in the introduction.

The successful modeling of the $Q^{(n)}$ -species distribution gives us some confidence that the simulated network structure resembles reasonably well the true structure, at least at the shorter length scales. However, this does not necessarily also imply that the local environments around the mobile sodium ions are well described. Indeed, as shown in Fig. 6.4, the oxygen coordination numbers of sodium in a spherical shell with radius 3 \AA display unphysical features. For example, there occurs a significant amount of sodium ions that are

⁸Close to $x = 1$ (binary borate glass), the theory in [195] predicts a few $P^{(0)}$ and $P^{(1)}$ units to appear in a narrow x interval. Preliminary MAS-NMR results by some of us [203] indeed give a fraction ≈ 0.05 of $P^{(1)}$ at $x = 0.9$

not coordinated by oxygens and this amount becomes larger with increasing x . The mean coordination calculated from the histograms in Fig. 6.4 yield values of about 3, which are clearly too small. It is to this last problem that we now turn.

6.2.3. RMC Model C: Consideration of oxygen coordination around sodium ions

In order to solve the remaining problem of the proper oxygen coordination of the sodium ions, we include the following additional constraints:

- A sodium ion is coordinated by at least one oxygen atom.
- The average oxygen coordination number around sodium ions is set to 5.
- The average ratio of the numbers of nbOs to the number of bOs in the local coordination sphere is the same as in the whole system.

The second assumption is motivated by the fact that the mean oxygen about sodium coordination number for both sodium phosphate [210, 211] and borate [212, 213] glasses with comparable compositions was found to be close to 5. A coordination between 4 and 6 was also reported for crystalline sodium borate and sodium phosphate systems [214]. The last two constraints resemble the general idea of "local typicality", which was recently suggested by Cliffe *et al.* [199]. As shown in Figs. 6.1 and 6.2, excellent agreement with the experimental results of $S(q)$ and $G(r)$ can still be obtained when including these additional constraints. Also, the $Q^{(n)}$ -species distribution from Model C (not shown) is found to be almost not distinguishable from that of Model B. The merit of Model C is that the oxygen coordinations around the sodium ions now show a reasonable distribution (see fig. 6.5). The coordination numbers scatter within a standard deviation of about 2 around the mean coordination 5 for each x value. For $x = 1$, this is consistent with earlier RMC results of Swenson *et al.* [25] for sodium borate glasses. The insensitivity of the standard deviation with respect to x is a bit surprising, since, with replacement of borate by phosphate, nbOs are created and these, due to their higher coordination flexibility, could arrange more likely into coordinations corresponding to the preferred value 5.

The RMC structures of Model C are in accordance with the scattering data from the XRD measurements and the knowledge about the distribution of $Q^{(n)}$ -species, and they fulfill the commonly applied chemical constraints. We are thus able to address the question (iii) posed in the introduction and are now therefore able to more accurately and reliably investigate additional structural features of the finally optimized structures.

6. Investigation of the Structures of Sodium Borophosphate Glasses by Reverse Monte Carlo Modeling to Examine the Origins of the Mixed Glass Former Effect

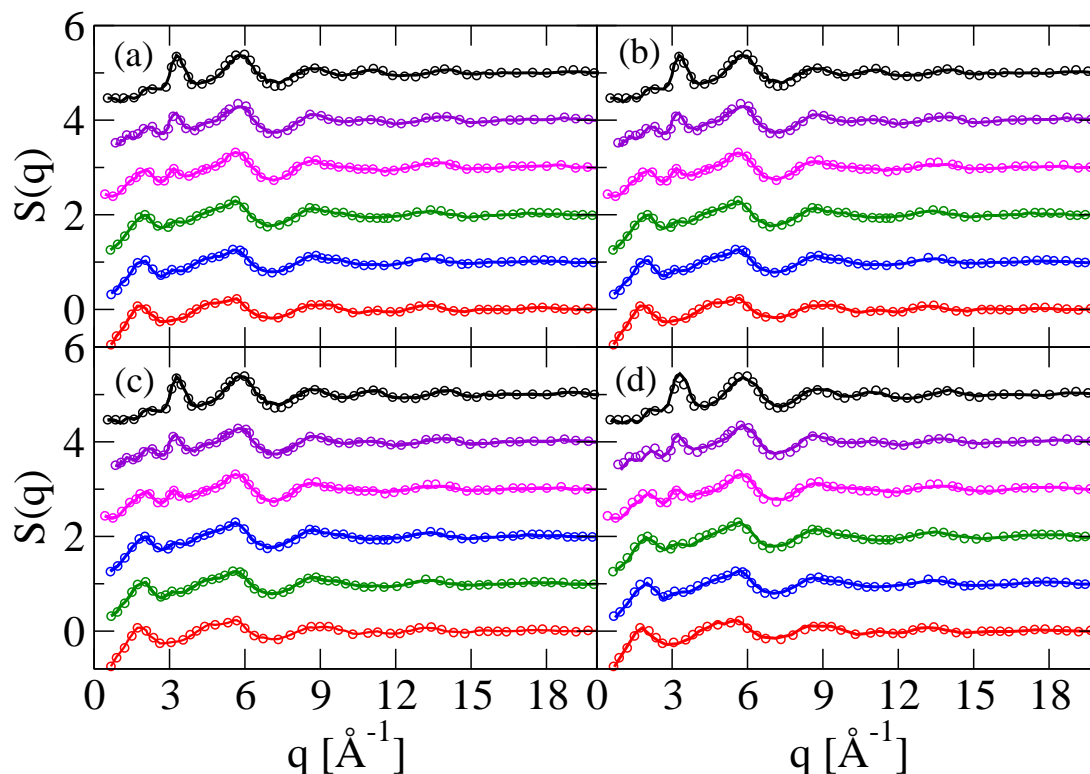


Figure 6.1.: High energy XRD structure factors $S(q)$ of $0.35\text{Na}_2\text{O}-0.65[x\text{B}_2\text{O}_3-(1-x)\text{P}_2\text{O}_5]$ glasses from the RMC Models A-C (a-c), and (d) redrawn from the RMC model developed in [128] in comparison with experimental data. The simulated structure factors are marked by solid lines and the experimental data by symbols (redrawn from [128]). The data have been offset by 1.0 to show the results for the different mixing parameters $x = 0, 0.2, 0.4, 0.6, 0.8,$ and 1 (from bottom to top).

x	model A	model B	model C
0.0	0.97	1.00	0.98
0.2	1.06	1.02	1.00
0.4	1.05	1.01	0.99
0.6	1.00	1.00	1.01
0.8	0.99	1.00	1.01
1.0	1.00	1.00	0.97

Table 6.4.: Charge Balance Value for the RMC models A-C (from left to right) As Defined by the total Charge of the $Q^{(n)}$ Species (Absolute Value Devided by the Total Charge of the Sodium Ions) (Value of 1 corresponds to perfect charge neutrality)

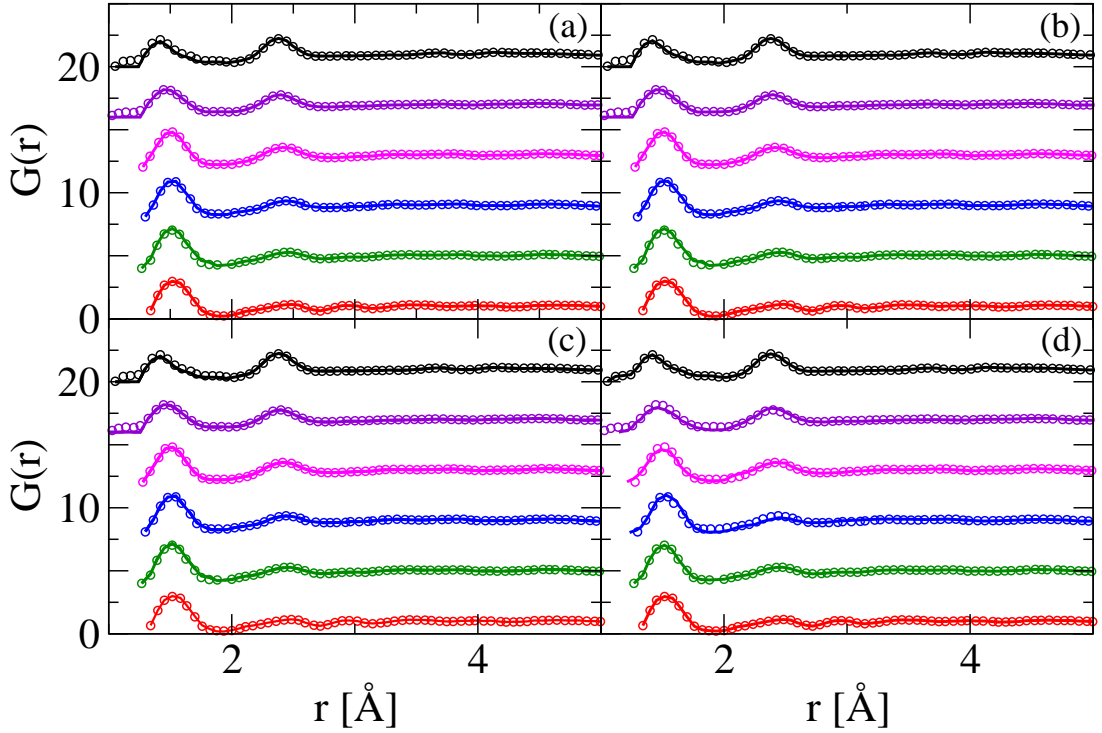


Figure 6.2.: Pair correlation functions $G(r)$ of $0.35\text{Na}_2\text{O}-0.65[x\text{B}_2\text{O}_3-(1-x)\text{P}_2\text{O}_5]$ glasses from the RMC Models A-C (a-c), and (d) redrawn from the RMC model developed in [128] in comparison with experimental data. The simulated pair correlations are marked by solid lines and the experimental data by symbols (redrawn from [128]). The data have been offset by 4.0 to show the results for the different mixing parameters $x=0, 0.2, 0.4, 0.6, 0.8,$ and 1 (from bottom to top).

6.3. The bridging oxygen connectivity and partial pair distribution functions

We first look at the connectivity between the different glass forming cations, i.e. the fractions of bOs bonded to two boron atoms, two phosphorous atoms, and to one boron and one phosphorous atom. The results from Model C, and used hereafter, are shown as open symbols in Fig. 6.6. It is instructive to compare these data with those which would be obtained when the network forming cations were connected randomly by the bOs. In this case, the probability for a bO to connect a $X^{(m)}$ with a $Y^{(n)}$ species ($X, Y = \text{B or P}$) is proportional to $\alpha mn N_{Xm} N_{Yn}$, where $\alpha = 1/2$ if both $X = Y$ and $m = n$, whereas $\alpha = 1$ otherwise. The bO fractions calculated from these probabilities are marked by the lines in Fig. 6.6. That the open symbols are close to these lines is, however, at variance with MAS-NMR findings for the linkages reported in [69, 87] for various stoichiometries of sodium borophosphate glasses. It is also not in agreement with basic considerations in the theoretical modeling

6. Investigation of the Structures of Sodium Borophosphate Glasses by Reverse Monte Carlo Modeling to Examine the Origins of the Mixed Glass Former Effect

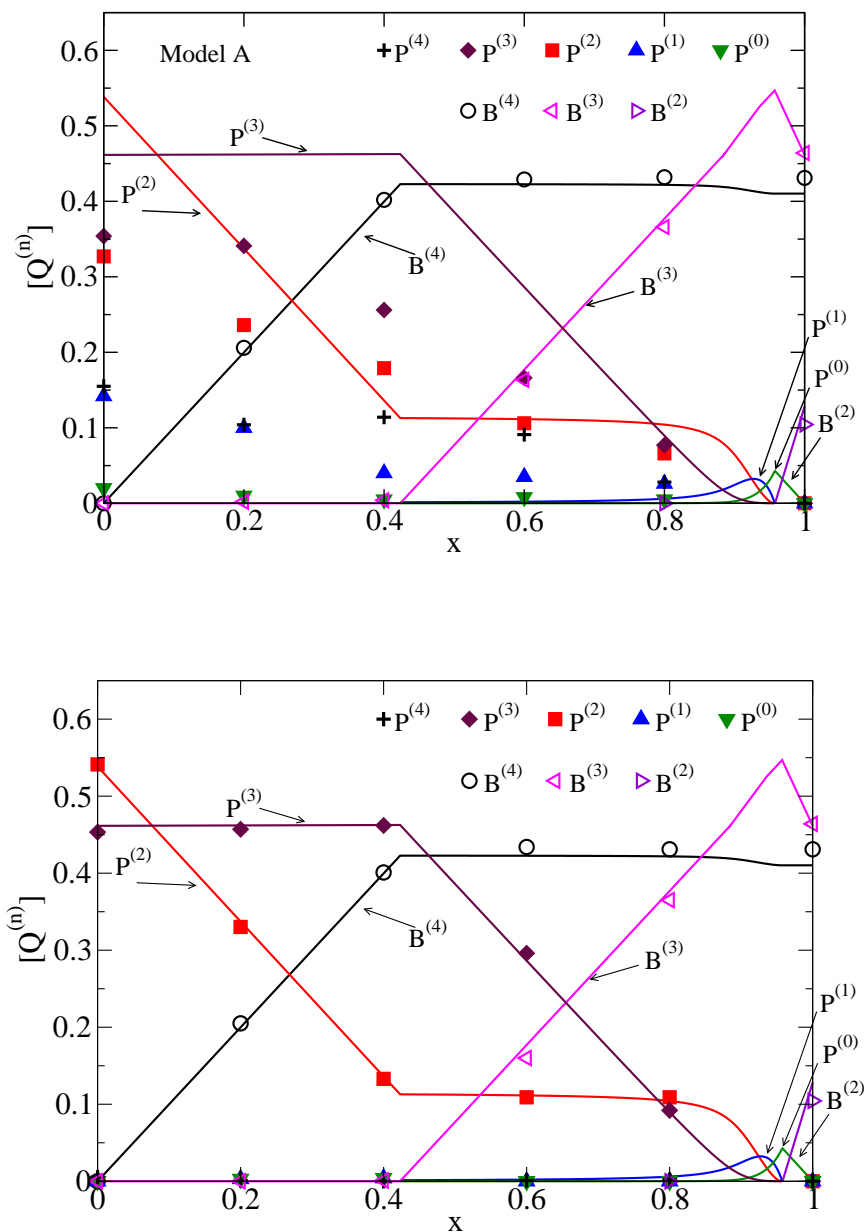


Figure 6.3.: The fraction of $Q^{(n)}$ -species with respect to the overall amount of network forming units for the Models A and B in comparison with calculated values from the theoretical model developed in [195]. Data for Model C can almost not be distinguished from those shown for Model B.

presented in [195]. In fact, to reason Eq. 6.7 it is important to take care that $B^{(4)}$ units do not like to become mutually linked. This tendency of avoidance of $B^{(4)}$ - $B^{(4)}$ linkages has been known for a sometime [148, 156]. The limiting case of complete avoidance of such linkages has been suggested by Beekenkamp [156] to describe results for $B^{(4)}$ fractions in alkali borate glasses obtained from pioneering MAS-NMR measurements [148]. In Ref. [195],

6. Investigation of the Structures of Sodium Borophosphate Glasses by Reverse Monte Carlo Modeling to Examine the Origins of the Mixed Glass Former Effect

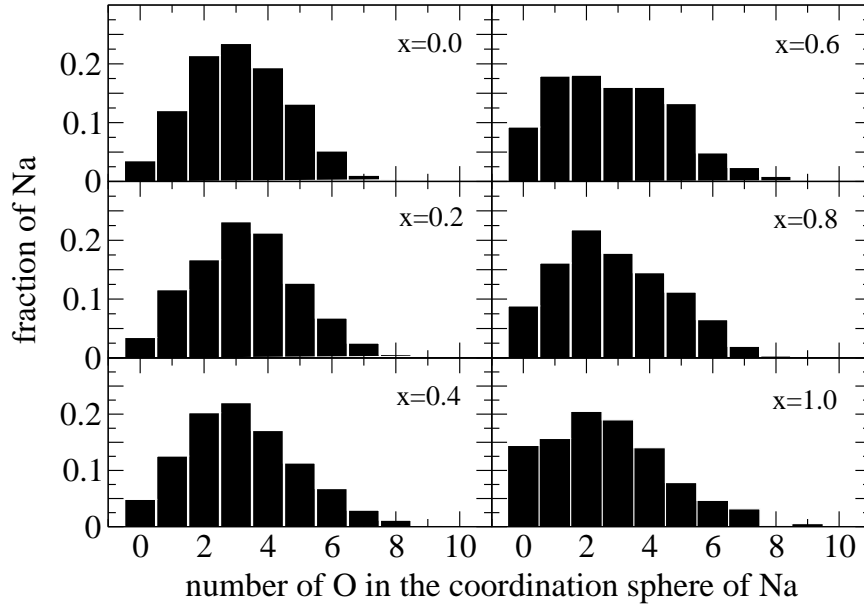


Figure 6.4.: Fraction of sodium ions with the given oxygen coordination numbers in the RMC structures generated from Model B.

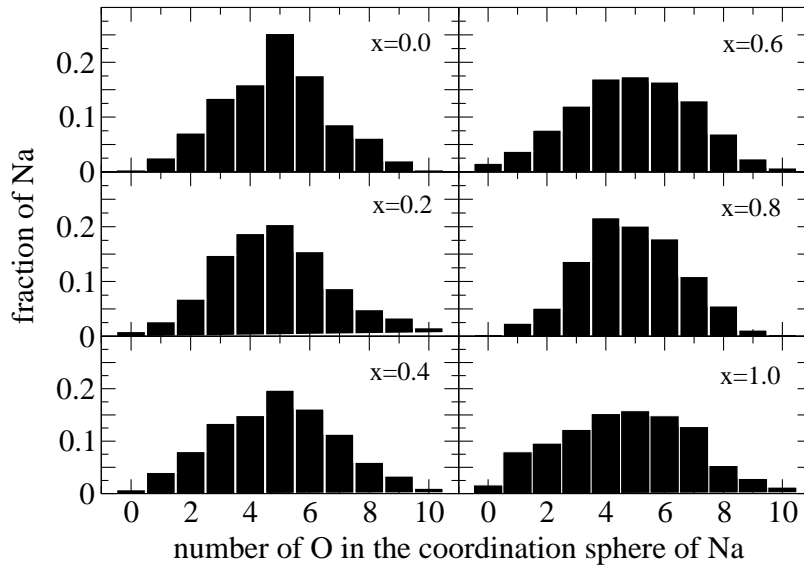


Figure 6.5.: Fraction of sodium ions with the given oxygen coordination numbers in the RMC structures generated from Model C.

it was shown that this principle can be applied also to the alkali borophosphate glasses. It provides, therefore, a good basis for an acceptable approximate account of the $Q^{(n)}$ species distribution, while refinements are necessary for a more accurate description.

In order to study what are the consequences of the forbidden $B^{(4)}-B^{(4)}$ linkages for our RMC structures, we have also implemented this constraint in the modeling. We find that

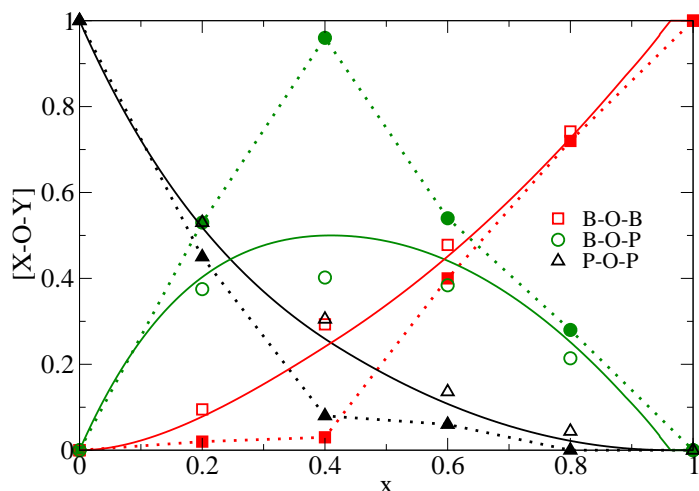


Figure 6.6.: Fraction of bOs connecting different network forming cations as a function of the mixing-parameter x for Model C. The full/open symbols correspond to the models with/without forbidden $B^{(4)}-B^{(4)}$ linkages. The solid lines mark the results in the case where the network forming cations would be randomly connected by the bOs. The dotted lines are guides to the eye connecting the data for forbidden $B^{(4)}-B^{(4)}$ linkages.

this extension has almost no effect on the results presented in Figs. 6.1 ($S(q)$), 6.2 ($G(r)$), 6.3 (fraction of $Q^{(n)}$ species for Model B), and 6.5 (oxygen coordinations of sodium ions), but it changes strongly the connectivities between the different glass forming cations (full symbols in Fig. 6.6), which are significantly distinct from a random linking.

Figure 6.7 shows the partial pair distribution functions for the pairs B-B, B-P and P-P for Model C without (solid lines) and with (dashed lines) forbidden $B^{(4)}-B^{(4)}$ linkages. The first peak in the B-B partial becomes more pronounced with increasing B content. Since in the glasses with high phosphate contents, all borate units are of $B^{(4)}$ type, the partials become almost structureless in the case of forbidden $B^{(4)}-B^{(4)}$ linkages. For the B-P partial, the forbidden $B^{(4)}-B^{(4)}$ linkages lead to a more pronounced first peak at intermediate x values. The most interesting feature in the partial distribution functions shown in Fig. 6.7 are the double peak structures in the P-P partials for $x = 0$. With increasing x , these are first transformed into a shoulder on the main peak and then vanish. The two length scales associated with the double peak can be interpreted as resulting from two types of P-P coordinations. In the first case, a P is linked to another P atom via a bO, and in the second case, a P is in the neighborhood of another P, but did not share a bO with it. The effect of forbidden $B^{(4)}-B^{(4)}$ linkages here shows up in a less pronounced second peak for larger x values.

Figure 6.8 shows the partial pair distribution functions for the pairs B-bO, B-nbO, P-bO and P-nbO for Model C without (solid lines) and with (dashed lines) forbidden $B^{(4)}-B^{(4)}$ linkages. The P-bO and P-nbO partials are similar and show a first peak between 1.5 and

6. Investigation of the Structures of Sodium Borophosphate Glasses by Reverse Monte Carlo Modeling to Examine the Origins of the Mixed Glass Former Effect

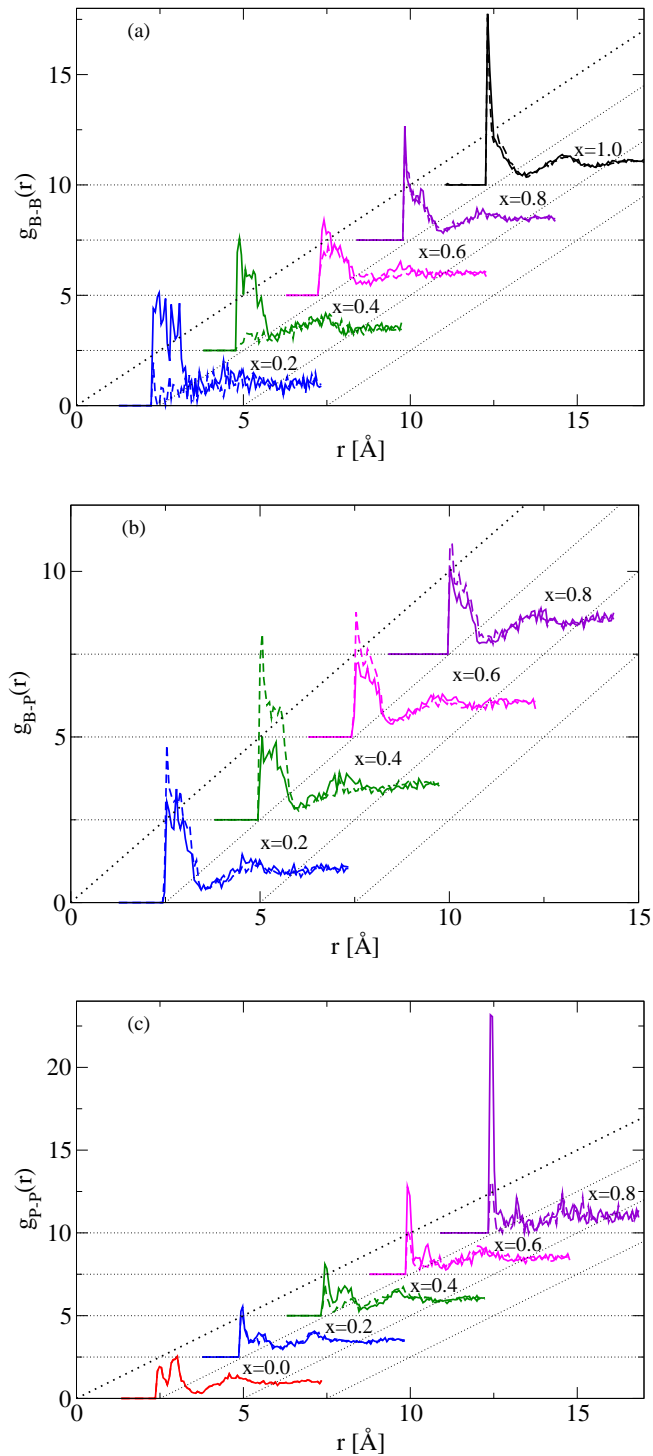


Figure 6.7.: Partial pair distribution functions for the pairs (a) B-B, (b) B-P, and (c) P-P. The dashed/solid lines correspond to the RMC models with/without forbidden $B^{(4)}-B^{(4)}$ linkages.

6. Investigation of the Structures of Sodium Borophosphate Glasses by Reverse Monte Carlo Modeling to Examine the Origins of the Mixed Glass Former Effect

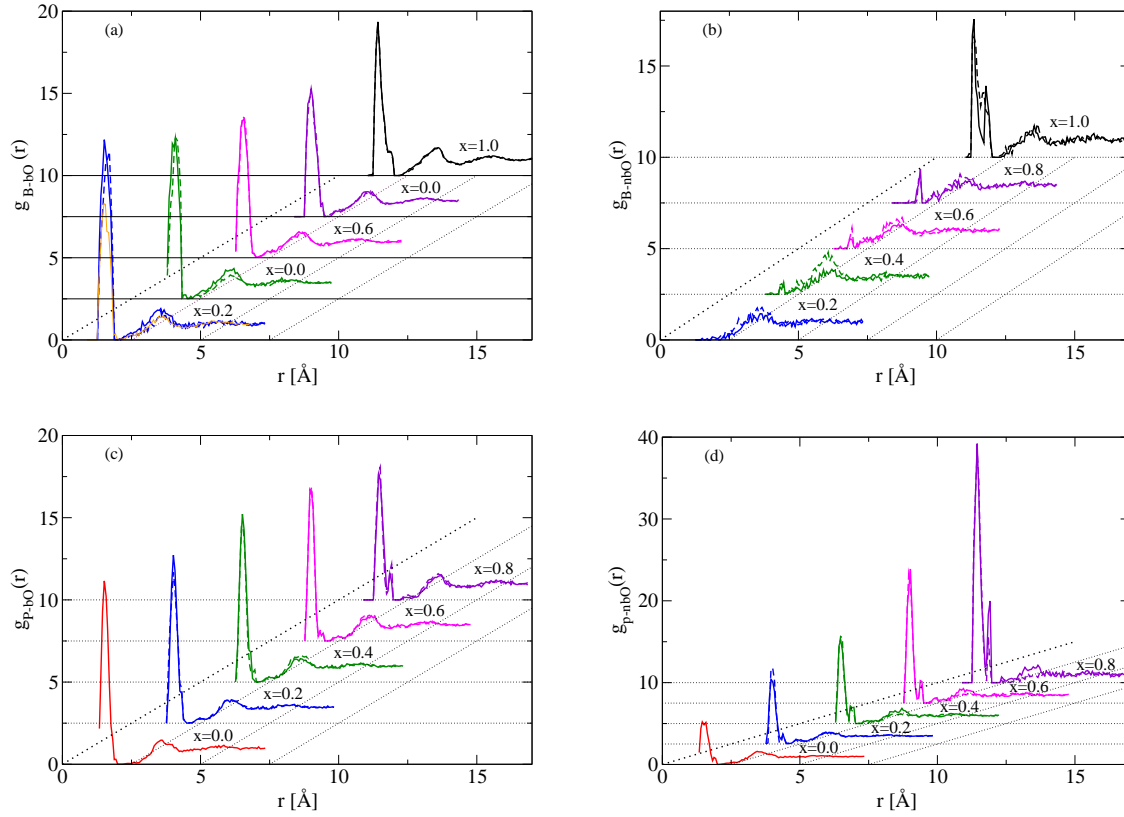


Figure 6.8.: Partial pair distribution functions for the pairs (a) B-bO, (b) B-nbO, (c) P-bO, and (d) P-nbO. The dashed/solid lines correspond to the RMC models with/without forbidden $B^{(4)}-B^{(4)}$ linkages.

1.6 Å. They are in overall agreement to the results of Le Roux *et al.* [128]. Contrary to the P-O partials, the B-O partials are significantly different for the pairs B-bO and B-nbO. There is always a pronounced first peak in the B-bO partials, while a pronounced peak in B-nbO partial can be identified for $x = 1$ only. The constraint of forbidden $B^{(4)}-B^{(4)}$ linkages has no significant influence on the P-O partials, but it causes a slight shift of the first peak position in the B-bO partial for small x .

6.4. Volume fraction of conduction pathways compared to the activation energy

With the proper Na-O coordinations being taken care of, Model C is at a level of description that allows us to address the question (iv) posed in the introduction, viz. that is to analyze the conducting cation pathways of the mobile sodium ions. The pathways for long-range conduction are considered here to consist of the percolating accessible volume for the sodium ions. The accessible volume V_{acc} is defined as the volume available to the cations for diffusive

motion consistent with the constraints of the RMC modeling. In order to determine V_{acc} from the RMC structures, all atoms of type X (X = B, P, O, and Na) are replaced by hard spheres with a given radius r_X . For sodium $r_{\text{Na}} = 1.1 \text{ \AA}$ is taken, which is close to the ionic radius of sodium. With the minimum distances $d_{X-\text{Na}}$ listed in Table 6.1, we have to require $r_X = d_{X-\text{Na}} - r_{\text{Na}}$, which fixes the hard sphere radii for X = B, P, and O⁹. The percolating accessible volume $V_{\text{acc,perc}}$ is that part of the accessible volume along which a sodium ions can move through the system (under the hard sphere constraints).

In order to determine V_{acc} and $V_{\text{acc,perc}}$ from the finally arrived at RMC structures, all sodium ions are first removed from the system. Then, the simulation box is divided into a grid of 400 x 400 x 400 cubic cells. By placing a test sodium ion successively into the centers of all of these cells, the minimum distance criteria are applied in order to decide whether the cells are accessible. The volume of all accessible cells is the accessible volume V_{acc} . With the known set of accessible cells, the percolating cluster of neighboring accessible cells is determined by using the Hoshen-Kopelman algorithm [215]. The volume of this percolating cluster is the percolating accessible volume $V_{\text{acc,perc}}$.

For binary alkali borate and phosphate glasses, a very interesting relation was proposed between the fraction $F = V_{\text{acc,perc}}/V$ of percolating accessible volume, V being the total volume of the system, and the activation energy E_a of the ionic conductivity. This relation states that E_a is a linear function of the cube root of F [216],

$$E_a/(k_B T) = a - bF^{1/3} \quad (6.8)$$

where a and b are constants and $k_B T$ is the thermal energy of the system. It should be noted that in [216], V_{acc} was determined by adding further constraints on bond valence sums to the hard sphere constraints. On the basis of MD simulations, it was shown [170], however, that V_{acc} calculated in this way gives results comparable to those where the constraints on the bond valence sums are not included. We, therefore, refrain here from introducing bond valence sums in the present analysis.

Figure 6.9 shows that there is no significant dependence of $F^{1/3}$ on x in the RMC structures of Model C. This holds true for both the modeling with and without the constraint of forbidden B⁽⁴⁾-B⁽⁴⁾ linkages. In contrast, the activation energy E_a measured by some of us [203] shown in the inset of Fig. 6.9 first decreases rapidly when phosphate is replaced by borate and then runs through a shallow minimum around $x = 0.4$. It increases slightly at the end of the compositional range $0.5 < x \leq 1$. From the data on binary alkali borate and phosphate glasses reported in [216], the values $a \approx 51$ and $b \approx -81$ can be estimated for sodium ion conduction in binary sodium borate and sodium phosphate glasses. From these values of a and b for the binary glasses, one would expect $F^{1/3}$ to vary between 0.18 and 0.32 for the E_a values shown in Fig. 6.9 at room temperature. The higher $F^{1/3}$ calculated by us from the data here for the ternary sodium borophosphate glasses, ≈ 0.38 to ≈ 0.46 ,

⁹It is important to note that these radii should not be misinterpreted as the real physical radii of the atoms but are rather chosen to be consistent with the RMC simulations

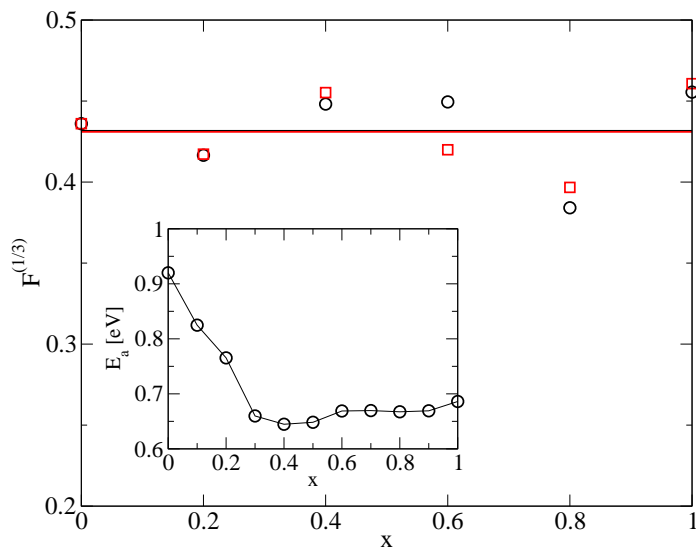


Figure 6.9.: Cube root $F^{1/3}$ of the fraction of the percolating accessible volume for the sodium ions as a function of the mixing-parameter x . Squares/circles refer to the results calculated from the RMC Model C without/with forbidden $B^{(4)}-B^{(4)}$ linkages. The line marks the average value around which the $F^{1/3}$ values scatter. The inset shows the variation of the conductivity activation energy E_a for $0.35\text{Na}_2\text{O}-0.65[x\text{B}_2\text{O}_3-(1-x)\text{B}_2\text{O}_5]$ glasses [203] (the line is drawn as a guide to the eye).

could be caused by the fact that we have deliberately not included additional constraints with respect to bond valence sums. However, the scatter in the $F^{1/3}$ data in Fig. 6.9 is much smaller than the change 0.14 (0.32-0.18) of $F^{1/3}$ expected from the analysis of the binary glasses in [216]. Accordingly, one could conclude that the application of relation 6.8 to the RMC structures generated here may not be helpful in exploring the origin of the MGFE in alkali ion conducting borophosphate glasses. Incorporation of recent neutron scattering data on this same series of glasses is in progress and will be reported in a future report ¹⁰.

6.5. Summary and outlook

Revisited investigations of the structures of $0.35\text{Na}_2\text{O}-0.65[x\text{B}_2\text{O}_3-(1-x)\text{P}_2\text{O}_5]$ glasses on the basis of RMC models have been carried out. The RMC models were generated by a further consideration of the XRD data reported in [128] using standard chemical constraints of bond distance and charge neutrality. It turned out that these were not sufficient to give satisfactory agreement with $Q^{(n)}$ species distributions as predicted by theoretical modeling

¹⁰see chapter 7

[195] and found by MAS-NMR measurements [69] for related glass compositions. By proper refinements of the modeling, RMC structures could be generated that are in agreement with both the XRD data and the $Q^{(n)}$ species distribution. Such refinements could also yield reasonable oxygen coordinations of the sodium ions. The fact known from MAS-NMR findings [69] that bOs are connecting network former cations in a correlated way was not automatically reproduced by the RMC models. It had to be enforced by taking into account the tendency of $B^{(4)}$ units not to become linked to each other. In this way, three-dimensional RMC structures were generated for $0.35Na_2O-0.65[xB_2O_3-(1-x)P_2O_5]$ glasses which reproduced well all currently available experimental information for this glass series.

Investigation of the percolating accessible volume for the sodium ions in the optimized RMC structures for different borate to phosphate mixing ratios points to the fact that there is no correlation between the percolating accessible volume and the conductivity activation energy across all mixing ratios of these glasses. Since it was shown by Müller *et al.* [170] that the additional consideration of neutron scattering data can significantly improve the quality of the RMC generated structures, it is worthwhile to include this further information in the future and to check whether the absence of significant correlations between the percolating accessible volume and the activation energy remains. On the other hand, the lack of these correlations in the present modeling suggests that other routes should be followed to explore the origin of the occurrence of the MGFE in alkali borophosphate glasses. Indeed, recent studies by some of us suggest that Coulomb trapping effects of the charges associated with various glass-forming units are playing the decisive role for understanding the MGFE in this system [195]¹¹. A further step for gaining deeper microscopic insight into the origin of the MGFE could be a combination of the RMC method with a Kinetic Monte Carlo approach. Such studies are in progress.

¹¹see chapters 4 and 5

7. Improvement of the RMC Models from Chapter 6 by Inclusion of Neutron Diffraction Data

Abstract

The results from chapter 6 were revisited under the additional inclusion of neutron diffraction data. The final structures from chapter 6 are in qualitative good agreement with the neutron diffraction data. Nevertheless, significant differences are present on all length scales in both $S(q)$ and $G(r)$. Therefore, a further refinement of the finally arrived at structures of chapter 6 is performed. This extended RMC analysis reveals the fact that disregarding the sodium-oxygen coordination constraints leads to a reasonable value of 4 for the average oxygen coordination number for sodium. In contrast, it was found that an average value of 5 is also compatible to the combination of neutron and X-ray diffraction data. The possible correlations of E_a with $F^{1/3}$ or V_{acc} were also investigated. It was confirmed that mechanisms corresponding to these correlations are from less relevance for the MGFE in sodium borophosphate glasses.

7.1. Introduction

In chapter 6 it was shown that high energy XRD-data entail only limited information about NFU concentrations, connectivities and alkali ion oxygen coordinations. Therefore, additional information must be added by further constraints. These constraints can be given by theoretical modeling (see chapters 4 and 5) or further experimental data (e.g. EXAFS or NMR data). A complementary procedure to increase significantly the quality of modeling is the introduction of additional diffraction data (e.g. neutron diffraction (ND) data) in the RMC optimization. This fact was proven by a recent study [208], where artificial diffraction data calculated from a MD model of $\text{Li}_2\text{O-SiO}_2$ glasses were used as input for the RMC procedure.

Therefore, the issue of the present chapter is the check and the improvement of the quality of the RMC modeling presented in the previous chapter¹ with respect to the ND-data for $0.35\text{Na}_2\text{O}-0.65[x\text{B}_2\text{O}_3-(1-x)\text{P}_2\text{O}_5]$ glasses. This further set of diffraction data was recently provided by the groups of S. W. Martin at Iowa State University (USA) and M. Karlsson at Chalmers University (Sweden) [129].

Figure 7.1 shows the experimental X-ray and ND-data in comparison with the final structures of Model C (with and without the additional constraint of reduced $\text{B}^{(4)}\text{-B}^{(4)}$ connections) from chapter 6². While the optimized configurations match excellently to the experimental XRD-data, one finds significant deviations in the ND-data on all length scales. The deviations of the nearest neighbor peak in $G(r)$ are weak for small x values, but they become more pronounced with increasing x . In addition, one finds that features in the second nearest neighbor shell around 2 \AA are not correctly described. Another important discrepancy between Model C and the ND-data is found in $S(q)$ for small q . This finding is critical, because the first sharp diffraction peak is assumed to be connected in some way with the long range transport properties [217, 218].

The main source of the discrepancies shown in fig. 7.1 is probably the lack of uniqueness in the RMC procedure [198, 202, 208]. Moreover, ND shows a different sensitivity to chemical elements than XRD, which results in different weighting factors for the pairs (e.g. O-O, P-P). This fact implies that structural deviations between the model and the real structure are less important in the fitted $G(r)$ and $S(q)$ if the weight of a corresponding pair is low. An additional probe (e.g. ND) with an increased weight for the same pair leads to an increased influence of this feature in the total $G(r)$ and $S(q)$. The comparison of the values given in the tables 6.2 and 7.1 reveals that for low x the most prominent change is found in the weighting factors for P-P and the O-O related pairs. These pairs are higher by a factor of approximately two than the corresponding XRD weights in the case of $x = 0.0$. The typical first coordination shell of these pairs lies between the minimum distances of closest

¹model C with and without the reduction of bOs bonded to 2 $\text{B}^{(4)}$

²weights are given in sec. 7.2

7. Improvement of the RMC Models from Chapter 6 by Inclusion of Neutron Diffraction Data

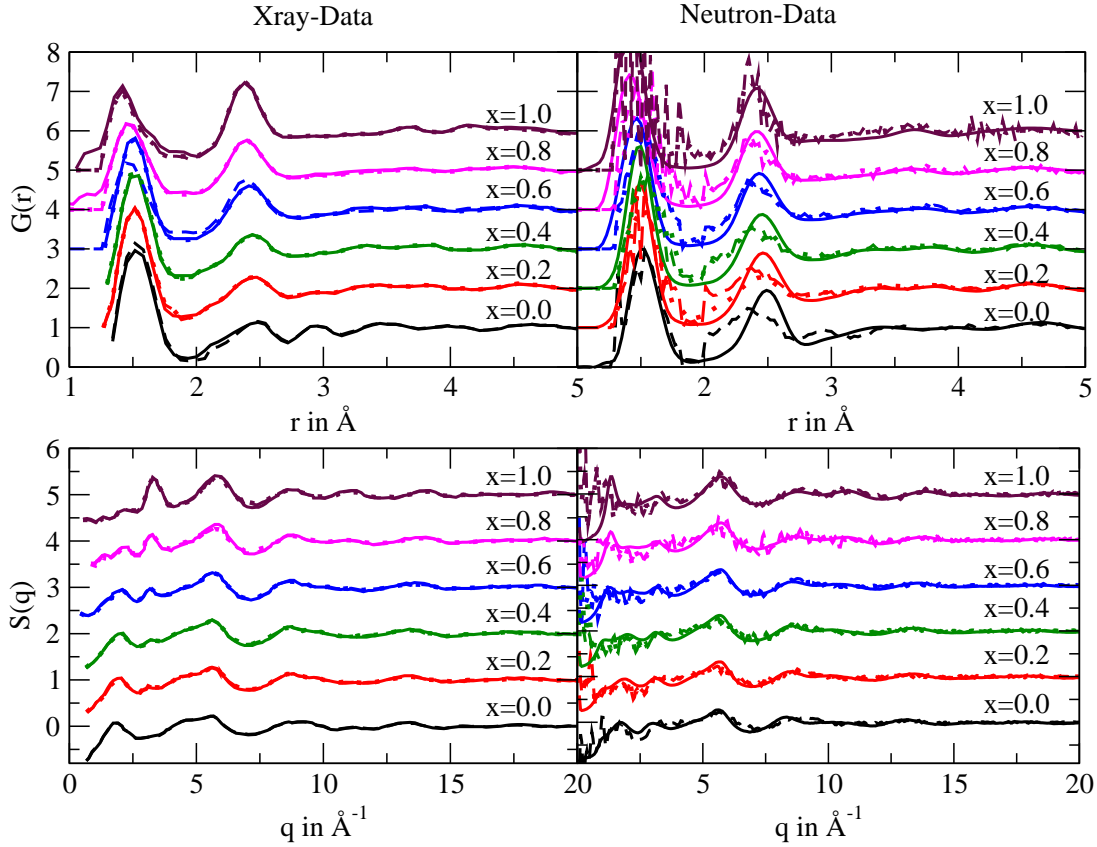


Figure 7.1.: Comparison of $S(q)$ and $G(r)$ calculated from model C of chapter 6 with the experimental X-ray (left) and neutron (right) diffraction data

approach and $\lesssim 3.0 \text{ \AA}$. This distance corresponds well with the distance where the most prominent deviations in fig. 7.1 are located. For large x , all boron related pairs contribute significantly more to the total pair correlation functions, too. Therefore, the deviations in the first peak in $G(r)$ for larger x is also explained by this argument.

However, it is also possible that structural peculiarities resulting from the sample preparation and handling processes influence the discrepancies between model C and the experimental ND data. These structural differences could be caused for instance by the production process of the glasses because different batches have to be produced, since ^{11}B enriched glasses were used in ND but not in the XRD experiments [128, 129, 219]. Since the IR/Raman spectra of both batches are quite similar [219], one can assume that this effect is of less importance. Nevertheless, it is possible that different storage and shipping protocols are an additional source for structural differences, since it is known that the network of sodium borophosphates can degrade due the inclusion of hydrogen in the glass structure [92, 220]. This effect will be enforced by the preparation protocol of the borophosphate glasses in the case of ND, since the samples were milled [129], whereas the XRD experi-

ments were performed on bulk samples [128, 219]. There is a lack of information about this topic. Therefore, it is not clear to what extent the glass structure investigated by ND experiments is the same as in the previous XRD study.

Summarizing all these facts, one has to address following questions:

- (i) Is it possible to generate structures by RMC that are compatible to both neutron and X-ray data, starting from the final structures of chapter 6? Is this agreement altered by the amount of bOs connecting two B⁽⁴⁾ units?
- (ii) In the case of a positive answer to question (i): How are the partial pair distribution functions affected?
- (iii) In the case of a positive answer to question (i): Does the combination of XRD and ND data entail sufficient information for physical reasonable Na-O coordinations?
- (iv) How are the properties of the accessible volumes affected by the Na-O coordination constraint?

To address these questions, the methodology of sec. 7.2 is applied and the results of this reinvestigation are discussed in sec. 7.3.

x	0.0	0.2	0.4	0.6	0.8	1.0
P-P	0.049	0.034	0.021	0.010	0.003	-
P-B	-	0.022	0.036	0.039	0.028	-
P-bO	0.137	0.137	0.127	0.093	0.051	-
P-nbO	0.171	0.109	0.057	0.029	0.009	-
P-Na	0.037	0.032	0.026	0.019	0.010	-
B-B	-	0.004	0.015	0.038	0.073	0.124
B-bO	-	0.044	0.109	0.182	0.264	0.360
B-nbO	-	0.035	0.050	0.056	0.049	0.023
B-Na	-	0.010	0.023	0.037	0.053	0.073
bO-bO	0.095	0.139	0.195	0.219	0.239	0.261
bO-nbO	0.238	0.221	0.176	0.134	0.089	0.034
bO-Na	0.052	0.065	0.080	0.089	0.097	0.106
nbO-nbO	0.149	0.088	0.040	0.021	0.008	0.001
nbO-Na	0.065	0.052	0.036	0.027	0.018	0.007
Na-Na	0.007	0.008	0.008	0.009	0.010	0.011

Table 7.1.: Weighting factors used for the inclusion of neutron diffraction data in the RMC modeling applied to the original version of model C (see chapter 6)

7.2. Methodology

The final structures of model C from the previous chapter were taken as the starting configurations³. During the whole RMC procedure all densities were kept at constant values and the cutoff distances from chapter 6 were used. In addition to the XRD data from [128], the ND data provided by the groups from Iowa State University (USA) and Chalmers University (Sweden) [129] were introduced. The corresponding weights for the ND data were calculated by eq. 6.3 under the consideration that all B atoms are ¹¹B (the values for the model without avoided bOs connected to two B⁽⁴⁾ are shown in table. 7.1) with the bound coherent scattering length taken from [221].

The RMC optimization was performed in two steps. In the first one the constraints that correspond to the adjustment of the Na-O coordination were neglected. If the reasonable agreements in the $S(q)$ and $G(r)$ were achieved, the coordination constraints for Na-O partials were reintroduced in a subsequent step.

It was defined in chapter 6 that the structure was assumed to be reasonable if 95% of all global coordination constraints were achieved⁴. Since the introduction of the ND data leads to structural frustrations, this condition must be lowered in a few cases to values $\gtrsim 93\%$.

7.3. Results and discussion

Figures 7.2 and 7.3 show the final structures of the further RMC optimization including both, XRD and ND data. For all x an excellent agreement is achieved to all diffraction data (see fig. 7.4). In the $G(r)$ minor discrepancies are present at ≈ 2 Å. Most importantly, almost all features in $G(r)$ and $S(q)$ are reproduced very well. Therefore, one could approve question (i). This result is independent of the amount of B⁽⁴⁾-B⁽⁴⁾ connections. Hence, this fact supports clearly the assumption that even the combination of XRD with ND data entails only limited information about the connectivity of glass former units. The partial pair correlation functions related to the pairs B-B, P-B and P-P are shown in fig. 7.5. Only minor changes are introduced by the additional information. The most prominent changes are in the P-P partial for small x . In this concentration regime the peaks are located at ≈ 3 Å and the maximum value of the first peak is lowered.

The peak in the B-B partial in the high x regime is shifted to higher distances by a value of ≈ 0.2 Å. Both changes, in the P-P and B-B partial, can be related to the increased weighting factors in the ND data.

Similar results were found for the partial pair distribution functions related to B-O and P-O distances. The most prominent change is found for small x values for the B-bO partial, where the first peak becomes more pronounced. This finding corresponds to an increased quality of measurement of the B-bO bonds. The integration of the first peak between cutoff

³with and without avoiding bOs connecting two B⁽⁴⁾

⁴Except the additional constraint of avoiding bOs which are bonded to two B⁽⁴⁾, this constraint was fulfilled typically by a value of 88% of all bOs

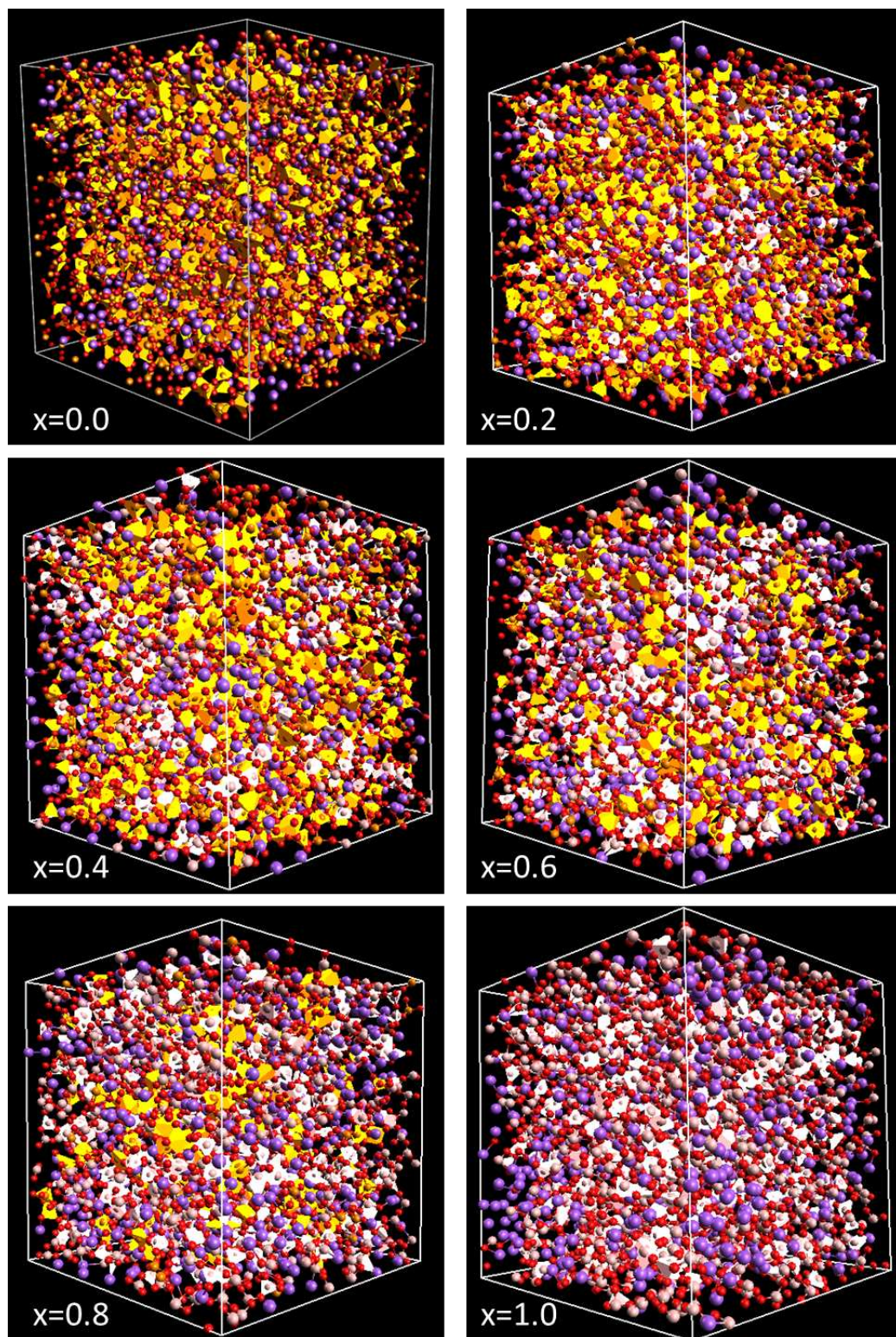


Figure 7.2.: Final structures of the RMC procedure without the additional constraint of avoiding bOs connecting two $B^{(4)}$ (red marks oxygen, yellow phosphorous, grey boron, and violet sodium atoms)

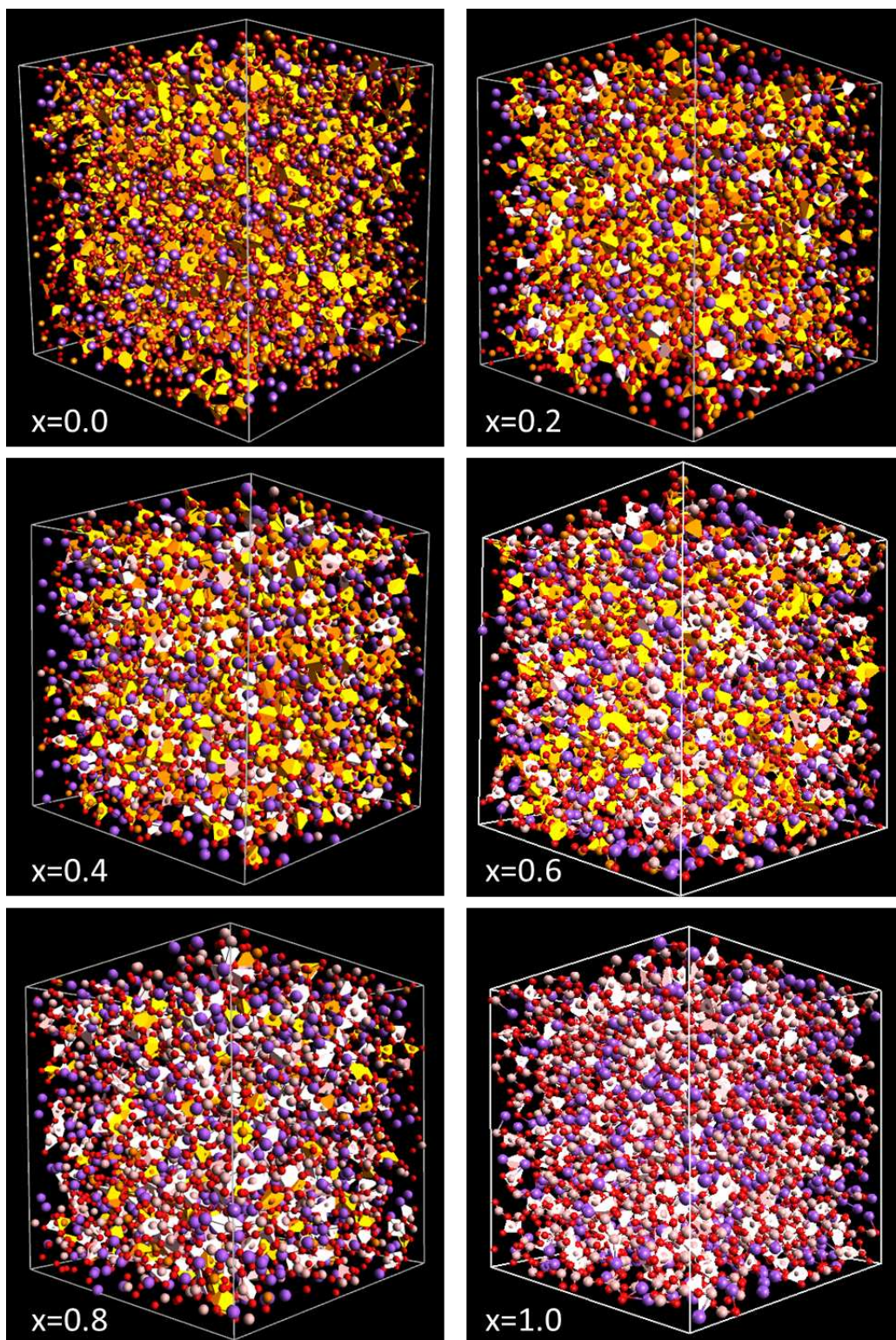


Figure 7.3.: Final structures of the RMC procedure with the additional constraint of avoiding bOs connecting two $B^{(4)}$ (red marks oxygen, yellow phosphorous, grey boron, and violet sodium atoms)

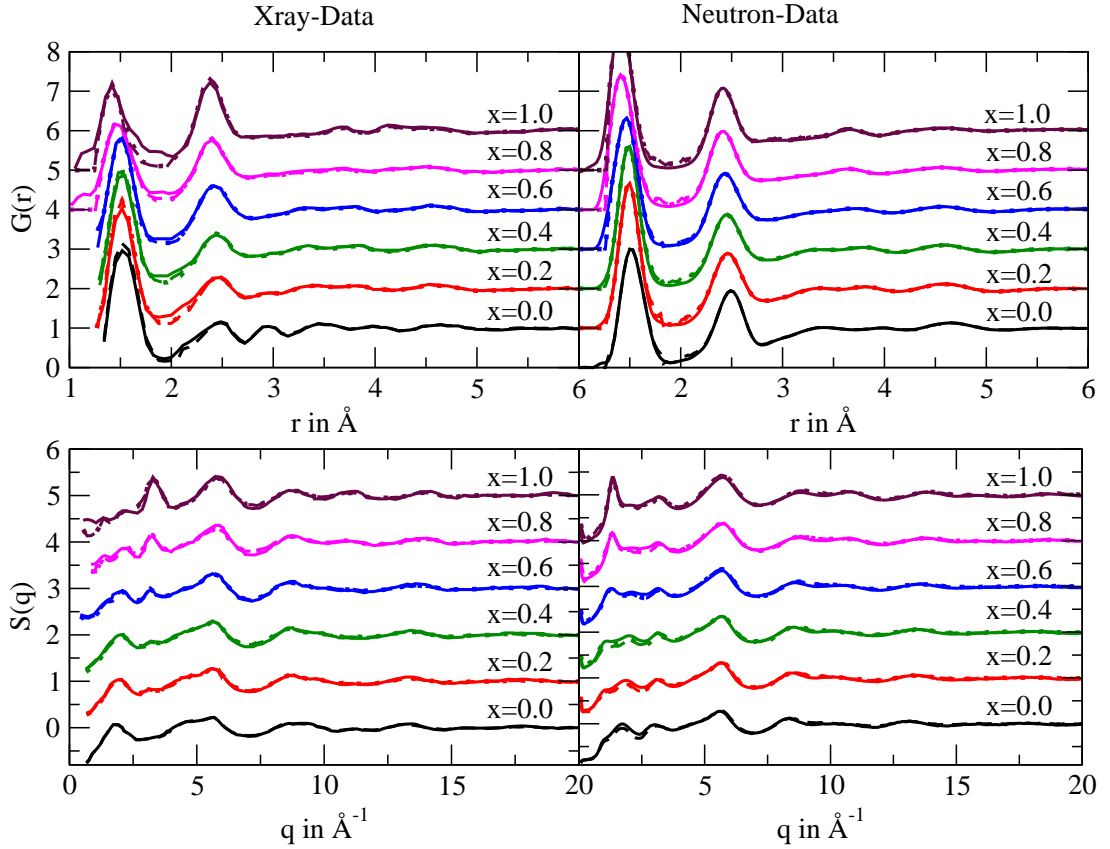


Figure 7.4.: Comparison of $S(q)$ and $G(r)$ after further RMC refinement (dashed and dotted lines) starting from model C with experimental (solid lines) X-ray (left) and neutron (right) diffraction data. The dashed lines correspond to the model with allowed and the dotted lines with avoided bOs connecting $B^{(4)}$ units

radius (see table 6.1) and 1.8 \AA for $x = 0.2$ and $x = 0.4$ leads to a mean bond length of $\approx 1.5 \text{ \AA}$ which corresponds well with the reported values of 1.47 \AA for the $B^{(4)}$ -bO bond length [150, 204, 205, 206]. For $x \geq 0.6$ some broadening of this peak is observed and can be related to the formation of three fold coordinated borate units with a B-bO distance of 1.37 \AA [150, 204, 205, 206].

Coming now to the partial pair distribution functions of the pairs P-bO and P-nbO. It is obvious that due to the additional consideration of ND data, the P-nbO first neighbor peak becomes more pronounced for $x \leq 0.4$. This finding allows to calculate the average bond length for both P-bO and P-nbO bonds. It was calculated for P-nbO bond the average bond length of $1.52 \pm 0.04 \text{ \AA}$ and for P-bO the bond length with an average value of $1.56 \pm 0.02 \text{ \AA}$. This finding reveals no compositional trend and agrees well with the reported values [167] for binary sodium phosphate glasses.

Next the effect of the Na-O coordination constraints is considered. These constraints (see

7. Improvement of the RMC Models from Chapter 6 by Inclusion of Neutron Diffraction Data

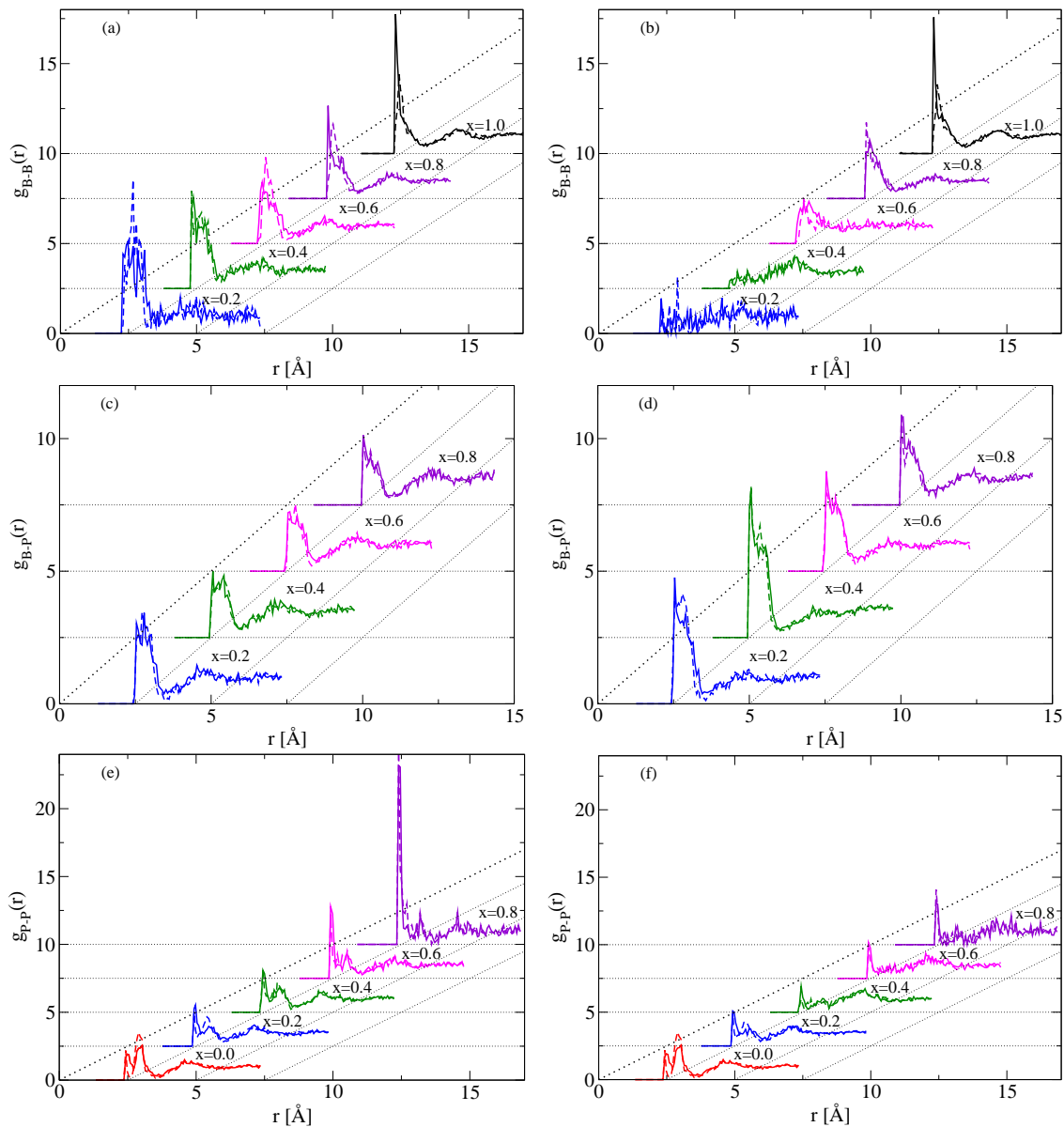


Figure 7.5.: Partial pair correlation functions for the partials B-B (a,b), B-P (c,d) and P-P (e,f), for the modeling with allowed (a,c,e) and with avoided (b,d,f) bOs connecting two $B^{(4)}$. The solid lines correspond to the results from chapter 6 and the dashed lines to the refined RMC models with X-ray and neutron diffraction data.

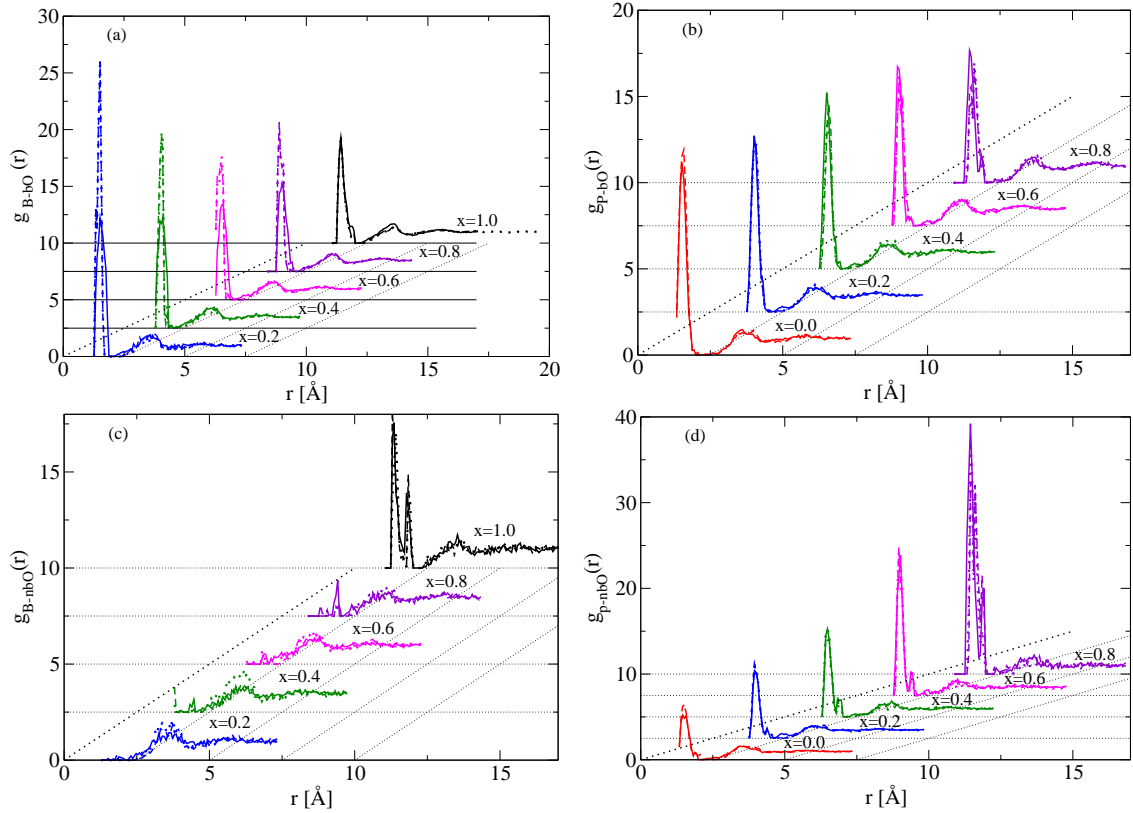


Figure 7.6.: The partial pair correlation functions for the partials B-bO (a), B-nbO (c), P-bO (b) and P-nbO (d). The solid lines correspond to the results from chapter 6 and the dashed and dotted lines to the refined RMC models with X-ray and neutron diffraction data with allowed and with avoided bOs connecting two $B^{(4)}$

chapter 6) are less justified and literature values of the corresponding parameters are not consistent. One may ask if the additional consideration of ND data in the RMC modeling allows one to disregard these constraints. Figure 7.7 shows the histograms of the oxygen coordination numbers for sodium atoms after RMC optimization when the Na-O constraints are neglected. The typical mean value for the oxygen coordination number is found to be ≈ 4 . This value shows again no dependence on x and is also unaffected when the amount of bOs connecting two $B^{(4)}$ is reduced. It is important to note that these values are reasonably close to the values reported in the literature of pure sodium phosphate [207, 210, 211] and borate glasses [25, 212, 213]. In addition, only a negligible fraction of sodium atoms is present with less than one oxygen atom in a coordination sphere of a radius of 3 Å. Therefore, one may conclude that the combination of ND and XRD data could be able to generate a more physical environment for the sodium atoms in RMC modeling.

As a counter-check, Na-O constraints are reintroduced to address the question to what extent the properties of the Na-O environments affect the agreement in $G(r)$ and $S(q)$. As can be seen in fig. 7.8, the increase of the mean coordination number to values ≈ 5 is also compatible to the ND data. It is not possible to decide at this point which mean coordination number would be the more appropriate, because of the lack of reference data for the mixed systems and the quite large fluctuations for the pure systems in the literature. Therefore, the discussions regarding the free volume fraction will be performed with all ND and XRD based RMC models.

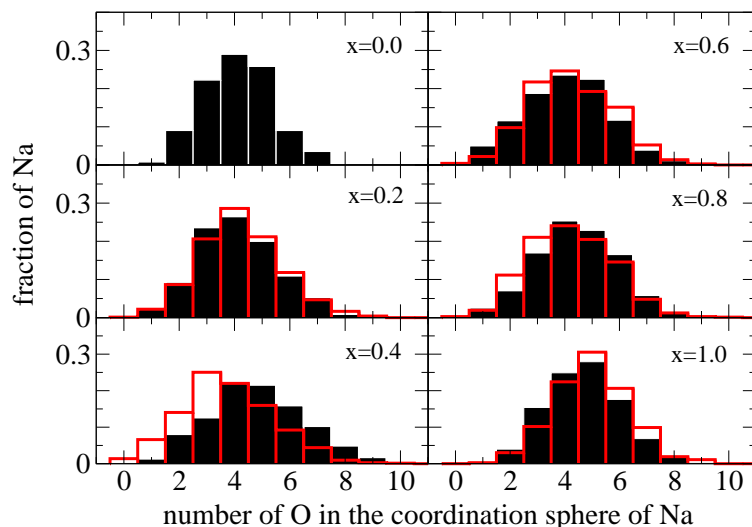


Figure 7.7.: Histograms for the number of oxygen coordinating sodium atoms in a coordination sphere with a radius of 3 \AA (black original version of model C, red optimization with a reduced fraction of bO bridging two $B^{(4)}$). Additional Na-O coordination constraints have been disregarded (for details, see text)

Finally, the behavior of $F^{(1/3)}$ as a function of x is revisited. As one can see in fig. 7.3, $F^{(1/3)}$ has lower values for $x \rightarrow 0$ and $x \rightarrow 1$ as in the intermediate mixing regime and one thus finds a clear maximum for $x \approx 0.4$. This trend was found for every set of constraints. Nevertheless, the overall behavior of $F^{(1/3)}$ does not resemble the behavior of E_a . However, it is not possible to rule out the existence of a mechanism that corresponds to a relation of E_a with $F^{(1/3)}$. Indeed, there is some weaker increase in the experimentally determined E_a with increasing borate content for $x > 0.4$. But there must be a more relevant effect which dominates the behavior of E_a as a function of x . It is important to note that for $x = 1.0$ no percolating pathway⁵ was found for the modeling without any constrain addressing both the proper Na-O coordination and the avoidance of $B^{(4)}$ - $B^{(4)}$ connections. Perhaps, this finding points to the fact that the quality of this model is lower than quality of the other models with high boron content.

⁵for atomic radii consistent to the RMC modelling

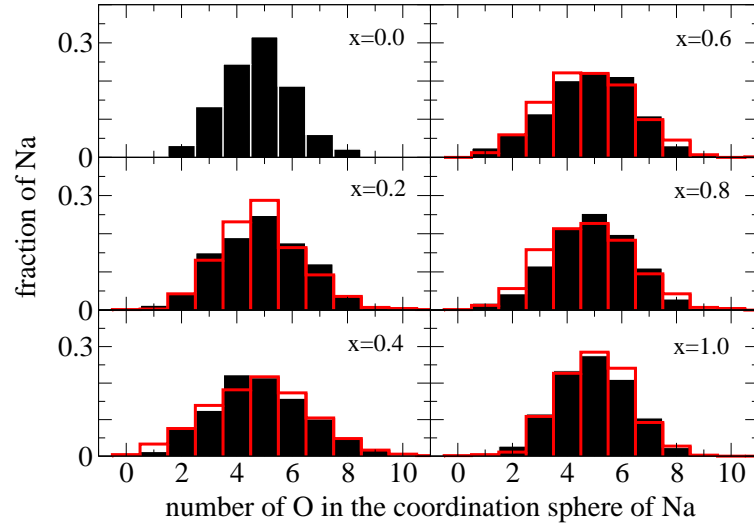


Figure 7.8.: Histograms for the number of oxygen coordinating sodium atoms in a coordination sphere with a radius of 3 Å (black original version of model C, red optimization with a reduced fraction of bO bridging two B⁽⁴⁾). Additional Na-O coordination constraints have been taken into account (for details, see text)

As an alternative to $F^{(1/3)}$, one can consider other structural properties that are related to the behavior of E_a . On the basis of the power law relation between the conductivity and the volume expansion in Halide Doped glasses, Swenson and Börjesson [30] suggest that the free access volume could be an important property that determines the transport of the cations. In addition, it is often assumed that the ionic conductivity in fast ion conducting glasses is higher than in the corresponding crystalline systems because the glass structure is more open and the density of vacancies is significantly increased [49, 50]. Therefore, it is straightforward to assume that the accessible volume V_{acc} per cation⁶ is somewhat correlated with the activation energy. This issue is addressed in fig. 7.3 (right side). It is clear that independent of the applied constraints, V_{acc} follows a unique compositional trend with a maximum at $x = 0.4$. This finding is a bit surprising since the number density is increasing almost linearly with x and the number of sodium cations is constant. Moreover, the overall behavior of V_{acc} does not follow the trend in the activation energy, because a comparison of E_a with V_{acc} would lead to the false conclusion that the activation energy for large x would be larger than for low x . Therefore, one has to conclude that mechanisms involving V_{acc} can have only a weak influence on E_a .

⁶i.e. the subset of all points accessible by point particles corresponding to the center of mass of the cations

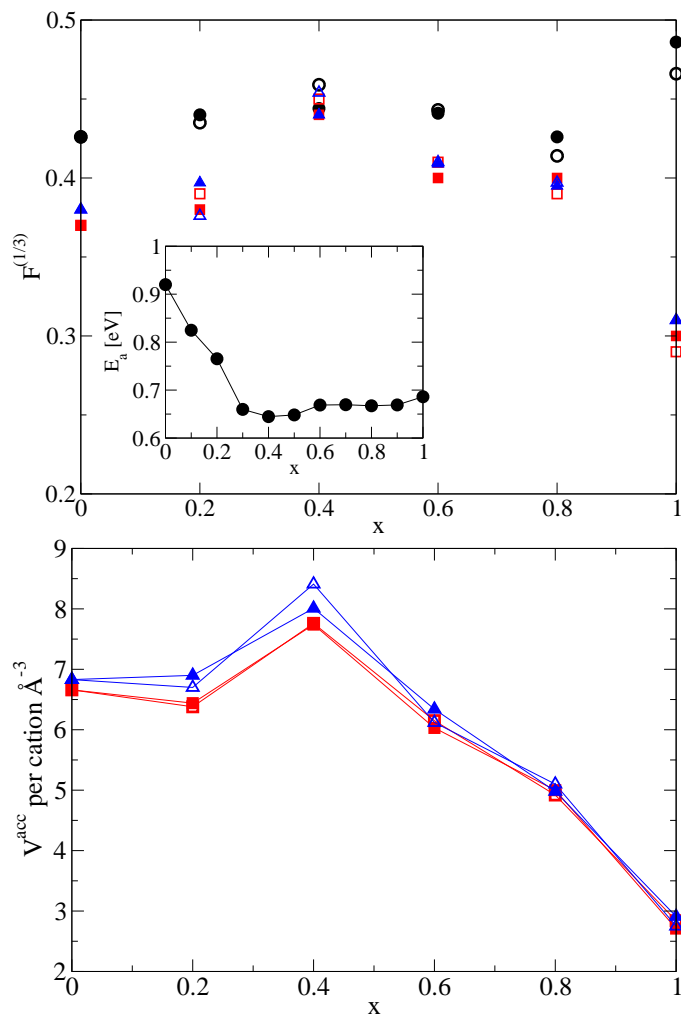


Figure 7.9.: Top: The cube root of the volume fraction F of the conduction pathways vs. x , RMC optimization with the XRD data taken from ref. [128] and the inclusion of Na-O constraints (circles), RMC optimization with X-ray [128] and neutron data [129] without (triangles) and with (squares) additional consideration of Na-O constraints. Inset shows the experimental determined activation energy [203]

Bottom: the accessible volume per cation for the RMC results with X-ray and neutron optimization.

(closed symbols correspond to the original version of Model C, open symbols correspond to the additional constraint of reduced $B^{(4)}$ - $B^{(4)}$ connections)

7.4. Summary

The results from chapter 6 were revisited under the additional inclusion of neutron diffraction data. This data set was provided by collaborating groups at Iowa State University (USA) and Chalmers University (Sweden) [129]. It was found that the final structures from chapter 6 are in qualitative good agreement with the neutron data. Nevertheless, minor but significant differences are present on all length scales in both $S(q)$ and $G(r)$. Therefore, a further refinement of the final structures was necessary in order to match both, the ND and XRD data. This refinement has only minor effects on the partial pair distribution functions.

It is important to note that the combination of XRD and ND data does not supply sufficient information to test the fraction of bOs connecting two P, two B or a B with a P atom in a satisfactory precision. Therefore, this information has to be introduced by additional constraints.

The analysis of the Na-O coordination environments reveals that the negligence of the constraints which have to be added in chapter 6 to ensure physical cation environments leads to a value for the average oxygen coordination number of sodium of ≈ 4 . This value is reasonably close to the values reported in the literature for pure borate and phosphate glasses. Nevertheless, it was found that an average value of ≈ 5 is also compatible to XRD and ND data. It is important to note that literature values of this properties are scattered and no experimental study addressing this issue is known for mixed borophosphate glasses. Therefore, it should be interesting to address this issue in a later study by molecular or *ab initio* molecular dynamic simulations. A very important finding of the present investigations is the fact that recently suggested correlations of E_a with $F^{1/3}$ or V_{acc} are from less relevance. This finding underpins the mechanism based on the NUT approach as the dominating effect affecting the MGFE in alkali borophosphate glasses.

7.5. Appendix: Constraining the number of bOs connecting two $B^{(4)}$

In the chapters 6 and 7 the influence of the avoidance of bOs connecting two $B^{(4)}$ was discussed. In the following we will shortly describe how this constraint was introduced. To date it is not possible to introduce second nearest neighbor constraints in any available RMC software package. Hence, the only way to introduce the rule controlling the $B^{(4)}$ - $B^{(4)}$ connectivity is to consider B atoms as a group $B^{(4)}$ -”atoms”, which are coordinated by four bOs, and a group of $B^{(X)}$ -”atoms”, which are coordinated by three oxygen atoms (both bOs and nbOs). The numbers N_P , N_{B4} , N_{BX} , N_{bO} , N_{nbO} and N_{Na} of P, $B^{(4)}$, $B^{(X)}$, bO, nbO and Na atoms are shown in table 7.2 the corresponding ND and XRD weights are presented in table 7.3 and 7.4. The avoidance of bOs that connect two $B^{(4)}$ NFU is introduced by the constraint that no bOs are connected to more than one $B^{(4)}$. Since this constraint leads to

7. Improvement of the RMC Models from Chapter 6 by Inclusion of Neutron Diffraction Data

strong frustrations and therefore to an extreme slowing down of the optimization procedure, not all bOs could follow this constraint. Nevertheless, it is sufficient that only $\approx 90\%$ of all bOs have to fulfill this rule, since it leads to a significant reduction of the amount of bOs which are connecting two B⁽⁴⁾ NFU by, a factor of ≈ 2 in comparison to the models without that rule.

x	N_P	N_{B4}	N_{B3}	N_{bO}	N_{nbO}	N_{Na}
0.2	1080	270	-	1932	1537	727
0.4	810	540	-	2202	997	727
0.6	540	550	260	2243	717	727
0.8	270	550	530	2243	447	727
1.0	-	550	800	2206	177	727

Table 7.2.: Number of the atoms for each chemical species in the RMC modeling, depending on the composition

Pair	$x = 0.2$	$x = 0.4$	$x = 0.6$	$x = 0.8$	$x = 1.0$
P-P	0.034	0.021	0.010	0.003	-
P-B ⁽⁴⁾	0.022	0.036	0.026	0.014	-
P-B ^(X)	-	-	0.012	0.014	-
P-bO	0.137	0.127	0.092	0.050	-
P-nbO	0.109	0.057	0.029	0.010	-
P-Na	0.032	0.026	0.019	0.010	-
B ⁽⁴⁾ -B ⁽⁴⁾	0.004	0.015	0.017	0.019	0.020
B ⁽⁴⁾ -B ^(X)	-	-	0.016	0.036	0.059
B ⁽⁴⁾ -bO	0.044	0.109	0.121	0.132	0.145
B ⁽⁴⁾ -nbO	0.035	0.050	0.039	0.026	0.011
B ⁽⁴⁾ -Na	0.010	0.023	0.025	0.027	0.029
B ^(X) -B ^(X)	-	-	0.004	0.017	0.043
B ^(X) -bO	-	-	0.058	0.128	0.210
B ^(X) -nbO	-	-	0.018	0.025	0.017
B ^(X) -Na	-	-	0.012	0.026	0.042
bO-bO	0.139	0.195	0.217	0.236	0.257
bO-nbO	0.220	0.176	0.138	0.094	0.041
bO-Na	0.065	0.080	0.088	0.096	0.104
nbO-nbO	0.088	0.040	0.022	0.009	0.002
nbO-Na	0.051	0.036	0.028	0.019	0.008
Na-Na	0.008	0.008	0.009	0.010	0.011

Table 7.3.: Weights for the ND Data $\gamma_{\alpha\beta}$ (see eq. 6.3) calculated for the composition $0.35\text{Na}_2\text{O}-0.65[x\text{B}_2\text{O}_3-(1-x)\text{P}_2\text{O}_5]$ in the RMC modeling that takes into account the avoidance of bOs bonded to two B⁽⁴⁾ NFU

Pair	$x = 0.2$	$x = 0.4$	$x = 0.6$	$x = 0.8$	$x = 1.0$
P-P	0.092	0.063	0.035	0.011	-
P-B ⁽⁴⁾	0.015	0.028	0.024	0.015	-
P-B ^(X)	-	-	0.011	0.014	-
P-bO	0.176	0.182	0.153	0.097	-
P-nbO	0.140	0.083	0.047	0.018	-
P-Na	0.091	0.083	0.068	0.043	-
B ⁽⁴⁾ -B ⁽⁴⁾	0.001	0.003	0.004	0.005	0.007
B ⁽⁴⁾ -B ^(X)	-	-	0.004	0.010	0.019
B ⁽⁴⁾ -bO	0.015	0.041	0.053	0.067	0.085
B ⁽⁴⁾ -nbO	0.012	0.018	0.016	0.012	0.007
B ⁽⁴⁾ -Na	0.008	0.018	0.024	0.030	0.038
B ^(X) -B ^(X)	-	-	0.001	0.005	0.014
B ^(X) -bO	-	-	0.024	0.062	0.124
B ^(X) -nbO	-	-	0.007	0.012	0.010
B ^(X) -Na	-	-	0.011	0.028	0.056
bO-bO	0.084	0.132	0.170	0.215	0.272
bO-nbO	0.134	0.120	0.104	0.080	0.044
bO-Na	0.087	0.120	0.151	0.191	0.247
nbO-nbO	0.053	0.027	0.016	0.007	0.002
nbO-Na	0.069	0.054	0.046	0.036	0.020
Na-Na	0.023	0.027	0.034	0.043	0.056

Table 7.4.: Weights for the high energy XRD data $\gamma_{\alpha\beta}$ (see eq. 6.3) calculated for the composition $0.35\text{Na}_2\text{O}-0.65[x\text{B}_2\text{O}_3-(1-x)\text{P}_2\text{O}_5]$ in the RMC modeling that takes into account the avoidance of bOs bonded to two B⁽⁴⁾ NFU

8. Summary and Conclusions

The aim of the present work was the study of the *mixed glass former effect* (MGFE) in ion conducting glasses. This effect is characterized by a non-monotonous dependency of the activation energy on the glass former mixing. So far, this effect was not well understood. Probably, this is related to the inherent chemical and physical complexity of these materials. As suggested in this work, different structural characteristics can lead to different mechanisms in the MGFE. Only a few mechanisms seem to be relevant to understand the MGFE and can thus be used for a classification.

In order to understand the MGFE, the major focus of the present thesis was the development of coarse grained models. To this end, two basic mechanisms were proposed which are described by the *mixed barrier model* (MBM) and the *network unit trap model* (NUT). The MBM relies on the assumption that the transport is dominated by energy barriers between the cation sites. The typical energies of these barriers are decreased in mixed regions in comparison to those where only one glass former species is present. This reduction corresponds to the finding that a number of mixed glass former systems show the tendency to phase separation, where the glass structure at the boundaries of the micro phases is assumed to be more open. The MBM was successfully applied to a number of mixed glass former systems and the effect of phase separation on the activation energies and the ac-conductivities were discussed. In particular, it was shown that the MBM implies a reduction of the extent of the MGFE if the typical size of the micro-phases is increased. Moreover, it was found that spatial correlations of the barrier energies introduced by the phase separations, have no effect on the commonly observed scaling of the frequency dependent conductivity in respect to a typical frequency. The last finding was underpinned by the fact that other short ranged correlations also have no effect on this frequency scaling. Complementary to the MBM, the NUT approach was introduced as well. In this model the site energies are the dominating factor for cation transport. In particular, one assumes that the effective charge of a network forming unit (NFU) is spread over the adjacent oxygen atoms. For example, the two nbOs of the $P^{(2)}$ units or the four bOs of the $B^{(4)}$ units are sharing one charge. This mechanism results in a spreading of the charges leading to different contributions of the NFUs to the site energies of adjacent ion sites. Assuming one knows the NFU concentrations of a mixed glass former system, one could predict the trend of the activation energy. To this end, a couple of theoretical concepts are presented that are applying charge balance and effective connectivity arguments to calculate the species concentrations in alkali borophosphate glasses. These concepts are based on a hierarchy of formation en-

enthalpies for the different NFU and the assumption that the number of bOs bridging two $B^{(4)}$ is somewhat limited. The comparison of the predicted with the NFU concentrations from several experimental studies shows an excellent agreement. Introducing the calculated NFU concentrations, it has been shown that the NUT approach can be successfully applied to sodium borophosphate glasses by including only one parameter. Furthermore, it turned out that the NUT-approach could also be used to understand the *mobile ion concentration effect* (MICE) in binary alkali borate glasses. As a further remarkable result, it was shown that the activation energy calculated according to the method proposed by Ambegaekar *et al.* [109] agrees well with results from the Monte Carlo hopping simulations. This result allows one to estimate E_a by analytical calculations according to the NUT model.

The second focus of the present thesis is related to the questions to what extent the local structure in sodium borophosphate glasses is affecting the transport of cations and whether other possible mechanisms for the MGFE can be ruled out. To address these issues, Reverse Monte Carlo Simulations (RMC) on $0.35Na_2O-0.65 [xB_2O_3-P_2O_5]$ glasses were performed. The RMC simulations are based on the XRD data that were reported by LeRoux *et al.* [128]. These authors have also performed a RMC-analysis but it was necessary to revisit the data, because the reported structures are violating chemical constraints, e.g. charge balance. By the introduction of further constraints and adding neutron diffraction data¹ it was possible to improve the quality of the RMC configurations. It was shown that the NFU concentrations calculated by the aforementioned model and the reduction of bridging oxygen connecting two $B^{(4)}$ are also compatible to the diffraction data. Moreover, a linear relationship between the activation energy and the cube root of the volume fraction of the conduction pathways was not found in the RMC models, despite the fact that this correlation was reported for binary borate and phosphate glasses [216]. In addition, possible correlations between the volume accessible for the cations and the activation energy could be clearly ruled out as well.

In summary, a multi scale study on the MGFE was performed. This study mainly addresses the development of models, capturing the main features of the MGFE in a remarkable group of glasses. A RMC study were additionally performed to address the structural origin of the MGFE in sodium borophosphate glasses.

For future work it would be interesting to check the mechanisms proposed here by the application of complementary methods. For example, one can test the MBM by the estimation of the local mechanic properties in the MD-simulated glass network. The NUT-model, in contrast, could be checked by measuring the effective binding energies for the mobile cations to their sites in glass models which are generated by MD. Moreover, another promising perspective, one could examine, is the extension of the NUT model to describe other stoichiometric effects, like the *halogen ion doping effect* or the *mixed alkali effect*.

¹which was supplied by cooperation partners from Iowa State University (USA) and Chalmers University (Sweden)

A. Testing the Mean Field Approach for Hopping Transport in Disordered Energy Landscapes on the Basis of a novel Linearized Pair Approximation

It was noted in sec. 5.3.2 that eq. 5.41 corresponds to a mean field approximation, since the exact formulation of a rate equation for the mean occupation number $n_i = \langle s_i \rangle$ is given by:

$$\frac{dn_i}{dt} = \sum_{j \neq i} \Gamma_{ji} n_j - \Gamma_{ij} n_i + (\Gamma_{ij} - \Gamma_{ji}) \langle s_i s_j \rangle \quad (\text{A.1})$$

,where s_i is the random variable describing the actual occupation state (i.e. 1 if occupied, 0 if not). Rewriting this variable as $s_i = n_i + \delta s_i$ leads to $\langle s_i s_j \rangle = n_i n_j + \langle \delta s_i \delta s_j \rangle$, since the expectation value of the fluctuation δs_i is zero. It is important to note that eq. 5.41 corresponds to $\langle \delta s_i \delta s_j \rangle = 0$. One should keep in mind that this ansatz is not correct in general [187]. In particular for one-dimensional systems, like Richards AB-model [189] or chains with random site energies [190, 222], significant deviations to the mean field behavior are found. In contrast, Cottaar and Bobert reported only weak deviations of the mean field results with the ones calculated by a pair approximation for arbitrary large fields [188] in a variable range hopping model on two-dimensional lattices. In this pair approximation Cottaar and Bobert divide the N sites of the system in $N/2$ pairs of adjacent sites. The hopping between both sites of a pair was described with the non-mean-field-correlator and all other transitions to the sites of a pair were considered with mean-field-correlators. This procedure implies that the vast majority of the possible transitions were still described in the framework of the mean field theory. An important drawback of this approach was the fact that the numerical solution of model was given only for comparatively high temperatures. In addition, it is not possible to study dispersive transport properties applying this ansatz. Hence, an alternative approximation is requested and will be presented in the following discussion. This derivation utilizes and generalizes the linearization scheme introduced by Pasveer *et.al* to solve mean field rate equations [223] to a second order approximation of the frequency dependent occupation correlators. Therefore, the presented novel approach is denoted as linearized pair approximation (LPA). The key idea is to describe the time

evolution of the occupation number correlator $\langle s_i s_j \rangle$ by an additional rate equation:

$$\begin{aligned}
 \frac{d\langle s_i s_j \rangle}{dt} &= \sum_{\{k\}} \Gamma_{ki} \langle s_k (1 - s_i) s_j \rangle - \Gamma_{ik} \langle (1 - s_k) s_i s_j \rangle \\
 &+ \{i, k \leftrightarrow j, l\} \\
 &= \sum_{\{k\}} [\Gamma_{ki} \langle s_k s_j \rangle - \Gamma_{ik} \langle s_i s_j \rangle] \\
 &+ \sum_{\{k\}} (\Gamma_{ik} - \Gamma_{ki}) \langle s_i s_j s_k \rangle \\
 &+ \{i, k \leftrightarrow j, l\}
 \end{aligned} \tag{A.2}$$

,where k is the index of a site connected to i , with $k \neq j, i$. If k is not directly connected to j the pair approximation could be introduced by the assumptions $\langle \delta s_k \delta s_j \rangle = 0$ and $\langle \delta s_k \delta s_i \delta s_j \rangle = 0$. This approximations result in $\langle s_k s_j \rangle = n_k n_j$ and $\langle s_k s_i s_j \rangle = n_j \langle s_i s_k \rangle + n_k \langle s_i s_j \rangle - n_i n_j n_k$. Therefore, eq. A.3 could be approximated by:

$$\begin{aligned}
 \frac{d\langle s_i s_j \rangle}{dt} &\approx \sum_{\{k\}} \Gamma_{ki} n_k n_j - \Gamma_{ik} \langle s_i s_j \rangle + (\Gamma_{ik} - \Gamma_{ki}) n_j \langle s_i s_k \rangle \\
 &+ (\Gamma_{ik} - \Gamma_{ki}) n_k \langle s_i s_j \rangle - (\Gamma_{ik} - \Gamma_{ki}) n_i n_j n_k \\
 &+ \{i, k \leftrightarrow j, l\}
 \end{aligned} \tag{A.3}$$

Solving the set of eqs. A.1 and A.3 is a highly non-linear problem. Since we are interested here in linear response measures, a concept, similar to the linearization scheme proposed by Pasveer *et al.* [223], would decrease the complexity of the problem to a system of linear equations. Therefore, the response of both the occupation numbers and the pair correlators to a small time dependent field $E(t) = \hat{E} \exp(i\omega t)$ will be investigated. The behavior of the occupation numbers and the hopping rates as a function of an external field is in first order given by $n_i = f_i + \delta n_i$ and $\Gamma_{ij} \approx \hat{\Gamma}_{ij} + \Gamma'_{ij}$. [223]. Where δn_i and Γ'_{ij} are the first order corrections to the equilibrium occupation numbers f_i and equilibrium hopping rates $\hat{\Gamma}_{ij}$. Following this logic, one may write for $\langle s_i s_j \rangle = f_i f_j + C_{ij}$, where C_{ij} is the linear correction in $\langle s_i s_j \rangle$. Introducing these expressions in eq. A.1 and neglecting terms which are not linear in the corrections one gets:

$$\sum_{j \neq i} \Gamma'_{ij} f_i (1 - f_j) - \Gamma'_{ji} f_j (1 - f_i) = \sum_{j \neq i} \left(\hat{\Gamma}_{ji} \delta n_j + (\hat{\Gamma}_{ij} - \hat{\Gamma}_{ji}) C_{ij} \right) - \left(\sum_{j \neq i} \hat{\Gamma}_{ij} + i\omega \right) \delta n_i \tag{A.4}$$

Applying the same operation on eq. A.3 one gets:

$$\begin{aligned}
 G_{ij} &= A_{ij}(\omega)C_{ij} + \sum_{\{k\}} B_{ijk}C_{ik} + \sum_{\{l\}} B_{jil}C_{jl} + D_{ikjl}\delta n_i + D_{jlik}\delta n_j \\
 &+ \sum_{\{k\}} F_{ijk}\delta n_k + \sum_{\{l\}} F_{jil}\delta n_l
 \end{aligned} \tag{A.5}$$

with:

$$G_{ij} = f_j \sum_{\{k\}} \left(\Gamma'_{ik} f_i (1 - f_k) - \Gamma'_{ki} f_k (1 - f_i) \right) + \{i, k \leftrightarrow j, l\} \tag{A.6}$$

$$A_{ij}(\omega) = \left(\left(\sum_{\{k\}} (\hat{\Gamma}_{ik} - \hat{\Gamma}_{ki}) f_k \right) + \{i, k \leftrightarrow j, l\} - i\omega \right) \tag{A.7}$$

$$B_{ijk} = (\hat{\Gamma}_{ik} - \hat{\Gamma}_{ki}) f_j \tag{A.8}$$

$$D_{ikjl} = \left(\sum_{\{l\}} \hat{\Gamma}_{lj} \right) - \left(\sum_{\{k\}} (\hat{\Gamma}_{ik} - \hat{\Gamma}_{ki}) f_k \right) f_j \tag{A.9}$$

$$F_{ijk} = \hat{\Gamma}_{ki} f_j \tag{A.10}$$

If a lattice contains N sites, where each site is connected to d neighbors eqs. A.4 and A.5 correspond to a system of $N(1 + d/2)$ linear equations and unknowns that has to be solved under the additional condition $\sum_i \delta n_i = 0$.

To illustrate the capabilities of this novel approach, the nearest neighbor hopping on a squared lattice with $N = 128^2$ lattice sites and uniformly distributed random site energies is studied. The averages were performed over 8 configurations. The LPA is tested against the mean field (MF) results that are calculated with the algorithm given by Pasveer *et al.* [223]. In addition, the results are compared with the mapping scheme proposed by Baranovskii and Cordes [18] to describe the motion as single particle hopping diffusion in an effective barrier landscape (i.e. *effective circuit approach* (ECA)). This calculation is performed by utilizing the VAC method [145].

An important question in the present thesis was to what extent the predictions of the *effective circuit approach* (ECA) for the activation energies of the long-time-ion-transport are correct. Figure A.1 shows the Arrhenius plots $\ln D_{lt} = F(\beta)$ for hopping particle concentrations $c_p = 0.05$ and $c_p = 0.5$. For high temperatures the results from the LPA and the MF approach differ slightly from the ECA results, but decreasing the temperature leads to increase of the incline of the $\ln D$ -functions for both LPA and MF independent of c_p . It is interesting to note that for low enough temperatures, the differences between ECA and LPA are almost independent of the temperature. In particular, it was found, that the low-temperature conductivity in the half filled system calculated by the LPA was a

factor ≈ 0.6 smaller than the corresponding one for MF calculations. This value could be explained by the additional consideration of forward and backward hops which are not taken into account by the mean field level description. For $c_p = 0.05$ the low temperature value of $E_a = 0.55$ is quite near to the value one would expect for the *critical path analysis* (CPA) in two dimensional systems in an energy landscape with uniform distributed site energies. Hence, one could argue that the CPA is adequate for $c_p \ll p_c$. However, from the Monte Carlo simulations reported in the chapters 4 and 5 one would expect that the incline in $\ln D_{lt}$ decreases for c_p . This fact is obviously not found in the LPA calculations. The origin of this discrepancy is not clear at the moment and calls for a deeper analysis. One could speculate that the different dimensionality of the system investigated here and the site energy distributions play an important role for these discrepancies. Perhaps there are some other effects that are connected to the correlators beyond the level of description given by the LPA.

As noted above, the LPA approach allows also to investigate the behavior of the dispersive conductivity. And one could wonder to what extent the outcome of such analysis is affected by the level of description. Figure A.2 shows the ac-conductivity for $c_p = 0.05$ ($c_p = 0.5$) and $\beta = 20$ ($\beta = 40$) calculated by the LPA approach in comparison to the MF approach. It is clear that for high ω MF and LPA have the same value. The mathematical origin is that the imaginary $i\omega$ term dominates the linear system of equations. Physically one can argue that fluctuations near the equilibrium on short time scales, which correspond to the high ω regime are dominated by the exactness of the relation $\langle s_i s_j \rangle = f_i f_j$ in the equilibrium case. However, fig. A.2 shows that for small c_p the outcome of both methods is almost not distinguishable over the whole ω -range. However, clear discrepancies between the MF and LPA results are found for higher c_p , which are most significant in the the low- ω regime and becomes less significant with increasing ω . This finding is somehow surprisingly because one would expect that for frequencies corresponding to time scales for multi particle rearrangements some clear differences must occur. Nevertheless, this is not the case. Probably these effects are related to higher order effects in the occupation correlators. Nevertheless, in fig. A.2 b.) significant deviations in the view of universality in the scaled ac-conductivity¹ do not appear. This fact supports the sufficiency of the MF-level description for the study of the universality phenomenon in the ac-conduction of disordered solids. For instance, it could be shown that a super-scaling appears in respect different c_p . Such a finding was reported in ref. [19] on the basis of MC-simulations at relatively high temperatures. In summary in the present chapter the *linearized pair approximation* was presented as a novel approach that includes a higher level description beyond the *mean field approach*. It could be shown that the low temperature activation energy for transport is almost independent from the level of description. Changes in E_a are in the order of few percent for a half filled systems. This gives some further support to the ECA used in chapter 5. It could

¹Remember this is defined by relation $\sigma(\omega)/\sigma_{dc} = F(\omega/\omega_c)$, where ω_c is the onset frequency for dispersive transport

A. Testing the Mean Field Approach for Hopping Transport in Disordered Energy Landscapes on the Basis of a novel Linearized Pair Approximation

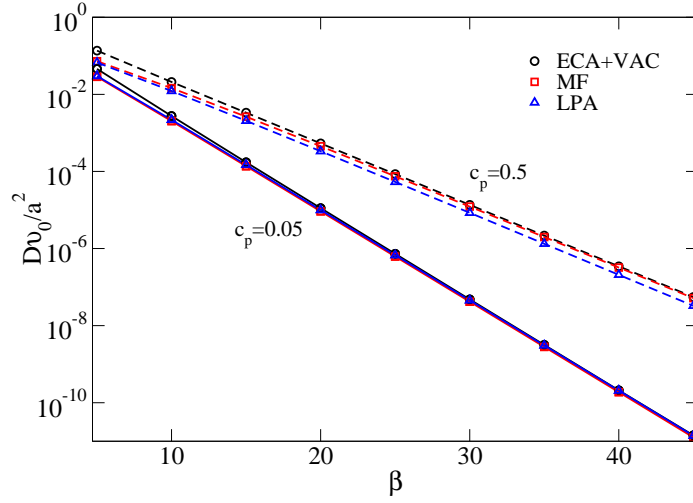


Figure A.1.: Arrhenius plots for the constant of Diffusion D estimated by the a linearization of the rate equation on the MF and LPA level of description (detail see text) and the application of the *effective circuit approach* (ECA) in combination with the *velocity auto correlation* (VAC) method [105]

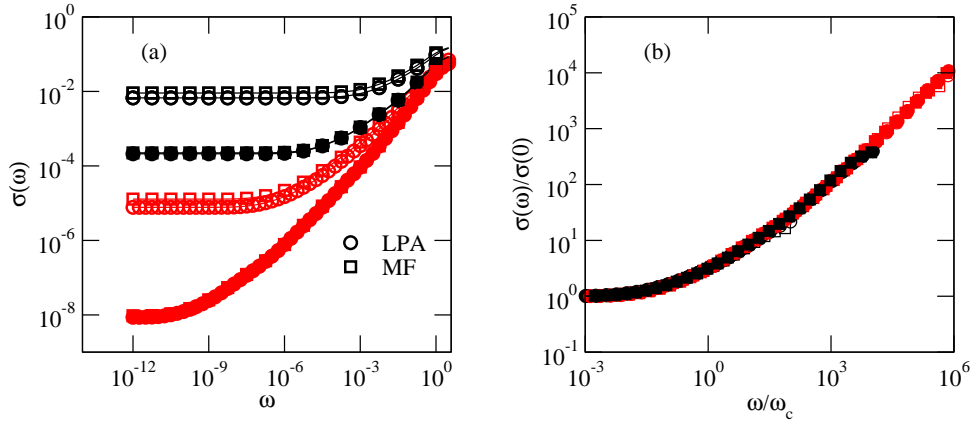


Figure A.2.: (a) Frequency dependent conductivity $\sigma(\omega)$ for $c_p = 0.05$ (full symbols) and $c_p = 0.5$ (open symbols) calculated for $\beta = 20$ (black) and $\beta = 40$ (red) with the *mean field approach* (MF) and the *linearized pair approximation* (LPA). (b) Scaling of the data from (a) in respect to relation $\sigma(\omega)/\sigma(0) = F(\omega/\omega_c)$ where ω_c is determined by the criterion $\sigma(\omega_c) = \sqrt{10}\sigma(0)$.

A. Testing the Mean Field Approach for Hopping Transport in Disordered Energy Landscapes on the Basis of a novel Linearized Pair Approximation

be shown also that the differences between MF and LPA are not thermally activated for low temperatures. This finding is related to forward and backward jumps of the hopping particles. As a further important result it was found that the MF level description could be sufficient if one is interested in the study of the universality in the ac-conduction. The usual scaling-relation is not affected by both the particle concentrations and the level of description. Hence one could use the MF- approach to investigate the deviations from universality, which are reported for instance in some MAE systems [108].

B. References

- [1] W. H. Zachariasen, *J. Chem. Soc.*, **54**, 3841, (1932)
- [2] F. Scholz, *J. Solid State Electrochem.*, **15**, 5, (2011)
- [3] J. Kawamura, R. Asayama, N. Kuwata, and O. Kamashima in "Physics of Solid State Ionics" chapter 7, ed. T. Sakuma and H. Takahashi, Research Signpost, Kerala, India (2006)
- [4] J.-M. Tarascon and M. Armand, *Nature*, **414**, 359, (2001)
- [5] J. O. Isard, *J. Non-Cryst. Solids*, **246**, 16, (1999)
- [6] B. Roling, C. Martini, and K. Funke, *J. Non-Cryst. Solids*, **249**, 201, (1999)
- [7] E. Bychkov, P. L. Price, A. Lapp, *J. Non-Cryst. Solids*, **293**, 211, (2001)
- [8] Á. W. Imre, H. Staesche, S. Voss, M. D. Ingram, K. Funke, and H. Mehrer, *J. Phys. Chem. B*, **111**, 5301, (2007)
- [9] M. D. Ingram, *Phys. Chem. Glasses*, **28**, 215, (1987)
- [10] R. Peibst, C. Schott and P. Maass, *Phys. Rev. Lett.*, **95**, 115901, (2005)
- [11] P. Maass, A. Bunde and M. D. Ingram, *Phys. Rev. Lett.*, **68**, 3064, (1992)
- [12] A. Bunde, M. D. Ingram and P. Maass, *J. Non-Cryst. Solids*, **172-174**, 1222, (1994)
- [13] A. Bunde, M. D. Ingram, and S. Russ, *Phys. Chem. Chem. Phys.*, **6**, 3663, (2004)
- [14] J. Swenson, A. Matic, C. Karlsson, L. Börjesson, C. Meneghini, and W. S. Howells, *Phys. Rev. B*, **63**, 132202, (2001)
- [15] J. Swenson and S. Adams, *Phys. Rev. Lett.*, **90**, 155507, (2003)
- [16] J. Tsuchida, J. Schneider, A. O. de Oliviera, M. T. Rinke, and H. Eckert, *Phys. Chem. Chem. Phys.*, **12**, 2879, (2012)
- [17] J. Epping, H. Eckert, A. W. Imre and H. Mehrer, *J. Non-Cryst. Solids*, **351**, 3521, (2005)
- [18] S. D. Baranovskii and H. Cordes, *J. Chem. Phys.*, **111**, 7546, (1999)

-
- [19] M. Porto, P. Maass, M. Meyer, A. Bunde and W. Dieterich, *Phys. Rev. B*, **61**, 6057, (2000)
- [20] D. Knödler, "Untersuchungen eines Gittergasmodells zum Ionentransport in Gläsern", PhD-Thesis, University of Konstanz, (1994)
- [21] H. Doweidar, Y. M. Moustafa, G. M. El-Damrawi and R. M. Ramadan, *J. Phys.: Condens. Matter*, **20**, 035107, (2008)
- [22] S. W. Martin, *J. Am. Ceram. Soc.*, **74**, 1767, (1991)
- [23] H. Muramatsu, A. Hayashi, T. Ohtomo, S. Harna, and M. Tatsumisago, *Solid State Ionics*, **182**, 116, (2011)
- [24] H. L. Tuller and D. B. Button, in "Transport-Structure Relations in Fast Ion and Mixed Conductors" ed. F. W. Poulsen, N. Hessel-Anderson, K. Clausen, S. Skaarup, and O. Soerensen (Risø National Laboratory, Roskilde, Denmark), 119, (1985)
- [25] J. Swenson, L. Börjesson, and W. S. Howells, *Phys. Rev. B*, **57**, 13514, (1998)
- [26] D. I. Novita, P. Boolchand, M. Malki, and M. Micoulaut, *Phys. Rev. Lett.*, **98**, 195501, (2007)
- [27] T. T. Duc, P. R. Rayavarapu, and S. Adams, *J. Sol. State Electrochem.*, **14**, 1781, (2010)
- [28] J. Kawamura and M. Shimoji, *J. Non-Cryst. Solids*, **88**, 295, (1986)
- [29] J. Kawamura and M. Shimoji, *Mat. Chem. Phys*, **23**, 99, (1989)
- [30] J. Swenson, and L. Börjesson, *Phys. Rev. Lett.*, **77**, 3569, (1996)
- [31] J. Swenson, R. L. McGreevy, L. Börjesson, and J. D. Wicks, *Solid State Ionics*, **105**, 55, (1998)
- [32] M. Tachez, R. Mercier, J. P. Malugani, and A. J. Dianoux, *Solid State Ionics*, **20**, 93, (1986)
- [33] J. P. Malugani, M. Tachez, R. Mercier, A. J. Dianoux, and P. Chieux, *Solid State Ionics*, **23**, 189, (1986)
- [34] M. Tachez, R. Mercier, J. P. Malugani, and A. J. Dianoux, *Solid State Ionics*, **25**, 263, (1987)
- [35] O. L. Anderson and D. A. Stuart, *J. Am. Ceram. Soc.*, **37**, 573, (1954)
- [36] M. M. Doeff, S. J. Visco, M. Yanping, M. Peng, D. Lei, and L. C. De Jonghe, *Electr. Chim. Acta*, **40**, 2205, (1995)

References

- [37] S. Wenzel, T. Hara, J. Janek, and P. Adelhelm, *Energy Environ. Sci.*, **4**, 3342, (2011)
- [38] C. Masquelier, *Nature Materials*, **10**, 649, (2011)
- [39] C. Daniel, *JOM*, **60**, 43, (2008)
- [40] J. Witacre, U.S. Patent, 20090253025, (2009)
- [41] P. E. Stallworth, J. J. Fontanella, M. C. Wintersgill, C. D. Scheidler, J. J. Immel, S. G. Greenbaum, and A. S. Gozdz, *Journ. Pow. Sources*, **81**, 739, (1999)
- [42] N. Kamaya, K. Homma, Y. Yamakawa, M. Hirayama, R. Kanno, M. Yonemura, T. Kamiyama, Y. Kato, S. Hama, K. Kawamoto, and A. Mitsui, *Nature Materials*, **10**, 682, (2011)
- [43] F. Croce, G. B. Appetecchi, L. Persi, and B. Scrosati, *Nature*, **394**, 456, (1998)
- [44] R. C. Agrawal, and G. P. Pandey, *J. Phys. D: Appl. Phys.*, **41**, 223001, (2008)
- [45] K. West, B. Zachau-Christiansen, T. Jacobsen, and S. Atlung, *J. Electrochem. Soc.*, **132**, 3061, (1985)
- [46] Y. Inaguma, C. Liqun, M. Itoh, T. Nakamura, T. Uchida, H. Ikuta, and M. Wakihara, *Solid State Comm.*, **83**, 689, (1993)
- [47] R. Kanno and M. Murayama, *J. Electrochem. Soc.*, **148**, A742, (2001)
- [48] G. -Y. Adachi, N. Imanaka, and H. Aono, *Advanced Materials*, **6**, 127, (1996)
- [49] M. Tatsumisago and A. Hayashi, *J. Non-Cryst. Solids*, **354**, 1411, (2008)
- [50] M. Tatsumisago, *Solid State Ionics*, **175**, 13, (2004)
- [51] D. P. Button, L. S. Mason, H. L. Tuller, and D. R. Uhlmann, *Solid State Ionics*, **9**, 585, (1983)
- [52] M. S. Halper and J. C. Ellenbogen, "Supercapacitors: A Brief Overview", MITRE-Nanosystems Group, <http://www.mitre.org>, (2006)
- [53] I. Shiyankovskaya, M. Hepel and E. Tewksbury, *J. New Mat. Electrochem. Systems*, **3**, 241, (2000)
- [54] I. Karakurt, J. Boneberg, and P. Leiderer, *Appl. Phys. A: Mat. Sci. and Proc.*, **83**, 1, (2006)
- [55] H. N. Hersh, W. E. Kramer, and J. H. McGee, *Appl. Phys. Lett.*, **27**, 646, (1975)
- [56] G. Jasinski, P. Jasinski, B. Chachulski, and A. Nowakowski, *Material Science-Poland*, **24**, 261, (2006)

-
- [57] G. Jasinski and P. Jasinski, *IOP Conf. Series: Materials Science and Engineering*, **18**, 212007, (2011)
- [58] A. Pradel, N. Kuwata and M. Ribes, *J. Phys.: Condens. Matter*, **15**, S1561, (2003)
- [59] D. Coppo, M. J. Duclot and J. L. Souquet, *Solid State Ionics*, **90**, 111, (1996)
- [60] B. V. R. Chowdari and P. P. Kumari, *Solid State Ionics*, **86-88**, 521, (1996)
- [61] B. V. R. Chowdari and P. P. Kumari, *J. Phys. Chem. Solids*, **58**, 515, (1996)
- [62] R. V. G. Sarma and S. Radhakrishna, *J. Mater. Sci. Letters*, **9**, 1237, (1990)
- [63] Y. Kim, J. Saienga and S. W. Martin, *J. Phys. Chem. B*, **110**, 16318, (2006)
- [64] Y. Kim and S. W. Martin, *Solid State Ionics*, **177**, 2881, (2006)
- [65] T. Tsuchiya and T. Moriya, *J. Non-Cryst. Solids*, **38**, 323, (1980)
- [66] A. Magistris, G. Chiodelli, and M. Duclot, *Solid State Ionics*, **9**, 611, (1983)
- [67] G. Chiodelli, G. Campari-Vigano, G. Flor, A. Magistris, and M. Villa, *J. Thermal Anal.*, **29**, 673, (1984)
- [68] G. Chiodelli, A. Magistris, and M. Villa, *Solid State Ionics*, **18**, 356, (1986)
- [69] D. Zielniok, C. Cramer and H. Eckert, *Chem. Mater.*, **19**, 3162, (2007)
- [70] F. Munoz, L. Montagne, L. Pascual, and A. Duran, *J. Non-Cryst. Solids*, **355**, 2571, (2009)
- [71] D. Larink and H. Eckert, personal communication, data not published yet
- [72] T. D. Tho, R. Prasada Rao, and S. Adams, *Phys. Chem. Glasses*, **52**, 91, (2011)
- [73] M. Tatsumisago, N. Machida and T. Minami, *Yogyo Kyokaishi*, **95**, 197, (1987)
- [74] L. F. Maia and A. C. M. Rodrigues, *Solid State Ionics*, **168**, 87, (2004)
- [75] K. Otto, *Phys. Chem. Glasses*, **7**, 29, (1966)
- [76] P. Kluvanek, R. Klement, and M. Karacon, *J. Non-Cryst. Solids*, **353**, 2004, (2007)
- [77] Y. Kowada, M. Tatsumisago, T. Minami, and H. Adachi, *J. Non-Cryst. Solids*, **354**, 360, (2007)
- [78] X. Wu and R. Diekmann, *J. Non-Cryst. Solids*, **357**, 2846, (2011)
- [79] D. W. Matson, S. K. Sharma, and J. A. Phillpotts, *J. Non-Cryst. Solids*, **58**, 323, (1983)

References

- [80] G. N. Greaves, A. Fontaine, P. Lagarde, D. Raoux, and S. J. Gurman, *Nature*, **293**, 611, (1981)
- [81] U. Voigt, H. Lammert, E. Eckert, and A. Heuer, *Phys. Rev. B.*, **72**, 064207, (2005)
- [82] S. P. Puls and H. Eckert, *Phys. Chem. Chem. Phys.*, **9**, 3992, (2007)
- [83] M. Schuch, R. Christensen, C. Trott, P. Maass, and S. W. Martin, *J. Phys. Chem. C*, **116**, 1503, (2012)
- [84] M. Zeyer-Düsterer, L. Montagne, G. Palavit, and C. Jäger, *Sol. State. Nucl. Magn. Res.*, **27**, 50, (2005)
- [85] D. B. Raskar, M. T. Rinke and H. Eckert, *J. Phys. Chem. C*, **112**, 12530, (2008)
- [86] M. Rinke: "Struktur-Eigenschafts-Korrelationen in Gläsern mit mehreren Netzwerkbildnern: Neue Erkenntnisse aus der Kombination von Festkörper-NMR-Methoden mit der Röntgenphotoelektronen-Spektroskopie", PhD-Thesis, University of Münster, (2009)
- [87] M. T. Rinke and H. Eckert, *Phys. Chem. Chem. Phys.*, **13**, 6552, (2011)
- [88] A. P. Ahoussou, J. Roges, and A. Kone, *Thermochim. Acta*, **441**, 96, (2006)
- [89] A. P. Ahoussou, J. Roges, and A. Kone, *J. Non-Cryst. Solids*, **353**, 271, (2007)
- [90] L. G. Baikova, Yu. K. Federov, V. P. Pukh, L. V. Tikhonova, T. P. Kanzannikova, A. B. Sinani, and S. I. Nikitina, *Glass Physics and Chemistry*, **29**, 276, (2003)
- [91] R. Christensen, J. Byer, T. Kaufmann, and S. W. Martin, *Phys. Chem. Glasses: Eur. J. Glass Sci. Technol. B*, **50**, 237, (2008)
- [92] D. Carta, D. Qiu, P. Guerry, I. Ahmed, E. A. A. Neel, J. C. Knowles, M. E. Smith, and R. J. Newport, *J. Non.-Cryst. Solids*, **354**, 3671, (2008)
- [93] R. Cristensen and S. W. Martin, personal communication, data not published yet
- [94] R. D. Banhatti, C. Cramer, D. Zielniok, A. H. J. Robertson and M. D. Ingram, *Z. Phys. Chem.*, **223**, 1201, (2009)
- [95] J. Frenkel, "Kinetic Theory of Liquids", pp. 10-11., Oxford University Press, New York, (1947)
- [96] D. K. McElfresh and D. G. Howitt, *J. Am. Ceram. Soc.*, **69**, C-237, (1986)
- [97] A. Heuer, H. Lammert and M. Kunow, *Z. Phys. Chem.* **218**, 1429, (2004)
- [98] M. Kunow and A. Heuer, *Phys. Chem. Chem. Phys.*, **7**, 2131, (2005)

-
- [99] J. L. Souquet, M. Lévy, and M. Duclot, *Solid State Ionics*, **70**, 337, (1994)
- [100] M. L. F. Nascimento, A. C. M. Rodrigues, and J. L. Souquet, *Phys. Chem. Glasses: Eur. J. Glass Sci. Technol. B*, **51**, 69, (2010)
- [101] S. W. Martin, W. Yao, and K. Berg, *Z. Phys. Chem.*, **223**, 1375, (2009)
- [102] A. Grandjean, M. Malki, and C. Simonnet, *J. Non-Cryst. Solids*, **352**, 2731, (2006)
- [103] H. Lammert and A. Heuer, *Phys. Rev. Lett.*, **104**, 125901, (2010)
- [104] K. Funke and R. D. Banhatti, *Solid State Ionics*, **169**, 4, (2004)
- [105] J. C. Dyre and T. B. Schrøder, *Rev. Mod. Phys.*, **72**, 873, (2000)
- [106] B. Roling, *Phys. Rev. B*, **61**, 5993, (2000)
- [107] J. C. Dyre and T. B. Schrøder, *Phys. Rev. Lett.*, **101**, 025901, (2008)
- [108] J. C. Dyre, P. Maass, B. Roling and D. L. Sidebottom, *Rep. Prog. Phys.*, **72**, 046501, (2009)
- [109] V. Ambegaokar, B. I. Halperin, and J. S. Langer, *Phys. Rev. B*, **4**, 2612, (1971)
- [110] I. Svare, F. Borsa, D. R. Torgeson and S. W. Martin, *Phys. Rev. B.*, **48**, 9336, (1993)
- [111] I. Svare, F. Borsa, D. R. Torgeson and S. W. Martin, *J. Non-Cryst. Solids*, **172**, 1300, (1994)
- [112] S. Sen, A. M. George and J. F. Stebbins, *J. Non-Cryst. Solids*, **197**, 53, (1996)
- [113] P. Maass, *J. Non-Cryst. Solids*, **255**, 35, (1999)
- [114] H. Lammert, R. D. Banhatti, and A. Heuer, *J. Chem. Phys.*, **131**, 224708, (2009)
- [115] A. H. Verhoeff and H. W. den Hartog, *J. Non-Cryst. Solids*, **182**, 235, (1995)
- [116] A. N. Cormack and Y. Cao, *Molecular Engineering*, **6**, 183, (1996)
- [117] M. Vogel, *Phys. Rev. B*, **70**, 094302, (2004)
- [118] A. Karthikeyan, P. Vinatier, A. Levasseur, and K. J. Rao, *J. Phys. Chem. B*, **103**, 6185, (1999)
- [119] C.-P. Varsamis, A. Vegiri, and E. I. Kamitsos, *Phys. Rev. B.*, **65**, 104203, (2002)
- [120] J. Habasaki and Y. Hiwatari, *Phys. Rev. B*, **69**, 144207, (2004)
- [121] C. R. Trott: "LAMMPSCUDA - a new GPU accelerated Molecular Dynamics Simulations Package and its Application to Ion-Conducting Glasses", PhD-thesis, Ilmenau University of Technology, Ilmenau, Germany, (2011)

References

- [122] L. Cormier, D. Ghaleb, J.-M. Delaye, and G. Calas, *Phys. Rev. B.*, **61**, 14495, (2000)
- [123] F. Gou, G. N. Greaves, W. Smith, and R. Winter, *J. Non-Cryst. Solids*, **293**, 539, (2001)
- [124] G. Ferlat, T. Charpentier, A. P. Seitsonen, A. Takada, M. Lazzeri, L. Cormier, G. Calas, and F. Mauri, *Phys. Rev. Lett.*, **101**, 065504, (2008)
- [125] A. J. Parsons, I. Ahmed, C. D. Rudd, G. J. Cuello, E. Pellegrini, D. Richard and M. R. Johnson, *J. Phys.: Condens. Matter*, **22**, 485403, (2011)
- [126] M. Benoit, S. Ispas, and M. E. Tuckerman, *Phys. Rev. B.*, **64**, 224205, (2001)
- [127] A. Tilocca, *Phys. Rev. B.*, **76**, 224202, (2007)
- [128] S. Le Roux, S. W. Martin, R. Christensen, Y. Ren, and V. Petkov, *J. Phys.: Condens. Matter*, **23**, 035403, (2011)
- [129] M. Karlsson, R. Christensen, S. W. Martin, S. Imberti and A. Matic, in preparation
- [130] P. S. Anantha and K. Hariharan, *Mater. Chem. Phys.*, **89**, 428, (2005)
- [131] D. E. Day, *J. Non-Cryst. Solids*, **21**, 343, (1976)
- [132] S. Tyč and B. I. Halperin, *Phys. Rev. B*, **39**, 877, (1989)
- [133] D. Le Messurier, V. Petkov, S. W. Martin, Y. Kim, and Y. Ren, *J. Non-Cryst. Solids*, in press.
- [134] D. P. Landau and K. Binder: "A guide to Monte Carlo Simulations in Statistical Physics", Cambridge University Press, p. 115 , (2005)
- [135] T. B. Schrøder, *Europhys. Lett.*, **81**, 30002, (2008)
- [136] B. Roling, A. Happe, K. Funke, and M. D. Ingram, *Phys. Rev. Lett.*, **78**, 2160, (1997); B. Roling, *Solid State Ionics*, **105**, 185, (1998); D. L. Sidebottom, *Phys. Rev. Lett.*, **82**, 3653, (1999)
- [137] J. Zhang and D. L. Sidebottom, *J. Non-Cryst. Solids*, **288**, 18, (2000)
- [138] Y. Kim and S. W. Martin, personal communication
- [139] N. F. Mott and E. A. Davis: "Electronic Processes in Non-crystalline Materials", second edition, Clarendon, Oxford, (1979)
- [140] C. Cramer, S. De and M. Schönhoff, *Phys. Rev. Lett.*, **107**, 028301, (2011)
- [141] J. R. Sangoro, A. Serghei, S. Naumov, P. Galvosas, J. Kärger, C. Wespe, F. Bordusa, and F. Kremer, *Phys. Rev. E*, **77**, 051202, (2008)

-
- [142] C. Cramer, S. Brückner, Y. Gao, and K. Funke, *Phys. Chem. Chem. Phys.*, **4**, 3214, (2002)
- [143] H. Cordes, S. D. Baranovskii, and J. Greif, *Phys. Stat. Sol. (B)*, **230**, 243, (2002)
- [144] Th. Koschny and L. Schweitzer, *Phys. Rev. B.*, **67**, 195307, (2003)
- [145] T. B. Schrøder, "Hopping in Disordered Media: A Model Glass Former and A Hopping Model", PhD-Thesis, Roskilde University, Denmark, (2000)
- [146] R. Kubo, *J. Phys. Soc. Japan*, **12**, 570, (1957)
- [147] M. Schuch, C. R. Müller, P. Maass, and S. W. Martin, *Phys. Rev. Lett.*, **102**, 145902, (2009)
- [148] P. J. Bray and J. G. O'Keefe, *Phys. Chem. Glasses*, **4**, 37, (1963)
- [149] P. J. Bray and M. L. Liu, in *Structure and Bonding in Noncrystalline Solids*, ed. G. E. Walrafen and A. G. Revesz, Plenum Press, New York, (1986)
- [150] A. C. Wright, *Phys. Chem. Glasses*, **51**, 1, (2010)
- [151] E. Ratai, J. C. C. Chan and H. Eckert, *Phys. Chem. Chem. Phys.*, **4**, 3198, (2002)
- [152] S. Kroeker, P. M. Aguiar, A. Cerquiera, J. Okoro, W. Clarida, J. Doerr, M. Olesiuk, G. Ongie, M. Affatigato and S. A. Feller, *Eur. J. Glass Sci. Technol. B: Phys. Chem. Glasses*, **47**, 393, (2006)
- [153] P. M. Aguiar and S. Kroeker, *J. Non-Cryst. Solids*, **353**, 1837, (2007)
- [154] V. K. Michaelis, P. M. Aguiar, S. Kroecker, P. J. Bray and J. G. O'Keefe, *J. Non-Cryst. Solids*, **353**, 2582, (2007)
- [155] L. Cormier, G. Calas and B. J. Beuneu, *J. Non-Cryst. Solids*, **353**, 1779, (2007)
- [156] P. Beekenkamp, in *Physics of Non-Crystalline Solids*, ed. J. A. Prins, North-Holland, Amsterdam, (1965), P. Beekenkamp: "Colour Centres in Borate, Phosphate and Borophosphate Glasses", PhD-Thesis, Technical University of Eindhoven, (1965)
- [157] E. I. Kamitsos, M. A. Karakassides and G. D. Chryssikos, *J. Phys. Chem.*, **91**, 1073, (1987)
- [158] P. K. Gupta, *Collected Paper XIV Int. Congr. Glass*, 1, (1986)
- [159] S. A. Feller, W. J. Dell and P. J. Bray, *J. Non-Cryst. Solids*, **51**, 21, (1982)
- [160] T. Uchino and Y. Ogata, *J. Non-Cryst. Solids*, **181**, 175, (1995)
- [161] A. F. Zatsepin, V. S. Kortov and Y. V. Shchapova, *Phys. Solid State*, **39**, 1212, (1997)

References

- [162] K. Suzuki and M. Ueno, *J. Phys. Paris*, **39**, 1212, (1985)
- [163] U. Hoppe, W. Walter, D. Stachel and A. C. Hannon, *Z. Naturforsch.*, **A51**, 179, (1996)
- [164] J. Haines, O. Cambon, R. Astier, P. Fertey and C. Chateau, *Z. Kristallogr.*, **219**, 314 2004
- [165] B. Ewald, Y.-X. Huang and R. Kniep, *Z. Anorg. Allg. Chem.*, **633**, 1517, (2007)
- [166] R. K. Brow, D. R. Talland, S. T. Meyers and C. C. Phifer, *J. Non-Cryst. Solids*, **191**, 45, (1995)
- [167] R. K. Brow, *J. Non-Cryst. Solids*, **263**, 1, (2000)
- [168] D.-B. Xiong, H.-H. Chen, X.-X. Yang and Y.-T. Zhao, *J. Solid State Chem.*, **180**, 233, (2007)
- [169] B. Ewald, Y. Prots, P. Menezes and A. C. Wright, *Inorg. Chem.*, **44**, 6431, (2005)
- [170] C. Müller, E. Zienicke, S. Adams, J. Habasaki, and P. Maass, *Phys. Rev. B*, **75**, 014203, (2007)
- [171] A. Cormack, J. Du and T. R. Zeitler, *Phys. Chem. Chem. Phys.*, **4**, 3193, (2002)
- [172] J. C. Dyre, *J. Non-Cryst. Solids*, **324**, 192, (2003)
- [173] H. Lammert, M. Kunow and A. Heuer, *Phys. Rev. Lett.*, **90**, 215901, (2003)
- [174] B. A. Shakhmatkin, N. M. Vedisheva, M. M. Schultz and A. C. Wright, *J. Non-Cryst. Solids*, **177**, 249, (1994)
- [175] N. M. Vedisheva, B. A. Shakhmatkin and A. C. Wright, *Adv. Mat. Res.*, **39**, 103, (2008)
- [176] M. T. Rinke, "Struktur-Eigenschafts-Korrelationen in Gläsern mit mehreren Netzwerkbildnern: Neue Erkenntnisse aus der Kombination von Festkörper-NMR-Methoden mit der Röntgenphotoelektronen-Spektroskopie", PhD-thesis, Westfälische Wilhelms-Universität Münster, Münster, Germany, (2009)
- [177] Á. W. Imre, F. Berkemeier, H. Mehrer, Y. Gao, C. Cramer, and M. D. Ingram, *J. Non-Cryst. Solids*, **354**, 328, (2008)
- [178] T. Yano, N. Kunimine, S. Shibata and M. Yamamane, *J. Non-Cryst. Solids*, **321**, 147, (2003)
- [179] L. Cormier, O. Majerus, D. R. Neuville and G. Calas, *J. Am. Ceram. Soc.*, **89**, 13, (2006)

-
- [180] R. Christensen, personal communication
- [181] D. Larink, personal communication
- [182] J. C. Dyre, *Phys. Rev. B.*, **48**, 12511, (1993)
- [183] P. Maass, M. Meyer, A. Bunde, and W. Dieterich, *Phys. Rev. Lett.*, **77**, 1528, (1996)
- [184] J. Reinisch, and A. Heuer, *Phys. Rev. B*, **66**, 064301, (2002)
- [185] R. Peibst, "Theorie anormaler Diffusions- und innerer Reibungsprozesse beim Mischkalkaliefekt in Gläsern", Diplomathesis, Technische Universität Ilmenau, Ilmenau, Germany (2005)
- [186] A. Miller and E. Abrahams, *Phys. Rev.*, **120**, 745, (1960)
- [187] B. I. Shlovskii and A. L. Efros: "Electronic Properties of Doped Semiconductors", Springer press, (1984)
- [188] J. Cottaar and P. A. Bobbert, *Phys. Rev. B*, **74**, 115204 (2006)
- [189] P. M. Richards, *Phys. Rev. B*, **16**, 1393, (1977)
- [190] K. S. Chase and D. J. Thouless, *Phys. Rev. B*, **39**, 9809, (1989)
- [191] P. Gartner and R. Pitis, *Phys. Rev. B*, **45**, 7739, (1992)
- [192] D. Stauffer and A. Aharony: "Introduction to Percolation Theory", 2nd ed., Taylor and Francis, London (1994)
- [193] S. Murugavel and B. Roling, *Phys. Rev. B*, **76**, 180202-1, (2007)
- [194] J. Kincs and S. W. Martin, *Phys. Rev. Lett.*, **76**, 70, (1996)
- [195] M. Schuch, C. Trott, and P. Maass, *RSC Adv.*, **1**, 1370, (2011)
- [196] R. Christensen, J. Byer, T. Kaufmann, and S. W. Martin, *Phys. Chem. Glasses: Eur. J. Glass Sci. Technol. Part B*, **50**, 237, (2009)
- [197] D. Zielniok, H. Eckert, and C. Cramer, *Phys. Rev. Lett.*, **100**, 035901, (2008)
- [198] R. L. McGreevy, and L. Pusztai, *Molec. Simul.*, **1**, 359, (1988)
- [199] M. J. Cliffe, M. T. Dove, D. A. Drabold, and A. L. Goodwin, *Phys. Rev. Lett*, **104**, 125501, (2010)
- [200] RMCA Manual (2005), <http://www.wisis2.isis.rl.ac.uk/rmc/>
- [201] D. A. Keen, *J. Appl. Crystallogr*, **34**, 172, (2001)

- [202] R. L. McGreevy, *J. Phys.: Condens. Matter*, **13**, R877, (2001)
- [203] R. Christensen and S. W. Martin personal communication, experimental NMR-Data (not published yet) and providing of the experimental values of E_a
- [204] O. Majerus, L. Cormier, G. Calas, and B. Beuneu, *Phys. Rev. B*, **67**, 024210, (2003)
- [205] J. Swenson, L. Börjesson, and W. S. Howells, *Phys. Rev. B*, **52**, 9310, (1995)
- [206] T. Uchino, and T. Yoko, *Solid State Ionics*, **105**, 91, (1998)
- [207] A. Hall, J. Swenson, C. Karlson, S. Adams, and D. T. Bowron, *J. Phys.: Condens. Matter*, **19**, 415115, (2007)
- [208] C. Müller, V. Kathirarachchi, M. Schuch, P. Maass, and V. G. Petkov, *Phys. Chem. Chem. Phys.*, **12**, 10444, (2010)
- [209] C. T. Chantler, K. Olsen, R. A. Dragoset, J. Chang, A. R. Kishore, S. A. Kotochigova, and D. S. Zucker, "X-Ray Form Factor, Attenuation and Scattering Tables (version 2.1)", (2005), <http://physics.nist.gov/ffast> (National Institute of Standards and Technology, Gaithersburg, MD); C. T. Chantler, *J. Phys. Chem. Ref. Data*, **29**, 597, (2000); C. T. Chantler, *J. Phys. Chem. Ref. Data*, **24**, 71, (1995)
- [210] U. Hoppe, D. Stachel, and D. Beyer, *Physica Scripta*, **T57**, 122, (1995)
- [211] D. M. Pickup, I. Ahmed, P. Guerry, J. C. Knowles, M. E. Smith, and R. J. Newport, *J. Phys.: Condens. Matter*, **19**, 415116, (2007)
- [212] G. Paschina, G. Piccaluga, and M. Magini, *J. Chem. Phys.*, **81**, 6201, (1984)
- [213] E. I. Kamitsos and G. D. Chryssikos, *Solid State Ionics*, **105**, 75, (1998)
- [214] R. D. Shannon, *Acta Cryst.*, **32**, 751 (1976).
- [215] J. Hoshen and R. Kopelman, *Phys. Rev. B*, **14**, 3438, (1976)
- [216] S. Adams and J. Swenson, *Phys. Chem. Chem. Phys.*, **4**, 3179, (2002)
- [217] M. Aniya, *Solid State Ionics*, **136**, 1085, (2000)
- [218] M. Aniya, and J. Kawamura, *Solid State Ionics*, **154**, 343, (2002)
- [219] R. Christensen personal communication
- [220] D. Qiu, P. Guerry, I. Ahmed, D. M. Pickup, D. Carta, J. C. Knowles, M. E. Smith, and R. J. Newport, *Mater. Chem. Phys.*, **111**, 455, (2008)
- [221] V. F. Sears, *Neutron News*, **3:3**, 26, (1992)
- [222] K. W. Kehr, O. Paetzold, and T. Wichman, *Physics Letters A*, **182**, 135, (1993)
- [223] W. F. Pasveer, P. A. Bobbert, and M. A. J. Michels, *Phys. Rev. B*, **74**, 165209, (2006)

List of Figures

1.1.	Sketch of the original version of the Zachariassen model [1] for network-forming glasses (for details see text)	3
1.2.	Typical behavior of the frequency dependent conductivity in disordered systems shown for 0.2Na ₂ O-0.8GeO ₂ glasses (redrawn from [104])	14
2.1.	Conductivity activation energy for 0.3Li ₂ S+0.7[(1-x)SiS ₂ +xGeS ₂] (■) [58], Li ₂ S +[(1-x)GeS ₂ +xGeO ₂] (▲) [63], and rapidly quenched xLi ₄ SiO ₄ +(1-x)Li ₃ BO ₃ (●) [73] glasses. The fits (solid lines) according to Eq. (2.1a) yield $E_{AB}/E_B = 0.69$, $z = 2.8$ for the SiS ₂ -GeS ₂ -system and $E_{AB}/E_B = 0.67$, $z = 2.0$ for the SiO ₂ -B ₂ O ₃ -system. Due to the missing value for $x = 1$ in the GeS ₂ -GeO ₂ -system, we fixed $z = 2$ and fitted $E_a(x)/E_a(x = 0.8)$, yielding $E_A/E_B = 0.63$ and $E_{AB}/E_B = 0.57$.	22
2.2.	Normalized activation energy $E_a(x)/E_a(0)$ for different domain sizes $l = 2.4$ (○), 4.3 (□) and 6.2 (△). The solid line marks the solution Eq. (2.1a) with $z = 4$, and the dashed lines are fits to Eq. (1a) with z as fitting parameter ($E_{AB}/E_B = 0.5$ fixed). Inset: Arrhenius plots of the conductivity (in units of σ_0 , cf. caption of Fig. 2.3) calculated by using the velocity auto-correlation method [135] for $x = 0.0$ (×), and for $x = 0.2$ with $l = 2.4$ (○), 4.3 (□), and 6.2 (△). The slopes of the lines agree with the E_a obtained from the critical path analysis.	24
2.3.	(a) Conductivity spectra $\sigma(\omega)$ (in units of $\sigma_0 = ne^2\nu a^2/E_A$ with n the number concentration of mobile ions) for fixed temperature, $k_B T/E_A = 0.01$, and $x = 0.0$ (triangles), 0.1 (diamonds), 0.2 (circles), and 0.4 (squares). Open symbols refer to the domain size $l = 2.4$ and full symbols to $l = 6.3$; Inset: Conductivity spectra of LiS ₂ +(1-x)GeS ₂ +xGeO ₂ glasses [138] for $x = 0.1$ (circles), $x = 0.2$, (crosses), and $x = 0.4$ (squares) at $T = 253 K$, as well as for $x = 0.6$, $T = 224 K$ (triangles), and $x = 0.8$, $T = 231 K$ (diamonds) (b) Scaled conductivity spectra for the data shown in (a).	25
3.1.	Visualization of a spatial barrier distribution in a squared lattice with $L = 256$ for uniform distributed barrier energies with a Gaussian shaped spatial correlation function and the correlation-length $\xi = 0, 2, 4$ (clockwise starting from upper-left). Blue areas correspond to low energy and red areas to high energy barriers.	30

3.2.	(a) the conductivity isotherms $k_B T \sigma(\omega)$ for a hopping process in a two dimensional system with uniform distributed and spatially correlated random barriers for $\xi = 0.0$ (black open symbols), 1.5 (blue shaded symbols), 3.0 (red closed symbols). (b) The dc conductivity $k_B T \sigma_{dc}$ as function of the characteristic length scale ξ for different β	31
3.3.	(a) $k_B T \sigma_{dc}/\omega_c = F(\xi^2)$, solid lines are linear fit, dashed lines are fits to a function $k_B T \sigma_{dc}/\omega_c = A \xi^{2B}$ with $B \approx 0.8$. for same data as shown in 3.2(a) (b) Mastercurve of $\sigma(\omega)$ scaled by the relation $\sigma(\omega)/\sigma_{dc} = F(\omega/\omega_c)$	32
4.1.	Sketch of the NFUs in alkali borate glasses: Below the chemical representations the charge numbers of the NFUs are given. The charge of the $B^{(4)}$ unit is delocalized over the four bOs, while the charge of the $B^{(2)}$ unit is more localized at the site of the nbO.	36
4.2.	$B^{(4)}$ fraction as a function of alkali fraction $\{M\}$ in alkali borate glasses. The symbols refer to results from MAS-NMR measurements [17, 148, 151, 152, 153, 154] and neutron scattering.[155] Different fillings for the same symbols correspond to different studies. Results from the theoretical modeling are indicated by lines. The dashed line corresponds to the regime of low alkali content ($\{M\} \leq \{M\}_*$). The solid line marks the Beekenkamp result in the regime of high alkali content ($\{M\} > \{M\}_*$) and the dashed line marks the modified Beekenkamp model with $f = 1/4$. The dashed-dotted line indicates the result from the refined modeling in Sec. 4.2.3 for $K = 1.3$	37
4.3.	Sketch of the phosphate NFUs with their charge numbers. The charges are considered to be equally spread over the nbOs.	42
4.4.	Theoretical NFU fractions as a function of x in alkali borophosphate glasses $yM_2O-(1-y)[xB_2O_3-(1-x)P_2O_5]$ for (a) low alkali content $\{M\} = 1/3$ ($y = 0.25$) as predicted by eqs. (4.11)-(4.14), and (b) large alkali content $\{M\} = 2/3$ ($y = 0.4$) as predicted by eqs. (4.11), (4.20)-(4.26). The open symbols in (b) refer to $f = 0$ and the full symbols to $f = 1/4$	45
4.5.	NFU concentrations in the glass $0.4Na_2O-0.6[xB_2O_3-(1-x)P_2O_5]$. The symbols mark MAS-NMR results from [69] and the open symbols at $x = 1$ correspond to the MAS-NMR measurements by [154]. The lines mark the results from the modeling in Sec. 4.3.1 with $f = 1/10$ [eqs. (4.11), (4.20)-(4.26)].	49
4.6.	NFU concentrations in the glass $0.4Na_2O-0.6[xB_2O_3-(1-x)P_2O_5]$. The symbols mark MAS-NMR results [69, 154] and the lines indicate results from the theoretical modeling. The dashed lines refer to the first refinement in Sec. 4.3.2 and the solid lines to the second refinement in Sec. 4.3.3.	50
4.7.	Schematic view of a diborate superstructural unit in $Na_5B_2P_3O_{13}$ -crystals. .	52
4.8.	Two-dimensional sketch of the NUT model. The arrows indicate charge transfer to ion sites as described in the text.	53

-
- 4.9. (a) Arrhenius plot of the simulated Na^+ diffusion coefficients D in $0.4\text{Na}_2\text{O}-0.6[x\text{B}_2\text{O}_3-(1-x)\text{P}_2\text{O}_5]$ for various x and $\Delta = 0.25$ in the case, where no ionic sites were blocked. D is given in units of νa^2 , where ν is the attempt frequency of the ion jumps and a is the lattice constant (mean jump distance). The slope of the regression lines yields the activation energies. (b) Comparison of simulated activation energies (open symbols) with the measured conductivity activation energy from [69] (full squares). The open squares and open triangles refer to the results for the modeling without and with blocked sites, respectively, and the solid and dotted lines are least square fits of sixth order polynomials to these data. For the system without blocked sites $\Delta = 0.25$, and for the system with blocked sites $\Delta = 0.3$. The open circle at $x = 1$ (connected with the dashed line) corresponds to the simulated E_a without blocked sites, if the NFU concentrations from [69] are taken. 54
- 4.10. NFU concentrations from the statistical mechanics approach with $f = 1/10$ (lines) for the glass $0.4\text{Na}_2\text{O}-0.6[x\text{B}_2\text{O}_3-(1-x)\text{P}_2\text{O}_5]$ in comparison with MAS-NMR results [69, 154] (symbols). 59
- 5.1. The experimental species distribution for $x_A\text{Na}_2\text{O}-(1-x_A)(\text{BPO}_4)$ determined by a combined MAS-NMR and XPS analysis [87, 176] in comparison to the modeling. Solids lines correspond to a model where $\text{B}^{(4)}-\text{B}^{(4)}$ linkages are effectively forbidden ($f = 0$), whereas the dotted lines correspond to a model where $\text{B}^{(4)}-\text{B}^{(4)}$ are stabilized by $\text{P}^{(2)}$ units. The vertical dashed-dotted line at $x_A = 0.4$ shows the composition, where the stoichiometry should be the same as $0.4\text{Na}_2\text{O}-0.6[x\text{B}_2\text{O}_3-(1-x)\text{P}_2\text{O}_5]$ (with $x = 0.5$) described by Zielniok *et al.* [69] corresponding to the open symbols 66
- 5.2. The experimental species distribution for $(1-x_B)\text{NaPO}_3-x_B\text{B}_2\text{O}_3$ determined by a combined MAS-NMR and XPS analysis [85, 176] in comparison with the modeling 71
- 5.3. The prediction of the NFU concentrations in an alternative scenario (Eqs. 5.21-5.24 for $\{M\} \leq \{M\}_* = 3/7$ (here $\{M\}=1/3$), which includes the formation of $\text{P}^{(4)}$ units 72
- 5.4. The site energy distribution generated by the model described in sec. 4.4 for a single cubic lattice with 48^3 lattice sites (symbols) and the corresponding values calculated eqs. 5.33 and 5.36 (solid lines). The curves for $x=0.5$ and $x=1.0$ are shifted by 1 and 2 for the sake of clarity 75

- 5.5. (a) The activation energy calculated with the *critical path analysis* (dotted lines) and the *effective circuit approach* (solid and dashed lines) in comparison with E_a estimated by the Arrhenius plots and the linear extrapolation of the apparent activation energies to $1/\beta \rightarrow 0$ as a function of x .
 (b) apparent activation energy for all x . Symbols are the simulation results and solid lines are the corresponding least squared fits.
 (c) Rescaling of $E_a \rightarrow E_a(x)/E_a(x=0)$. The species distributions used in the simulations were generated with the f -model described in sec. 4.3.
 (d) The time dependent diffusion function $D(t) = \langle r^2(t) \rangle / (6t)$ for $x=0.0$. The MC-simulations were performed according the NUT model with $\Delta = 0.25$. 80
- 5.6. (a) Arrhenius plots for the diffusion constant for $0.005 \leq \{M\} \leq 0.16$. (continuous decrease of the incline with increasing $\{M\}$) (b) apparent activation energy for all $\{M\}$ (symbols are the same as in (a)) as a function of β^{-1} . Solid lines corresponds to linear fits. Dashed lines are fitted by eq. 5.52 (c) The comparison between activation energies predicted by the *critical path analysis* with $E^{min} = -\infty$ (blue dotted line), $E^{min} = E_f$ (red dotted line) and the *effective circuit approach* with $p_c^{bond} = 0.08, 0.10, 0.12$ (lower dashed, solid, upper dashed line) with the results given by the incline of the Arrhenius plots (circles), linear extrapolation (filled squares) and the extrapolation according eq. 5.52 (open squares) of E_a^{app} to the zero temperature lines. (d) The time dependent diffusion function for $\{M\} = 0.16$. The MC-simulations were performed according to the NUT model with $\Delta = 0.25$ 82
- 5.7. Schematic explanation why $E_a^{(app)}(T)$ increases with decreasing T . The energies E_1 and E_2 are the boundaries of the subset of sites, which form the relevant cluster for long range transport (a) $T \rightarrow 0$ $E_a^{(app)}(0) = E_a^{(\infty)} = E_2(0) - E_1(0)$ is larger than the apparent activation energy for case (b) $T \gg 0$ with $E_a^{(app)}(T) = E_2(T) - E_1(T)$
 Note: The area under the curve between E_1 and E_2 has the same value . . . 83
- 6.1. High energy XRD structure factors $S(q)$ of $0.35\text{Na}_2\text{O}-0.65[x\text{B}_2\text{O}_3-(1-x)\text{P}_2\text{O}_5]$ glasses from the RMC Models A-C (a-c), and (d) redrawn from the RMC model developed in [128] in comparison with experimental data. The simulated structure factors are marked by solid lines and the experimental data by symbols (redrawn from [128]). The data have been offset by 1.0 to show the results for the different mixing parameters $x = 0, 0.2, 0.4, 0.6, 0.8$, and 1 (from bottom to top). 95

6.2.	Pair correlation functions $G(r)$ of $0.35\text{Na}_2\text{O}-0.65[x\text{B}_2\text{O}_3-(1-x)\text{P}_2\text{O}_5]$ glasses from the RMC Models A-C (a-c), and (d) redrawn from the RMC model developed in [128] in comparison with experimental data. The simulated pair correlations are marked by solid lines and the experimental data by symbols (redrawn from [128]). The data have been offset by 4.0 to show the results for the different mixing parameters $x=0, 0.2, 0.4, 0.6, 0.8,$ and 1 (from bottom to top).	96
6.3.	The fraction of $\text{Q}^{(n)}$ -species with respect to the overall amount of network forming units for the Models A and B in comparison with calculated values from the theoretical model developed in [195]. Data for Model C can almost not be distinguished from those shown for Model B.	97
6.4.	Fraction of sodium ions with the given oxygen coordination numbers in the RMC structures generated from Model B.	98
6.5.	Fraction of sodium ions with the given oxygen coordination numbers in the RMC structures generated from Model C.	98
6.6.	Fraction of bOs connecting different network forming cations as a function of the mixing-parameter x for Model C. The full/open symbols correspond to the models with/without forbidden $\text{B}^{(4)}\text{-B}^{(4)}$ linkages. The solid lines mark the results in the case where the network forming cations would be randomly connected by the bOs. The dotted lines are guides to the eye connecting the data for forbidden $\text{B}^{(4)}\text{-B}^{(4)}$ linkages.	99
6.7.	Partial pair distribution functions for the pairs (a) B-B, (b) B-P, and (c) P-P. The dashed/solid lines correspond to the RMC models with/without forbidden $\text{B}^{(4)}\text{-B}^{(4)}$ linkages.	100
6.8.	Partial pair distribution functions for the pairs (a) B-bO, (b) B-nbO, (c) P-bO, and (d) P-nbO. The dashed/solid lines correspond to the RMC models with/without forbidden $\text{B}^{(4)}\text{-B}^{(4)}$ linkages.	101
6.9.	Cube root $F^{1/3}$ of the fraction of the percolating accessible volume for the sodium ions as a function of the mixing-parameter x . Squares/circles refer to the results calculated from the RMC Model C without/with forbidden $\text{B}^{(4)}\text{-B}^{(4)}$ linkages. The line marks the average value around which the $F^{1/3}$ values scatter. The inset shows the variation of the conductivity activation energy E_a for $0.35\text{Na}_2\text{O}-0.65[x\text{B}_2\text{O}_3-(1-x)\text{B}_2\text{O}_5]$ glasses [203] (the line is drawn as a guide to the eye).	103
7.1.	Comparison of $S(q)$ and $G(r)$ calculated from model C of chapter 6 with the experimental X-ray (left) and neutron (right) diffraction data	107
7.2.	Final structures of the RMC procedure without the additional constraint of avoiding bOs connecting two $\text{B}^{(4)}$ (red marks oxygen, yellow phosphorous, grey boron, and violet sodium atoms)	110

7.3. Final structures of the RMC procedure with the additional constraint of avoiding bOs connecting two B ⁽⁴⁾ (red marks oxygen, yellow phosphorous, grey boron, and violet sodium atoms)	111
7.4. Comparison of $S(q)$ and $G(r)$ after further RMC refinement (dashed and doted lines) starting from model C with experimental (solid lines) X-ray (left) and neutron (right) diffraction data. The dashed lines correspond to the model with allowed and the dotted lines with avoided bOs connecting B ⁽⁴⁾ units	112
7.5. Partial pair correlation functions for the partials B-B (a,b), B-P (c,d) and P-P (e,f), for the modeling with allowed (a,c,e) and with avoided (b,d,f) bOs connecting two B ⁽⁴⁾ . The solid lines correspond to the results from chapter 6 and the dashed lines to the refined RMC models with X-ray and neutron diffraction data.	113
7.6. The partial pair correlation functions for the partials B-bO (a), B-nbO (c), P-bO (b) and P-nbO (d). The solid lines correspond to the results from chapter 6 and the dashed and doted lines to the refined RMC models with X-ray and neutron diffraction data with allowed and with avoided bOs connecting two B ⁽⁴⁾	114
7.7. Histograms for the number of oxygen coordinating sodium atoms in a coordination sphere with a radius of 3 Å (black original version of model C, red optimization with a reduced fraction of bO bridging two B ⁽⁴⁾). Additional Na-O coordination constraints have been disregarded (for details, see text) .	115
7.8. Histograms for the number of oxygen coordinating sodium atoms in a coordination sphere with a radius of 3 Å (black original version of model C, red optimization with a reduced fraction of bO bridging two B ⁽⁴⁾). Additional Na-O coordination constraints have been taken into account (for details, see text)	116
7.9. Top: The cube root of the volume fraction F of the conduction pathways vs. x , RMC optimization with the XRD data taken from ref. [128] and the inclusion of Na-O constraints (circles), RMC optimization with X-ray [128] and neutron data [129] without (triangles) and with (squares) additional consideration of Na-O constraints. Inset shows the experimental determined activation energy [203] Bottom: the accessible volume per cation for the RMC results with X-ray and neutron optimization. (closed symbols correspond to the original version of Model C, open symbols correspond to the additional constraint of reduced B ⁽⁴⁾ -B ⁽⁴⁾ connections) . .	117

A.1. Arrhenius plots for the constant of Diffusion D estimated by the a linearization of the rate equation on the MF and LPA level of description (detail see text) and the application of the <i>effective circuit approach</i> (ECA) in combination with the <i>velocity auto correlation</i> (VAC) method [105]	V
A.2. (a) Frequency dependent conductivity $\sigma(\omega)$ for $c_p = 0.05$ (full symbols) and $c_p = 0.5$ (open symbols) calculated for $\beta = 20$ (black) and $\beta = 40$ (red) with the <i>mean field approach</i> (MF) and the <i>linearized pair approximation</i> (LPA). (b) Scaling of the data from (a) in respect to relation $\sigma(\omega)/\sigma(0) = F(\omega/\omega_c)$ where ω_c is determined by the criterion $\sigma(\omega_c) = \sqrt{10}\sigma(0)$	V

Acknowledgments

Writing a PhD-thesis is an extraordinary intellectual and mental challenge and the search of knowledge leads often not to the desired inspiration but to death ends. In such a situation it is advantageous if not necessary to work in an environment that offers help and support. I had the big luck that my supervisor Prof. P. Maass gave me such an environment. I am not sure if I had finished the present thesis without his patience and the large number of his very helpful suggestions.

I have also to acknowledge Prof. S. W. Martin and his students R. Christensen and Y. Kim from Iowa State University for support of the present thesis, providing me the experimental data and helped me to improve in particular the quality of the presentations in chapters 2 and 6. I remember gratefully the very interesting discussions with them.

Further I thankfully acknowledge the support of Prof. Eckert and his students M. Rinke and D. Larink from Münster University. The discussion with them about the MGFE gave me deeper insights in this effect.

But many other people helped me writing the present thesis. I have to note in particular my former colleagues, C. Trott, T. Hennig, M. Sandbrink, S. Engel, S. Hahne, M. Dierl, M. Einax and W. Beenken at TU Ilmenau or University of Osnabrück and my actual colleagues E. Wittney and A. Dere at the WIWeB Erding. The discussion with those people give me many input and help me to refine the quality of the present thesis.

Last but not least I have to mention the help and patience of my family and my spouse S. Kokott - without their support I had never finished the present work and therefore the present script is dedicated to them.

Erklärung über die Eigenständigkeit der erbrachten wissenschaftlichen Leistung

Ich erkläre hiermit, daß ich die vorliegende Arbeit ohne unzulässige Hilfe Dritter und ohne Benutzung anderer als der angegebenen Hilfsmittel angefertigt habe. Die aus anderen Quellen direkt oder indirekt übernommenen Daten und Konzepte sind unter Angaben der Quelle gekennzeichnet.

Bei der Auswahl und Auswertung folgenden Materials haben mir die nachstehend aufgeführten Personen in der jeweils beschriebenen Weise entgeltlich/unentgeltlich geholfen:

1. _____

2. _____

3. _____

Weitere Personen waren an der inhaltlichen materiellen Erstellung der vorliegenden Arbeit nicht beteiligt. Insbesondere habe ich hierfür nicht die entgeltliche Hilfe von Vermittlungs- bzw. Beratungsdiensten (Promotionsberater oder andere Personen) in Anspruch genommen. Niemand hat von mir unmittelbar oder mittelbar geldwerte Leistungen für Arbeiten erhalten, die im Zusammenhang mit dem Inhalt der vorgelegten Dissertation stehen.

Die Arbeit wurde bisher weder im In- noch im Ausland in gleicher oder ähnlicher Form einer anderen Prüfungsbehörde vorgelegt.

Erding, 22.11.2017
Ort, Datum


Unterschrift